Baldo Sahlmüller

Probing Hot and Dense Matter: Measurement of Neutral Mesons and Direct Photons in Ultrarelativistic Au+Au Collisions

— 2010 —

Experimentelle Physik

Probing Hot and Dense Matter: Measurement of Neutral Mesons and Direct Photons in Ultrarelativistic Au+Au Collisions

Inauguraldissertation
zur Erlangung des Doktorgrades
der Naturwissenschaften im Fachbereich Physik
der Mathematisch-Naturwissenschaftlichen Fakultät
der Universität Münster

vorgelegt von
Baldo Sahlmüller
aus Münster

— 2010 —

Dekan:	Prof. Dr. J. P. Wessels
Erster Gutachter:	Prof. Dr. J. P. Wessels
Zweiter Gutachter:	PD. Dr. K. Reygers
Tag der Disputation:	28.01.2010
Tag der Promotion:	28.01.2010

Contents

1. Introduction

> Nothing in life is to be feared, it is only to be understood. Now is the time to understand more, so that we may fear less.
>
> *M. Curie*

Since the year 2000, the Relativistic Heavy Ion Collider (RHIC), located at the Brookhaven National Laboratory (BNL) on Long Island, near New York City, USA, has carried out collisions of atomic nuclei at ultrarelativistic energies. RHIC is one of several particle accelerators in a row of increasing collision energies to study the behavior of nuclear matter under extreme conditions. Its predecessors in terms of energy were the Super Proton Synchroton (SPS) at CERN in Geneva, and the Alternating Gradient Synchroton (AGS) at BNL. Nowadays, a new energy regime will be reached when the Large Hadron Collider (LHC) will smash nuclei into each other at more than 10 times the energy available at RHIC while the planned FAIR facility at the GSI in Darmstadt will focus on creating higher net baryon densities at lower energies.

The main goal of all these experimental programs is the discovery and the study of the so-called Quark-Gluon Plasma (QGP), a state of nuclear matter predicted in the 1970s for large energy or baryon densities. This QGP is studied through a variety of possible signatures that are measured by large detectors constructed around the collision zones. In 2000, CERN announced the discovery of a new state of matter at SPS, with many signatures that would be expected in the presence of a QGP [Hei00]. Three years later, BNL released a press statement, stating that experimental results from RHIC hint at the creation of an unusually hot and dense form of matter. In 2005, the four experiments at RHIC jointly published articles [Ada05, Adc05, Ars05, Bac05] summarizing the key measurements and conclusions from the first years of RHIC collisions, announcing the discovery of a state of matter similar to the predicted QGP, however differing from the predictions in some of the signatures. For example, the matter created at RHIC did not behave like an ideal gas, rather it inhibited characteristics of a perfect fluid. Therefore, it is sometimes referred to as sQGP (Strongly Coupled Quark-Gluon Plasma).

Though a new state of matter was shown to be created at RHIC with the data from the first three run periods, the accelerator continued to collide heavy ions and protons, delivering significantly larger amounts of data as well as new colliding particle species,

allowing the search of rare signatures as well as the study of the system size dependence, and the possibility of obtaining quantitatively significant results in contrast to the more qualitative discoveries in the first years.

One of the key signatures attributed to the presence of a QGP in RHIC collisions is the measured suppression of neutral pions and other hadrons in central Au+Au collisions at center-of-mass energies of 200 GeV per nucleon. This suppression is explained by the quenching of particle jets that traverse the hot and dense matter. This measurement is of further interest due to the following reasons. First, the dependence of the suppression on the transverse momentum (p_{T}) of the measured hadron towards higher p_{T} is an important input for the theoretical understanding of jet quenching effects in the QGP and the nature of the energy loss. The study of different hadrons can also shed further light on the mechanisms of energy loss in the medium. Moreover, a reduction of the uncertainties of the measurement allows to constrain parameters attributed to the energy loss mechanism in such theoretical models.

Another key observable are direct photons. Here, the absence of a suppression measured in the early RHIC runs, helped establishing the energy loss picture for hadrons as mentioned above. But a more detailed study of direct photon production, with reduced uncertainties, is important to allow disentangling different production mechanisms of such direct photons in collisions of heavy nuclei, helping in the understanding of interactions of partons inside the medium. Direct photons can be produced in hard scattering processes as well as in terms of thermal radiation or via the interaction of a scattered parton with the QGP and are thus expected to be partially sensitive to medium properties.

This thesis is organized as follows: In Chapter 2, theoretical basics necessary for the understanding of hot and dense matter and for the understanding of the studied signatures are presented. The experimental setup is described in Chapter 3, followed by a description of the data analyses for the measurement of neutral pions, η mesons and direct photons in the Chapters 4 to 6. The results of the analyses are presented and discussed in Chapter 7, including comparisons to theoretical model descriptions.

2. Theroretical Basics

Now follow we out by Starloe!
Three quarks for Muster Mark!
Sure he hasn't got much of a bark
And sure any he has it's all beside the mark.

J. Joyce - Finnegans Wake

2.1 Matter and the Quark-Gluon Plasma

Since millennia, humans have thought about the structure of the matter that makes up the universe. Several centuries BC, the Greek philosopher Demokrit already postulated the existence of a smallest unit of matter, he called it $\alpha\tau o\mu o\sigma$, the greek word for indivisible. His idea was again picked up more than 2000 years later by the English chemicist John Dalton from the observation of chemical reactions. Another 100 years later, in 1909, Ernest Rutherford observed that atoms must have a substructure by scattering alpha particles off a gold foil [Rut11]. This observation was subsequently explained with the existence of an atomic nucleus, consisting of protons and neutrons, and a shell, consisting of electrons. After more and more hadrons were observed in the 1950s and 1960s, a substructure of the nucleons - and all other hadrons - was postulated in 1964 by Murray Gell-Mann [GM64] and George Zweig [Zwe64], and later confirmed experimentally [Blo69, Bre69]. In the following years, the standard model of particle physics evolved.

2.1.1 The Standard Model

The fundamental structure of matter as well as the fundamental interaction forces can be very well described by the *Standard Model of Particle Physics*. The basic „ingredients" of this theory are three types of particles: *quarks*, *leptons* and *gauge bosons*. There are six different quarks (down, up, strange, charm, bottom and top) and their corresponding antiquarks, six different leptons (electron, electron neutrino, muon, muon neutrino, tau and tau neutrino) and the corresponding antileptons and four types of gauge bosons as the force-carrying particles (gluon, photon, $W^{\pm}$/Z-boson). Each of the bosons has an integer spin and mediates one fundamental interaction force. The $W^{\pm}$- and Z-bosons carry the weak interaction, the photon the electromagnetic force and the gluon is the force-carrying particle of the strong force. The electromagnetic and the weak interaction can be described in one unified theory as the so-called electroweak interaction. The so-called *Higgs boson*

is responsible for the existence of mass of elementary particles in the Standard Model, this particle is still to be experimentally confirmed. The model does not include gravitation and its gauge boson, the graviton. The quarks and leptons that make up the standard model are shown in Table 2.1. [Per00, Pov06, Yag08]

Fermions	Family			electric	color
	1	2	3	charge	charge
Quarks	u	c	t	+2/3	r, b, g
	d	s	b	-1/3	
Leptons	ν_e	ν_μ	ν_τ	0	–
	e^-	μ^-	τ^-	-1	–

Table 2.1: Quark and lepton families.

These quarks and leptons, together with the gauge bosons, are assumed being fundamental particles without further substructure. They are fermions with a spin of $\pm 1/2$. One can sort both quarks and leptons into three different classes, the so-called generations or families. Each generation consists of two strongly interacting quarks – one with an electric charge of $-1/3e$ and the other with one of $+2/3e$ –, a charged lepton and a neutrino. Quarks carry another charge, the so-called *color charge*, that can have three states, called red, green, and blue, and the corresponding anti states. This color charge is necessary for quarks to comply with the Pauli principle. The strong interaction is one of the fundamental forces in the standard model. For it couples to the color charge, it only affects quarks and gluons. Unlike the other fundamental forces, the gluon as the force-carrying gauge boson itself is also affected by the force. The strong interaction is described by quantum chromodynamics (QCD). The coupling constant is the parameter in such quantum field theories that describes the strength of the interaction. The coupling constant α_s of QCD shows a unique feature, as it heavily depends on the momentum transfer Q^2 in a collision of quarks or gluons. Regarding large momentum transfers, the coupling constant can be approximated as [Pov06]

$$\alpha_s(Q^2) \approx \frac{12\pi}{(33-2N_\mathrm{f})\cdot \ln(Q^2/\Lambda^2_\mathrm{QCD})\,.} \tag{2.1}$$

Λ is an experimentally determinded QCD scale parameter, being $\Lambda \approx 250$ MeV/c. N_f is the number of the accessible quark flavors and can obviously not become larger than six, however, virtual quark antiquark pairs can only be separated for large momentum transfers Q^2, therefore N_f depends on Q^2 and is between 3 and 6. The equation is only valid for momentum transfers that are large compared to the scale parameter ($Q^2/\Lambda^2 \gg 1$), but it still shows the phenomenon that the coupling becomes weaker with increasing momentum

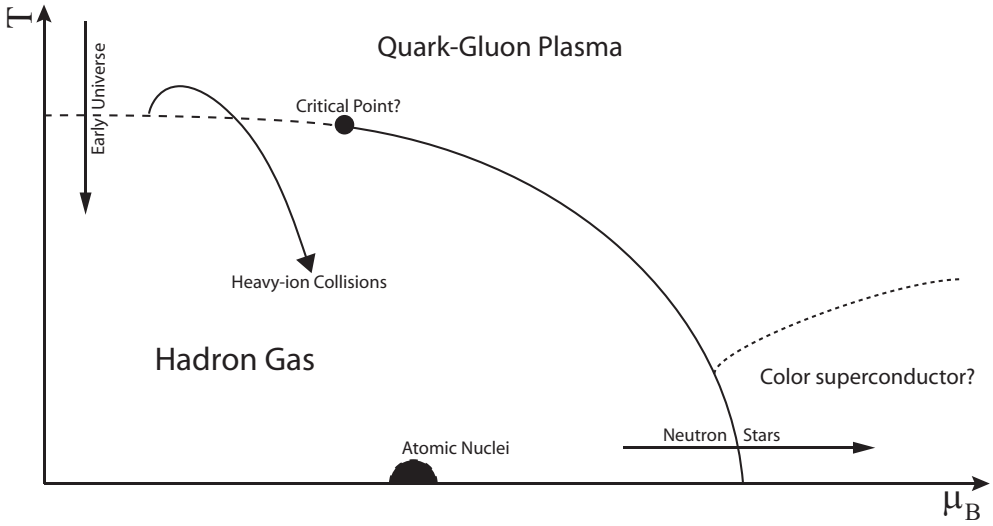

Figure 2.1: Phase diagram of strongly interacting matter. The transition towards the quark-gluon plasma or a possible color superconductor can be seen at high temperatures and high baryochemical potentials, respectively.

transfers.
Looking at the phenomenological potential of the strong interaction [Per00]

$$V_s(r) = -\frac{4}{3}\frac{\alpha_s(r)}{r} + k \cdot r \,, \tag{2.2}$$

one can distinguish two contributions to the overall potential: a Couloumb-like term $\sim 1/r$, dominating at small distances, and a linear term $\sim r$, dominating at larger distances. The first term depends on α_s which depends on r itself. Because $\alpha_s \to 0$ for $r \to 0$, this leads to the asymptotic freedom. The second term leads to a confinement of the field lines into small tubes or strings, which can be explained by gluon-gluon interactions. Therefore it is not possible to observe single quarks or to separate two quarks. When e.g. a quark-antiquark pair is separated, only new color-neutral particles are created because it is energetically favored.

2.1.2 QCD Phase Diagram and Deconfinement

The *phase diagram of strongly interacting matter*, shown schematically in Figure 2.1, depicts possible phases of nuclear matter depending on its temperature T and the baryochemical potential μ_B. At low temperatures and low baryochemical potentials, nuclear matter exists in its ordinary form, e.g. as in atomic nuclei. Under extreme conditions, i.e. at high temperatures or at high baryonchemical potentials, a phase transition occurs. After such a phase transition, the matter exists in a state called quark-gluon plasma (QGP).

In this QGP, quarks and gluons can interact over much larger distances than in nuclear matter where they are bound into the volume of a nucleon. As seen in the phase diagram, two extreme cases can be distinguished: a QGP at low temperatures and high net baryon densities, or a QGP at high temperatures and low densities.

The first case is expected to occur e.g. inside neutron stars, such a "cold" quark-gluon plasma was first predicted in 1975 [Col75]. There is also the possibility of color superconductivity under these conditions, this idea was proposed in 1977 [Bar77]. The second case of a "hot" QGP was first suggested in 1980 [Shu80], it is assumed to have existed in nature shortly after the big bang and can nowadays be accessed experimentally in particle colliders where in head-on collisions of heavy nuclei the temperatures are expected to rise above the critical temperature T_C where hadronic matter transforms into a QGP.

The QGP can be described by different models, one of these models is the *MIT Bag Model* [Cho74], a phenomenological model assuming quarks and gluons inside a so-called bag. Within the bag, the partons have zero masses while outside, their masses are regarded as infinite. The model assumes that the quarks can move freely inside the bag and that it needs energy to pull a quark out of the bag. This is modeled by the introduction of a pressure B with a pressure gradient towards the bag which is counteracted by the pressure of the quarks inside the bag due to their kinetic energy. The bag pressure for a radius R filled with N quarks is

$$B^{\frac{1}{4}} = \left(\frac{2.04N}{4\pi}\right)^{\frac{1}{4}} \frac{1}{R} \,. \tag{2.3}$$

The critical temperature T_C can be estimated by looking at the (outward) pressure P of a quark-gluon plasma at a temperature T while regarding the partons as free particles:

$$P = 37\frac{\pi^2}{90}T^4. \tag{2.4}$$

The critical temperature is now the temperature for which P and the bag pressure are equal, therefore it is

$$T_C = \left(\frac{90}{37\pi^2}\right)^{\frac{1}{4}} B^{\frac{1}{4}} \,. \tag{2.5}$$

With an assumed hadron radius of 0.8 fm, and three quarks in a baryon, the obtained bag pressure constant is $B^{1/4} = 206$ MeV[Won94].

Another way of calculating the critical temperature are lattice QCD calculations. Here, space and time are discretized on a lattice; this method is necessary as currently results from pure QCD calculations are not accessible due to the non-linear nature of the theory. Nowadays, lattice QCD calculations start taking into account more realistic quark masses

which was not possible some years ago due to the lack of sufficiently fast enough computers. Modern lattice calculations also use more advanced algorithms enabling the use of more realistic parameters. They yield results on QGP properties such as the energy density or the speed of sound. Furthermore, they calculate observables such as baryon masses with increasing accuracy [Jan08, Pet09]. Such lattice calculations have shown a rapid increase of the energy and entropy density at temperatures $T = (185 - 195)$MeV [Baz09], an indication for deconfinement.

2.2 Ultrarelativistic Heavy-Ion Collisions

Throughout the last more than 20 years, heavy nuclei have been collided at experimental facilities with increasing energy, in an attempt to create a quark-gluon plasma. So far, the energy regime has been increased by a factor of 40, starting with collisions at the AGS[1] at BNL with energies up to $\sqrt{s_{\mathrm{NN}}}$ = 5 GeV, then with energies of $\sqrt{s_{\mathrm{NN}}}$ = 17.3 GeV at the CERN-SPS[2] and nowadays at RHIC at energies up to $\sqrt{s_{\mathrm{NN}}}$ = 200 GeV. The next step will be the upcoming experimental program at the LHC[3] at CERN which will collide heavy ions with energies up to $\sqrt{s_{\mathrm{NN}}}$ = 5 TeV.

Nucleon-Nucleon Collisions

In general, a collision of two heavy nuclei can be viewed as a superposition of collisions of two nucleons. Therefore, the understanding of $p+p$ collisions is important for the understanding of heavy-ion collisions. In $p+p$ collisions, mainly basic soft and hard scattering processes are observed, the latter can be well described by pQCD calculations at next-to-leading order (NLO). The total cross section of such collisions is almost independent of the collision energy over a large range of 10 GeV$\leq \sqrt{s} \leq$ 1000 GeV, for $\sqrt{s} = 10$ GeV, it is about 40 mb, only slightly increasing with increasing center-of-mass energies [Ams08]. This total cross section is dominated by inelastic scattering processes in which new particles are produced, the total inelastic cross section for $p+p$ collisions at $\sqrt{s}$ = 200 GeV is $\sigma_{inel}(p+p) \approx 42$ mb. The production of charged particles in such collisions can be described depending on the center-of-mass energy, the simple relation between the number of produced charged particles is [Tho77, Won94]

$$\langle N_{ch} \rangle = 0.88 + 0.44 \ln s + 0.118 (\ln s)^2 \,, \tag{2.6}$$

s is given in GeV^2 here. A large fraction of the produced particles are pions ($\pi^{\pm}$,π^0), neglecting the production of other partons and assuming that all three pions are produced

[1] Alternate Gradient Synchroton
[2] Super Proton Synchroton
[3] Large Hadron Collider

with equal cross-section, one can calculate the total number of produced particles as well as $\langle N_{total} \rangle = 3/2 \cdot \langle N_{ch} \rangle$, or

$$\langle N_{total} \rangle \simeq 1.32 + 0.66 \ln s + 0.177 (\ln s)^2 \, . \tag{2.7}$$

These particles are produced in two different regimes. Soft processes account for the majority of particle production, they dominate at low transverse momenta $p_{\mathrm{T}} \leq 1\mathrm{GeV}/c$. The average transverse momentum $\langle p_{\mathrm{T}} \rangle \approx 0.3\mathrm{GeV/c}$. The spectral shape of these particles is well described by an exponential function $e^{-\alpha p_{\mathrm{T}}}$, with α denoting a constant. Soft processes are characterized by a small momentum transfer Q^2 which is of the order of the QCD scale. However, it was found that the cross section for these soft particles cannot be extrapolated to high p_{T}, in that region, so-called hard processes become dominant for particle production. These hard processes are characterized by high momentum transfers and can be treated in QCD perturbatively (pQCD). In pQCD, the cross section for a hadron can be written as [Col85, KB04]

$$E \frac{\mathrm{d}^3 \sigma_h}{\mathrm{d}p^3} = \sum_{a,b,c} f_a(x, Q^2) \otimes f_b(x, Q^2) \otimes \frac{\mathrm{d}\sigma_{ab \to c}}{\mathrm{d}^3 \mathrm{p}} \otimes D_{c/h}(z, Q^2) \, . \tag{2.8}$$

Here, four terms are distinguishable. The first two terms, $f_{q,g}(x, Q^2)$, are the parton distribution functions in the colliding nuclei a and b. They are experimentally accessible in deep inelastic scattering of electrons and nuclei and depend on the momentum transfer and the fraction of momentum x the parton carries. The third term is the term describing parton scattering in the form $ab \to c$, it can be calculated perturbatively. $D_{c/h}(z, Q^2)$ after all is the non-perturbative, universal fragmentation function of the scattered parton c into the hadron h. It depends on the momentum transfer and on the momentum fraction of the hadron with respect to the parton's momentum $z = p_h / p_c$. The fragmentation functions can also be determined experimentally. If the outgoing particle in the hard scattering process is a photon, the fragmentation function becomes a δ function.The hard spectrum at high p_{T} is best described by a power law function.

Nucleus-Nucleus Collisions

Ultrarelativistic heavy-ion collisions can generally be divided into different stages. In the beginning, the incoming nuclei approach each other with relativistic velocities, thus being Lorentz-contracted and pancake shaped. The two nuclei collide then in a collision geometry, characterized by the impact parameter b which is the minimum distance between the centers of the two nuclei. Central collisions are thus characterized by a small impact parameter, in such collisions, the highest energy densities are reached. In more

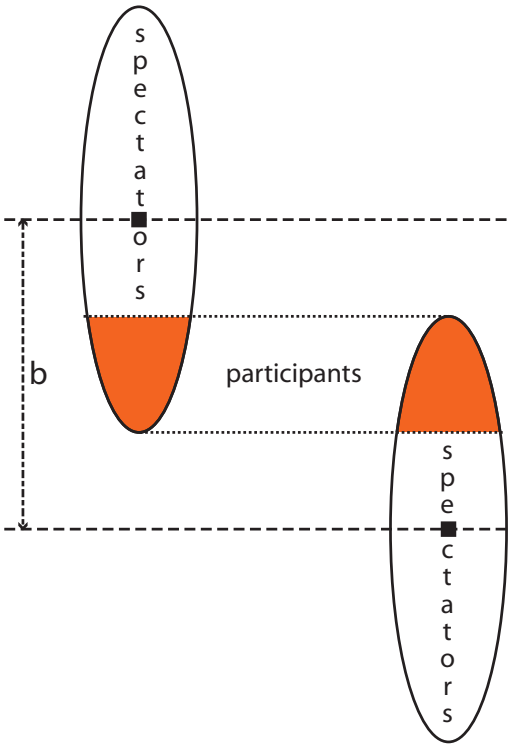

Figure 2.2: Two nuclei shortly before the collision. The nuclei are Lorentz contracted. The impact parameter b is the distance between the centers of the two nuclei. The region of the participants is shaded, the spectators are the nucleons outside this overlap region.

peripheral collisions, with rising impact parameters, only parts of the nuclei overlap. The nucleons in the nuclei can now be classified into two categories: the *spectators* are those nucleons outside the collision region, they can leave the collision region without further interaction. The nucleons in the overlap region are called *participants*, they undergo collisions with nucleons from the other nucleus in the interaction. A sketch of two nuclei before the collision is shown in Figure 2.2. This participant-spectator model is valid due to the short de Broglie wavelength of the nucleons in ultrarelativistic collisions, compared to the size of the nucleus.

The space-time evolution of the medium created in an ultrarelativistic heavy-ion collision is depicted schematically in Figure 2.3. The Landau picture [Lan53a] describes high-energy hadron collisions assuming that the colliding nucleons are slowed down significantly and remain in the collision zone, subsequently particles are produced within the nuclear matter, creating a hot region filled with baryons. This region then expands hydrodynamically along the beam axis [Yag08]. However, this picture can only be applied at lower collision energies of $\sqrt{s_{\mathrm{NN}}} \leq 10\mathrm{GeV}$, at higher center-of-mass energies, the Bjorken picture [Bjo76] has to be regarded instead. In contrast to Landau, Bjorken

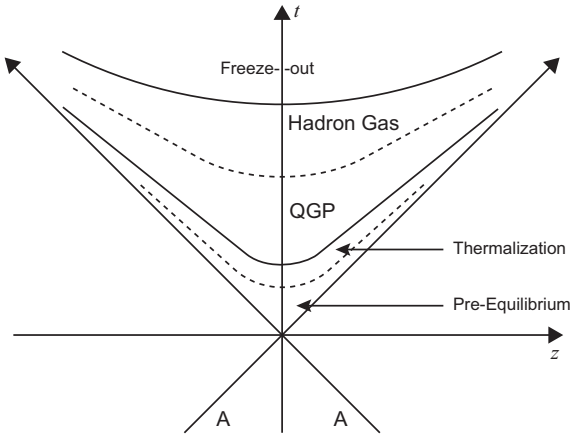

Figure 2.3: Idealized space-time view of a central ultrarelativistic nucleus-nucleos collision and the phases after the collision.

bases his picture on the existence of partons, particle production is affected by time dilation and so-called wee partons reside in the nucleons. These wee partons carry a much smaller momentum fraction x than the valence quarks in the nucleons, they originate from vacuum fluctuations or from the color glass condensate, a coherent classical field created by the source of fast partons. In the Bjorken picture, a collision of two ultrarelativistic nuclei leaves behind a region of highly excited matter with a low net baryon number, formed by the wee partons. These wee partons exist in a pre-equilibrium stage of the collision, they need a certain decoherence time, τ_{de} do de-excite into real quarks and gluons. These real particles then can interact with each other and compose a (quark-gluon) plasma that equilibrates after a time τ_0, the equilibration or formation time. τ_0 is of course larger than τ_{de}, it is about 1 fm/c [Yag08].
The phase in the thermal equilibrium is commonly assumed to be the quark-gluon plasma, it undergoes hydrodynamic expansion. At RHIC energies, recent experimental results suggest that the phase is not like an ideal gas of quarks and gluons but similar to a perfect fluid, i.e. it has vanishing viscosity. With further expansion, the temperature decreases and the QGP phase transforms into a hot hadron gas (HHG), it is expected that there is a mixed phase between QGP and HHG. After further expansion and decrease in temperature, the hadron gas freezes out. At the chemical freeze-out, no further inelastic collisions between particles in the gas occur and the particle composition is fixed. When elastic collisions also cease, the thermal freeze-out takes place, at this point, the system falls out of kinetic equilibrium, too. [Won94, Yag08]

2.3 Signatures of a Quark-Gluon Plasma

There is no single signature that provides evidence for the creation of a quark-gluon plasma alone, therefore, a variety of signatures together have to be taken into account when studying heavy-ion collisions in the light of a QGP creation. Those signatures were already proposed before the startup of RHIC (see e.g. [Har96]). The possible signatures have been reviewed based on the results from the first years of RHIC by different authors [Gyu05, BM07, Ull] and also in different books [Yag08, Vog07]. Furthermore, the RHIC experiments themselves reviewed their experimental results from the first three years in four so-called white papers [Ada05, Adc05, Ars05, Bac05]. Therefore, only a short summary of such signatures will be given in the following.

The measurement of global observables such as the transverse energy E_{T} or the rapidity distributions of charged particles allow to determine thermodynamic properties of the medium such as the energy density or the temperature. The rapidity distribution for different collision energies at RHIC has been measured by PHOBOS [Bac03b], showing an increase in the charged particle multiplicity $\mathrm{dN_{ch}}/\mathrm{d}\eta$ with increasing energy. PHENIX has measured the transverse energy together with the charged multiplicity [Adc05]. Using a formula by Bjorken for the energy density [Bjo83]

$$\varepsilon_0 = \frac{1}{\pi R^2 \tau_0} \frac{\mathrm{d}E_{\mathrm{T}}}{\mathrm{d}y}\bigg|_{y\simeq 0} \tag{2.9}$$

the initial energy density for Au+Au collisions at $\sqrt{s_{\mathrm{NN}}}$ = 200 GeV can be derived from the data as $\varepsilon_0 \sim 4(7)$ GeV/fm^3 for τ_0 =1.0 (0.5) fm, respectively. This is much higher than the critical energy density for the phase transition of about 1 GeV.

The chemical equilibrium of the system is characterized by particle ratios such as $\bar{p}/p$, $\bar{\Omega}/\Omega$, or K^-/π^-. The measured particles ratios can be compared to thermochemical models that depend on a temperature T and a baryochemical potential μ_B. In 200 GeV Au+Au collisions, such a model agrees well with the data for $T = (160.5 \pm 2)$MeV and $\mu_B = (20 \pm 4)$MeV [And06]. An enhancement of strangeness, i.e. an enhanced production of strange particles in $A+A$ compared to $p+p$ collisions has also been observed. QGP models indeed predict such an enhancement due to thermal production of strange quarks and a possible restoration of chiral symmetry. The restoration of chiral symmetry leads to a possible change in the masses and widths of light vector mesons such as ρ or ω [Har96].

Hanbury-Brown-Twiss interferometry (HBT) can be used to determine the radius of a source via the Bose-Einstein correlation of two particles of the same type emitted by the source. The geometrical source information is extracted from the data via multidimensional Gaussian fits that yield in the radii of the source at freezeout in different directions. Such HBT correlations have been measured at RHIC [Ada04a, Adl04a]. The resulting

radii were of the order of about 5 fm, however, the ratio of the radii showed an unexpected behaviour with respect to the expectation from a prolonged source lifetime. This HBT puzzle might have been solved by improved theoretical models [Pra09], including factors such as pre-equilibrium flow, a stiffer equation of state, and adding viscosity. These factors make the evolution of the source more explosive.

The hydrodynamic properties of the medium can be investigated by looking at its hydrodynamic flow. This flow can be addressed by the measurement of the azimuthal anisotropy of particles at different momenta with respect to the so-called reaction plane. The reaction plane is the plane spanned by the impact parameter b and the direction of the colliding beams z. The anisotropy is generally described in terms of the parameter v_2 which is the second harmonic of the Fourier transformation of the angular distribution at a given p_{T}. When the impact parameter is not negligibly small, the colliding nuclei leave behind an almond-shaped interaction region. Particles at low transverse momenta are now influenced by the pressure gradient in the medium. This leads to an increase of the particle momenta in the reaction plane which corresponds to emission in the direction of the minor axis. High-p_{T} particles, on the other hand, are expected to lose energy in the medium, therefore particles headed perpendicular to the reaction plane have to traverse a longer distance within the medium and lose more momentum than particles within the reaction plane. The realtively large v_2 measured at RHIC [Adl03d, Ada04b] suggests that the expanding fireball reaches the equilibrium rapidly. The p_{T} dependence of v_2 is explained by hydrodynamic models assuming the existence of a perfect fluid, i.e. a fluid with no viscosity [Yag08].

Another interesting signature is the predicted dissociation of quarkonia states such as J/ψ or Υ due to color screening in the medium, first proposed in 1986 [Mat86]. It manifests itself in a suppression of J/ψ in central $A+A$ collisions, such a suppression has been observed both at SPS and RHIC. However, one could also think of other mechanisms leading to a suppression of quarkonia production without the presence of a QGP, but due to a decrease of E_{T} distributions [Cap02]. Therefore, the picture behind the measured suppression of J/ψ is still not understood. Interestingly, the suppression is almost the same at SPS and RHIC, which lead to assumptions that at RHIC energies $c\bar{c}$ pairs produced in hard scattering processes possibly recombine later and thus enhance the J/ψ yield again. This effect might even lead to an overall enhancement of J/ψ's at LHC energies [BM09].

One of the most compelling observations in central 200 GeV Au+Au collisions at RHIC was the suppression of high-p_{T} hadrons such as π^0 when compared to a binary-scaled $p+p$ reference [Adl03f]. Hadrons at high transverse momenta originate from hard scattered partons and are part of a particle jet emerging from such partons, therefore they are a measure for the suppression of the jets themselves. Another measurement showing this so-called jet quenching were angular correlations of hadrons with respect to a trigger particle at high p_{T} which showed a disappearance of the back-to-back correla-

tion [Adl03a]. Jet quenching can be explained by the energy loss of partons that traverse the QGP created in such collisions. It is sensitive to high color charge densities in the medium. Jet quenching will be discussed further in Section 2.4.

Direct photons, i.e. photons not from particle decays, serve as a unique probe in heavy-ion collisions as well. Photons do not interact strongly and can thus traverse a possibly created quark-gluon plasma (mostly) unaffected. Therefore, photons produced in hard scattering processes serve as a test of binary scaling from $p+p$ collisions. Furthermore, a hot medium as the QGP is itself emitting thermal photons. Such thermal photons are difficult to measure. First results on thermal photon production have been obtained by attributing an excess of low mass dileptons to thermal photon production [Ada08a]. At SPS energies, so far no evidence for thermal photons has been found [Bau09]. More information on direct photons in heavy-ion collisions will be given in Section 2.5.
Dileptons are also interesting in their own right. At SPS, an enhancement of intermediate-mass dileptons over the background from hadronic decays was observed [Len99], later RHIC results also showed an enhancement of e^+e^- pairs below the ρ meson mass peak in 200 GeV Au+Au collisions [Afa07]. The enhancement is still not fully understood, contributions are assumed to be the annihilation of thermal pions [Yag08], a strong in-medium modification of and ω and ψ in addition to the modification of the ρ, and a thermal component [Tse05].

2.4 Jets and Jet Quenching

At large transverse momenta, particles are usually produced in hard parton-parton scattering processes. In the QCD vacuum, the scattered partons subsequently fragment into jets, something that happens in $p+p$ collisions. In collisions of heavy nuclei, the particles from initial hard scattering processes have to travel through the subsequently created hot and dense medium before fragmentation, therefore the jets can be used to probe the matter produced in such collisions.

2.4.1 The Nuclear Modification Factor

An inclusive measure to quantify effects of nuclear matter or the particles produced in ultrarelativistic heavy-ion collisions is the so-called *Nuclear Modification Factor* R_{AB}.[4] It is a measure to compare the production of particles in collisions of nuclei with the production of particles in $p+p$ collisions, under the assumption of binary-scaling. Binary scaling means the assumption, that an $A+B$ collision can be regarded as a superposition of a certain number of independent nucleon-nucleon ($N+N$) collisions. A further

[4] A and B represent different nuclei here. In the case of Au+Au collisions, R_{AB} is often replaced by R_{AA} .

assumption to be made is that each $N+N$ collision can also be taken as a $p+p$ collision, the yield of particle production in $A+B$ collisions is simply given by the yield in $p+p$ collisions, scaled with the number of binary collisions. These assumptions can be made for large momentum transfers as the partons then can be regarded as asymptotically free and hard scatterings occur on such short timescales that multiple scatterings of one nucleon do not affect each other. Therefore, the nuclear modification factor can be written as

$$R_{AB} = \frac{\mathrm{d}^2N/\mathrm{d}p_\mathrm{T}\mathrm{d}y|_\mathrm{AB}}{\langle N_{coll}\rangle_\mathrm{AB} \cdot \mathrm{d}^2N/\mathrm{d}p_\mathrm{T}\mathrm{d}y|_{NN}} \,. \tag{2.10}$$

$\mathrm{d}N/\mathrm{d}p_\mathrm{T}$ is the particle yield for the different collision systems, and $\langle N_{coll}\rangle$ is the number of inelastic nucleus-nucleus collisions. This number is proportional to the nuclear thickness function $\langle T_{AB}(b)\rangle$, the average nuclear thickness for a given centrality a is given as:

$$\langle T_{AB}\rangle_a = \frac{\int_a T_{AB}(b)\mathrm{d}^2b}{\int_a (1-e^{-\sigma_\mathrm{NN}T_{AB}(b)})\mathrm{d}^2b} \,, \tag{2.11}$$

or also as

$$\langle T_{AB}\rangle_a = \frac{\langle N_{coll}\rangle_a}{\sigma_{NN}} \,. \tag{2.12}$$

Here, σ_{NN} is the inelastic cross section of nucleus-nucleus collisions, and $\langle N_{coll}\rangle_a$ is the average number of inelastic binary collisions for a given centrality a. The nuclear modification factor can therefore also be written depending on T_{AB} and the cross section measured in $p+p$ collisions:

$$R_{AB} = \frac{\mathrm{d}^2N/\mathrm{d}p_\mathrm{T}\mathrm{d}y|_\mathrm{AB}}{\langle T_{AB}\rangle \cdot \mathrm{d}^2\sigma^{p+p}/\mathrm{d}p_\mathrm{T}\mathrm{d}y} \,. \tag{2.13}$$

$\langle T_{AB}(b)\rangle$, and $\langle N_{coll}\rangle_a$ are calculated with a Monte-Carlo simulation using a Glauber model. The model is purely based on nuclear geometry, with individual nucleons traveling on straight line trajectories. A review of this model and its application at PHENIX and other heavy-ion experiments is given in [Mil07].

The nuclear modification factor is expected to be unity above a certain p_T , in the regime of hard scattering processes, when no medium affects the scattered partons or the subsequent jets. A deviation from unity can also be attributed to e.g. a change in the parton distribution of the incoming nucleons.

2.4.2 Cold Nuclear Matter Effects

In order to understand the nuclear modification factor in heavy-ion collisions and to quantify effects of hot nuclear matter, it is very important to understand all other effects on the

particle production that are not due to the presence of a hot and dense medium. Such effects include modifications of the initial state, as well as effects of cold nuclear matter that a jet might have to go through, or multiple soft scatterings of a parton before the final hard scattering process.

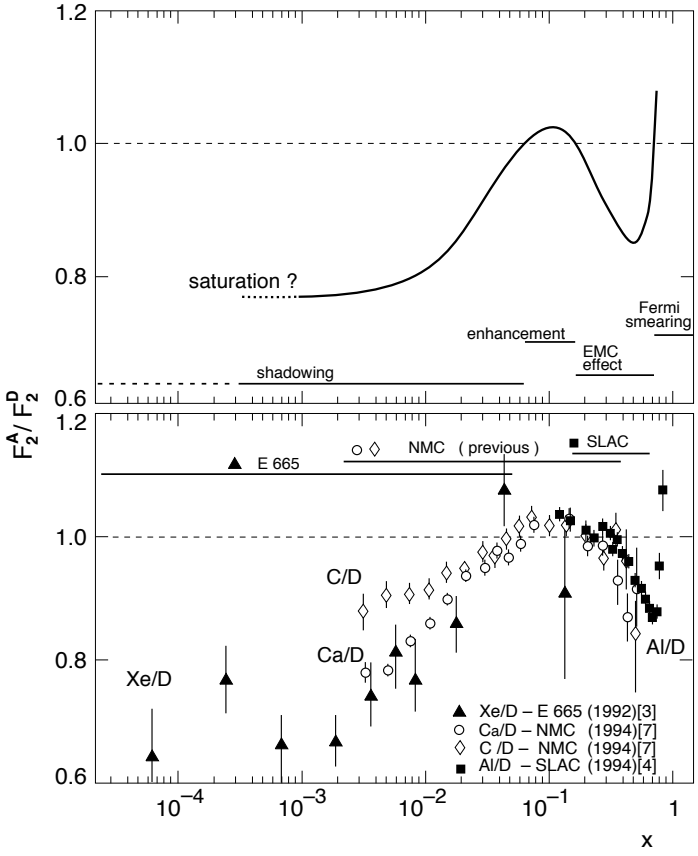

Figure 2.4: A phenomenological curve for the nuclear structure function ratio $F_2^A(x,Q^2)/F_2^D(x,Q^2)$, and a collection of experimental data on the same structure function. [Arn95]

Nuclear Shadowing In 1983, the EMC group observed that the nuclear structure function per nucleon, F_2^N, differs significantly for iron and for deuterium [Aub83]. The nuclear structure function of deuterium, $F_2^D(x,Q^2)$ is often used as a baseline because the deuteron is a system containing both a proton and a neutron and is thus isospin-averaged. Initial state nuclear effects in a nucleus A can now be attributed by looking at the ratio of the nuclear structure functions $F_2^A(x,Q^2)/F_2^D(x,Q^2)$. A phenomenological curve for this ratio is shown in the upper panel of Figure 2.4, the curve is derived from a collection of experimental data, a selection of such data is shown in the lower panel of the

same figure [Arn95]. The variable x for the scattered parton is connected to the transverse momentum of the leading hadron after fragmentation via the center of mass energy:

$$x \sim \frac{2p_{\mathrm{T}}}{\sqrt{s_{\mathrm{NN}}}} \,. \tag{2.14}$$

Four different regions with respect to x are visible in both data and the curve: Shadowing occurs at $x \leq 0.1$, with $F_2^A(x,Q^2)/F_2^D(x,Q^2) \leq 1$, antishadowing with $F_2^A(x,Q^2)/F_2^D(x,Q^2) \geq 1$ shows up for $0.1 < x < 0.3$, the region $0.3 < x < 0.7$ with $F_2^A(x,Q^2)/F_2^D(x,Q^2) \leq 1$ shows the so-called EMC effect[5], and at $x \geq 0.7$, Fermi smearing or Fermi motion lead to an increase of $F_2^A(x,Q^2)/F_2^D(x,Q^2)$ again.

The Cronin Effect In the 1970s it was observed that the cross section of particles produced in $p+\mathrm{A}$ collisions does not simply scale with the number of target nucleons when compared to the particle production in $p+p$ collisions [Cro75, Ant79]. Instead, it was found that the parameter α, used as parameter for the exponent in the parameterization of the $p+\mathrm{A}$ cross section for a given p_{T}

$$E\frac{\mathrm{d}^3\sigma}{\mathrm{d}p^3}(p_{\mathrm{T}},A) = E\frac{\mathrm{d}^3\sigma}{\mathrm{d}p^3}(p_{\mathrm{T}},1)\cdot A^{\alpha(p_{\mathrm{T}})} \,, \tag{2.15}$$

is greater than one for p_{T} above ~ 2 GeV/c. Therefore, an enhancement of particle production in $p+\mathrm{A}$ collisions, compared to the expectation from $p+p$ collisions was observed. The observation is shown in Figure 2.5 as seen in one of the original publications of the data. This enhancement is explained as multiple soft scattering of the incoming partons while passing through the nucleus which leads to a broadening of their transverse momentum distribution. This effect is usually called the *Cronin effect*.

2.4.3 Hot Nuclear Matter Effects

A scattered parton traversing a medium of hot and dense matter loses energy via elastic and inelastic scattering processes. Inelastic processes are expected to be the dominant source of energy loss. Several theoretical models describe this energy loss, well-established models are summarized in the following. In general, one can distinguish between collisional and radiative energy loss, collisional energy loss is equivalent to elastic scatterings while radiative energy loss is the emission of gluon radiation in inelastic scattering processes. There are several reviews summarizing jet quenching models and phenomenology in heavy-ion collisions, e.g. [Bai00, Bai03, Loi05, Zap08, d'E09, Wie09].

[5] named after the EMC collaboration

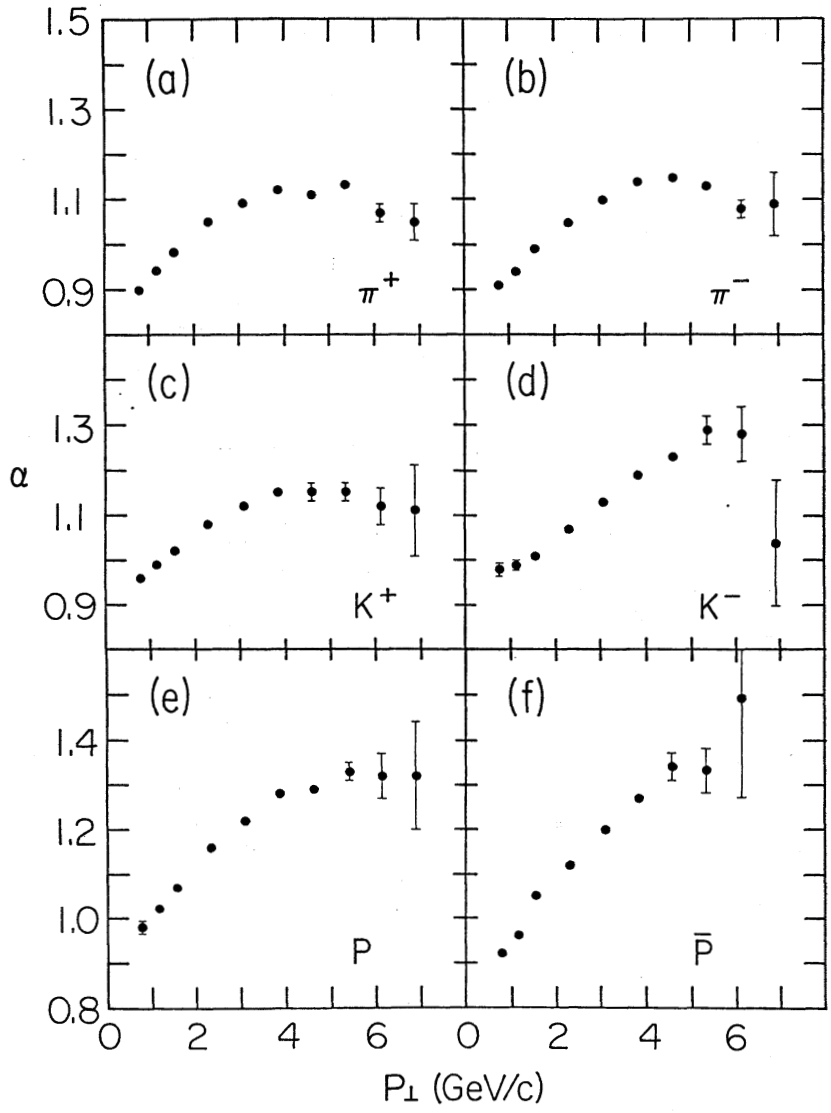

Figure 2.5: The observation of the so-called Cronin effect in [Ant79] in collisions of proton beams on different nuclear targets (d_2, Be, Ti, W). In the absence of nuclear effects, α should reach unity at high p_T. The deviation from unity therefore shows a nuclear effect that was later called Cronin effect.

Collisional Energy Loss

Jet quenching due to partonic energy loss in a hot and dense medium – the quark-gluon plasma – was first proposed by Bjorken in 1982 [Bjo82]. He developed the idea of collisional energy loss via elastic scattering of the traversing partons in the plasma which in case of production near the surface could lead to the depletion of one jet while the other jet is escaping the medium unaffected. The amount of this collisional energy loss is estimated to be about $dE/dx \simeq \alpha_s^2\sqrt{\varepsilon}$ [Loi05], its magnitude is calculated to be $\approx 0.1-0.2\,\mathrm{GeV/fm}$ [Tho95, Zak07] for a quark with an energy $E = 10-20\mathrm{GeV}$.

Radiative Energy Loss

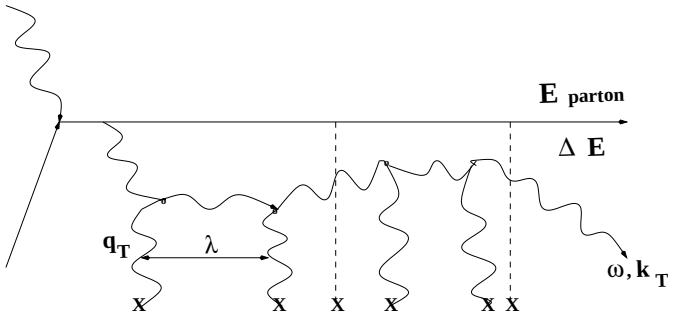

Figure 2.6: Typical gluon-radiation diagram, from [Bai00].

Radiative energy loss occurs when the medium induces gluon radiation in inelastic scattering processes from a parton traversing the medium. For $L \ll \lambda$, where L is the thickness of the medium and λ denotes the mean free path, the traversing parton only experiences one scattering process, thus the process is analoguos to Bethe-Heitler [Bet34] bremsstrahlung in QED [d'E09]. The process of bremsstahlung emission is the analog to the Landau-Pomeranchuk-Migdal (LPM) effect in QED [Lan53b, Mig56] for thick media with $L \gg \lambda$, here, multiple scatterings of the traversing parton occur. Theoretical treatment of this radiative energy loss is complicated, as destructive interference effects have to be considered. These effects occur when the formation time of the gluon is large compared

to the mean free path in the medium, i.e. the bremsstahlung probability is smaller for a denser medium and vice versa.

The BDMPS-Z Model The general idea of the BDMPS-Z model by Baier, Dokshitzer, Mueller, Peigné, Schiff [Bai97a, Bai97b, Bai98], and Zakharov [Zak97] is the description of energy loss of a traveling parton in a coloured medium via multiple soft scatterings. The medium itself is described consisting of multiple scattering centers. The parton splits into an outgoing parton and a gluon in each scattering process. One main assumption is that the scattering centers are static and uncorrelated. In this picture, the collisional energy loss vanishes [Bai00]. The average energy loss of a parton with very large energy due to gluon radiation is found to be [Bai00, Loi05]

$$\Delta E = \int^{\omega_c} \omega \frac{dI}{d\omega} d\omega \propto \alpha_s C_{\mathrm{R}} \omega_c \propto \alpha_s C_{\mathrm{R}} \hat{q} L^2 \,. \tag{2.16}$$

Here, ω is the energy of the emitted gluon, α_s denotes the strong coupling constant, C_{R} is the QCD coupling factor between the parton and the gluons in the medium, it is 4/3 (3) for quarks (gluons). $\hat{q}$ is the so-called transport coefficient of the medium which is the product of the medium's color-charge density and the cross-section of the parton-medium interaction. It can be seen that the energy loss is proportional to the square of L, the thickness of the medium.

The **parton quenching model** (PQM) [Dai05] is a Monte Carlo model based on the BDMPS theory, using the quenching weights of BDMPS and a realistic collision geometry. The only free parameter in the PQM monte carlo is the medium transport coefficient $\hat{q}$.

The GLV Model The model by Gyulassy, Levai, and Vitev (GLV) [Gyu00a, Gyu01] treats the energy loss via the emission of bremsstrahlung perturbatively by an expansion in the opacity $\chi = L/\lambda$. The opacity determines the number of scattering centers, therefore it is a scale for the number of interactions in the medium. An analytic expression is used to apply the expansion at all orders in opacity, including a plasmon frequency that gives an infrared cut-off. Within the GLV framework, the initial density of gluons or the local color charge density can be extracted. This density is simply written as dN^g/dy, it can be calculated taking into account longitudinal Bjorken expansion of the medium. These calculations also take into account initial state multiple scatterings and the modification of nuclear parton distribution functions (PDFs).

The WHDG Model Wicks, Horowitz, Djordjevic, and Gyulassy [Wic07] use the GLV model for radiative energy loss in their model (WHDG). In addition it includes also collisional energy loss which is convoluted with the radiative energy loss. Parton paths through

the medium are then calculated using a realistic collision geometry and a Bjorken time expansion. However, the model does not include modified PDFs or multiple scattering processes in the initial state. The main parameter of this model is also the initial gluon density dN^g/dy.

The ZOWW Model In the model by Zhang, Owens, Wang, and Wang (ZOWW) [Zha07], the suppression of scattered partons is calculated within a pQCD parton model at next-to-leading order. Initial hard scattering processes are factorized as in $p+p$ collisions, jet quenching is taken into account using modified fragmentation functions. The modification of the fragmentation functions is connected to parton energy loss that is calculated with the so-called Higher Twist formalism. The model uses a 1-d expanding medium and assumes a uniform gluon density ρ_0. Its main free parameter is the energy loss parameter ε_0 which should be proportional to ρ_0. It explicitly includes only radiative energy loss.

The AMY Formalism The formalism based on Arnold, Moore, and Yaffe (AMY) [Arn00, Tur05] uses thermal field theory at finite temperatures to calculate the energy loss. In contrast to the aforementioned BDMPS-Z and GLV models, the scattering centers in AMY are dynamic. The model also fully includes the absorption of a thermal quark or gluon by a traversing hard parton, as well as pair annihilations with those thermal partons. The model is based only on perturbative QCD. On the other hand, the model does not account for vacuum radiation or vacuum-medium interference and thus might not be applicable to non-thermalized media. The overall free parameter in the AMY model is $\alpha_s = g^2/4\pi$, g is the coupling constant of the strong interaction. The model keeps α_s constant, not depending on e.g. momentum transfer Q^2 or on the evolution of the medium, thus is has to be regarded as an average effective coupling [Gal09].

Each of the models discussed above is based on an overall free parameter that affects the predictions of these models. Therefore, measuring a value such as R_{AA} that is calculable in the framework of such theoretical models can help constraining the possible range of the parameters. Furthermore, the shape of the measured R_{AA} can be compared to the shape predicted by the models.

2.5 Direct Photons

Photons are created in numerous different processes in heavy-ion collisions. Basically, photons can be separated into two groups, one contains all photons from hadronic decays (e.g. π^0 , or $\eta \rightarrow \gamma\gamma$), the other one consists of all photons from the collision itself and

the subsequent partonic and in-medium processes. The second group of photons is called *direct photons*, the measurement of such photons can shed light on the different production mechanisms of photons in the matter created in heavy-ion collisions as the matter itself is expected to have a significant effect on the production of direct photons. Direct photons can be further divided into different groups, e.g. the so-called prompt photons are those created in early hard scatterings while thermal photons are emitted from matter in a phase of thermal equilibrium. Another group are photons that are created by interactions of particles traversing a hot and dense medium.

2.5.1 Direct-Photon Production Processes

In heavy-ion collisions, direct photons are created during different stages of the collision. So-called prompt direct photons are produced in hard scattering processes in the earliest stage of a collision. Both the QGP and the hot hadron gas emit thermal direct photons. Furthermore, photons can be emitted when a scattered parton interacts with the hot and dense matter. The different contributions to the overall direct-photon spectrum cannot be seperated experimentally, therefore one relies on theoretical calculations to interpret the measured direct photons in the light of the different production processes.

Prompt Direct Photons

The earliest processes producing direct photons are initial parton scattering processes. In such hard scatterings, direct photons can be produced via quark-gluon Compton scattering and via quark-antiquark annihilation. These leading order (LO) pQCD processes occur in $p+p$ collisions as well as in collisions of nuclei. A Feynman graph of the $q(\bar{q})+g \rightarrow q(\bar{q})+\gamma$ reaction is shown in Figure 2.7a, the Feynman graph for the $q+\bar{q} \rightarrow g+\gamma$ process is shown in Figure 2.7b.

The corresponding cross sections of such LO processes can be calculated analogously to the equivalent QED processes, either the Compton scattering $e^-(e^+)+\gamma \rightarrow \gamma+e^-(e^+)$ or the electron-positron annihilation $e^+ + e^- \rightarrow \gamma+\gamma$. Together with the Mandelstam variables[6], the differential cross section for the two LO photon production processes can be written as [Won94]:

$$\frac{d\sigma}{dt}(qg \rightarrow \gamma q) = \left(\frac{e_q}{e}\right)^2 \frac{8\pi\alpha_s\alpha_e}{(s-m^2)^2} \left\{ \left(\frac{m^2}{s-m^2} + \frac{m^2}{u-m^2}\right)^2 + \left(\frac{m^2}{s-m^2} + \frac{m^2}{u-m^2}\right) - \frac{1}{4}\left(\frac{s-m^2}{u-m^2} + \frac{u-m^2}{s-m^2}\right) \right\}, \tag{2.17}$$

[6]The Mandelstam variables are defined in Appendix A.

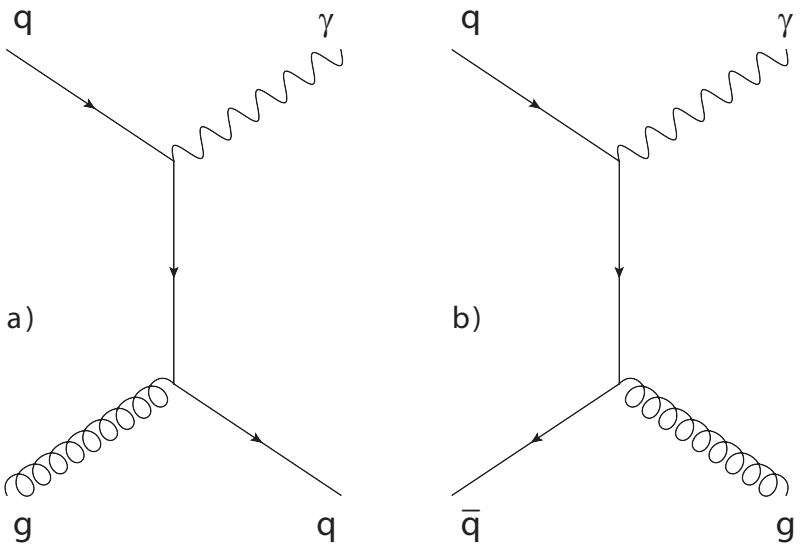

Figure 2.7: Feynman diagrams of leading order prompt photon production. a) Quark-gluon Compton scattering, and b) quark-antiquark annihilation.

$$\frac{d\sigma}{dt}(q\bar{q}\to\gamma g) = \left(\frac{e_q}{e}\right)^2 \frac{8\pi\alpha_s\alpha_e}{s\cdot(s-m^2)}\left\{\left(\frac{m^2}{t-m^2}+\frac{m^2}{u-m^2}\right)^2 + \left(\frac{m^2}{t-m^2}+\frac{m^2}{u-m^2}\right) - \frac{1}{4}\left(\frac{t-m^2}{u-m^2}+\frac{u-m^2}{t-m^2}\right)\right\}. \tag{2.18}$$

Here, m is the quark mass, e_q is the quark charge, and e is the elementary charge. The Mandelstam variables are s, t, and u; α_s, and α_e are the coupling constants of the strong interaction and the electromagnetic interaction, respectively. In the relativistic case, the rest mass of the quarks m is small compared to the other energy scales, therefore it can be neglected (see e.g. [Won94]). In that case, the first two terms in the sum become insignificant and only the last term remains. Then Equations 2.17 and 2.18 become maximal when one of the Mandelstam variables (u and s in the first case, u and t in the second case) are minimal, and $P_\gamma \approx P_q$, or – for the $q+\bar{q}$ process – $P_\gamma \approx P_{\bar{q}}$. Therefore, the processes can be seen as a conversion of one of the annihilating quarks, or of the quark taking part in the Compton scattering, into a photon with approximately the same energy and momentum.

Next-to-leading-order processes (NLO) also produce direct photons in both $p+p$ and Au+Au collisions. A Feynman diagram of such an NLO process is shown in Figure 2.8a for the bremsstrahlung emission of a photon from a scattered quark. Bremsstrahlung photons are emitted electromagnetically from a scattered quark in a process similar to the bremsstrahlung emission of a gluon.

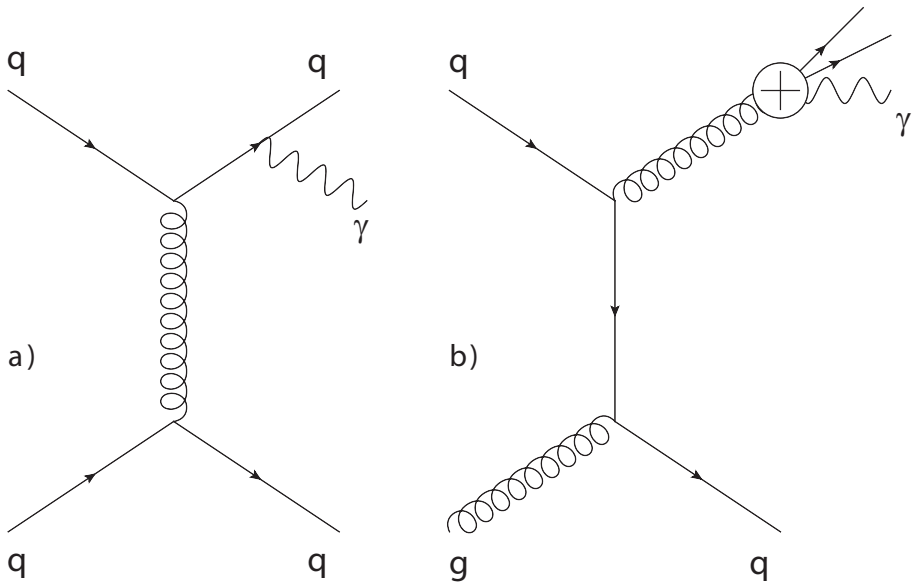

Figure 2.8: Feynman diagrams of a) next-to-leading order prompt photon production: Emission of a bremsstrahlung photon by a scattered quark; and b) emssion of a photon during the fragmentation of a scattered gluon.

Figure 2.8b shows photons emission during the jet fragmentation of a scattered gluon or quark. Scattered quarks or gluons can fragment into a photon, amongst other particles. Such fragmentation photons are usually accompanied by hadrons that are also produced during the fragmentation process. The initial cross section of the LO process that foregoes the fragmentation, e.g. $q+g \rightarrow q+g$, or $q+q \rightarrow q+q$, can be calculated in QCD at leading order. But for a complete theoretical description of fragmentation photon emission, the parton-to-photon fragmentation function (FF) also has to be taken into account. As these FF's are only accessible by experimental studies, a theoretical prediction of the amount of fragmentation photons suffers from additional uncertainties.

The processes described above will occur in both $p+p$ and $A+A$ collisions and can therefore be used to test binary N_{coll} scaling.

Thermal Direct Photons

Both a quark-gluon plasma and a hot hadron gas produce thermal photons. As the mean free path of photons is large compared to the size of these media created in heavy-ion collisions, they are likely to survive and leave the respective medium. As the photon production rate depends on the temperature, photons could be a good thermometer for the medium. However, it was shown that their production rates are quite similar for a QGP and a HHG at the same temperature [Kap91], therefore the separation of photons from

these two origins is complicated. The emission of photons from a thermalized QGP can be calculated with thermal field theories, taking into account the so-called photon self-energy [KB04]. In a hot hadron gas, in principle the same techniques are used to calculate direct-photon production, using mesons such as π, η, and ρ as the main constituents of the matter instead of quarks and gluons in the QGP. However, the large number of hadrons makes such calculations more complicated.

Photons from Jet-Medium Interactions

The production of photons by hard scattered partons traversing the QGP was proposed to be another source of direct photons in 2002 [Fri03]. Processes include the annihilation of a fast moving quark with a thermal antiquark in the medium ($q + \bar{q} \rightarrow g + \gamma$) or the Compton scattering of the fast moving quark with a gluon from the medium ($q + g \rightarrow q + \gamma$). Furthermore, the medium can induce bremsstrahlung emission from the traversing partons.

Additional Factors Influencing Direct-Photon Production

Initial state effects such as nuclear shadowing or antishadowing, or the EMC effect (see Section 2.4.2) also affect the direct-photon production in $A + A$ collisions when comparing to $p + p$ collisions. Especially at high transverse momenta – more precisely at large Bjorken x – where the valence quarks themselves are involved in the scattering processes, the so-called Isospin effect [Arl06], originating in the different isospin constitution of protons and nuclei composed of protons and neutrons, may lead to a reduction of direct photons in Au+Au collisions. Jet quenching (see Section 2.4) is also expected to lead to a reduced direct photon production in the jet fragmentation channel due to the reduced jet energy.

2.5.2 Photon Spectra

The aforementioned different contributions to the overall spectrum of direct photons are experimentally indistinguishable. Therefore, theoretical calculations, including the photon production processes, are an important piece in the understanding of direct-photon data, showing which production process is expected to dominate the overall photon yield in a given p_{T} range. In [Tur08, Gal09], a 2+1D hydrodynamic model is used to calculate the photon spectrum in 200 GeV Au+Au collisions, including the aforementioned different photon sources. The energy loss of jets is accounted for using the AMY formalism (see Section 2.4), prompt direct photons are treated with pQCD. The results of this calculation are shown for low transverse momenta in the left panel of Figure 2.9, for high transverse momenta in the right panel of Figure 2.9. The calculation predicts a p_{T} window for

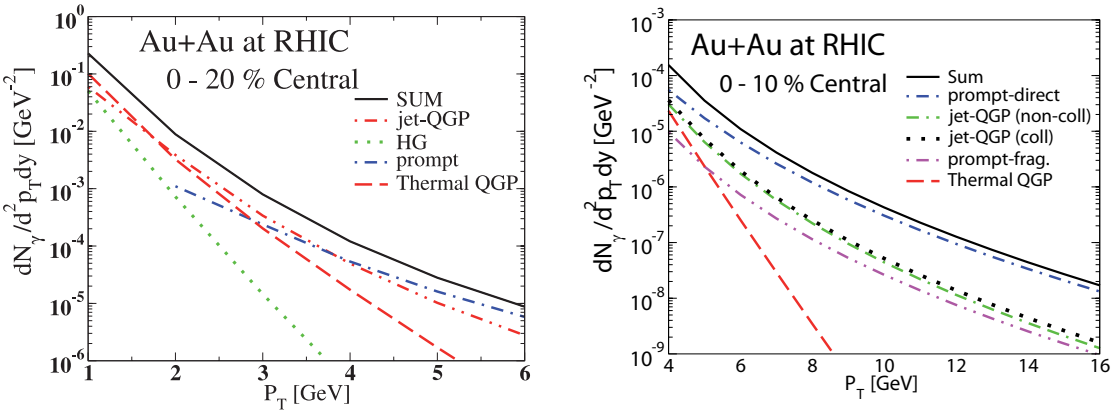

Figure 2.9: The calculated spectrum of direct photons in 200 GeV Au+Au collisions (taken from [Gal09]). The left panel shows the result for the 20% most central events for low p_{T}, the right panel depicts the result for the 10% most central events for high p_{T}. The different contributions to the direct-photon spectra are also shown.

1 GeV/$c \leq p_{\mathrm{T}} \leq$2.5 GeV/$c$ where thermal photons from the QGP are the dominant contribution to the overall spectrum. At high p_{T}, the spectrum is dominated by prompt direct photons from initial hard scattering processes. Photons from jet-medium interactions are expected to be visible for $\sim$2 GeV/$c \leq p_{\mathrm{T}} \leq$4.5 GeV/$c$ and also beyond, however, they are dominated by several other contributions over the whole range. Photons from the hot hadron gas are negligible for almost the whole range in p_{T}, except at about $p_{\mathrm{T}} \simeq$1 GeV/c. The spectra were then been used to calculate the nuclear modification factor R_{AA}^{γ}, using pQCD calculations as $p+p$ reference. The contributions from jet-plasma photons on the one hand and from the isospin effect on the other hand are treated independently in R_{AA}^{γ}, allowing to disentangle the different effects.

The nuclear modification factor was also calculated in [Vit08]. Here, different nuclear effects such as the Cronin effect, shadowing, the isospin effect, and the energy loss in cold nuclear matter are included. Furthermore, the model accounts for jet-medium interactions such as jet-conversion and medium-induced bremsstrahlung emission. A further discussion of the theoretical calculations of R_{AA}^{γ} will follow in the light of the analysis results in Section 7.3.

2.6 Earlier Results

2.6.1 Earlier Results on Jet Measurements

The nuclear modification factor R_{AA} of mesons has been measured at different energies by many different experiments. Notable results have been obtained at CERN SPS in Pb+Pb

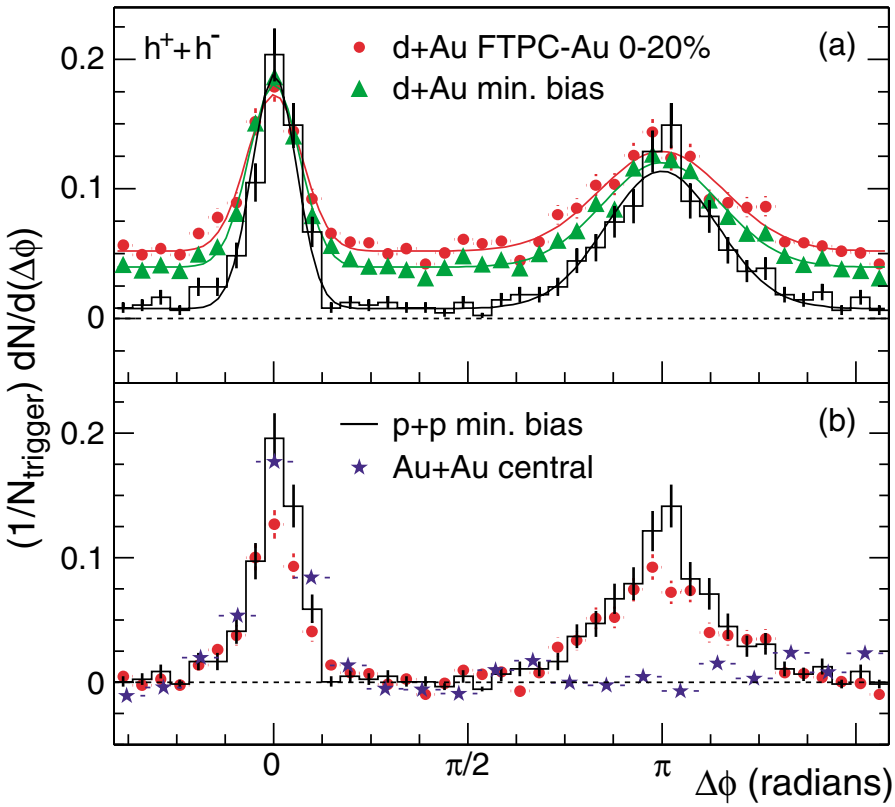

Figure 2.10: Back-to-back correlations of high-p_T hadrons in Au+Au, d+Au, and $p+p$ collisions at $\sqrt{s_{NN}}$ = 200 GeV, as measured by STAR. In Au+Au collisions, the correlations disappear while they are clearly present in $p+p$ and d+Au collisions [Ada03b].

collisions and at RHIC in Au+Au and Cu+Cu collisions. The measurements at these two facilities span about one order of magnitude in $\sqrt{s_{NN}}$ from 17.3 GeV at SPS to 200 GeV at RHIC.

First measurements at RHIC at $\sqrt{s_{NN}}$ = 130 GeV/c already showed a significant suppression of pions and charged hadrons in central Au+Au collisions [Adc02, Adl02, Adc03a]. Since then, RHIC measurements have established a more detailed picture of high-p_T particle suppression in the energy range of 62 GeV $\leq \sqrt{s_{NN}} \leq$ 200 GeV. STAR has measured a charged hadron suppression [Ada03c] in 200 GeV Au+Au collisions and has shown the disappearance of back-to-back correlations of high-p_T hadrons in the same collisions [Adl03a]. PHENIX has observed a suppression of charged hadrons [Adl04b], and of neutral pions [Adl03f] and η mesons [Adl06] – these two by a factor of ~ 5 – in central Au+Au collision at 200 GeV. These results were also confirmed by measurements of BRAHMS and PHOBOS at the same energy [Ars03, Bac04].

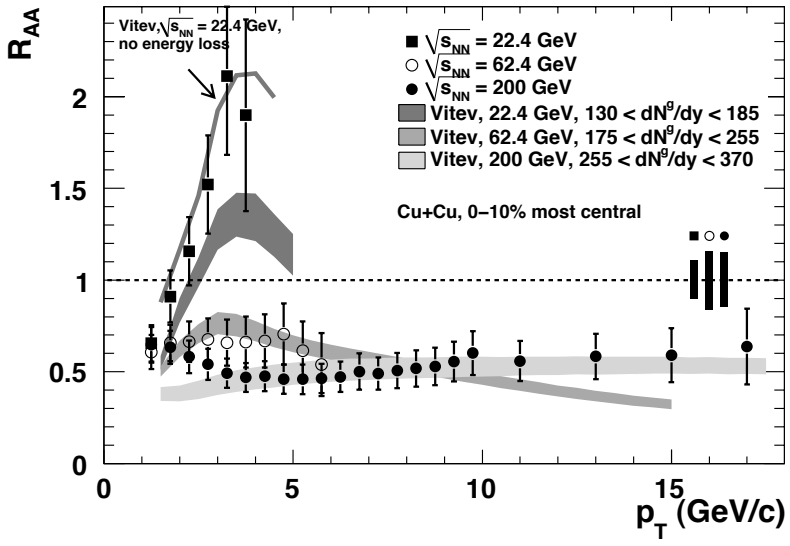

Figure 2.11: Nuclear modification factor R_{AA} for π^0's in Cu+Cu collisions at 200, 62.4, and 22.4 GeV, measured by PHENIX [Ada08b]. The data are compared with theoretical calculations from [Vit06].

Jet suppression as a signature of a possibly created quark-gluon plasma was further supported by measurements of high-p_{T} particles in d+Au collisions at $\sqrt{s_{\mathrm{NN}}}$ = 200 GeV. STAR measurements of back-to-back correlations showed that these correlations do not disappear in d+Au collisions [Ada03b], this finding is depicted in Figure 2.10. In the same paper, STAR also measured the absence of a suppression of high-p_{T} hadrons described with the nuclear modification factor $R_{d\mathrm{A}}$ in such collisions. The same observation was made by PHENIX with the measurement of neutral pions and charged hadrons [Adl03c].

PHENIX also examined the energy dependence of jet quenching in Cu+Cu collisions from 22.4 to 200 GeV using π^0's [Ada08b]. The resulting nuclear modification factors for the 10% most central events at collision energies of 200, 62.4, and 22.4 GeV are shown in Figure 2.11 together with a theoretical calculation. Partonic energy loss is strongly supported by the data for 62.4 and 200 GeV collisions where the production of neutral pions is strongly suppressed. The data at 22.4 GeV on the other hand are also consistent with a scenario without energy loss in a hot and dense medium. A more detailed summary of the energy depencence of jet quenching can be found in [Bau09].

PHENIX measurements of the production of direct photons in 200 GeV Au+Au collisions showed that these particles are not suppressed [Adl05]. Together with the observed suppression of π^0's and η's at the same energy – as depicted in Figure 2.12 – and the absence of suppression in d+Au collisions, this is a strong indication for the presence of hot and dense matter in central Au+Au collisions which photons can traverse mostly unaffected as they do not interact strongly.

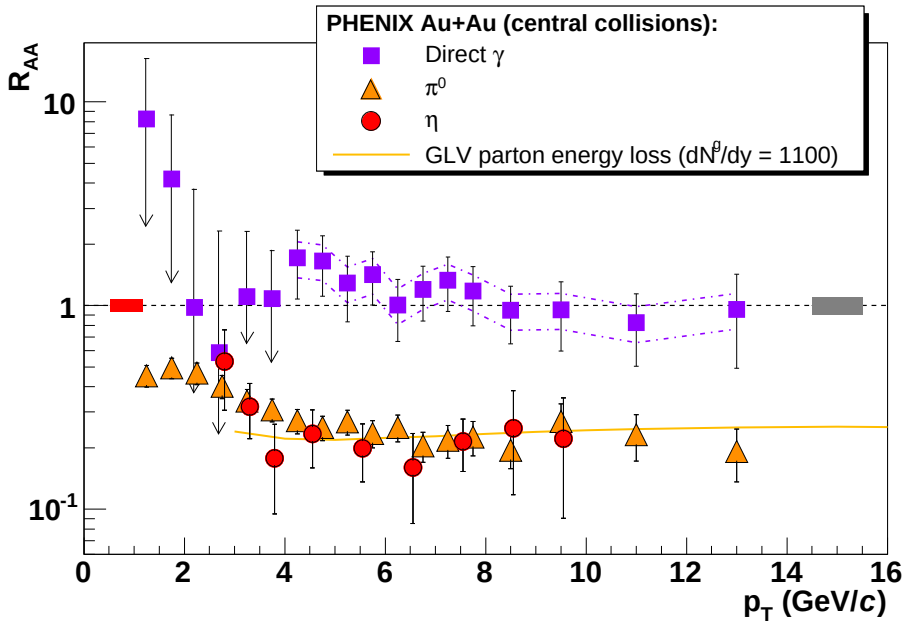

Figure 2.12: Nuclear modification factor of π^0, η, and direct photons in central Au+Au collisions at $\sqrt{s_{NN}}$ = 200 GeV measured by PHENIX. The mesons are suppressed by a factor of ~ 5 while direct photons are not suppressed [Adl06].

2.6.2 Earlier Results on Direct-Photon Production

In heavy-ion collisions, direct photons have so far been measured at the CERN SPS in Pb+Pb collisions at $\sqrt{s_{NN}}$ = 17.3 GeV/c by the WA98 experiment [Agg00], and at RHIC in Au+Au and Cu+Cu collisions at $\sqrt{s_{NN}}$ = 200 GeV/c by PHENIX [Adl05, Lue07, Ada08a]. Preliminary results have also been presented by PHENIX on Au+Au collisions at collision energies of 62.4 GeV [KB08].

WA98 has measured direct photons over the range 0.2 GeV/$c \leq p_T \leq$4.0 GeV/c, significant data points have been acquired for 1.5 GeV$c \leq p_T \leq$3.5 GeV/c. A comparison with theoretical model calculations showed that the photon excess was consistent with the existence of a QGP phase transition in central Pb+Pb collisions at SPS [Agg00]. Unfortunately, recent measurements by WA98 in p+Pb and p+C collisions at the same energy, resulting in upper limits of direct-photon production in such collisions, could neither confirm nor rule out an excess of direct photons in Pb+Pb collisions [Bau09]. The WA98 results are summarized in Figure 2.13.

The PHENIX 200 GeV Au+Au result for direct photons at high p_T [Adl05] supports binary scaling of direct photon production in Au+Au collisions, the nuclear modification factor for central collisions is consistent with unity, however, the large statistical and systematic uncertainties do not allow conclusions on the different production mechanisms of direct photons. The nuclear modification factor is shown in Figure 2.12. The picture in

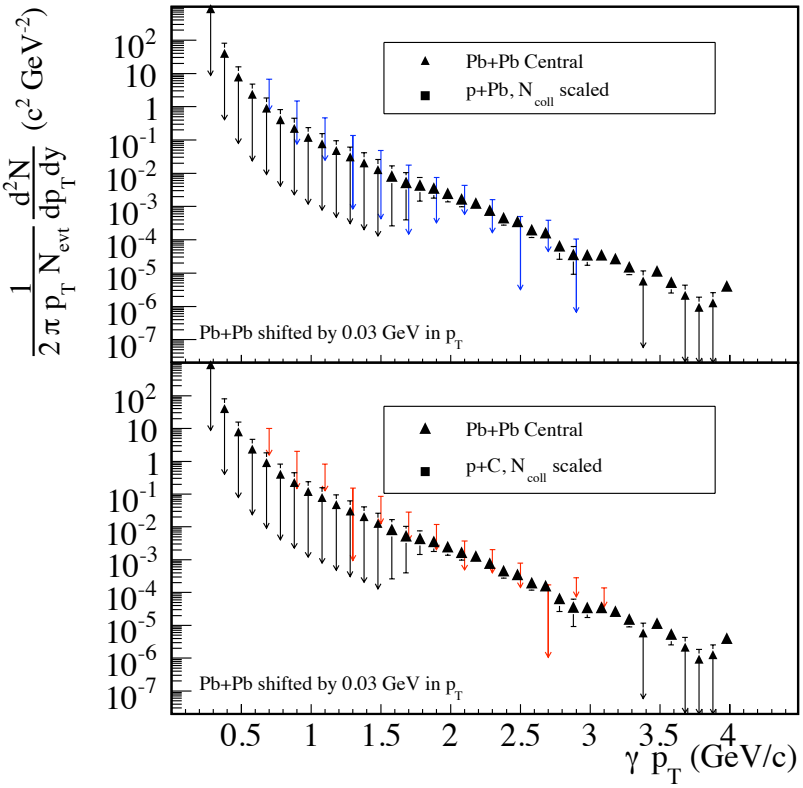

Figure 2.13: Direct photons measured by WA98 in central Pb+Pb collisions at 17.3 GeV (black) [Agg00], in p+Pb (top, blue), and in p+C collisions (bottom, red) at the same energy [Bau09]. The results employ binary scaling with N_{coll}.

Cu+Cu collisions at the same energy is basically the same, no apparent enhancement of direct photons when comparing to $p+p$ collisions is visible from the data [Lue07]. Using the internal conversion of virtual direct photons into e^+e^- pairs, PHENIX has recently measured direct photons also at low transverse momenta [Ada08a], where thermal direct photons would be expected to show up from hydrodynamic models. The result of this measurement is depicted in Figure 2.14. The data measured in Au+Au collisions clearly exceed the expectation from scaling $p+p$ collisions with T_{AA}. This excess can be attributed to a thermal photon signal. An exponential fit to the excess in central Au+Au collisions gives an inverse slope of $T = 221 \pm 23(\mathrm{stat}) \pm 18(\mathrm{sys})$MeV which is in qualitative agreement with hydrodynamic models with an initial temperature $T_{init} \approx 300 - 600$MeV and a thermalization time of $0.6 - 1.5$fm/c [Ada08a].

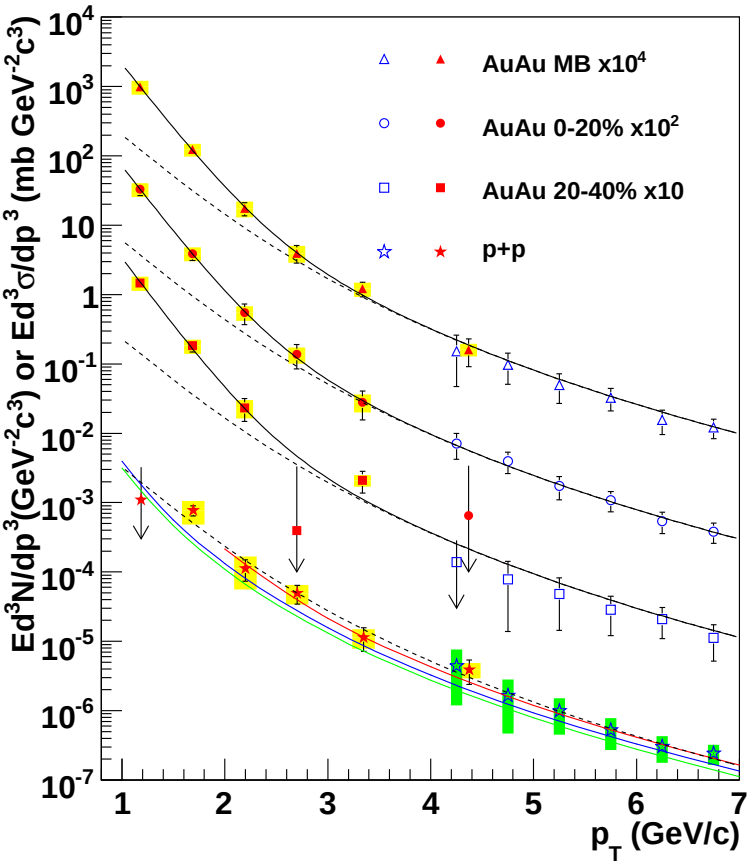

Figure 2.14: Direct photons measured by PHENIX in Au+Au and $p+p$ collisions at 200 GeV. The solid data points have been measured via electron-positron pairs from internal conversions of virtual photons. The full lines at the $p+p$ data points are the results from pQCD calculations with different scales, the dashed lines show a fit to the $p+p$ data, scaled with T_{AA}. The full lines at the Au+Au data points are the scaled $p+p$ data plus an exponential [Ada08a].

3. Experimental Setup: RHIC and PHENIX

> Aethiopes atque Indi discolores maxime et inenarrabiles ferunt aves et ante omnes nobilem Arabiae **phoenicem** [...]. aquilae narratur magnitudine, auri fulgore circa colla, cetero purpureus, caeruleam roseis caudam pinnis distinguentibus, cristis fauces caputque plumeo apice honestante.
> primus atque diligentissime togatorum de eo prodidit Manilius, [...]: neminem extitisse qui viderit vescentem, sacrum in Arabia Soli esse, vivere annis DXL, senescentem casiae turisque surculis construere nidum, replere odoribus et superemori. ex ossibus deinde et medullis eius nasci primo ceu vermiculum, inde fieri pullum, principioque iusta funera priori reddere et totum deferre nidum prope Panchaiam in Solis urbem et in ara ibi deponere.
>
> *C. Plinius Secundus - Naturalis Historia, Liber X*

The data analyzed in this thesis have been measured with the Pioneering High Energy Nuclear Interactions eXperiment (PHENIX) at the Relativistic Heavy-Ion Collider (RHIC), a $\sim$3.8 km long collider consisting of two independent accelerator rings which is located in the town of Brookhaven on Long Island. Four experiments have been constructed at RHIC, the two smaller ones – PHOBOS and BRAHMS – are as of 2008 not taking data anymore, while the two larger ones – STAR and PHENIX – are still running and further upgraded. New sub-detectors are being added to their configuration. For example, since 2004, when the data used in this thesis have been measured, several new detectors such as the western time-of-flight detector (TOF-W), the hadron-blind detector (HBD), the reaction plane detector (RXNP) or the muon piston calorimeter (MPC) have been added to PHENIX.

3.1 The Relativistic Heavy-Ion Collider

The Relativistic Heavy-Ion Collider [Hah03, Har03] is the largest of the accelerators located at Brookhaven National Laboratory (BNL). The smaller accelerators, many years

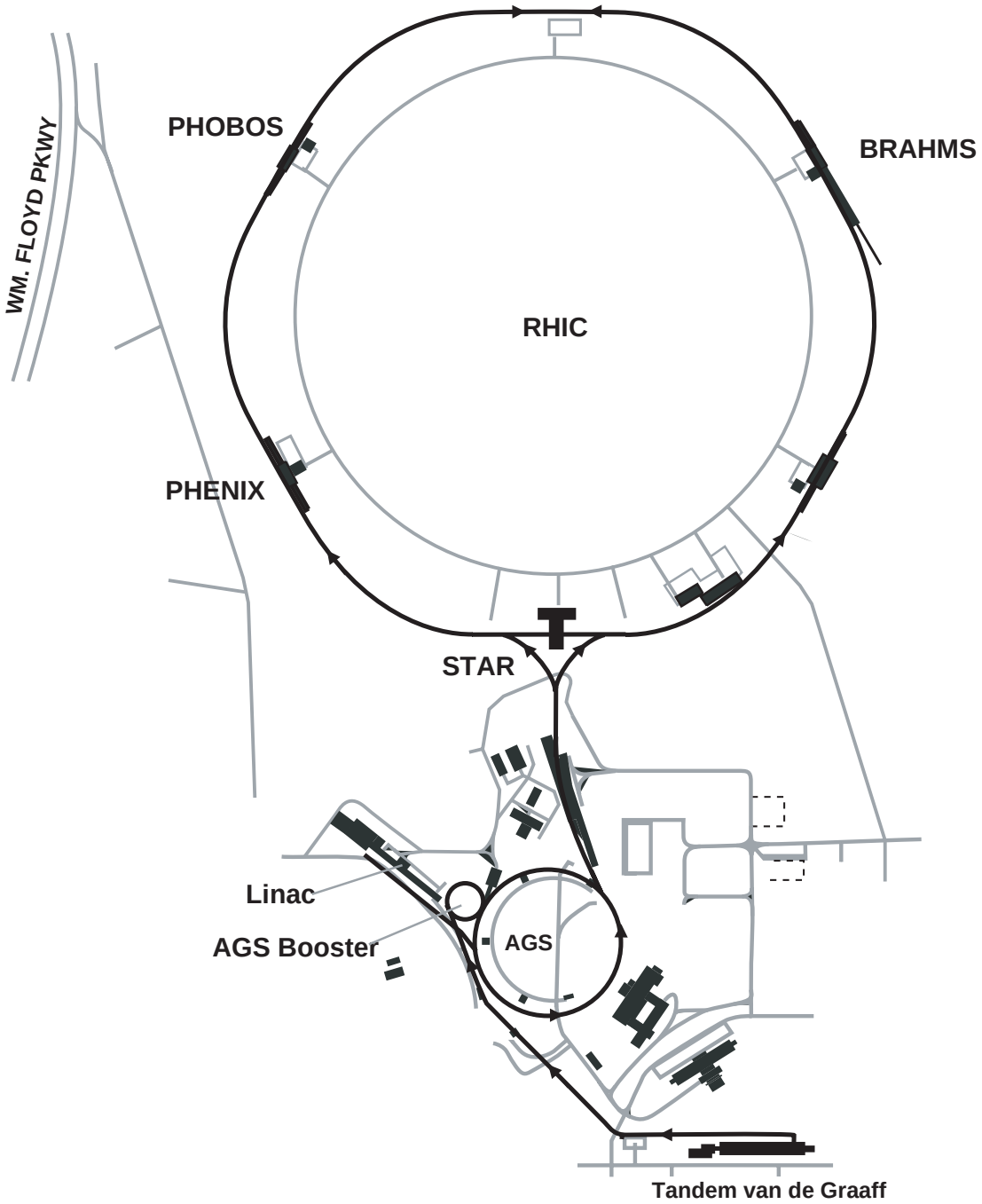

Figure 3.1: The RHIC complex at Brookhaven National Laboratory [Har03].

ago having delivered particle beams for their own experiments, are now used as pre-accelerators accelerating the particles prior to their injection into RHIC. The complete RHIC accelerator complex with the adjacent experiments is shown in Figure 3.1.
RHIC itself consists of two independent accelerator rings located on the same horizontal plane, namely the so-called "blue" ring for clockwise and the so-called "yellow" ring for counter-clockwise beams. The two rings cross each other at 6 distinguished interaction regions where collisions of beam particles can occur. The circumference of each ring is about 3.8 km, divided into six arc sections of 356 m and six insertion regions of 277 m with a collision point in the middle of the latter.
In Au+Au collisions, the first of three pre-accelerators is the Tandem Van de Graaff. Gold ions are produced in a pulsed sputter ion source and stripped off their electrons in the accelerator, which finally boosts their energy up to 1 MeV/u. At the end of the Tandem Van de Graaff, more electrons are stripped and ions with a charge state of +32 are selected with the help of bending magnets and injected to the Booster Synchrotron where they are accelerated to 95 MeV/u. Before being transferred to the AGS (Alternative Gradient Synchrotron) in 24 bunches, further stripping is performed until the ions have a charge of +77. In the AGS, the ions are accelerated up to the RHIC injection energy at 10.8 GeV/u and rebunched into four bunches which are then transferred to RHIC through the AGS-to-RHIC Beam Transfer Line. During this transfer, at the exit of the AGS the last two electrons are stripped off and the ions reach their final charge state of +79. For $p+p$ collisions, the first pre-accelerator is a different one. Polarized protons are created in the LINAC and accelerated up to 200 MeV before being injected into the Booster.
The maximum beam energy RHIC can deliver depends on the mass of the colliding particles. The maximum beam energy of RHIC is 100 AGeV for heavy nuclei such as Au or Cu, and 250 GeV for protons, which translates into collision energies of 200 GeV and 500 GeV, respectively.

3.2 The Experiments at RHIC

As mentioned above, four experiments have been constructed at four of the six interaction regions to study the different collision systems at RHIC. The two larger experiments, STAR and PHENIX, are located at the six and at the eight o'clock position of RHIC, respectively. The two smaller experiments, PHOBOS and BRAHMS, were built at the ten and the two o'clock interaction regions, respectively. STAR and PHENIX are as of 2009 still taking data while PHOBOS and BRAHMS have been shut down.

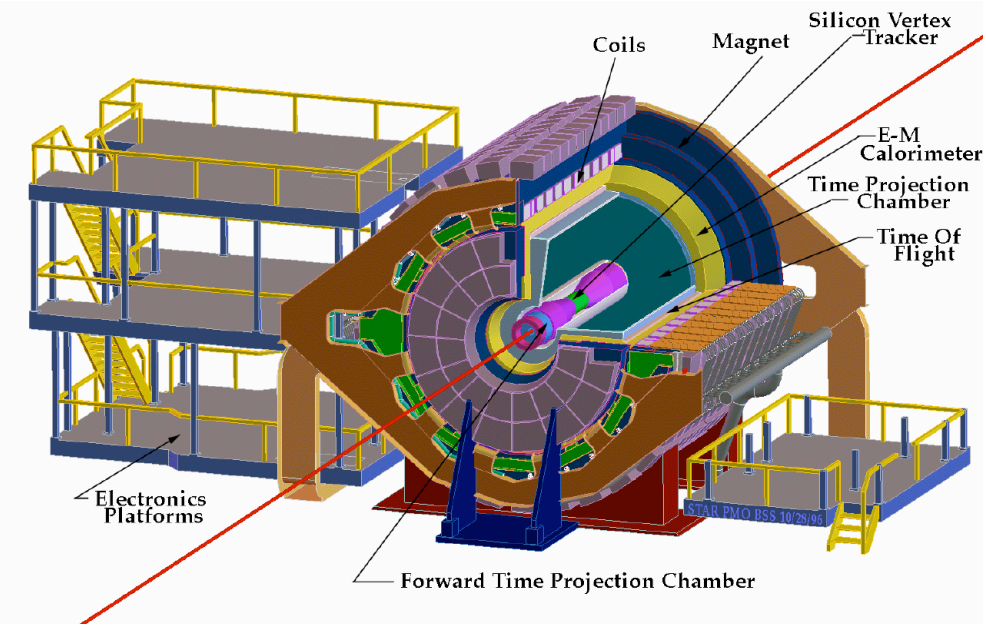

Figure 3.2: The STAR experiment [Ack03].

3.2.1 STAR

The STAR[1] detector's [Ack03] main design goal is the measurement of hadrons over a large solid angle. Therefore, it contains several detector systems for high precision tracking, momentum measurements and particle identification. Its general setup can be seen in Figure 3.2. The STAR detector is constructed inside a large solenoidal magnet with a uniform magnetic field up to 0.5 T. The main detector inside STAR is a large Time Projection Chamber (TPC) which allows charged particle tracking and identification. It covers the full azimuthal range and a pseudorapidity range of $|\eta| < 1.8$. Around the interaction point, the Silicon Vertex Tracker consisting of silicon drift detectors allows both charged particle tracking and the localization of the primary collision vertex as well as secondary vertices from weak decays of hadrons. Outside the TPC, STAR contains an electromagnetic calorimeter, a lead scintillator sandwich calorimeter adds the ability to measure high transverse momentum photons, electrons, and hadrons decaying into photons. Also outside the TPC, a ring-imaging Čerenkov detector and a time-of-flight patch extend the PID ability of STAR. Another detector of the experiment is a radial-drift TPC located along the beam axis, extending the tracking ability into the forward rapidity region.

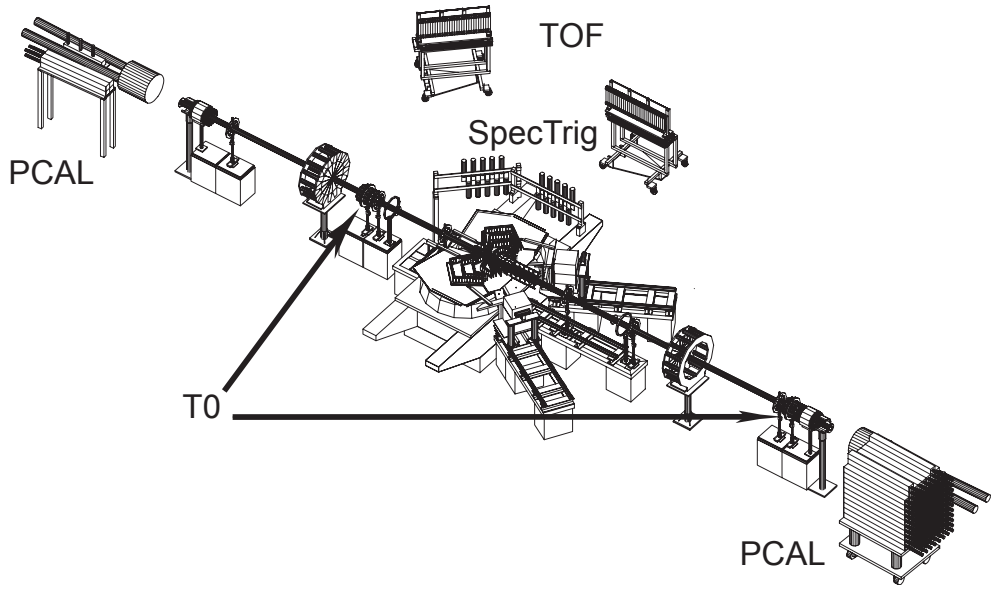

Figure 3.3: The PHOBOS detector [Bac03a].

3.2.2 PHOBOS

PHOBOS[2] [Bac03a] was constructed for measuring charged particles over the full solid angle. The detector is depicted in Figure 3.3, it consists mainly of four parts. Several trigger detectors trigger on collisions and measure the centrality of collisions. A multiplicity array, a single layer of silicon detectors, measures the angular distribution and number of charged particles. It is composed of a central octagon-shaped detector and six ring detectors located along the beam pipe. The PHOBOS spectrometer consists of two arms, each constructed with 15 silicon layers and located on both sides of the beam pipe, providing tracking for $\sim$2% of all charged particles being emitted in a typical collision. One key feature of the spectrometer is its ability to track particles at very low p_{T}. Particle identification is done via measuring the energy loss in each Si layer. Finally, two arrays of time-of-flight detectors allow particle identification up to higher momenta.

3.2.3 BRAHMS

The BRAHMS[3] experiment's [Ada03a] main purpose was the measurement of charged hadrons over the widest possible range of transverse momentum and rapidity. A sketch of the detector is shown in Figure 3.4. Besides global detectors for event characterization, BRAHMS consists mainly of two spectrometers for charged hadron measurement,

[1] **S**olenoidal **T**racker **a**t **R**HIC
[2] PHOBOS it not an acronym [Fer09].
[3] BRoad Range Hadron Magnetic Spectrometer

one forward and one mid-rapidity spectrometer. The larger forward spectrometer consists of two parts, one for intermediate and one for high momentum measurements. It is mounted such that it can be rotated between angles of 2.3 to 30 degrees (15 degrees for the high momentum part) w.r.t. the beam line. It constists of four dipole magnets, five tracking detectors – two time projection chambers closer to the collision point and three drift chambers further away – and four detectors for particle identification – two time-of-flight hodoscopes, a Čerenkov and a ring imaging Čerenkov detector. The mid-rapidity spectrometer is smaller due to easier PID at the expected lower particle momenta; it can be rotated between 30 and 95 degrees w.r.t. the beam line. It constists of a dipole magnet between two time projection chambers for particle identification and tracking, and a time-of-flight detector for particle identification.

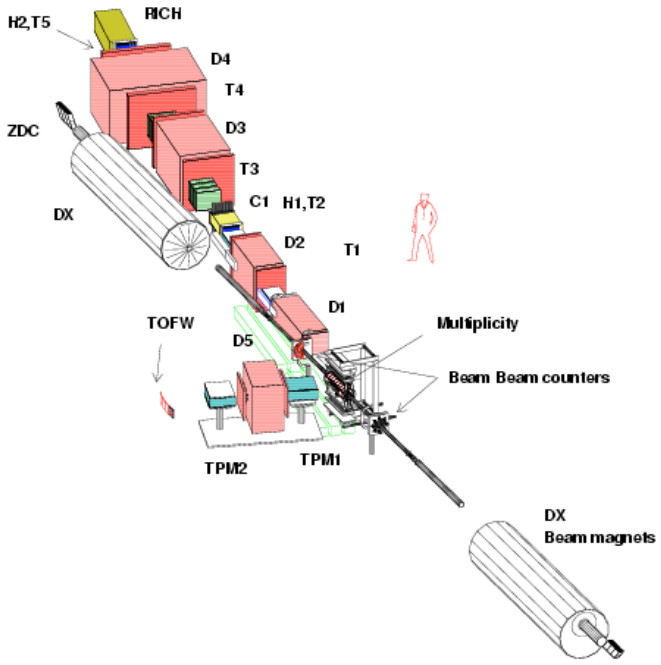

Figure 3.4: The BRAHMS detector [Ada03a].

3.3 The PHENIX Experiment

The PHENIX experiment [Adc03c] is a multipurpose experiment with the feasibility to measure leptons, hadrons and photons. Looking at PHENIX, two main parts of the detector are distinguished: the central spectrometer on the one hand and the muon arms on the other hand. Both these spectrometers consist of two arms, these being composed of several detectors for different analysis tasks. The central spectrometer is located at

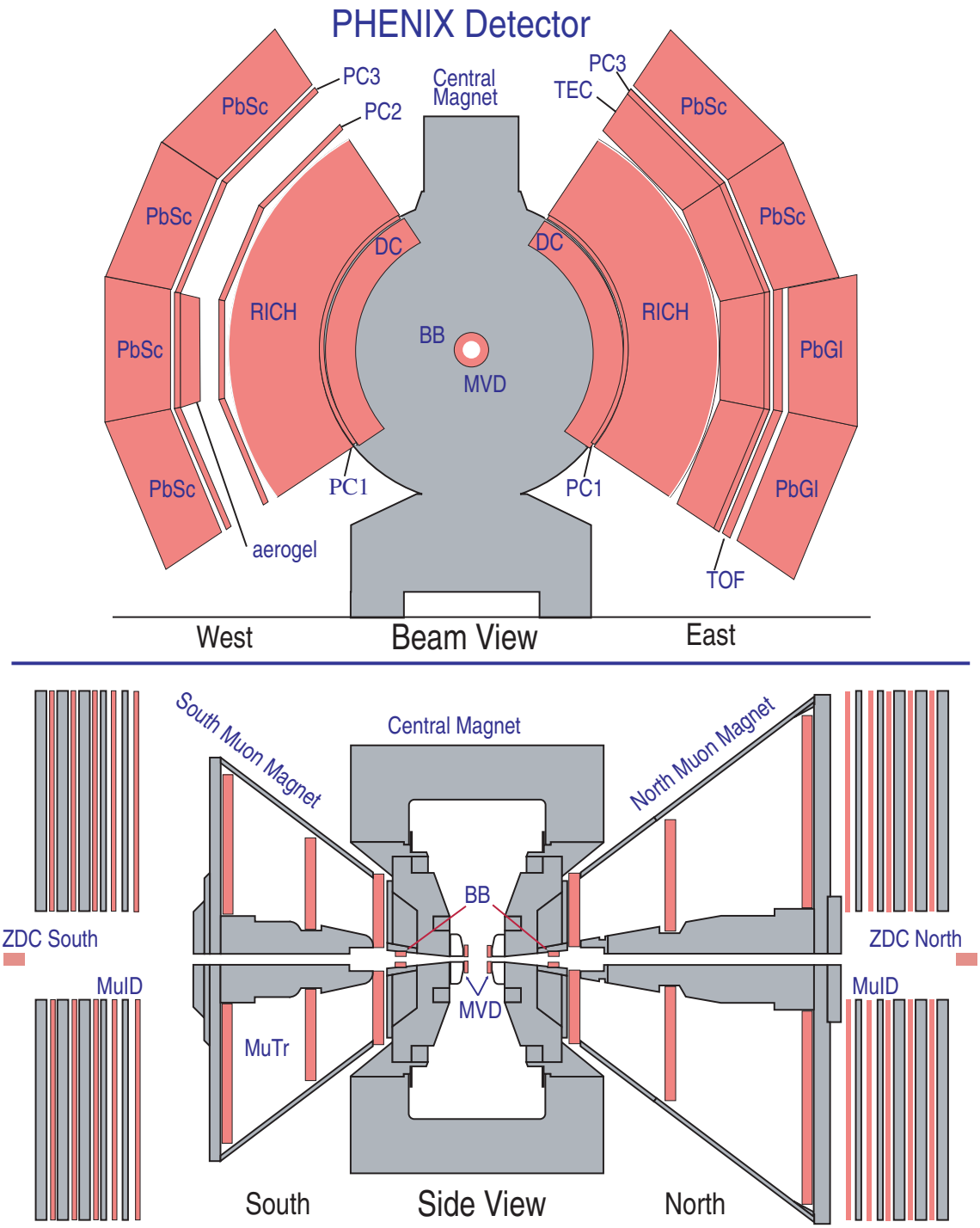

Figure 3.5: The PHENIX experiment [Adc03c] during the 2004 run. The top panel shows a beam view cross section of the central spectrometer, the bottom panel depicts a side view cross section of the muon arms.

midrapidity at both the east and the west side of the collision region. Its angular coverage in azimuth is 180 degrees, while in pseudorapidity it covers the region of $|\eta| < 0.35$. The muon arms, on the other hand, are located north and south of the collision region, at forward rapidity. They have a full azimuthal coverage together with a pseudorapidity coverage of $-2.25 < |\eta| < -1.15$ (south arm) and $1.15 < |\eta| < 2.44$ (north arm). Besides the detectors of the spectrometers, PHENIX also has some detectors to measure global variables for event classification, though they are physically located in the region of one of the spectrometers, they are not part of them. Another important component of PHENIX is the central magnet that creates a magnetic field in parts of the central spectrometer.

3.3.1 PHENIX Magnets

For the analysis of charged particle momenta and the momentum separation of different charged particles with certain detectors in PHENIX, a large magnetic field is required. This magnetic field is provided by the large central magnet for parts of the central spectrometer, and by two muon magnets for the two muon arms, respectively [Aro03].

Central Magnet There were several requirements for the central magnet's (CM) [Aro03] construction. On the one hand, the magnet should have enough material along the beam line to absorb hadrons emerging from the collisions, but on the other hand, there should be no material in front of the central spectrometer to minimize particle interactions with the material of the magnet. Furthermore, a uniform field with precision mapping was required, as well as the possibility to create a "zero-field" along the beam line, with the field integral becoming minimal for the central spectrometer region outside the drift chamber, especially in the RICH detector. A mechanical requirement was a good movability of the magnet to allow access to detector components. For the final design, some compromises had to be found, as the requirements partially contradict each other. The CM now consists of two coils that can be operated independently and yield an axial magnetic field of $\int B\mathrm{d}l = 0.43 - 1.15$ Tm, depending on the current setup of the magnet.

Muon Magnets The muon magnets [Aro03] are arranged around the beam line in both muon spectrometer arms, north (MMN) and south (MMS) of the collision region. The two magnets have the same function in their respective spectrometer, but they are not identical, e.g. the MMS is 1.5 m shorter than the MMN due to space limitations. The requirements for the magnets were the provision of a uniform field with a minimal effect on the beams within RHIC, while having an acceptance as large as possible. The magnets are funnel shaped and produce a radial magnetic field with a gradient of 0.72 Tm.

3.3.2 Global Detectors

In 2004, two different global detectors, the Beam-Beam Counters (BBC) and the Zero-Degree Calorimeters (ZDC) were used to characterize the nature and properties of an event after a collision of two protons, protons with heavy ions or two heavy ions [All03]. Most parts of the originally installed Multiplicity Vertex Detector (MVD) have been removed for that run again. For the 2007 run, another global detector, the Reaction-Plane Detector (RxNP) has been added to the PHENIX setup.

The Beam-Beam Counter The PHENIX Beam-Beam Counter consists of two identical arrays of Čerenkov counters located at both the north and south side of the collision zone, just outside the poles of the central magnet. Each BBC array consists of 64 single elements, a quartz radiator with a photomultiplier readout, and covers a pseudorapidity range of 3.0 to 3.9 over the full azimuth.
The BBC is used as a minimum bias trigger for PHENIX, requiring a certain number of PMTs fired as trigger condition. It is – also together with the ZDC – used for measuring the collision centrality in collisions of nuclei, as its charge sum is monotonically rising with the centrality. The position of the collision vertex is measured with the BBC, on correlation with the ZDC, too. Furthermore, the BBC provides a start signal for time-of-flight measurements.

The Zero-Degree Calorimeter The RHIC Zero-Degree Calorimeters [Adl03b] are hadronic calorimeters installed in each of the RHIC experiments for common event characterization. They are built to detect spectator neutrons – some of them scatter off the beam axis after a collision of nuclei – and measure their total energy. The ZDCs consist of tungsten plates alternating with optical fibers, the ernergy deposit is measured via Čerenkov light produced in the optical fibers.

The Multiplicity Vertex Detector The MVD [All03] was originally designed to characterize and select events, to measure fluctuations of charged particle production and to gain information about the vertex position. The detector consisted of two parts, two concentric silicon strip detector barrels, and two endcaps made from silicon pad detectors. In the 2004 run, only these disk-shaped endcaps were still in PHENIX. They are located at a z position of ± 35 cm, covering a pseudorapidity range of $1.79 < |\eta| < 2.64$ for an event at $z = 0$.

3.3.3 The Central Spectrometer

The PHENIX central spectrometer consists of several detectors, arranged like onion skins around the collision vertex. The detectors can be classified into three categories: a) detectors for tracking [Adc03b], b) detectors for particle identification [Aiz03], and c) calorimeters [Aph03]. Tracking detectors at PHENIX are the drift chamber (DC), the pad chambers (PC), and – during the first runs – the time expansion chamber (TEC). Each of these subsystems has different advantages, the drift chamber allows high resolution p_{T} measurements, the three pad chambers (two in the east arm) measure three-dimensional space points for charged tracks, while the TEC, located only in the east arm, adds additional tracking and further particle identification. Particle ID detectors at PHENIX in 2004 were the ring-imaging Čerenkov detector (RICH), the time-of-flight detector (TOF) and the aerogel Čerenkov counter (ACC or AGEL). Since 2004, more detectors have been added to the central spectrometer, namely another time-of-flight detector in the west arm (TOF-W), and a hadron-blind detector (HBD).

The Drift Chamber The cylindrically shaped PHENIX drift chamber [Adc03b] is located from 2 to 2.4 m away from and 2 m along the beam pipe. The residual magnetic field in this region has a maximum of 0.6 kG. The DC consists of two parts, one in each spectrometer arm, it measures the trajectories of charged particles in $r-\phi$ direction. Due to the magnetic field and the geometry of PHENIX, particles can be detected in the outer parts of the central spectrometer without passing the drift chamber.

The Pad Chambers The pad chambers [Adc03b] are multiwire proportional chambers that are located at different distances from the beam pipe. The innermost pad chambers (PC1) in each arm of the central spectrometer are located between the drift chamber and the RICH detector. In front of the electromagnetic calorimeter, or – in case of the lead glass calorimeter – in front of the TOF detector, the outermost pad chamber (PC3) is also present in both arms of PHENIX. Another pad chamber (PC2) exists only in the west arm, located behind the RICH detector. The pad chambers measure three dimensional space points for charged tracks and allow determining $p_{\mathrm{z}}/p_{\mathrm{T}}$. As all pad chambers are located outside the magnetic field, they can measure the straight line particle trajectories in this space region.

The Time Expansion Chamber The TEC [Adc03b] consists of 24 multi-wire tracking chambers in four sectors, such that each sector is composed from six chambers arranged in radial succession. The TEC is located in the east arm of PHENIX, between the RICH and the PC3. Each sector covers $\pi/8$ in azimuth and ± 0.35 in pseudorapidity. The detector measures tracks of charged particles passing through RICH and EMCal in the $r-\phi$

direction. After two years of running, the TEC was upgraded to a tracking transition radiation detector by adding radiators in front of the drift region. This upgrade enhances the momentum range of electron identification significantly.

The Ring-Imaging Čerenkov Detector The RICH [Aiz03] is located in both arms at a radial distance of 2.5 to 4 m. Each RICH detector has a volume of 40 m^3, the entrance window has an area of 8.9 m^2 and the exit window one of 21.6 m^2. The RICH volume is filled with ethane as drift gas, particles are detected by Čerenkov light emission that is focused by an overall of 48 arrays of spherical mirrors onto arrays of photomultipliers. The RICH main particle ID capability is the separation of electrons and pions below the π Čerenkov threshold of 4 GeV/c. Together with the EMCal in both and the TEC in one arm, the false identification of hadrons as electrons is expectred to be minimized to less than 1 per 10^4 for such momenta. To minimize conversion of photons into e^+e^- pairs in the RICH, the mirrors, windows and the radiator gas have to be as thin as possible. Therefore, RICH has a total thickness of 2% of a radiation length while in operation.

The Aerogel Čerenkov Counter The ACC [PC03] was added to the PHENIX setup for the 2004 run, it is located in the west arm at a radial distance of ≈4.5 m, between the PC2 and the PC3 in the W1 sector, thus covering $\sim \pi/8$ in azimuth. The detector consists of 160 single detector cells, each cell has three parts: a piece of hygrophobic silica aerogel with a refractive index of 1.0114 ± 0.0008, attached to an integration air gap and two photomultiplier tubes at the side surfaces of the air gap. The ACC increases the PID capabilities of PHENIX, allowing pion-kaon separation or proton-kaon separation in the momentum range of $\approx 1-5$ GeV/c and $\approx 5-9$ GeV/c, respectively.

The Time-of-Flight Detector The TOF [Aiz03] is only present in half of the east arm of the spectrometer, being located in front of the PbGl calorimeter in the lower part of the arm. The detector measures the time of flight of particles, which is compared to the particle momentum for distinguishing between different particle species. The PHENIX TOF detector is located at a radial distance of 5.1 m, between PC3 and the PbGl, it consists of 960 scintillator slats with a timing resolution of about 100 ps. This resolution allows a 4σ separation of π and K up to 2.4 GeV/c. The scintillators are oriented in $r-\phi$ direction, 96 of them are part of a panel, the TOF consists of 10 such panels.

3.3.4 The Muon/Forward Spectrometer

The PHENIX muon arms [Aki03], located north and south of the collision region, along the beam line, are designed to detect muons and antimuons in the rapidity range $1.2 < |\eta| < 2.4$ while rejecting pions and kaons by a factor of about 10^3. Therefore, two

different detectors are present in each spectrometer arm, a radial field magnetic spectrometer, the Muon Tracker (MuTR), and a Muon Identifier (MuID) constructed with absorber and tracking layers. The measurement of muons is an important method of reconstructing vector mesons such as J/Ψ or Υ which play an important role when studying a possible quark-gluon plasma. After 2004, another detector, the so-called Muon Piston Calorimeter (MPC), an electromagnetic calorimeter, was included in the muon arms of PHENIX to measure photons and particles with photonic decay channels such as π^0 at forward rapidities.

The Muon Tracker Each of the two muon trackers [Aki03] consists of a funnel-shaped magnet around the beam line. The magnet provides a radial magnetic field. Muons are detected at three stations of cathode-strip readout tracking chambers inside the magnet. The cathode strips have multiple orientations and readout planes in each of the stations. The stations are located at distances of $z = \pm 1.60$ m, $z = \pm 3$ m, and $z = \pm 4.60$ m. This design allows a relative mass resolution of $\sigma(M)/M = 6\%/\sqrt{M}$ and so a clear separation of the J/Ψ from the Ψ' or the ρ/ω from the ϕ.

The Muon Identifier The MuID detectors [Aki03] are located behind the muon magnets in each arm. This detector was designed to suppress the charged pion background in the muon measurement such that the misidentification of pions as muons in the MuID is below 2.4×10^{-4}. Therefore, the detector is constructed of alternating layers of four steel absorbers and five detector planes. The first absorber plate is the backplate of the MuTR detector with a thickness of 30 cm and 20 cm in the north and the south arm respectively. The four other steel absorbers have thicknesses of 10, 10, 20, and 20 cm. The detector planes between the absorbers are made of so-called Iarocci tubes, planar drift tubes.

3.4 The Electromagnetic Calorimeter

As the Electromagnetic Calorimeter [Aph03] is the main detector for measuring photons and thus is the main detector for the measurements performed in this thesis, it is described in more detail in the following. The EMCal is located in both arms of the central spectrometer, convering a pseudorapidity range of $|\eta| < 0.35$ at an azimuthal coverage of π. The calorimeter is divided into eight sectors, each of them covering 22.5 degrees in azimuth. Six of these sectors (all four in the west and the two upper ones in the east arm) are a lead scintillator (PbSc) sandwich calorimeter, the two other sectors in the east arm are a lead glass (PbGl) Čerenkov calorimeter.

3.4.1 Detection Principles

The detection of particles in electromagnetic calorimeters is based on the creation of so-called "electromagnetic showers" in the detector material. Energetic photons hitting the calorimeter can generate an e^+e^- pair via pair production. These electrons and positrons subsequently lose energy via bremsstrahlung and therefore emit photons again. If the incoming particle is an electron or positron, the particle first undergoes bremsstrahlung emission. A sequence of such interactions leads to a cascade of photons, electrons, and positrons. These processes stop when the energy of the particles is below a certain threshold E_c, the energy at which electrons lose energy dominantly by ionizing or exciting atoms and not by bremsstrahlung any more. For lead, $E_c \approx 7$ MeV.
An important quantity to describe a material's ability of creating electromagnetic showers is the so-called radiation length X_0 which is connected to the cross section of both pair production and bremsstrahlung. X_0 is a material dependent constant and can be approximated as [Ams08]

$$X_0(\mathrm{g/cm^2}) \simeq \frac{716.4 \cdot \mathrm{g} \cdot \mathrm{cm}^{-2} A}{Z(Z+1)\ln(287/\sqrt{Z})} \,. \tag{3.1}$$

Z and A are the atomic number and the atomic weight of the element, respectively. The radiation length is the average distance x an electron travels within the material until its energy is reduced to $1/e$ of its original energy. For photons, it corresponds to 7/9 of the distance x where $1/e$ of their intensity is lost which means that about 54 % $(1-e^{7/9})$ of all photons undergo pair production within X_0.
The depth of the shower maximum can be described in units of radiation length and depends on the energy of the primary particle. It is given as [Fab03]

$$\frac{X_{max}}{X_0} \approx \ln\left(\frac{E_0}{E_C}\right) + C \,. \tag{3.2}$$

The constant C depends on the initial particle, $C = +0.5$ for photons and $C = +-0.5$ for electrons and positrons. Equation 3.2 shows the necessary thickness of a calorimeter in terms of the maximum particle energy to be measured. The lateral extension of an electromagnetic shower is explained by multiple scattering of shower particles, it can be characterized via the Molière radius [Fab03]

$$R_M \approx \left(\frac{E_S}{E_0}\right) X_0 \,, \tag{3.3}$$

where E_S is the so-called scattering energy of 21 MeV. In a homogeneous calorimeter, an average of 95 % of the shower energy are in an area with a radius of $2R_M$. The shape of electromagnetic showers as described by the shower depth and the Molière radius can be used to distinguish them from hadronic showers that also occur in electromagnetic calorimeters.

Hadronic Showers Strongly interacting particles, though only losing a negligible amount of energy via bremsstrahlung, also induce showers in a medium. These so-called hadronic showers evolve due to hadronic interactions of hadrons such as pions or protons with the nuclei of the material, they can also be characterized by an interaction length, the nuclear interaction length λ_a, the distance within which about 63 % of all hadrons react inelastically with the absorber and produce further hadrons. 95 % of the energy in a hadronic shower is deposited within a radius of λ_a. As neutral pions can also decay electromagnetically, hadronic showers also have an electromagnetic component, thus they are more complex than sole electromagnetic showers. Charged hadrons that do not interact strongly, can still lose a fraction of their energy by ionization and Čerenkov radiation, such hadrons are called Minimum Ionizing Particles. As their energy loss, described by the Bethe-Bloch formula, is constant over a wide energy range, such hadrons lead to a characteristic peak in the energy distribution, the so-called minimum ionizing particle (MIP) peak.

3.4.2 The PbSc Calorimeter

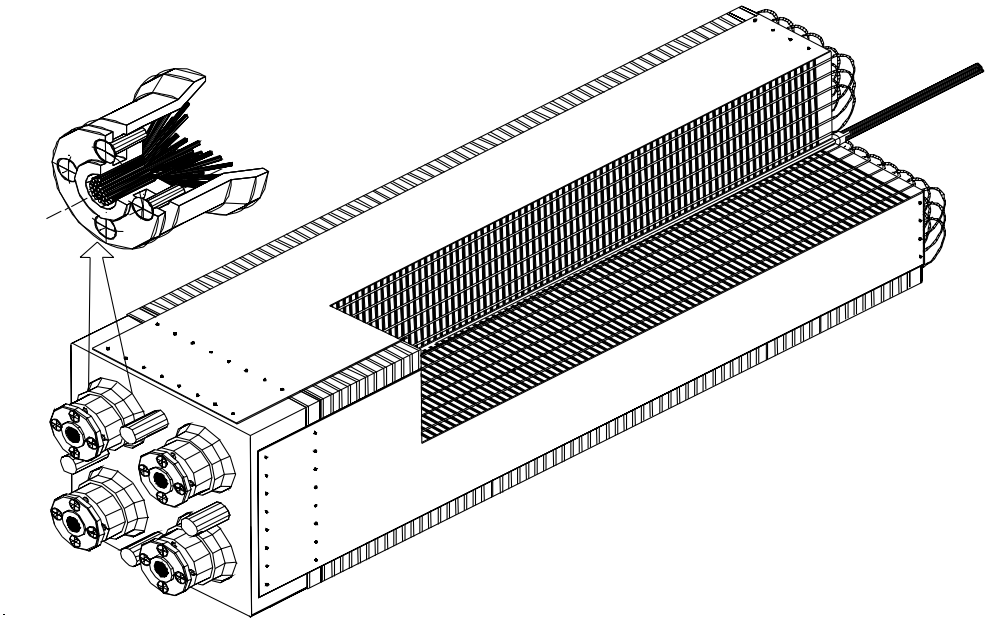

Figure 3.6: Schematic view of one PbSc module [Aph03]. The sandwich structure of alternating Pb and scintillator is clearly visible. Each PMT belongs to one tower. The plastic fiber for the calibration system can be seen in the middle of the four towers as well.

The PbSc electromagnetic calorimeter [Aph03] is built of alternating tiles of Pb and scintillator, it consists of an overal of 15,552 individual towers with an active depth of 37.5 cm and a width of 5.535 cm $\times$ 5.535 mm. The tower length accounts for 18 electro-

magnetic radiation lengths. The optical readout of the towers is performed by wavelength shifting fibers penetrating each of the 66 sampling cell's scintillators and yielding the light to phototubes at the back of the towers. The towers are arranged in so-called modules, the four towers in each such module are optically isolated. Thirty six modules are attached in the same steel frame, called a supermodule. Eighteen of these supermodules make up a sector of the detector which is again mounted inside a steel frame. The total area covered by the six sectors adds up to ≈ 48 m^2. A schematic view of one PbSc module is shown in Figure 3.6.
The PbSc detector has a monitoring system based on ultraviolet YAG lasers. The laser light distribution to each tower is done by splitting the light with partially reflecting mirrors first. The light is further partitioned by optical splitters in each sector and transported to each module by optical fibers that penetrate the center of the module and are thus connected to each of the four towers in a module. The fiber is constructed to leak light into the detector such that is simulates the depth profile of a 1 GeV electromagnetic shower in the four towers. PIN photodiodes finally monitor the laser light intensity in each supermodule. The initial calibration for the PbSc was obtained with the help of cosmic ray muons penetrating the supermodules nearly orthogonal to the tower axis. Test beam measurements with electrons of known energy were used to establish the absolute energy scale for such muons. The same test beam delivered charged pions with an energy of 1 GeV/c, leaving a MIP peak at an energy of 270 MeV for longitudinally traversing particles.
Particle beams, together with GEANT simulations, were also used to obtain the initial energy resolution of the calorimeter. It was found to be $8.1\%/\sqrt{E(\mathrm{GeV})} \oplus 2.1\%$ experimentally, close to the expected resolution from GEANT. The position resolution of the PbSc was also estimated with the data, leading to an angular dependent resolution of $\sigma_x(E,\theta) = \sigma_0(E) \oplus \Delta \times \sin(\theta)$, with $\sigma_0 = 1.55 \oplus \frac{5.7}{\sqrt{E}}(\mathrm{mm})$ as the position resolution for normal incidence and $\Delta \sim L_{\mathrm{rad}}$ [Aph03].

3.4.3 The PbGl calorimeter

The PbGl electromagnetic calorimeter [Aph03] is the same as used in the WA98 experiment at CERN. The components of the WA98 LEDA calorimeter were shipped to BNL after the end of the WA98 measurements and reassembled there in a different geometric design. The detector consists of 9216 PbGl modules which are wrapped with aluminized mylar and shrink foil and read out with a *FEU-84* photomultiplier. Each module measures 4 cm $\times$ 4 cm $\times$ 40 cm, the small face arranged towards the beam line. The length of the modules is an equivalent of 14.4 electromagnetic radiation lengths. 24 of these models (6×4) are glued together and make up one supermodule, 192 of which are in each sector, 16 of them in width and 12 in height. A schematic view of one PbGl sector can be seen in Figure 3.7.

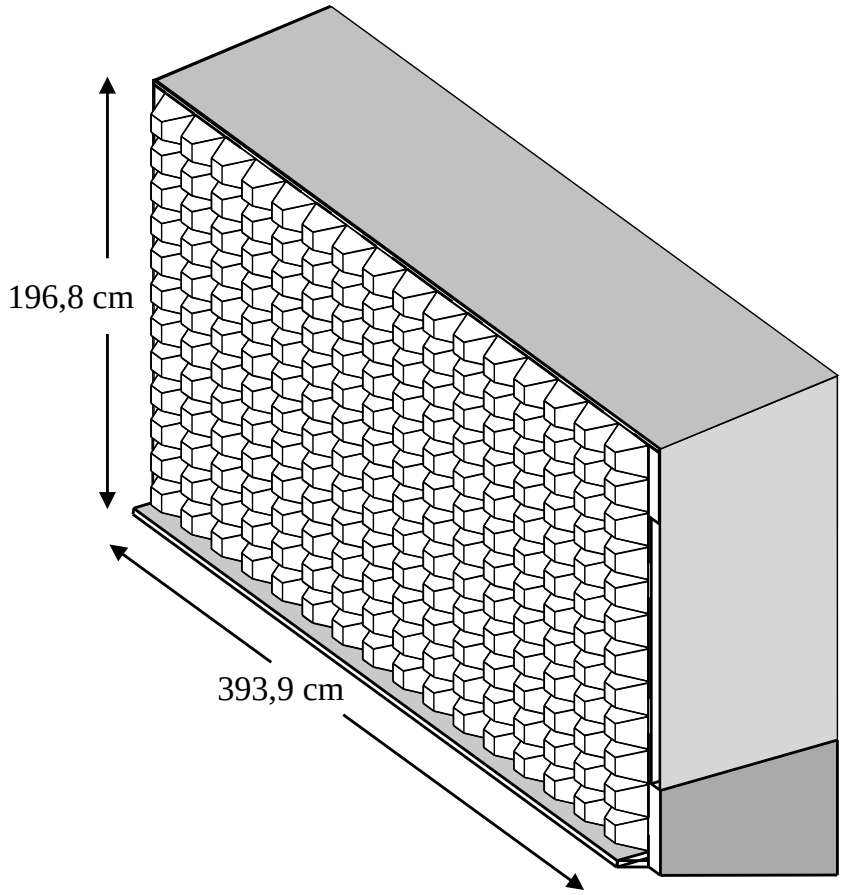

Figure 3.7: Schematic view of one PbGl sector [Aph03].

The PbGl calorimeter uses a gain monitoring system based on 3 LEDs per supermodule that are seen by all 24 modules. The LEDs have different characteristics, one is a fixed amplitude avalanche yellow LED having a pulse shape similar to real showers, the other two LEDs are a yellow and a blue one respectively, with a variable amplitude. A photodiode monitors the absolute light yields of the LEDs in each supermodule. The original calibration of the avalanche LED was done in 1993 and 1994 in the CERN X1 beamline, using 10 GeV electrons. The monitoring system helps keeping the PbGl calibration within $\approx 10\%$. One PbGl supermodule with the monitoring system is depicted in Figure 3.8.

The initial energy and position resolution of the PbGl detector were studied in test beams at the AGS at BNL and at the SPS at CERN. Positron showers have been used to obtain the energy resolution of the calorimeter, which was found to be $[5.9 \pm 0.1]\%/\sqrt{E(\mathrm{GeV})} \oplus [0.8 \pm 0.1]\%$. The position resolution does not show a significant angular dependence and can be parameterized as $\sigma_x(E) = [0.2 \pm 0.1]\mathrm{mm} \oplus \frac{[8.4 \pm 0.3]\mathrm{mm}}{\sqrt{E/\mathrm{GeV}}}$ [Aph03].

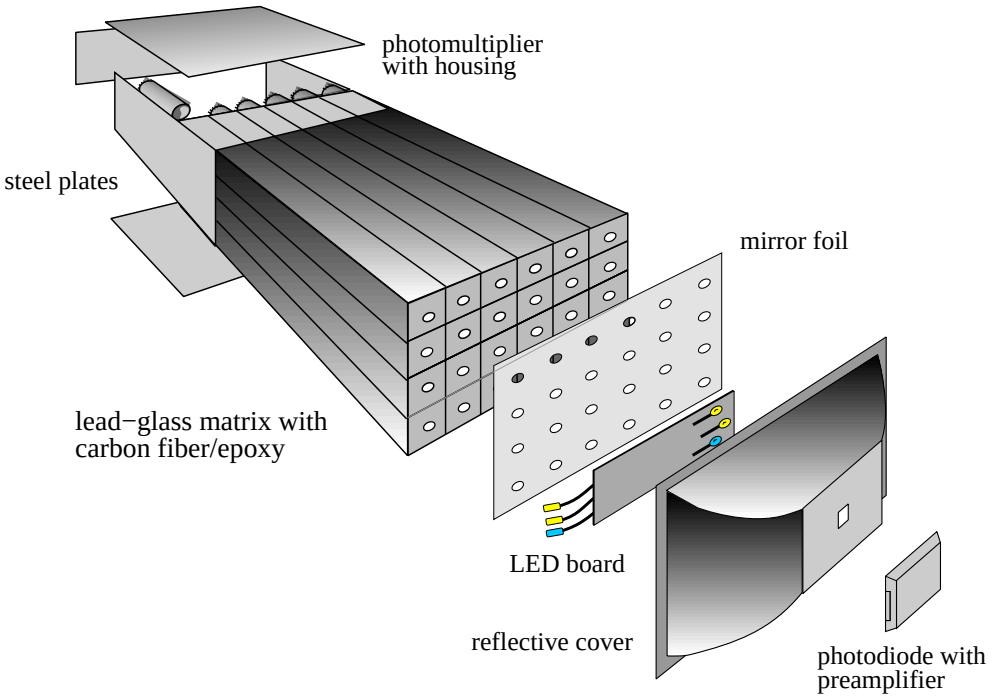

Figure 3.8: Schematic "exploded" view of one PbGl supermodule [Aph03]. The single PbGl modules are visible with the PMTs attached in the back. In the front, the monitoring system with the LEDs, the reflective cover, and the photodiode is visible.

3.4.4 EMCal Front End Electronics

The EMCal readout electronics is located on the so-called Front End Modules (FEMs) [Aph03]. Each of these FEMs reads out 144 individual towers, they are identical for PbGl and PbSc, therefore, one FEM serves 2×3 PbGl supermodules and 1 PbSc supermodule respectively. The negative current pulses emitted by the EMCal PMT's are first integrated passively and then processed as both a charge and a timing signal to an ASIC[4] chip specially designed for the EMCal. Each of these chips serves four PMT's. The energy signal is first amplified in a Variable Gain Amplifier (VGA) which gain can be set remotely. Afterwards, it is split into a low gain and a high gain signal, the latter further amplified 16 times. This allows a quite large dynamic range for the energy measurement.

3.5 PHENIX Online System

The purpose of the PHENIX online system [Adl03e] is to select, process, and record the events that take place in the interaction region. The need to analyze events from differ-

[4] Application Specific Integrated Circuit

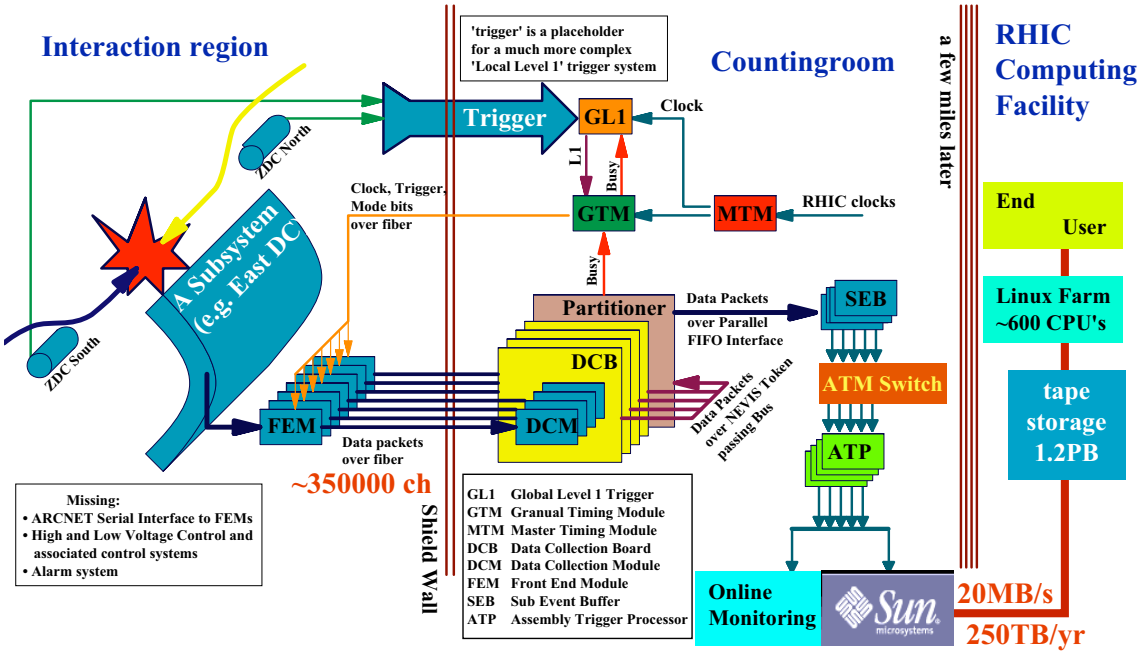

Figure 3.9: Schematic view of the PHENIX online system [Adl03e]. The general event data flow goes from left to right, or from top to bottom respecively [Adl03e].

ent collision systems over a broad range of collision energies requires a system that can handle both high event rates and large event sizes, the latter at lower event rates. Such a system needs to include triggers to select for interesting signatures, e.g. events with hard scattering processes. Basically, two different trigger approaches are distinguished at PHENIX. The Level-1 (LVL1) triggers are controlled by the RHIC beam clock, having a rate of 9.43 MHz. This clock also steers the lower levels of the parallel readout at PHENIX. The Level-2 (LVL2) triggers, on the other hand, are driven by decisions on the already measured data, therefore they are applied after an event already has been processed to a certain level. A full overview of the online system, depicting the general flow of the data as well as the general flow of control signals is shown in Figure 3.9.

Front End Modules The calorimeter specific characteristics of the Front End Modules have already been outlined in Section 3.4.4. In general, the FEMs at PHENIX [Adl03e] are constructed modularly and are thus similar for the different detector subsystems as many of the used functions are the same. The general purpose of the Front End Electronics (FEE) is the digitalization of the analog detector output and the storage of the data until receiving a LVL1 trigger decision. The digitalization of the signals is done in two ways at PHENIX. One approach, also used e.g. by the EMCal, is the use of so-called Analog

Memory Units (AMUs), arrays of capacitors, to sample and store the analog data. The data are digitized only after reception of the LVL1 accept signal.The other approach is the direct digitalization of the data and their buffering in so-called Digital Memory Units (DMUs).
The control of the FEE is performed by a Heap Manager (HM) that is responsible for e.g. mode interpretation and execution, timing and control, data formatting and communication, and management of read-out requests.

Level-1 Trigger The PHENIX Level-1 trigger [Adl03e] consists of two different systems. The Local Level-1 system (LL1) collects the data from different detector subsystems such as BBC, ZDC, RICH, EMCal, and MuID, and processes this input and converted into a bit pattern for each RHIC bunch crossing. This information is sent to the Global Level-1 (GL1) system where the LL1 data are combined and a raw trigger is generated. The GL1 then checks if trigger system or the PHENIX Data Acquisition (DAQ) is busy. If the raw trigger passes this test, it is converted into a live trigger. Finally, the live trigger is further converted into the scaled trigger by comparing it to a scaledown counter, just if this scaled trigger generates an accept signal, the FEMs are read out.
The BBC plays the major role in the minimum bias trigger decision, the trigger for inelastic collisions. Depending on the collision system, the minimum bias trigger condition can be varied by requiring a certain minimum of BBC PMTs having fired. Other LVL1 trigger conditions can be used to search for rare events, e.g. for events containing a highly energetic particle in one of the PHENIX detectors. Highly energetic photons and leptons e.g. are selected with the EMCal-RICH trigger which has not been used in this analysis but played and plays a crucial role in other PHENIX datasets [KB04, Zau07].

Data Collection The data of each event passing certain selected trigger thresholds, for example the LVL1 trigger, are transferred to the Data Collection Modules (DCMs) [Adl03e] in the counting house by optical fibers. The DCMs collect the approximately 375000 channels and format, zero suppress, and check them in parallel. Each of the DCMs has four data input streams and thus serves four FEMs. Up to five events can be buffered in the DCMs before being processed to the Event Builder. The so-called Granule Timing Module (GTM) is used to control the FEM readout, it provides the clock, the LVL1 accept signals and mode bits for the FEMs. The GTM distributes the central RHIC clock to the different Granules, configurable sets of detector data streams to be read out.

Event Builder The final system in the DAQ is the Event Builder (EvB) [Adl03e] which performs the final event assembly in PHENIX before the data are sent to the PHENIX Online Control System (ONCS). The EvB collects the fragments from each data stream and assembles them into complete events, furthermore, Level-2 (LVL2) triggers are processed

in the EvB, before the accepted events are further transmitted. These Level-2 triggers are used to further reduce the data rate, they are necessary when the data rate of the LVL1 triggered exceeds the data rate the online system is able to archive. In such a case, a set of different algorithms analyze certain detector information. The LVL2 trigger is software based, in contrast to the hardware LVL1 trigger and therefore can perform more sophisticated operations such as track reconstruction. Thereby, interesting events can be selected more precisely.
The EvB consists of a set of Sub-Event Buffers (SEBs) that are used to read out the different Granule settings independently. After checking, the data are transferred from the SEBs to the Assembler/Trigger Modules (ATMs), where LVL2 triggers can be applied to the data, the data rate that has to be written to disk is reduced by this. If the trigger decision is positive, the event is assembled, putting together the different data streams. Finally, events that are assembled, are stored on disk for online monitoring and eventually archived at the RHIC Computing Facility (RCF) on a High Performance Storage System (HPSS), a tape storage system.

4. Analysis of the PHENIX Data

```
Computers make excellent and efficient servants, but I have
no wish to serve under them.
```

Mr. Spock - Star Trek

Before the actual measurement of π^0's, η's, or direct photons in PHENIX events, some preparatory work is necessary. The detector information has to be translated into useable physics information, the detectors need to be calibrated and events have to be selected based on defined criteria. Furthermore, global event information is needed to classify the events into subsets that are needed during the analysis or for the interpretation of the results.

4.1 PHENIX Event Building

Several steps are necessary to process the original detector output into a form that allows good access for later analyses. During this processing, the dataset is reduced by triggers that select certain events only, and raw detector information such as voltages or currents are transformed into physics variables such as energy or position of a detector hit.

4.1.1 Online System

Each detector within PHENIX contains Front End Modules (FEM) that digitize the analog data from the detector components themselves and also buffer the data such that LVL1 trigger decisions can be made and latencies in data readout can be handled. If the LVL1 trigger accepts an event, the Granule Timing Module (GTM) generates a signal to accept the event, that is subsequently sent to the FEM's. The data is then processed in the FEM's and sent to the Data Collection Modules (DCM) where zero suppression, error checking and data formatting take place. The data packets are transferred from the FEM's in the PHENIX Interaction Region (IR) to the DCM's in the Counting House (CH) by fiber-optic cables.

4.1.2 Offline System

PHENIX offline computing is responsible for data reconstruction, i.e. the processing of the raw detector data into useable event data ready for analysis tasks, for data analysis, i.e.

the extraction of physics quantities and variables from the data, and for simulations, i.e. the simulation of physics processes to understand the data and effects of e.g. the detector, or of analysis cuts. A framework called PISA (PHENIX Integrated Simulation Application) incorporates the full PHENIX geometry and can be used to evaluate events simulated within PHENIX. The Fun4All framework is the interface between the underlying analysis software and the stored event data on one hand and the user's analysis programs on the other hand.

4.1.3 Data Summary Tables

The event data are stored in so-called *Data Summary Tapes* (DSTs) after reconstruction. Simulation output can also be processed to be stored in a DST with the same structure as real data. The DSTs contain physics variables obtained from the detector output, e.g. the energy and position of a hit on a PHENIX subdetector or further variables used for particle identification. Data within the DSTs are organized event-wise, global event characteristics are stored with information for detector hits etc. The DSTs are tailored to the needs of different analyses, hence there are different DSTs available for the same collisions, one e.g. optimized for dilepton analyses and another one for photon analyses. Furthermore, data reduction is applied during DST production, to save disk space and to accelerate specific analysis tasks. Therefore there are different levels of DSTs, called microDSTs, nanoDSTs, or picoDSTs. In this analysis, so-called PWG-nanoDSTs have been used, these DSTs are optimized for analyses with photons. They in particular store global event information, information about hits on the calorimeter and also the closest hits in the PC3 with respect to calorimeter hits.

4.2 QA and Event Selection

As no experiment is perfect, before each physics analysis, certain criteria have to be defined for data to be further analyzed. Such criteria are used to discard data taking periods with problems in the apparatus, as well as to reject data that do not contribute to the physics result but might increase the background. Of course, it has to be made sure that applying such criteria does not lead to cutting out possible effects that would have to be considered in the data analysis.

4.2.1 Run Selection and Run QA

The aim of the Run quality assurance (QA) is the removal of those data taking runs with problems in the detector or the data acquisition system. For example, the first runs taken in

the 2004 RHIC data taking period[1] are completely discarded because the east arm of the PHENIX central spectrometer was not moved into its correct position and therefore the reconstruction of invariant masses or the transverse momenta of particles is impossible. Other runs are rejected due to a bad π^0 peak position when compared to the expectation and the average behavior of the peak position, bad centrality distributions, or because a thick photon converter was put into PHENIX. Additionally, a few runs were removed from the data sample due to deviations in the average hit multiplicity on the calorimeter, in the average hit energy, or because the sum of charge measured in the BBC was off the average.

4.2.2 Event Selection

In the analysis of the runs that were accepted during the QA studies, events are analyzed when they fulfill certain conditions. The collision vertex as measured by the BBC has to be in the range -30cm $< z <$ 30cm. The event also has to have a valid information on centrality and the reaction plane, that means that the centrality percentage has to be in the range between 0 and 92.2 % while the reaction plane of the event has to be within a maximum angle of 2π. If one of the values lies outside the mentioned values, the event has been misreconstructed during the DST production.

4.2.3 Exclusion of Bad Towers

Especially for the measurement of direct photons, but also for the measurement of the π^0 and η , it is essential to make sure that all calorimeter towers that do not work correctly are excluded from the analysis, as each malfunctioning tower would lead to a non-physical change of the measured raw cluster spectrum on the EMCal. Malfunctioning towers are called *dead* when they do not produce any energy signal at all, this can happen for instance when PMTs fail. On the other hand, so-called *hot* towers are those towers that produce an energy signal without having been hit.

Some towers are already removed during the DST production, based on quality criteria such as the energy spectra of the single towers. Further hot and cold towers are found on a statistical basis. The distribution of total hits in each tower is checked for different hit energy ranges, and under the assumption of a Gaussian or – at higher hit energies where the medium hit number per tower gets small – a Poisson distribution, towers that show a significant deviation (usually being away more than $\approx 5-7\sigma$ from the mean hit number) are regarded as bad.

[1] These data taking periods are also known as “runs”, not to be mistaken with the single data taking runs that usually are equivalent to about 30 minutes of data taking.

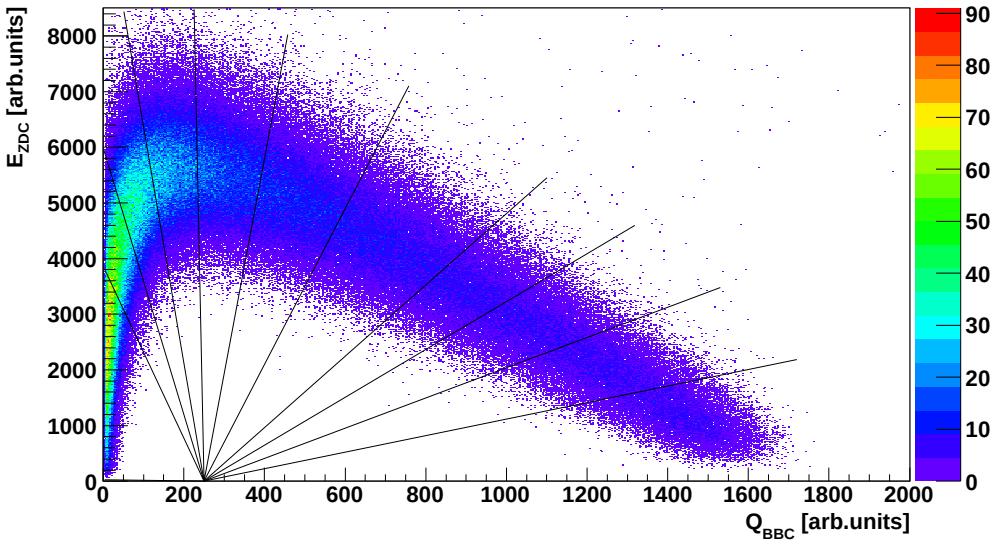

Figure 4.1: Correlation plot of BBC charge sum and ZDC energy deposit as used for the centrality determination. The lines represent the centrality cuts.

4.3 Global Variables

Global variables are those variables measured by PHENIX that characterize an event as such. These variables include the centrality, reaction plane, or the vertex position of an event.

4.3.1 Centrality Determination

The centrality of an event is an important quantity for understanding collisions of heavy nuclei such as gold or copper. In principle, the measured event centrality should be directly connected to the impact parameter b, which describes the distance of the centers of the colliding nuclei. Since this parameter cannot be measured directly, other ways of determining the centrality have to be used. These methods rely on measured observables, hence they are subject to statistical fluctuations. Thus the $n\%$ most central events are not identical to the $n\%$ events with the smallest impact parameter.

The centrality of a Au+Au collision in PHENIX can be determined in different ways. The most straightforward one is measuring the multiplicity of charged particles in the BBC for each event. It is expected that the number of created particles is increasing towards more central events since more and more collisions of nucleons or partons can occur. Therefore, when determining the BBC charge sum for each event, one can simply set cuts after a certain fraction of events for the centrality selection. Another method to

measure the event centrality is determining the correlation of the aforementioned BBC signal and the energy deposit in the ZDC. The latter one is expected to drop towards central collisions since the number of spectator nucleons is decreasing, though the picture is not that simple for ultra peripheral collisions. The centrality selection will lead to different results depending on the used method, this can already be seen in Figure 4.1, the cuts in the BBC-ZDC plane could not be reproduced with the BBC information alone. Therefore, the experimental centrality definition has to be accounted for when calculating values such as the number of binary nucleon-nucleon collisions or the number of participant nucleons. This analysis uses the second method for centrality selection, with the help of a predefined method in the PHENIX analysis framework, the so-called getCentralityByClockRun4 method [Kel00]. Here, the events are divided into different classes depending on an angle ϕ_{cent} in the plane of the BBC charge sum Q_{BBC} and the ZDC energy sum E_{ZDC}:

$$\phi_{\text{cent}} = \arctan\left(\frac{(Q_{\text{BBC}} - Q_0)/Q_{\text{max}}}{E_{\text{ZDC}}/E_{\text{max}}}\right) . \tag{4.1}$$

Here, E_{max} and Q_{max} stand for the maximum ZDC energy and the maximum BBC charge, respectively. The value Q_0, the origin of the cuts, is chosen as 250. The centrality classes are then simply chosen by cutting on the angle of each event. The centrality selection is depicted in Figure 4.1.

Initially, events have been divided into 11 different classes of centrality. The 20% most central events have been divided into four classes of the same size, each representing 5% of all events. The 20-80% most central events have then been divided into 6 classes of the same size, here each class contains 10% of all events. Finally, the eleventh class contains the most peripheral events, namely the 80-92.2% most “central” events. The remaining very peripheral events did not satisfy the minimum bias trigger condition and were thus not even measured by PHENIX.

4.3.2 Determination of the Reaction Plane

The reaction plane in a collision of nuclei is the plane spanned by the impact paramter b and the direction of the colliding nuclei which is the same as the beam direction. The beam direction is a known quantity, but it is impossible to directly observe the impact parameter. Therefore, it has to be meausred indirectly, by the azimuthal distribution of particle production itself [Pos98]. In the 2004 PHENIX run, the BBC was used to determine the reaction plane of an event.

4.3.3 Determination of the Vertex Position

The knowledge of the vertex position of an event is not only important for the event selection as described in Section 4.2.2, but also for the calculation of the transverse momentum of photons or the invariant mass of photon pairs. The vertex in PHENIX is measured with the BBC. The difference of the northern and the southern BBC time signals is used for this measurement. Since the timing resolution of the BBC is about 50 ps, the vertex can be determined with a precision of about 1.5 cm.

4.4 PID Cuts

To get rid of at least some non-photonic hits in the calorimeter, two different particle identification (PID) cuts have been applied in this analysis. The first one is simply a cut on the hit energy, with a threshold of 200 MeV. This cut mainly removes the amount of data to be processed and removes noisy channels as well, but it has no further effect in the measurement of high transverse momentum mesons or photons.

The other PID cut applied is a cut on the shape of the electromagnetic shower. This cut is based on the observation, that hadronic showers in a calorimeter have quite different shower profiles as compared to electromagnetic showers. For the PbSc, the shower shape cut is realized via a χ^2 cut. The χ^2 of the shower is connected to the probability of the shower to be electromagnetic or not and based on comparing the measured shower with the ideal energy deposit of a photon in the calorimeter. This expected energy deposit has been estimated by test beam measurements and simulations. For this analysis, all clusters with a $\chi^2 > 3$ are removed. Further information on the χ^2 cut is given in [KB04].

For the PbGl, a different approach was used. Here, an angular dependent dispersion cut, derived in simulations [KB00], is applied:

$$D_{\text{cut}}(\theta) = 0.27 - 0.145 \cdot \theta + 0.00218 \cdot \theta^2 \, . \tag{4.2}$$

The angle θ is the incident angle of the incoming particle with repect to the calorimeter surface. The actual shower's dispersion in x and y direction is calculated during the DST production from the energies deposited in the towers within the cluster [KB04]. It is defined as

$$D = \frac{\sum E_i x_i^2}{\sum E_i} - \left(\frac{\sum E_i x_i}{\sum E_i} \right)^2 = \bar{x^2} - \bar{x}^2 \, , \tag{4.3}$$

here, E_i are the energies in the detector modules at position x_i. This dispersion is calculated in x and y direction. It has to be corrected for the intrinsic minimum dispersion

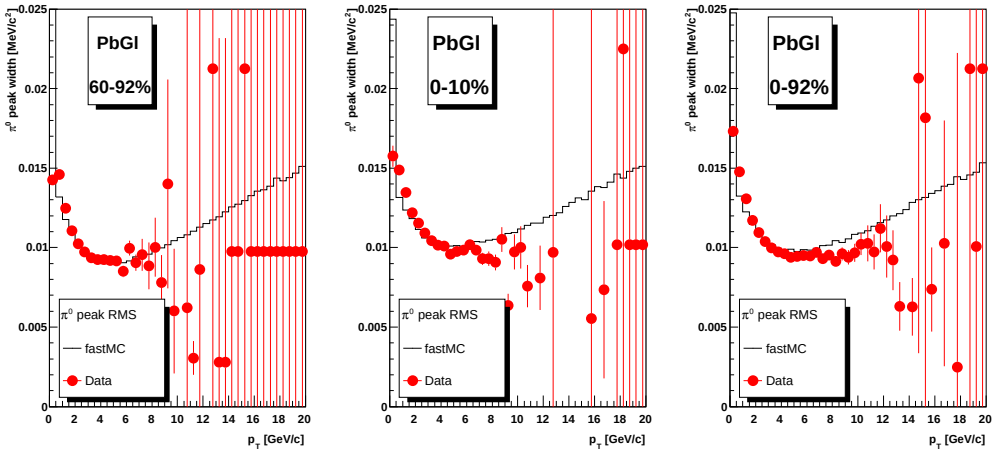

Figure 4.2: π^0 peak width in the PbGl from real data and from the fast Monte-Carlo simulation, for three different centrality selections.

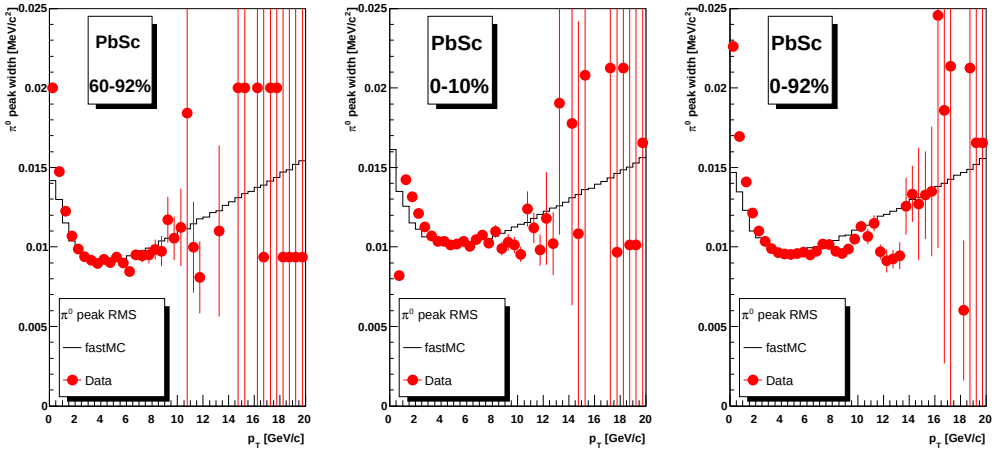

Figure 4.3: π^0 peak width in the PbSc from real data and from the fast Monte-Carlo simulation, for three different centrality selections.

due to the finite size of the PbGl towers. In the analysis, the maximum dispersion in x and y direction is calculated and compared to the cut condition in Equation 4.2.

4.5 Energy Calibration

The energy calibration of the lead glass calorimeter was initially obtained from a test beam at CERN [Aph03]. For this analysis, the fine tuning of the energy calibration was done with the help of the π^0 peak. For this purpose, the analysis is performed the same

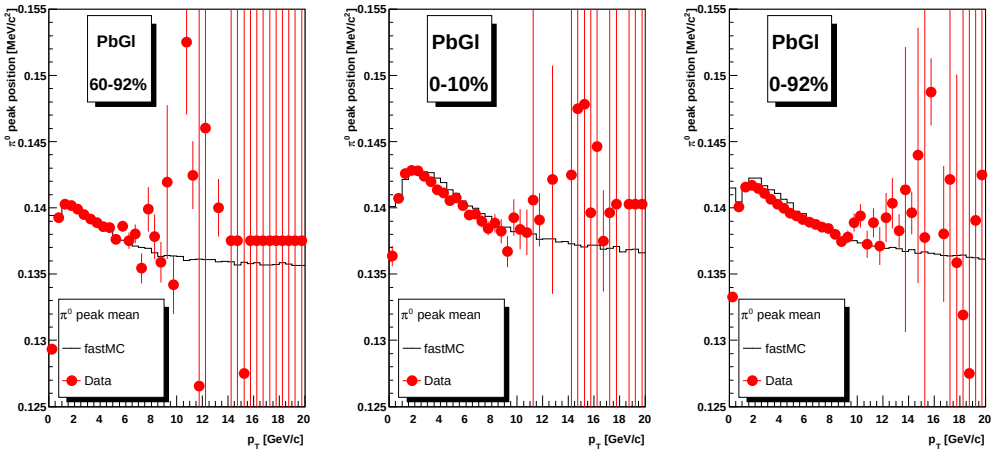

Figure 4.4: π^0 peak position in the PbGl from real data and from the fast Monte-Carlo simulation, for three different centrality selections, after the calibration.

way as described later in Section 5.1, but with a sharp asymmetry cut, allowing only symmetric π^0 decays with a decay photon asymmetry smaller than 0.2. In addition, the transverse momentum p_T is replaced by $(E_{\gamma,1} + E_{\gamma,2})/2$. These changes in the analysis lead to proportionality between the energy of the π^0 and the energy of the decay photons, the quantity the detector actually measures as one can assume that the energy of each decay photon is approximately half the π^0 energy and that both decay photons have almost the same energy. In addition, this method allows to correct for the energy scale nonlinearily.

To obtain the correction factor, the measured position of the π^0 peak has to be compared to a known value. To calculate that value, the same fast Monte-Carlo simulation program as for the acceptance and the efficiency correction (see Section 5.2) is used. This program is run with the same parameters – i.e. the asymmetry cut and the replacement of p_T – as described above for the data. The parameters for the energy smearing are tuned to the π^0 peak width (the RMS of a Gaussian fit to the peak) from the data such that the simulated and the real peak width match each other. A comparison of the peak width within the data and in the simulation is shown in Figures 4.2, and 4.3, for the PbGl and the PbSc, respectively. The peak width of data and simulation agree very well, the deviation at higher p_T is caused by the limited sample size of the data. The energy smearing parameterization in the simulation differs from the original test beam data, including an additional smearing that can be attributed to aging of the detector or a non-perfect initial calibration of the detector. The energy correction factor is then calculated by comparing the positions (the mean of the same Gaussian fit to the peak) the π^0 peak in data and in the simulation. Only peripheral events are used for the energy calibration, as the high cluster

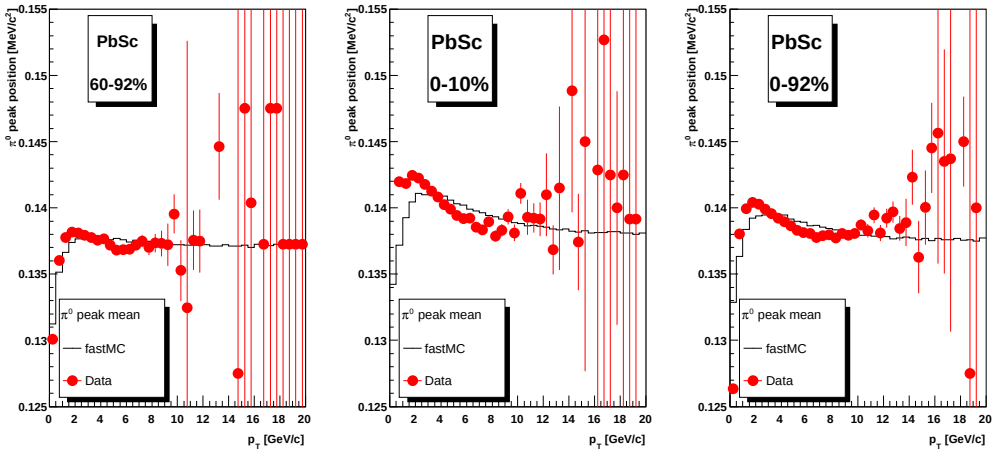

Figure 4.5: π^0 peak position in the PbSc from real data and from the fast Monte-Carlo simulation, for three different centrality selections, after the calibration.

multiplicity in central events leads to an overlap of the showers of different particles and thus to an additional smearing of the energy information and thus of the π^0 peak width. The correction factor includes both a constant term a and a nonlinear correction in the form $a_0 + a_1 \cdot e^{a_2 * E}$, it is calculated by a fit to the ratio of the peak position in the data and in the simulation.

The PbSc energy calibration, originally also obtained with electron test beams, is obtained based on the MIP peak position and the position of the π^0 peak which is compared to a GEANT simulation that incorporates an additional smearing. The correction of the energy scale of the PbSc includes both an overall constant scale and a nonlinear term. The calibration procedure is described elsewhere [Iso07].

The validity of the energy calibration can be tested by comparing the peak widths and positions of the π^0 peak in data and simulation again. The comparison of the peak width was shown before in Figures 4.2, and 4.3. The peak positions are now compared in Figures 4.4, and 4.5, for the PbGl and the PbSc, respectively. Three different centrality selections are shown. For both detectors, the calibration was obtained using peripheral events, which is the left panel of the two figures. In central and minimum bias events, the high multiplicity affects the π^0 peak position. This effect is well reproduced in the simulation for the PbGl by parameterizing effects of overlapping showers in the calorimeter. For the PbSc, the peak positions vary on the percent level in central and minimum bias events. In this detector, due to its coarser granularity, overlapping showers affect the π^0 peak more than in the PbGl. However, it is important to keep in mind that the actual mean of the Gaussian fit is influenced by the fit range in case of smeared peaks which are not

pure Gaussian anymore, therefore the deviation between simulation and data also depends on the chosen fit range. This systematic fit uncertainty has not been studied in detail as the deviations are small compared to the systematic uncertainty on the energy scale (see Section 5.3).

5. Analysis of Neutral Pions and Eta Mesons

> Behold now, Bhikkhus, I exhort you: All compounded things are subject to decay. Strive with diligence.
>
> *Gautama Buddha*

Both the π^0 and the η meson are light pseudoscalar mesons with a $\gamma\gamma$ decay channel. This decay channel gives the opportunity to measure these mesons with the Electromagnetic Calorimeter at PHENIX.

The π^0 meson has a mass of (134.9766 $\pm$ 0.0006) MeV/c^2. Its most important decay channel is the decay into two photons with a branching ratio of (98.798 $\pm$ 0.032) %. Other decay channels include decays into leptons or leptons and photons[1], the most significant of those being the decay $\pi^0 \rightarrow e^+e^-\gamma$ with a branching ratio of (1.198 $\pm$ 0.032) % [Ams08].

The η meson is about four times heavier than the π^0, having a mass of (547.853 $\pm$ 0.024) MeV/c^2. The decay into two photons is also the η meson's most important decay channel, but only with a branching ratio of (39.31 $\pm$ 0.20) %. Other significant decay channels include the decay $\eta \rightarrow 3\pi^0$ with a branching ratio of (32.56 $\pm$ 0.23) % and charged modes such as $\eta \rightarrow \pi^+\pi^-\pi^0$ or $\eta \rightarrow \pi^+\pi^-\gamma$ with branching ratios of (22.73 $\pm$ 0.28) % and (4.6 $\pm$ 0.16) % respectively [Ams08].

Both mesons can be produced in hard scattering processes when a hard scattered quark or gluon fragments into a jet of particles. They can also be produced in a thermalized medium during freeze-out via recombination of quarks.

5.1 Invariant Mass Analysis

Both π^0 and η mesons are reconstructed via the invariant mass, m_{inv}, of photon pairs that is calculated from the energies of the decay photons measured with the Electromagnetic Calorimeter and the angle between the two decay photons. This invariant mass is calculated as a function of the pair transverse momentum p_T. The invariant mass is given as

[1] So far, only decays including electrons and positrons have been measured.

the absolute value of the sum of the four-momenta of the decay photons. Therefore the square of invariant mass is

$$m_{inv}^2 = (E_1 + E_2)^2 - (\vec{p}_1 + \vec{p}_2)^2 \, . \tag{5.1}$$

Since photons are massless, the invariant mass of two photons from a π^0 or η decay can be calculated as

$$m_{inv} = \sqrt{2E_1E_2 \cdot (1 - \cos\theta)} \, . \tag{5.2}$$

However, the invariant mass is not calculated for all photon pairs, only certain sector combinations are allowed. First, the analysis is performed for the two calorimeter types – PbGl and PbSc – independently, for a better understanding of systematic uncertainties. Furthermore, the two decay photons are required to be in one arm of the calorimeter. Due to decay kinematics, no decays of π^0 or η at relevant transverse momenta above ≈ 1 GeV/c have opening angles large enough to be in the different arms. Therefore, there are in principle three allowed sector combinations: either both decay photons are detected in any of the PbGl sectors, or in any of the PbSc West, or in any of the PbSc East sectors.

5.1.1 Real Events

In a given event it is not possible to reconstruct each π^0 or η individually due to the event's multiplicity. Usually more than two particles create a signal in the EMCal and it is impossible to know which of those come from a real π^0 or η and which are combinations of one decay photon with another calorimeter hit that can be e.g. a decay photon from another original particle, a direct photon, an electron or also a hadron that passes the PID cuts. Therefore, in a first step the invariant mass of all photon candidate pairs is calculated, including all random pair combinations that do not come from one single mother particle. The result of doing so is an invariant mass distribution versus transverse momentum. The combination of all possible photon candidate pairs in a given event leads to a large background of uncorrelated pairs that needs to be subtracted. Overall, the number of possible pair combinations N_{pair} in one single event can be simply calculated from the number n of photon-like EMCal hits on the considered detector surface as $N_{\text{pair}} = \frac{n}{2} \cdot (n-1)$.

Asymmetry cut Though the PID cuts already reduce the number of photon-like clusters on the calorimeter, still a huge amount of uncorrelated pair combinations remains. Further reduction of such pairs can be achieved by applying a so-called asymmetry cut on the

cluster pairs. The asymmetry describes the difference of the energies of the two decay photon candidates, defined as

$$\alpha = \left| \frac{E_1 - E_2}{E_1 + E_2} \right| .$$

E_1 and E_2 denote the energies of the two photon candidates. The distribution of α for decay photons from one given original particle is flat. For uncorrelated photon pairs, the asymmetry distribution shows a different pattern. The single photon candidate spectrum in heavy-ion collisions follows roughly a falling exponential (at lower p_{T}) or power law (at higher p_{T}) spectrum, so each high-energy photon candidate is paired with a large number of photon candidates at low energy, leading to an increase of highly asymmetric pairs. Removing pairs above a certain pair asymmetry will eliminate such pairs from the analysis. Of course, also pairs from asymmetric particle decays will be discarded, therefore the cut will have to be a compromise between the rejection of uncorrelated pairs without losing too many correlated pairs. In other words, a value for the cut has to be found that improves the signal-to-background ratio by reducing the background without increasing the statistical error too much by reducing the signal. The experience of earlier analyses (e.g. [Awe01b, Adl03f]) has shown that an asymmetry cut of $\alpha < 0.7$ yields the optimal signal to background ratio. The loss of π^0's and η's because of the asymmetry cut is corrected during the acceptance and efficiency corrections. The correction is straightforward due to the construction of the cut.

5.1.2 Event Mixing

To estimate the combinatorial background described above, a sample of photon pairs is needed where the photons are by construction not correlated. In this work, the method used to get such a sample is the so called "event mixing". Therefore, all photons from an analyzed event are paired with all photons from one or more different events of a similar multiplicity, reaction plane and vertex position and the invariant mass of these uncorrelated photon pairs is calculated as well. This calculation also leads – as the calculation performed in single events – to an invariant mass distribution versus transverse momentum. This distribution of the mixed-event invariant mass should match the shape of the combinatorial background in the real-event invariant mass distribution, but it still has to be normalized to match this distribution. The number of pair combinations can be calculated as $\frac{n_{\gamma,i} \cdot (n_{\gamma,i}-1)}{2}$ – with $n_{\gamma,i}$ as the number of measured photon candidates in the event – for a real event i, while for mixing a real event i with another event j, one gets $n_{\gamma,i} \cdot n_{\gamma,j}$ pair combinations. As only events with a similar multiplicity are used for event mixing, $n_{\gamma,i}$ is approximately $n_{\gamma,j}$, and the normalization factor for an analysis with N events used for mixing is roughly $1/(2 \cdot N)$, not regarding the correlated photons in a real

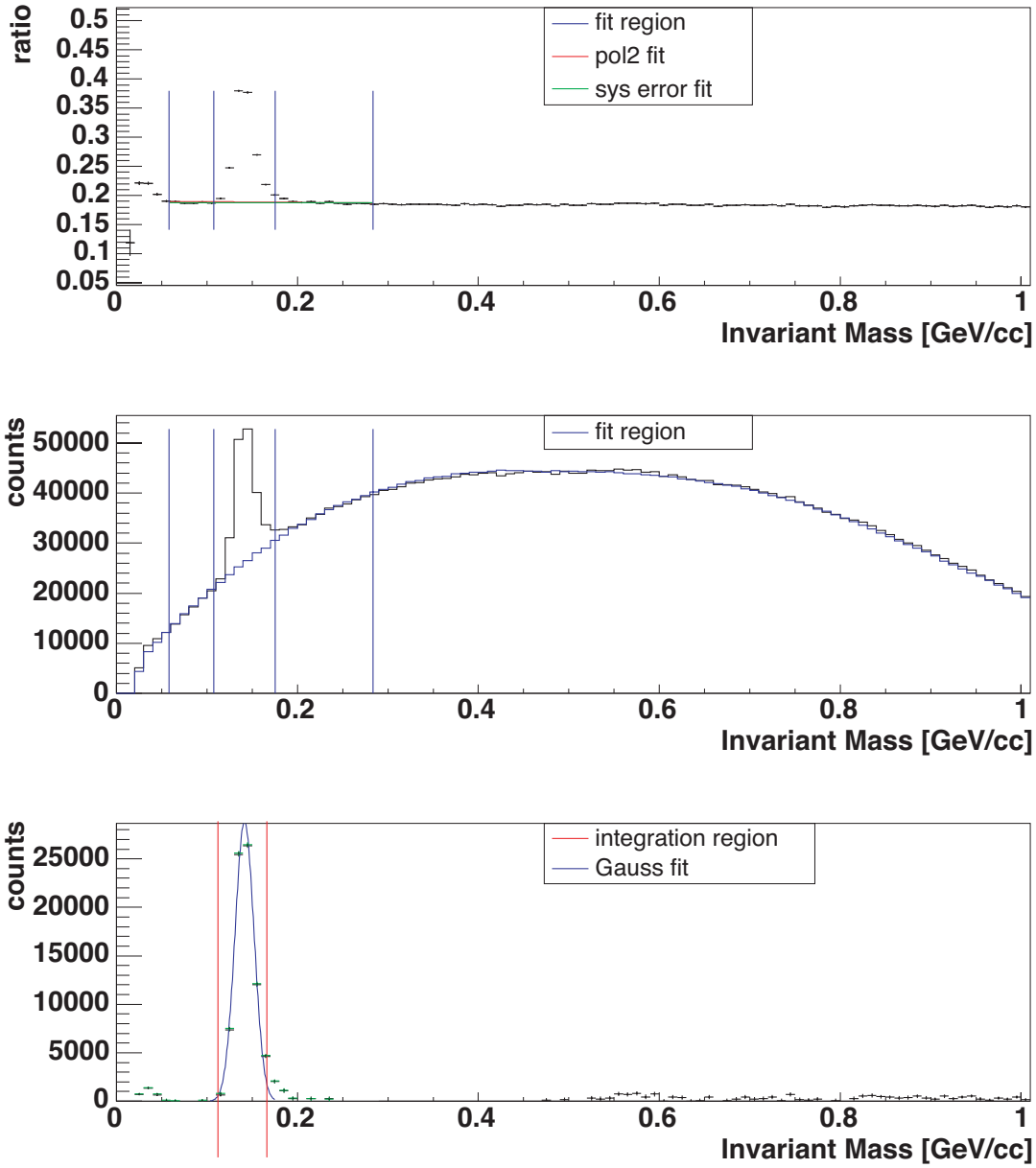

Figure 5.1: Control output of the π^0 peak extraction for 0-10% most central events in the range 3.5 GeV/c $< p_T <$ 4.0 GeV/c for PID 3 in the PbGl. Top: real/mixed-ratio and background fit, the red fit is used for the background parameterization, the green fit for estimating the systematic uncertainty; middle: real invariant mass spectrum and scaled background; bottom: real – scaled background (black entries), the green entries result from the background fit for estimating the systematic uncertainty. The remaining peak contains 76536 ± 565.5(stat.) π^0's.

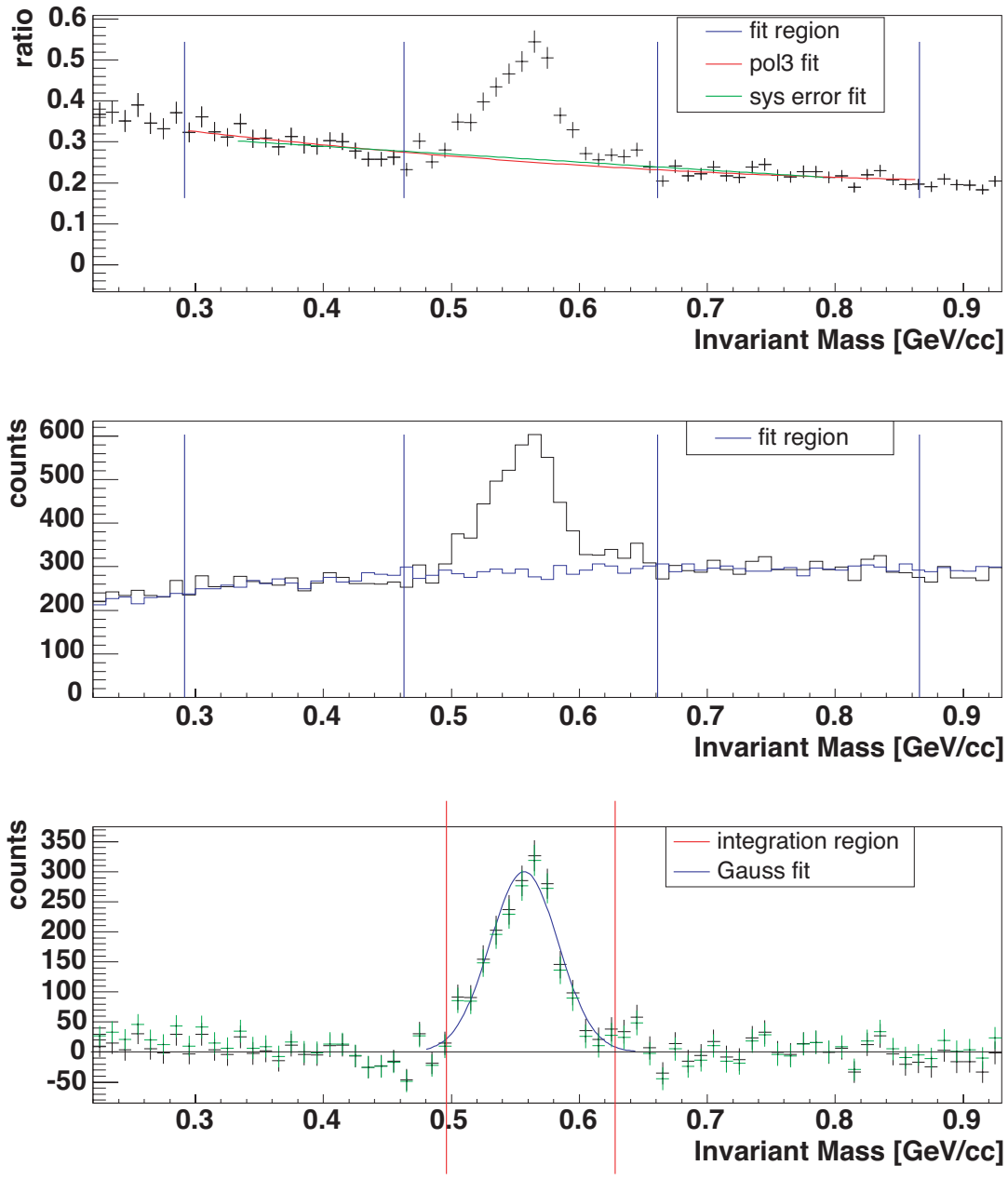

Figure 5.2: Control output of the η peak extraction for minimum bias events in the range 7 GeV/c $< p_{\mathrm{T}} <$ 8 GeV/c for PID 3 in the PbGl. Top: real/mixed-ratio and background fit, the red fit is used for the background parameterization, the green fit for estimating the systematic uncertainty; middle: real invariant mass spectrum and scaled background; bottom: real – scaled background (black entries), the green entries result from the background fit for estimating the systematic uncertainty. The remaining peak contains 2021.6 ± 106.2(stat) η's.

event.

The exact scaling of the background is obtained by calculating the ratio of the real and the mixed events distribution for each p_T bin and by fitting this ratio outside the peak region with an adequate function describing the background as well as possible. The ratio and the scaling functions – an additional fit function is used for systematic uncertainty estimation – can be seen in the upper panel of Figures 5.1, and 5.2. If the mixed-event method yielded a perfect description of the background, a constant fit would be sufficient, however, with the real PHENIX data, a residual background can remain and has to be included into the fit choice. This residual background can be explained by flow effects or jet correlations which lead to a non-uniform spatial distribution of photons within an event. The π^0 background is estimated by fitting the region outside the peak with a second order polynomial to describe the residual background. The background around the η peak was parameterized separately for the η yield extraction. Here, a third order polynomial was used.

For higher transverse momenta, the background almost vanishes and can contain several zero entries, thus the estimation of the scaling by a fit leads to large errors or even wrong values. Therefore an alternative background scaling estimation has to be used at high p_T. The fit function is replaced by the ratio of the number of photon pairs in the normalization region in the real and the mixed events distributions, leading to a constant scaling parameter. An example of the invariant mass distribution of the real events and the scaled mixed events background are shown in Figure 5.3 for the PbGl. The π^0 peak is visible for each p_T, the signal to background ratio clearly increases towards higher transverse momenta. A "zoom" into the η region is shown in Figure 5.4 for the PbSc. The same two invariant mass distributions are also shown in the middle panel of the peak extraction control output in Figures 5.1, and 5.2.

The mixed-event distribution is scaled with the parameterized fit function - or, in case of large transverse momenta, with the constant as described above - and then subtracted from the real events distribution. The π^0 or η are then finally counted within a certain integration region which is p_T dependent in the π^0 case and fixed for the η, this region is depicted in the lower panel of Figures 5.1, and 5.2. The π^0 integration region is chosen p_T dependent because the π^0 peak position is also p_T dependent and because the integration window is smaller than the η integration window due to the smaller peak width of the π^0. As an example, the extracted raw yields for both particles are shown in Figure 5.5 for the π^0 in the PbGl, and in Figure 5.6 for the η in the PbSc. The spectra are cut off at high transverse momenta in case the peak is not significantly above background fluctuations. The highest p_T reach for the π^0 is achieved in the overall minimum bias sample with

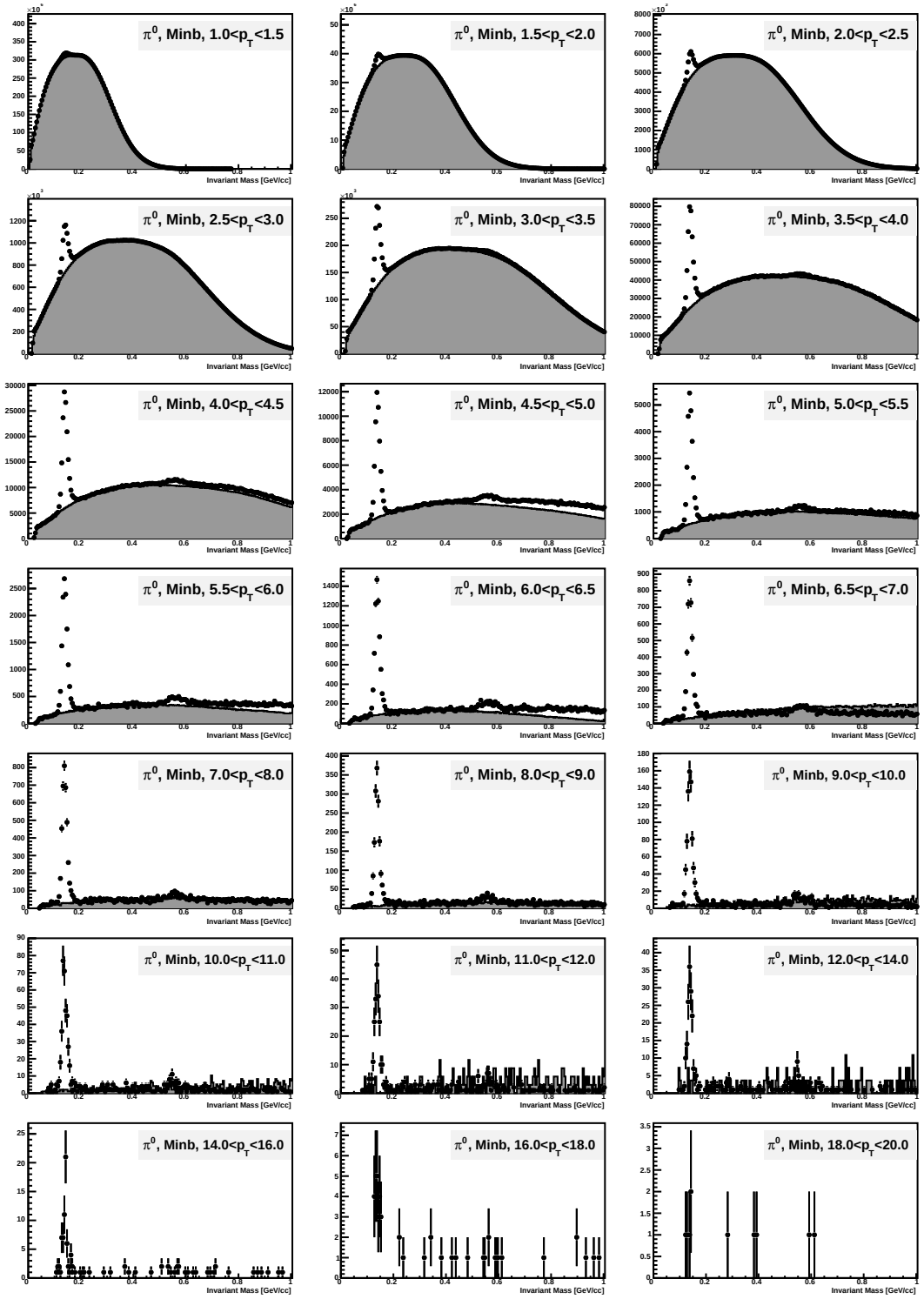

Figure 5.3: π^0 invariant mass distribution for different p_T for minimum bias events in the PbGl. The scaled mixed event background is depicted as the gray area.

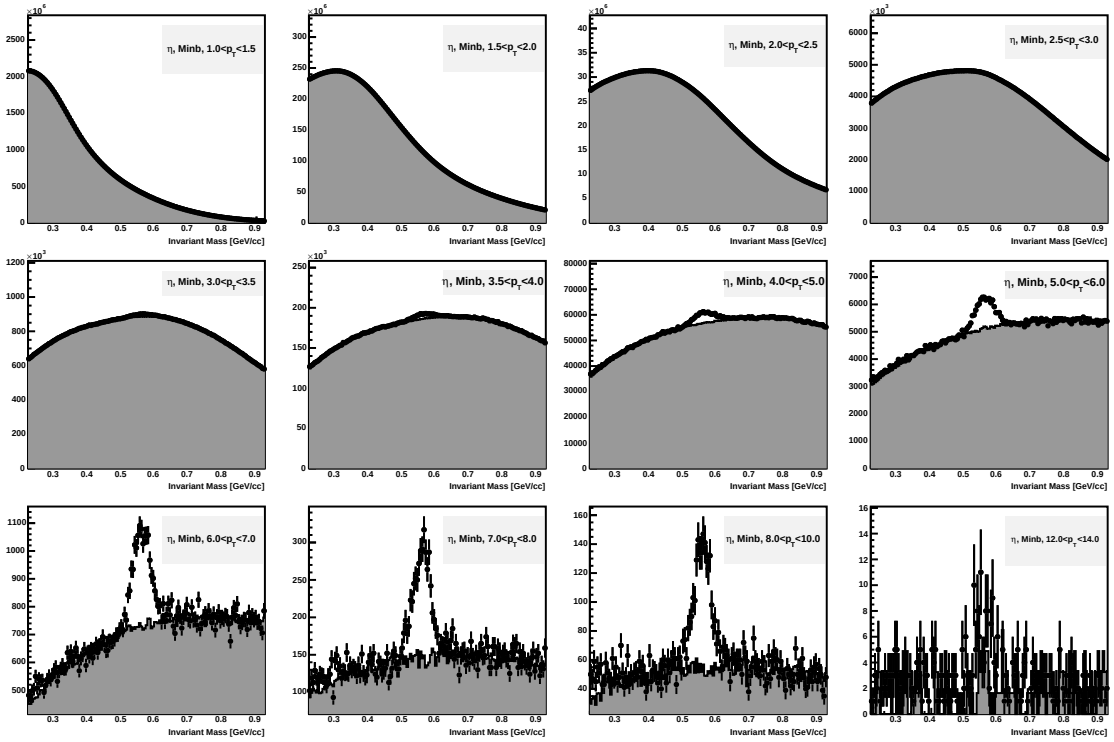

Figure 5.4: η invariant mass distribution for different p_{T} for minimum bias events in the PbGl. The scaled mixed event background is depicted as the gray area.

$p_{\mathrm{T}} = 20$ GeV/c. This value is reached in no single centrality selection where the peak is insignificant compared to background fluctuations.

5.1.3 Statistical Error

The determination of the statistical error follow the procedure outlined in [Awe01a]. They are based on the following argument:
The measured number of π^0- or η-meson candidates per p_{T}-interval in the real event distribution (N) is considered to be the sum of the number of correlated (S) and uncorrelated (B) pairs:

$$N = S + B \; . \tag{5.3}$$

The background B itself is unknown, but can be estimated from the mixed-events distribution M with

$$B' = kM \; , \tag{5.4}$$

where k is the background scale parameterization. The expected value $\langle B' \rangle$ is the same as the expectation value of the true background $\langle B \rangle$. Now – with Equation 5.4 – the number

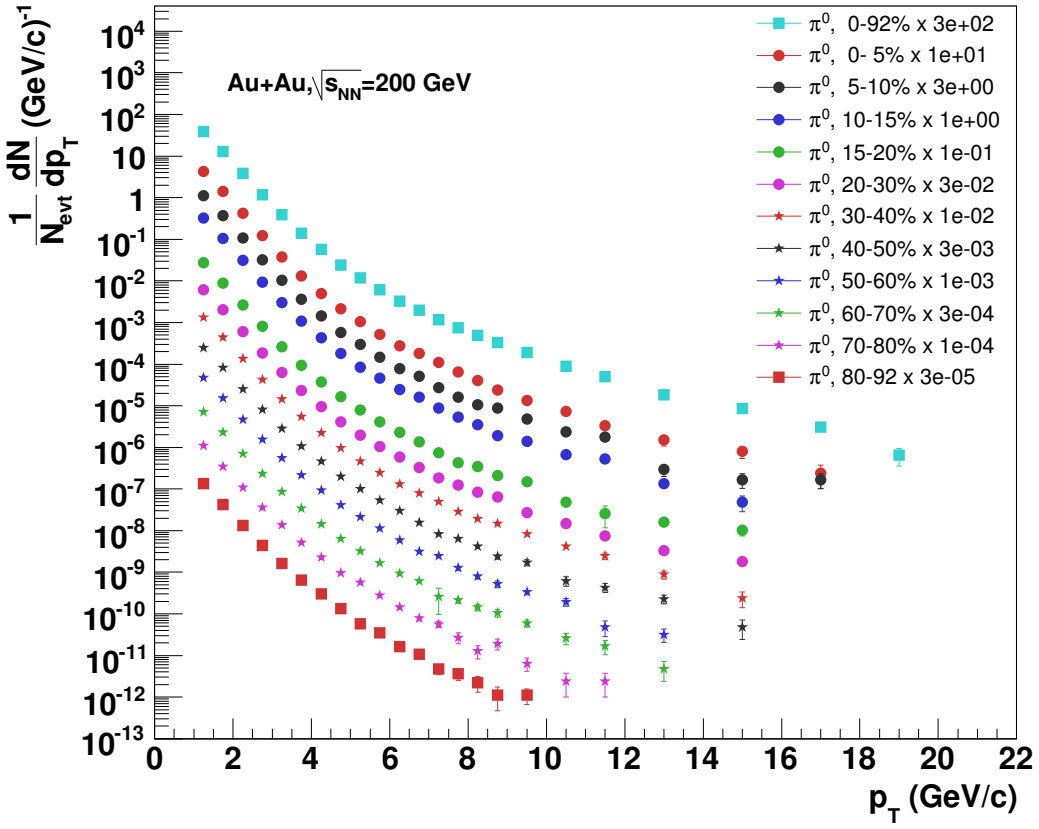

Figure 5.5: Uncorrected (raw) π^0 yield in the PbGl in Au+Au collisions at $\sqrt{s_{\mathrm{NN}}}$= 200 GeV/c.

of the measured π^0- or η- mesons and respectively the number of correlated pairs S can be estimated as

$$S' = N - B' = N - kM \; . \tag{5.5}$$

Again, the condition $\langle S' \rangle = \langle S \rangle$ is assumed to hold. These assumptions allow to calculate the statistical error of the number of correlated pairs, i.e. the number of measured π^0 or η mesons:

$$\begin{aligned} \varepsilon^2(S') &= \varepsilon^2(N) + \varepsilon^2(k)M^2 + k^2\varepsilon^2(M) && (5.6)\\ &= N + \varepsilon^2(k)M^2 + k^2 M && (5.7)\\ &= S' + B' + \varepsilon^2(k)M^2 + k^2 M \; . && (5.8) \end{aligned}$$

5.2 Corrections to the Raw Yield

The result of the event-mixing method and the integration of the π^0 or η peak is a spectrum containing the number of particles for each step – called bin – in transverse momentum,

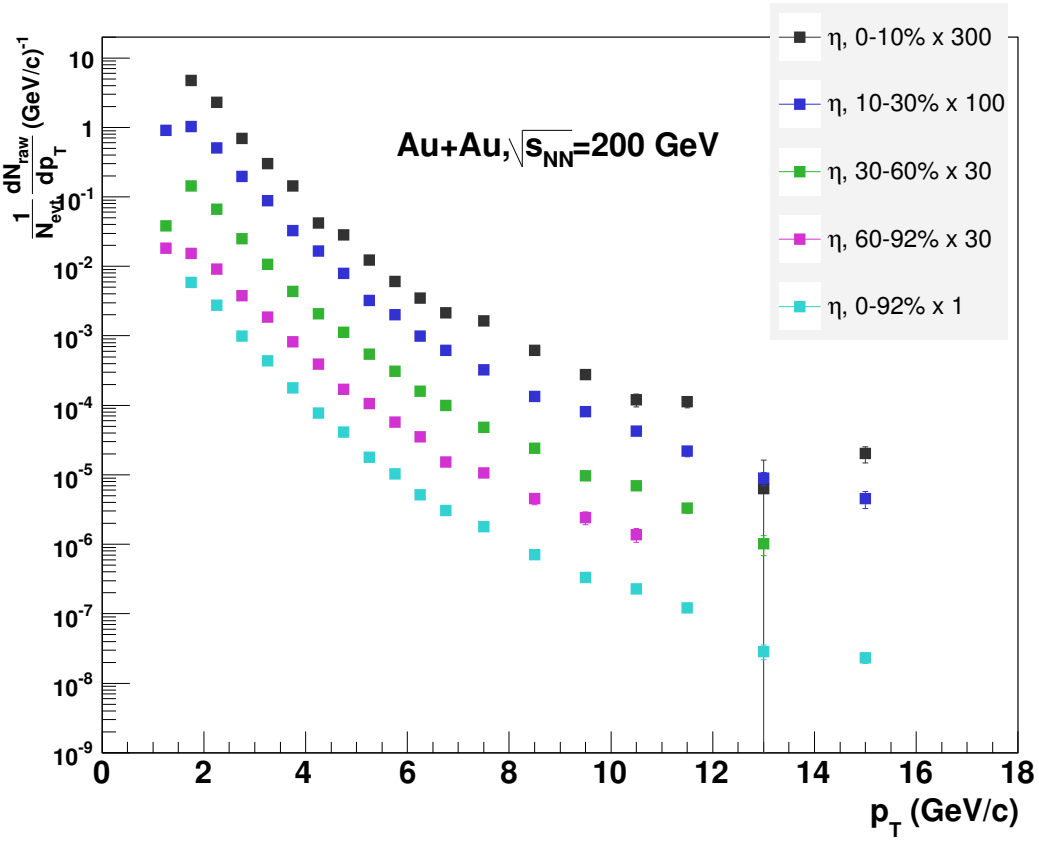

Figure 5.6: Uncorrected (raw) η yield in the PbSc in Au+Au collisions at $\sqrt{s_{\mathrm{NN}}}$= 200 GeV/c.

for different centrality selections, and different PID cuts. This so-called "raw yield" has to be corrected for the response of the calorimeter and for other effects to obtain a result such as the Lorentz invariant particle yield that represents the particle production in the collision itself. As this quantity is defined for a certain range in rapidity and the full azimuthal coverage within this rapidity range, the raw yield has to be corrected for the detector acceptance. In a next step, detector effects have to be considered that influence the response of the detector to the particles that hit its active surface. These effects can be subsumed together with effects of the PID cuts to the detector efficiency. Furthermore, the steeply falling spectra of the particles have to be taken into account as the average value within on p_{T} bin does not represent the actual value in the center of the bin. Other corrections account for the loss of decay photons due to conversion into electron-positron pairs, for the two-photon branching ratio of the π^0 and the η, and for the possible merging of the π^0 decay photons at high π^0 p_{T}.

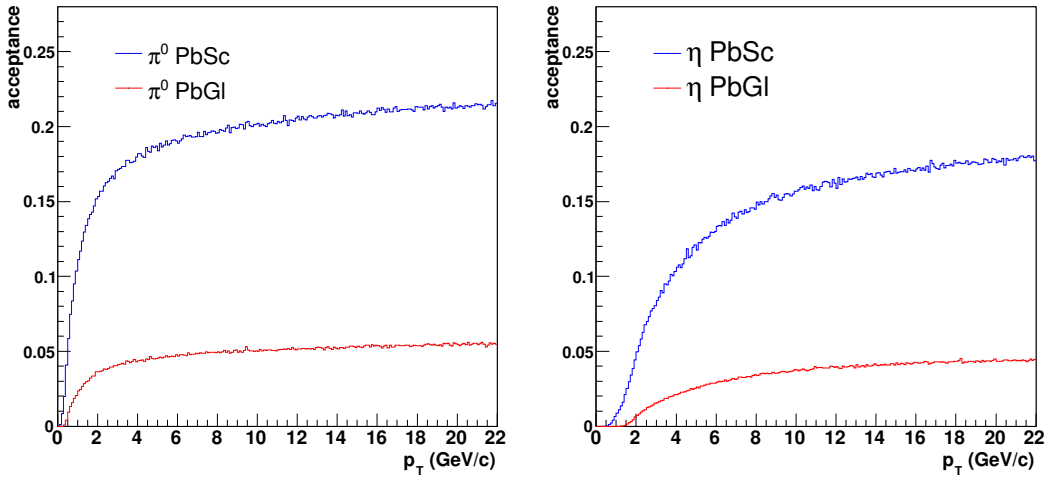

Figure 5.7: Acceptance for π^0 (left) and η (right) in the PbSc (blue) and the PbGl (red).

5.2.1 Acceptance Correction

The acceptance correction accounts for the limited geometrical coverage of the used detector. It therefore takes into account both the nominal detector surface in azimuth and z, and the active detector surface for the specific analysis task. For example, clusters on towers on the edges of the sectors are not used in this analysis, because in such a case, a part of the energy is likely to leak outside the detector. Bad towers – i.e. towers with a wrong or suspicious energy information – are also excluded in the analysis together with their neighbors, this also has to be corrected for in the acceptance correction.

The acceptance correction is calculated with a fast Monte-Carlo simulation program. In this program, π^0's or η's are simulated and decayed with the Jetset library [Sjo94]. The PHENIX experiment is simplified in the program, only the geometry of the EMCal is modeled there on the base of the single modules or towers, respectively. The original particles are simulated in a certain p_T and rapidity range, the p_T distribution is simulated flat from 0 to 32 GeV/c while the rapidity is between -0.45 and +0.45. The particle vertex is distributed in a gaussian shape with $\sigma = 30$ cm in the same vertex region allowed by the vertex cut in the analysis, $|z| < 30$ cm. Only the decay into two photons is allowed in the simulation program. The program allows the calculation of different detector acceptances, i.e. considering different possible definitions of the acceptance. The first one is the nominal geometric coverage of the detector, therefore also including such parts of the detector that are taken out in the analysis – this acceptance definition could be used only if the other correction accounts for these towers. The acceptance correction used in this thesis however is based on looking at the active detector surface only. The active detector surface consists of all towers that are used during data taking, that are included during re-

construction and that are not excluded while calculating the invariant mass. Therefore, the simulation program allows the exclusion of modules from the analysis of the decay photons. The acceptance is then defined as the ratio of the the output spectrum and the original input spectrum, the first is filled every time both decay photons lay on the active detector surface. To account for the true physical spectrum, the flat p_T distribution is weighted with the true spectrum[2] derived from the analysis, therefore an iterative procedure is used. As the acceptance correction basically only accounts for the decay kinematics of the original particles, it is in principle the same for each centrality. However, especially at low p_T, in the turn-on region of the acceptance, the finite bin size in the simulation requires a realistic input spectrum as the calculated acceptance can be dominated by only a part of the bin. The different acceptance corrections for the two mesons in the two different calorimeters are shown in Figure 5.7 for minimum bias collisions. The PbSc acceptance is larger than the PbGl acceptance by more than the factor of 3 expected from the number of sectors. This is caused by the larger number of bad modules in the PbGl. The larger mass of the η meson leads to larger opening angles of the decay photons and thus to a smaller acceptance, especially at low p_T.

Parameterization of the Meson Spectra

For the different corrections such as the acceptance, the reconstruction efficiency or the bin-shift of the spectrum, a good knowledge of the spectrum of the analyzed particle is necessary. Therefore, a parameterization has to be found that describes the physical spectrum well over the whole p_T range and that does not depend on too many free parameters. For high p_T, it is known from pQCD that particles are produced with a power law distribution, however, such a parameterization does not work for low transverse momenta where soft physics comes into play and the particle production is not dominated by processes that are described by pQCD anymore. Instead of the power law, at low p_T, the spectrum shows an exponential behavior.

Two possibilities to describe the whole p_T spectrum with a function remain: either an exponential or a Hagedorn type function [Hag84] – which is a modified power law – at low p_T and a power law at high p_T are connected in the intermediate p_T region, using a Woods-Saxon type function [Woo54] to connect them smoothly, or a function is used, that behaves exponentially for low p_T and as a power law at high p_T . Such a function was proposed within the PHENIX collaboration [Zaj04], it is found to give a good representation of the data for all different centrality classes.

[2] the fully corrected, non-invariant yield

The compositefunction is in general a good choice as it parameterizes the spectrum with functions that are known to give a good description of the true physical spectrum in a certain p_{T} range. However, it has a disadvantage in the connection region of the two fits where its curvature changes significantly within a small p_{T} range. This discontinuity can have an effect on the simulations of the efficiency or – even more – on the simulations of the decay photons in a direct-photon analysis. The two functions that are connected are the following:

$$f(p_T)_{low} = a_0 \cdot (\frac{a_0}{p_0 + p_T})^{n_0} \, , \tag{5.9}$$

and

$$f(p_T)_{high} = \frac{a_1}{p_T^{n_1}} \, . \tag{5.10}$$

For connecting the two functions, another – Woods-Saxon type – function is used:

$$f(p_T)_{ws} = \frac{1}{1 + e^{\frac{p_T - p_2}{a_2}}} \, . \tag{5.11}$$

The three functions from Equations 5.9, 5.10, and 5.11 are then used together as

$$f(p_T)_{comb} = f(p_T)_{ws} \cdot f(p_T)_{low} + (1 - f(p_T)_{ws}) \cdot f(p_T)_{high} \, . \tag{5.12}$$

Even if the parameters for the Woods-Saxon function are fixed, the resulting composed function has five free parameters which is still acceptable for the spectra in this analysis but might become a problem in other analyses which cover a smaller p_{T} region, for the number of degrees of freedom should be significantly smaller than the number of data points in a data sample that the function is describing.

The other function proposed within the PHENIX collaboration only uses three free parameters. It is constructed in a way that it becomes similar to an exponential at low p_{T} and to a power law at high p_{T}. The function is written as

$$f(p_T) = b \cdot e^{-\frac{2\Lambda}{a}\sqrt{\log[1+\left(\frac{p_T}{\Lambda}\right)^2]}} \, , \tag{5.13}$$

at low p_{T} its limit approaches

$$f(p_T \to small) \approx b \cdot e^{-\frac{2p_T}{a}} \, . \tag{5.14}$$

In this exponential case, the parameter a can be interpreted as the mean p_{T}, $\langle p_{\mathrm{T}} \rangle \approx a$. The advantage of this function is that it relies on only three free parameters and it does not

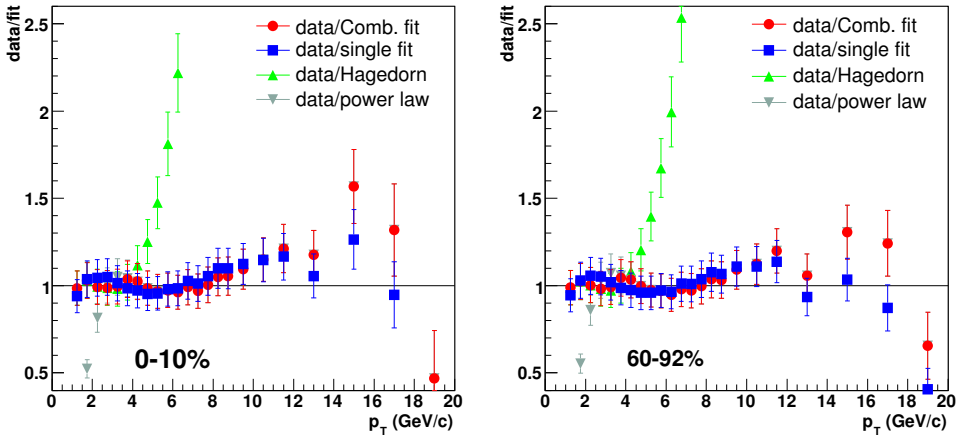

Figure 5.8: π^0 data points divided by different fit functions for central (left) and peripheral (right) events. The red circles are for the combined function (Eq. 5.12), the blue squares for the function in Eq. 5.13. The dark green triangles for the power law (Eq. 5.10) and the light green triangles for the Hagedorn type function (Eq. 5.9) show that none of those functions alone can describe the entire spectrum.

have a sudden change of its curvature.

Figure 5.8 shows the ratio of the data to the different fits. Both fit functions (Eqs. 5.12, and 5.13) lead to a good agreement between the data and the fit. The composite function is a little better, however, the differences between the two are not significant and thus the function with fewer parameters is the better choice. The large deviations of the pure Hagedorn fit (Eq. 5.9) and the power law function (Eq. 5.10) are clearly seen in Figure 5.8 at high and low p_T, respectively.

5.2.2 Efficiency Correction

The efficiency correction describes the response of the detector to decay particles that hit its surface. Therefore it has to take into account different effects in the detector as well as in the analysis. Due to analysis cuts such as the PID cuts, some decay photons are rejected even though they hit the detector. Furthermore, the detector does not have perfect energy and position resolution but "smears" the particle's energy and its actual impact position. In the extreme case of a flat p_T distribution of particles, a Gaussian "smearing" to neighboring bins would be compensated by the smearing from the same neighboring bins, therefore the efficiency would be one. However, due to the steeply falling particle spectra in heavy-ion collisions, this energy smearing has an impact on the measured particle yield as more particles are "smeared" towards higher energies than towards lower ones and since the smearing itself is note purely Gaussian due to multiplicity effects. Thus the shapes of the spectra have to be accounted for when calculating the efficiency correction.

The position resolution has an effect on the reconstruction of the transverse momenta of the particles. In more central Au+Au collisions – the 60 % most central events –, the efficiency is also influenced by the high multiplicity, as calorimeter showers from different particles become more likely to overlap and form one common cluster. The efficiency correction can thus be generally defined as

$$\varepsilon(p_T) = \frac{dN/dp_{\mathrm{T}}|_{\mathrm{output}}}{dN/dp_{\mathrm{T}}|_{\mathrm{input}}} , \tag{5.15}$$

with $dN/dp_{\mathrm{T}}|_{\mathrm{output}}$ denoting the measured spectrum and $dN/dp_{\mathrm{T}}|_{\mathrm{input}}$ denoting the true input spectrum of particles within the calorimeter's acceptance.

For proton-proton collisions at PHENIX, the efficiency correction is calculated with the aforementioned Monte-Carlo simulation program that is also employed for determining the acceptance correction. In the program, the detector effects and the effects of analysis cuts are parameterized to represent the behavior of the real detector. The same program can also be applied to understand these effects in Au+Au collisions. However, since only single particles on the detector are simulated, the program cannot directly be used to calculate the effects of the high-multiplicity regime in more central collisions of heavy ions, such effects have to be parameterized. In central collisions, the electromagnetic showers from different particles are likely to overlap and form one single cluster with an energy not connected to one single incident particle. This so-called shower overlap leads to an additional smearing of the energy measured with the calorimeter that has to be accounted for. As the simulation of a sufficient number of full events would need too much CPU time, the shower overlap is modeled by embedding simulated particles into real events. The embedding also gives a more realistic description of the detector occupancy in the events as a real occupancy is used.

Embedding

Studying the behavior of simulated particles that are embedded into real events allows the evaluation of the influences of a real-event environment on the measured particle spectrum which is not possible with the usual fast Monte-Carlo simulation. For analyzing the embedded particles, the same framework as for the analysis of the real data is used. The embedding method consists of the following steps: First, single particles such as π^0's are simulated within the PHENIX environment, these particles are then embedded into real PHENIX events, and finally the output of the embedding is evaluated with the π^0 analysis software.

Single Particle Simulation At PHENIX, single particles are simulated within the PISA[3] framework. In PISA, particles are simulated using the EXODUS [Ave03] event generator within the complete PHENIX setup, modeled with the GEANT3 [Bru93] package. The PISA output is then used to generate DSTs that contain the same data nodes as the real-event DSTs, such as the EMCal cluster information or the vertex position, but in addition also contain nodes with information on the original simulated particles, e.g. their momentum, and with further information on the particles that hit the detector, e.g. their particle ID or their ancestry.

Embedding into Real Events For the embedding, a module of the PHENIX Fun4all framework is used. During the process, three different input files are read, one contains the EMCal tower information from the real event, a second one contains the information necessary to synchronize the three inputs as well as the general event information, e.g. the vertex position or the centrality, and the third file is the simulated DST. Before the embedding takes place, it is checked that the simulated and the real event's vertices match within 5 cm, furthermore, the real event has to satisfy the minimum bias trigger condition. It is possible to reuse real events in the embedding process.

Now, for each event, the EMCal tower information is extracted for both the real event and the simulated particle DST. These tower informations are subsequently merged by adding the energy values for each single tower. This new tower energy information is used to find clusters in the detector with the clustering algorithm. Due to the added energy from the simulated particle, the merged clusters differ from the original clusters in the real event. To save disk space, only such clusters are stored which contain a contribution from the simulation. The other clusters are only those that were not changed at all during the embedding process.

Since the PISA simulation is based on the original energy smearing parameterization of the two calorimeters, it does not match the actual energy resolution of the real calorimeters in the 2004 run due to aging of the detectors and due to gain imbalances during data taking. Therefore, an additional smearing, degrading the energy resolution, is included in the embedding process. It is applied to the simulated contribution, a certain value is chosen and applied within a random Gaussian distribution. For the PbSc, this additional smearing is 0.02 [Iso07], or 2%, and for the PbGl it is 0.05, or 5%. It is chosen based on comparisons of the π^0 peak in real data and in the embedding output such that the positions and widths of both peaks match.

[3]PHENIX Integrated Simulation Application

Analysis of the Embedding Output In general, there are different possibilities to analyze the output of the embedding. However, all of them are based on the usage of the same analysis program as used for the analysis of the real data, using the same PID and analysis cuts, centrality selection, or maps of excluded towers. Since the PISA simulation uses a flat particle input distribution, during the analysis the output is weighted with a parameterization of the true π^0 spectrum, using the p_T of the original simulated particle as parameter. Otherwise, effects of energy smearing would not be reproduced by the embedding.

The most straightforward method would be to analyze the embedded output as is and divide it by the known simulated input spectrum. Doing this would in principle lead to an overall correction factor. However, since the original particles were not simulated in the aimed η range, one could not take advantage of the existing simulation files.

For the embedding method is mainly used to account for effects of the high cluster multiplicity in more central collisions, another method is suitable. Besides the normal embedding, the corresponding framework is also used to add only the additional smearing parameter to the simulated particles without embedding them into real events, the output then corresponds to particles on an empty detector. Now for both the embedded data and the data on the empty detector, π^0's are reconstructed with the analysis framework. The ratio of the π^0 reconstructed after embedding and without embedding then represents the contribution of overlapping showers to the efficiency, it could be called "overlap efficiency".

Embedding is also used to estimate the effects of the PID cuts by simply comparing the reconstructed π^0's after the application of the different cuts with the output obtained without cuts. As expected, the shower shape cut takes out a larger fraction of clusters with a simulated contribution in central than in peripheral events as the overlap of showers from different particles often leads to a broader common shower of both particles.

Fast Monte-Carlo Efficiency Calculation

The fast Monte-Carlo simulation program uses a parameterization of the different detector effects such as energy smearing or smearing of the impact position information. The effects of the PID and analysis cuts are also simulated, either by using the same cuts in the simulation, or by a parameterization of the probability that a photon passes the cut. The first method is used for the energy cut and for the asymmetry cut while the second one is applied for the shower shape cut where the real cut

Detector (sector)	energy dependent term (A)	constant term (B)
E0	0.080	0.065
E1	0.080	0.065
E2	0.080	0.050
E3	0.080	0.050
W0	0.080	0.050
W1	0.080	0.050
W2	0.080	0.050
W3	0.080	0.050

Table 5.1: Parameters for energy smearing following Eq. 5.16 as used in the fastMC for the different EMCal sectors.

cannot be applied within the simulation as the showers themselves are not simulated at all.

For each particle where both decay photons are accepted (see Section 5.2.1), the energy and position information of the corresponding photons is smeared according to the corresponding parameters, and it is checked whether both photons survive the PID cuts and whether their asymmetry is within the allowed range. The energy smearing parameters are chosen based on the data such that the width of the π^0 peak as seen in the data is reproduced by the simulation. As in more central events the peak width is also influenced by the high multiplicity environment, the simulation is tuned to match the data in peripheral events, using the centrality 60-92%. Energy smearing is parameterized using an energy dependent and a constant term using the functional form

$$\sigma_E/E = \frac{A}{\sqrt{E/GeV}} \oplus B \,. \tag{5.16}$$

The parameters are chosen for each sector independently, based on the calibration scan of the data (see Section 4.5). The parameters for Equation 5.16 are given in Table 5.1 for the different sectors of the EMCal.

As mentioned in Section 3.4, the calorimeter has a finite position resolution. This resolution has to be modeled in the fast Monte-Carlo program since it influences the reconstruction efficiency, for a shift in the hit position affects the calculation of p_{T} as well as the π^0 peak width at high p_{T}. The parameterization of the position smearing at zero incident angle ($\sigma_{xy}^{\theta=0^\circ}$) uses a constant and an energy dependent term; furthermore, a term

Detector	c_0[mm]	c_1[mm]	c_2[mm]
PbGl	28.0	6.73	1.61
PbSc	20.0	8.35	0.15

Table 5.2: Parameters for position smearing as used in the fastMC for the different EMCal sectors.

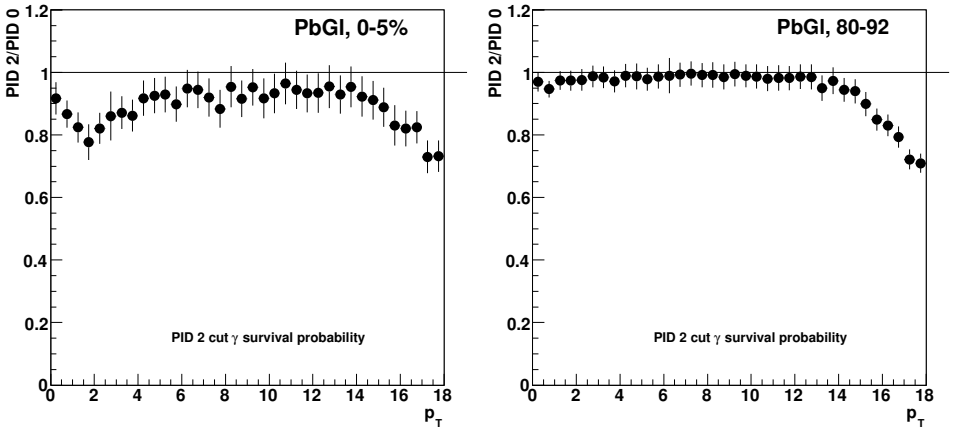

Figure 5.9: Dispersion cut survival probability in the PbGl for 0-5% central (left) and for 80-92% peripheral events.

describing the angular dependence (σ_{xy}^{θ}) has to be included. The two individual terms are given as

$$\sigma_{xy}^{\theta=0^\circ} = \frac{c_1}{\sqrt{E/\mathrm{GeV}} \oplus c_2} \,, \qquad \sigma_{xy}^{\theta} = c_0 \cdot \sin(\theta) \,. \tag{5.17}$$

For the overall smearing at a nonzero angle, the two terms have to be added in quadrature:

$$\sigma_{xy}(\theta) = \sigma_{xy}^{\theta=0^\circ} \oplus \sigma_{xy}^{\theta} \,. \tag{5.18}$$

The parameters are different for the PbGl and the PbSc, c_1 and c_2 are taken from [Aph03] for the PbGl and scaled by the ratio of the different tower dimensions in PbGl and PbSc to account for the different granularities of the two subsystems. The parameter c_0 used in the angular dependent term corresponds to the radiation length. All the parameters are listed in Table 5.2.

As mentioned above, the PID cuts on the shower shape, i.e. the dispersion cut for the PbGl and the χ^2 cut for the PbSc, cannot be directly applied in the fast Monte-Carlo simulation, for it does not include a simulation of the cluster. Therefore, it is modeled by a probability for a photon to pass the cut. This probability $p_{survival}^{\gamma}$ used to be estimated

by comparing the raw π^0 yields with and without the cut applied, extracted with a sharp asymmetry cut and p_T replaced by the average of the two decay photon energies. The probability is then given as $p^{\gamma}_{survival} = \sqrt{p^{\pi^0}_{survival}}$ [Awe01a]. However, since in the PISA simulation the full cluster information is available, the effect of the shower shape cut is applied with the help of the embedding output in this analysis, comparing the decay photon spectra with and without the corresponding cut applied. Actually, the survival probability is not independent on centrality, and it is found to be p_T dependent especially for central events. This effect is likely to be attributed to the overlap of different showers in such events. The probability for the PbSc is parameterized with a third degree polynomial for photon energies below 6 GeV and with a constant above 6 GeV. The parameters are chosen based on embedding data such that the two functions are the same or very similar in the transition region. For the lead glass, the effect of the dispersion cut was parameterized with two constants, one below a photon energy of 4 GeV, one above a photon energy of 8 GeV, conencted with a linear function between these energies, such that the result from embedding is well matched for π^0's. The survival probability for π^0 decay photons passing the shower shape cut is shown in Figure 5.9 for the PbGl. A clear difference between central (left) and peripheral (right) events is visible. The drop at high p_T is due to merging of decay photons as merged photons are effectively removed by the shower shape cut.

The shower overlap is also parameterized in the fast Monte-Carlo simulation. It is more feasible to use this simulation for the calculation of the overall efficiency correction, since much more particles can be simulated in a reasonable amount of time and statistical fluctuations are reduced. There are two ways of applying the effects of shower overlap in the simulation, either an additional energy smearing can be used, or a certain energy is added to the energy of the simulated particle in the detector. In this work, the second method was chosen as it is closer to the real effects in the detector. The added energy represents another particle hitting the calorimeter, therefore the hit energy distribution for each sector is used in the simulation, and an energy added based on a random pick from this distribution. Of course, this method also does not completely reproduce the shower overlap on the real detector. Often only part of the whole cluster is overlapping with another cluster and merged into one reconstructed cluster while the remaining energy is still within its own reconstructed cluster. Therefore, the shower overlap probabilities used in the fast MC do not represent the same probability for real towers, but the probabilities used in the simulation are tuned such that the change in efficiency due to overlapping showers as observed in the embedding simulation is reproduced in the fast Monte Carlo. The efficiency derived from the embedding and the used fast Monte-Carlo efficiency are shown in Figure 5.10 for the PbGl case. They show a good agreement.

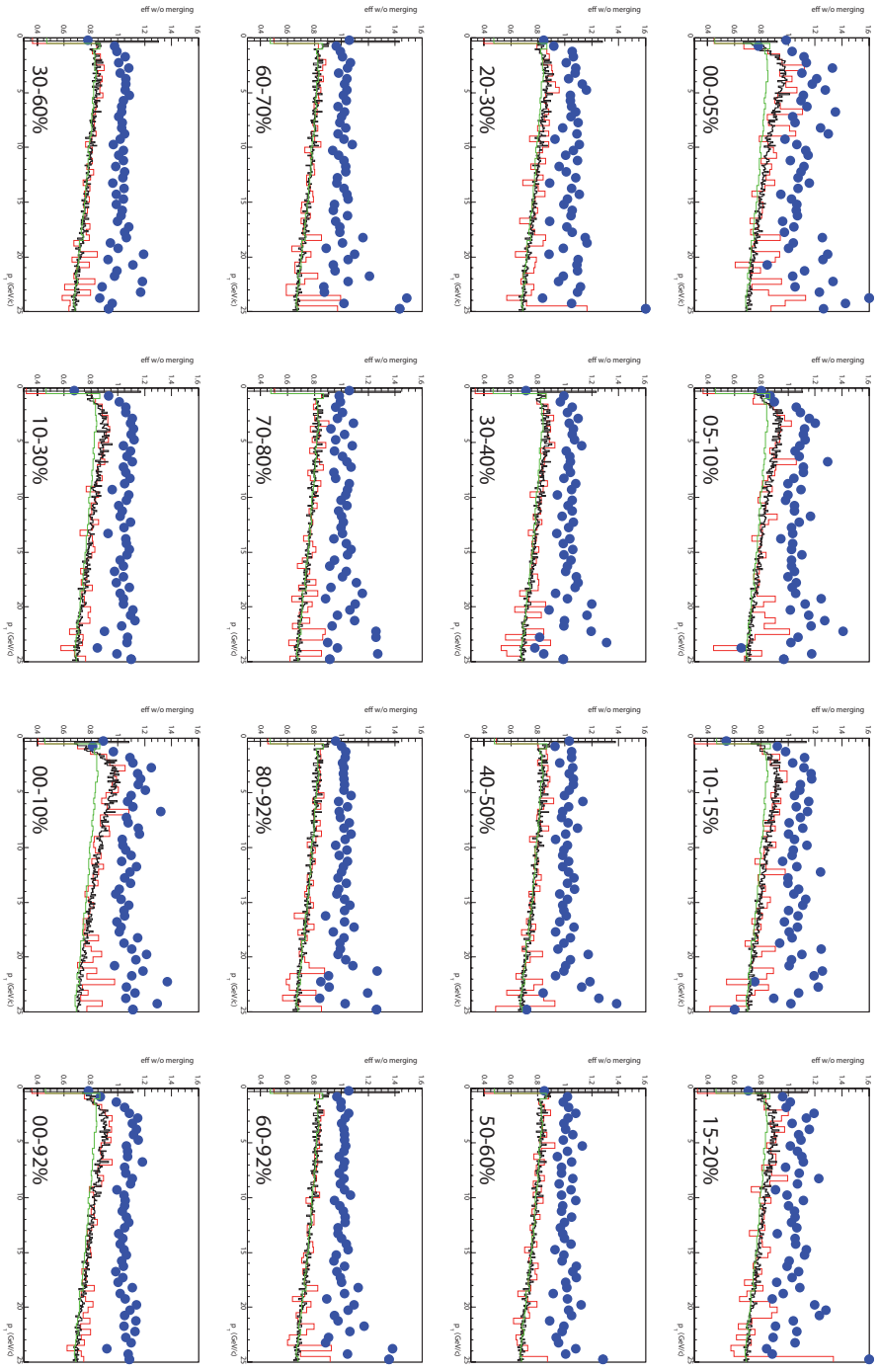

Figure 5.10: Tuning of the fast Monte Carlo to the embedding results for the PbGl. The green curve shows a detector efficiency for the hypothetical absence of shower overlap. The blue points result from embedding and show the efficiency only due to shower overlap. Combining these two leads to the efficiency, which is shown in red. The tuned fast Monte Carlo efficiency is shown in black. The two efficiencies agree well for all centralities.

Centrality	Shower overlap probability in simulation	
	PbGl	PbSc
0-5%	0.258	0.280
5-10%	0.140	0.165
10-15%	0.120	0.130
15-20%	0.086	0.100
20-30%	0.060	0.080
30-40%	0.058	0.050
40-50%	0.020	0.030
50-60%	0.010	0.010
60-70%	0.000	0.000
70-80%	0.000	0.000
80-92%	0.000	0.000
0-10%	0.160	0.175
10-30%	0.110	0.120
30-60%	0.040	0.040
60-92%	0.000	0.000
0 -92%	0.130	0.110

Table 5.3: Probability for shower overlap as used in the fast Monte Carlo simulation. These parameters are tuned using an embedding simulation and do not represent a shower overlap probability in the real detector.

The parameters for PbGl and PbSc are different. This is the result of the different tower size in the two detectors, they are given in Table 5.3. In general, the probability is larger for the PbSc.

After the decay photons are processed in the simulation with the simulated detector response parameterization, their invariant mass is calculated and it is checked whether it lies within an allowed range which is the same as in the peak extraction program used for the analysis of the real data. The reconstruction efficiency for the π^0 is shown again in Figure 5.11 for four different centrality selections for PID0 and PID3.

The reconstruction efficiency for the η meson is calculated with the same simulation program, using the same detector and overlap parameterizations. The only difference between the π^0 and the η simulation are the different masses of the particles, the different invariant mass windows in which the particles are counted, and the use of different input spectra parameterizations. The η reconstruction efficiency is depicted for four different centrality selections in Figure 5.12 for PID0 and PID3. Again, a centrality dependence is

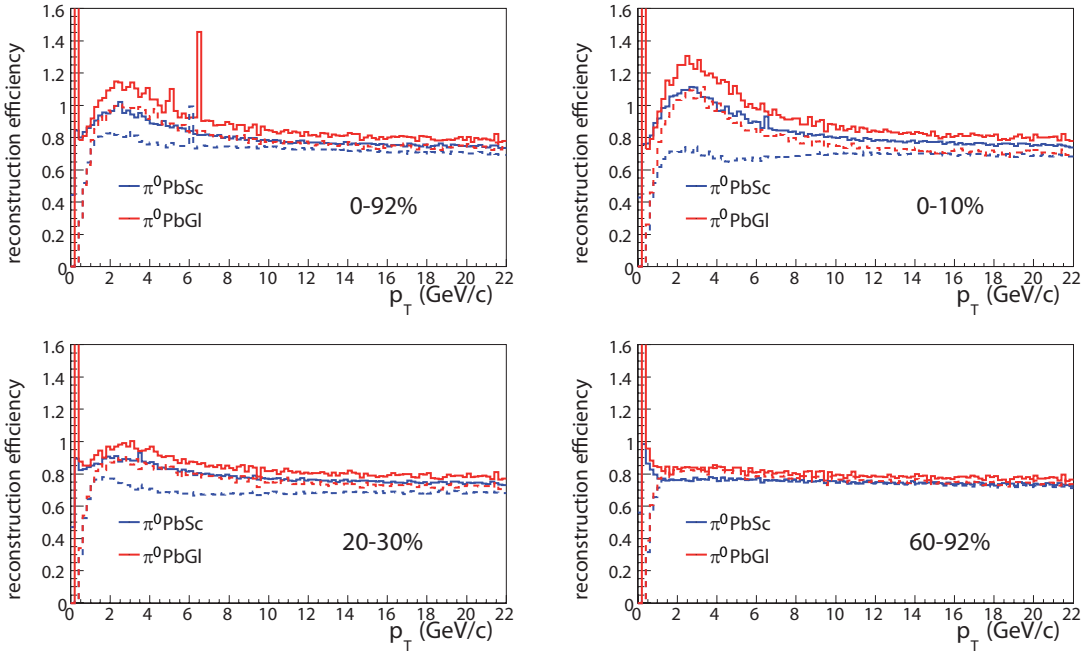

Figure 5.11: π^0 reconstruction efficiency in the PbSc (blue) and the PbGl (red), for four different centrality selections for PID0 (continuous) and PID3 (dashed). The effect of overlapping showers in more central events is seen as an increase of the efficiency for $p_T \leq \approx 6\text{GeV}/c$, it is larger in the PbSc.

clearly visible, the shower overlap leads to an increase of the efficiency in more central events compared to peripheral events. The large fluctuations at low p_T are attributed to the almost zero acceptance of the η at low p_T, therefore only very few simulated particles contribute to the efficiency calculation.

5.2.3 Bin-Shift Correction

The yields of produced particles in heavy-ion collisions such as photons, π^0, or η are following roughly a falling exponential (at lower p_T) or power law (at higher p_T) distribution and are thus steeply falling towards high transverse momenta. Therefore, the value of the particle yield or cross section in the center of each finite-sized p_T bin does not represent the true value, the center-of-gravity, in the center of the bin without applying a further correction. The correction either moves the data points vertically to the true yield or cross section value, keeping the same p_T, or the data points keep their position in y direction and are move horizontally, moving them in p_T. For this analysis, the first method is used, keeping the x values of the spectra makes it easier to calculate ratios such as η/π^0 or R_{AA}, or to compare with older measurements.

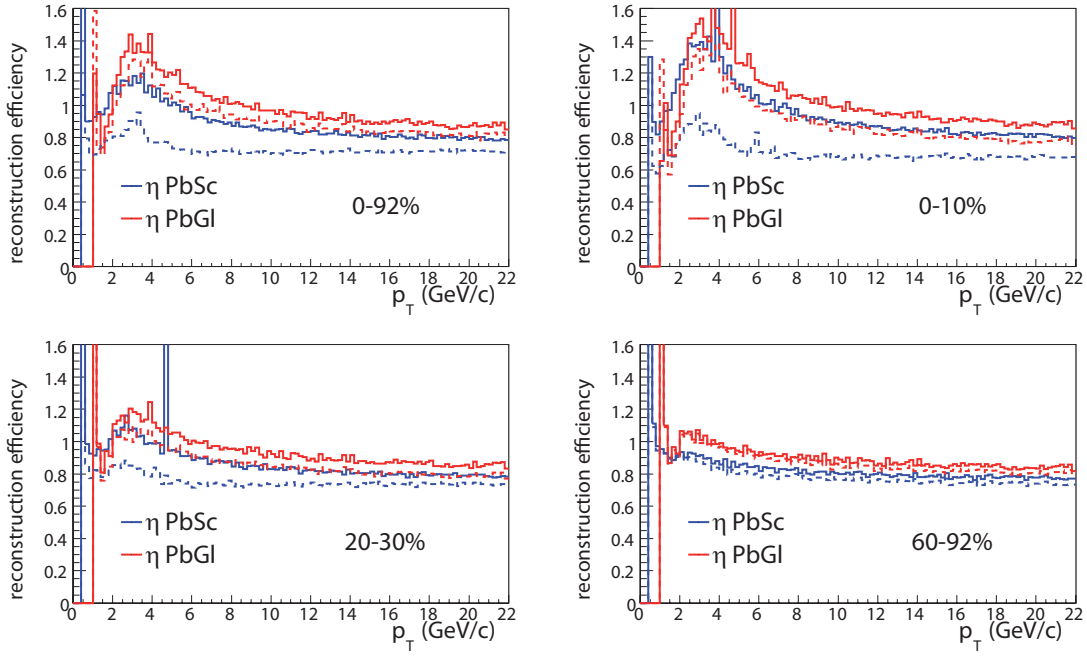

Figure 5.12: η reconstruction efficiency in the PbSc (blue) and the PbGl (red), for four different centrality selections for PID0 (continuous) and PID3 (dashed). The effect of overlapping showers in more central events is seen as an increase of the efficiency for $p_{\mathrm{T}} \leq\approx 6\mathrm{GeV}/c$, it is larger in the PbSc.

For the correction, in principle the true shape of the spectrum has to be known. Since this is to be measured, an iterative procedure is applied to correct for the bin-shift. Therefore, the measured spectrum is approximated by a fit function that itself should follow the true spectrum. With the help of this fit function, the true value of the yield in the middle of a given p_{T} bin is calculated with the help of the ratio of the average yield in the interval and the approximated true value:

$$r = \frac{1/\Delta \cdot \int_{p_T^c-\Delta/2}^{p_T^c+\Delta/2} f(p_T)dp_T}{f(p_T^c)} \tag{5.19}$$

The average (measured) y value is then divided by r, therefore the corrected yield Y_{corr} is $Y_{corr} = Y_{uncorr}/r$.

The challenge in calculating the bin-shift correction is the choice of an appropriate function. In earlier analyses, usually a Hagedorn-type function was used. However, with the larger p_{T} reach of the data analyzed in this thesis, the limit of such functions is reached. The alternatives are either a composite function, connecting an exponential fit at low transverse momenta with a power law function at high p_{T}, or the use of another type of function describing the whole p_{T} distribution better than the Hagedorn-type functions.

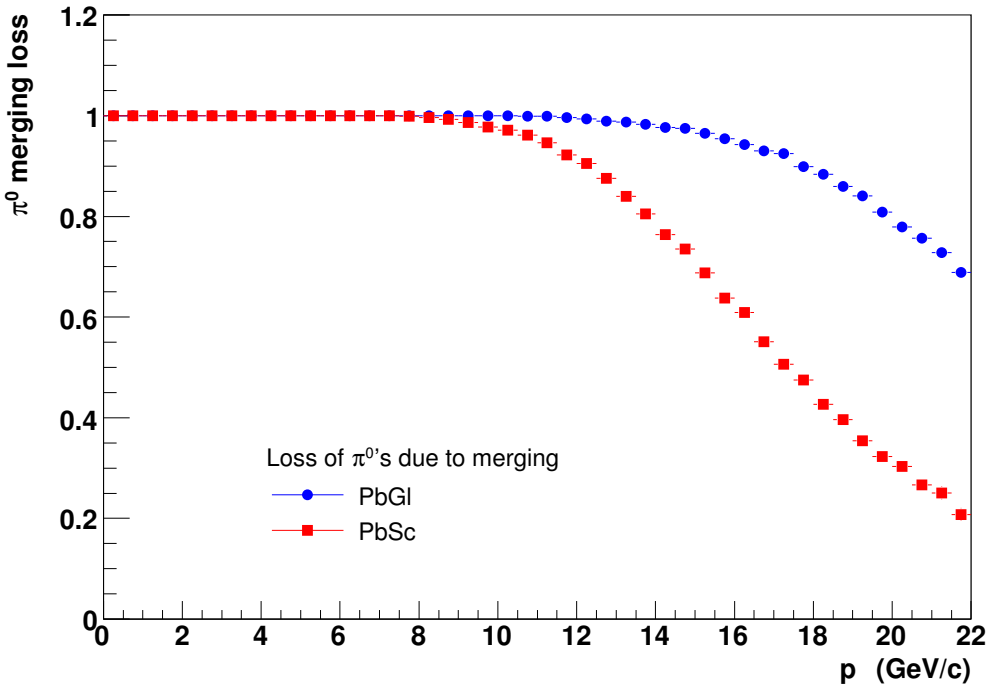

Figure 5.13: Loss of π^0's due to merging of the decay photons. The finer granularity of the PbSc (red) leads to an earlier setting in of merging and to larger merging compared to the PbGl (blue).

These two parameterizations have already been discussed in Section 5.2.1. In this analysis, the continuous function is used.

5.2.4 Correction for Shower Merging

Due to the decay kinematics, the average angle between the decay photons of π^0 or η decreases with increasing p_T of the original particle, and thus the distance of the two photons on the calorimeter also becomes smaller. Due to the limited granularity of the PbSc and PbGl calorimeters and the lateral expansion of electromagnetic showers, it can happen that the showers of both decay photons overlap and are reconstructed by the clustering algorithm as one single cluster. This so-called merging sets in for π^0's at $p_T \geq 8$ GeV/c for the PbSc, and at $p_T \geq 11$ GeV/c for the PbGl, respectively. For the η, the opening angle of the two photons is larger due to the larger rest mass of the η and thus merging does not occur in the analyzed p_T range.

The fast Monte-Carlo simulation used to calculate the detector depending corrections to the raw π^0 yield does not include any clustering routine, therefore it cannot be used to obtain the correction necessary to account for cluster merging. Another simulation was

	Conversion correction factors			
	PbGl	PbSc East	PbSc West	PbSc total
π^0	1.088 ± 0.025	1.054 ± 0.015	1.073 ± 0.026	1.067 ± 0.022
η	1.076 ± 0.025	1.052 ± 0.015	1.077 ± 0.026	1.069 ± 0.022

Table 5.4: Correction factors for the π^0 and the η yield that are applied due to decay photon loss via conversion, for different sector combinations.

therefore used, including a parameterization for the real energy distribution within the clusters of electromagnetic showers in the PbGl and the PbSc detectors. It was obtained from test beam data, including bad modules besides the shape of the real neutral pion spectrum and the EMCal detector geometry [Bat05]. This simulation leads to a value for the loss of π^0's due to merging, as depicted in Figure 5.13. The merging in the PbSc starts at lower p_T as expected due to its coarser granularity and the its larger Moliere radius, and it is larger than the merging in the PbGl.

5.2.5 Conversion Correction

Due to the material between the collision vertex and the calorimeters in PHENIX, each photon can – with a certain probability – convert into an electron positron pair on its way to the calorimeter. When one of the π^0 or η decay photons converts and the e^+e^- pair does not end up in one photon-like cluster, the original meson cannot be reconstructed and has thus to be regarded as lost. Therefore, a correction has to be applied during the analysis to account for such losses. Two methods can be used to estimate the loss of photons due to conversion: Either the known radiation lengths of the different detectors and structures between vertex and EMCal are used to calculate the conversion probability [d'E04], or a full PISA simulation where the PHENIX detector is modeled with GEANT3 is used to look for the amount of converting decay photons [Hie05]. The second method is more reliable, since the first method is based on general conversion probabilities derived from the radiation lengths for the different subsystems as published in technical publications while the second one not only considers a realistic material distribution inside the single subsystems but also accounts for mesons that can be reconstructed even after the conversion of a decay photon. Therefore, for the PbGl case where the material between the vertex and the detector did not change between 2003 and 2004, the corrections as reported in [Hie05] are used. For the PbSc on the other hand it has to be taken into account that the aerogel detector was installed in front of the W1 sector after run 03, which adds $\approx 20\%$ of X_0 for that one sector which rises the π^0 or η correction factor. Without the aerogel, $(6.3 \pm 2.1)\%$ of the π^0 and $(6.7 \pm 2.1)\%$ of the η mesons are lost due to conversion in the

west arm. The 20% X_0 of the aerogel account for another theoretical 14.4% for W1, or 3.6% for the west arm. However, it was shown, that not all converting photons are lost because the e^+e^- pair can still be reconstructed in the calorimeter, an effect becoming more probable the further away from the vertex the conversion takes place. Since the aerogel is close to the W1 calorimeter, it is assumed that most of the conversion pairs are not lost, and so the total conversion probability is increased by 1.0% compared to [Hie05]. The different correction factors that are multiplied to the raw yield during the analysis are given in Table 5.4.

5.3 Systematic Uncertainties

Each step of the analysis can contribute systematic uncertainties to the result of the measurement. Systematic uncertainties are caused by the limits of each analysis technique in fully understanding physics or experimental backgrounds, analysis cuts, and normalization, or by the limits of techniques modeling the response of the detector to particles generated in the collision. Significant contributors to the systematic uncertainties on the final π^0 yield are e.g. the absolute energy scale of the calorimeter which can be only estimated by a certain precision, or the efficiency, caused by detector effects that can not be completely and exactly modeled in simulations. In principle, (systematic) uncertainties are divided into three types.

- **Type A:** p_{T}uncorrelated uncertainties that fluctuate from point to point.
- **Type B:** p_{T}correlated uncertainties that move all points into the same direction.
- **Type C:** scale uncertainties that move all points by the same amount.

The systematic uncertainties for the π^0 and η spectra are all of type B.

The different sources of systematic uncertainties and their values are summarized in Table 5.5 for the π^0 measured with the PbGl, in Table 5.6 for the π^0 measured with the PbSc, and in Table 5.7 for the η. The different systematic uncertainties are added quadratically to get the total systematic uncertainty. A depiction of the uncertainties versus p_{T} is shown for the PbGl π^0 in Figure 5.14, for the PbSc π^0 in Figure 5.15, and for the η in Figure 5.16, for three different centrality selections. It is clearly visible that at different transverse momenta different contributions dominate the overall uncertainty.

5.3.1 Peak Extraction

The systematic uncertainty of the peak extraction comes about because the “true” parameterization of the residual background is not known. It is approximated by an appropriate

p_T [GeV/c]	3	8	13	18
centrality	0-92 % (0-10 %; 60-92 %)			
peak extraction	3.1 (2.9; 2.9)	2.4 (2.4; 2.7)	2.3 (2.4; 2.6)	2.3 (2.3; 2.6)
acceptance	4	4	4	4
efficiency	3.6 (5.0; 2.6)	3.6 (4.1; 3.6)	3.8 (4.3; 3.6)	4.1 (4.2; 3.9)
energy scale	6.9 (6.5; 7.1)	7.5 (7.3; 7.9)	6.8 (6.7; 7.2)	6.3 (6.3; 6.7)
e-scale nonlin.	3.9	0.5	3.7	6.1
non vertex corr	1.5	1.5	1.5	1.5
conversion corr	2.5	2.5	2.5	2.5
merging corr	0	0	1.2	8.0
total sys uncert.	10.3 (10.6; 10.2)	9.9 (10.0; 10.2)	10.2 (10.3; 10.5)	13.6 (13.6; 13.8)

Table 5.5: Systematic uncertainties of the π^0 spectra, measured with the PbGl. The uncertainty of the peak extraction has a very high slope at low p_T. Each uncertainty is given for minimum bias, and additionally for central and for peripheral events if there is a centrality dependence. All uncertainties are given in %.

p_T [GeV/c]	3	8	13	18
centrality	0-92 % (0-10 %; 60-92 %)			
peak extraction	5.4 (5.6; 3.6)	2.9 (2.8; 2.8)	2.6 (2.6; 2.7)	2.5 (2.5; 2.7)
acceptance	2.5	2.5	2.5	2.5
efficiency	3.6 (5.0; 2.6)	3.6 (4.1; 3.6)	3.8 (4.3; 3.6)	4.1 (4.2; 3.9)
energy scale	6.9 (6.5; 7.1)	7.5 (7.3; 7.9)	6.8 (6.7; 7.2)	6.3 (6.3; 6.7)
e-scale nonlin.	3.9	0.5	3.7	6.1
non vertex corr	1.5	1.5	1.5	1.5
conversion corr	2.2	2.2	2.2	2.2
merging corr	0	0.2	10.4	39.4
total sys uncert.	10.7 (10.7; 9.8)	9.4 (9.5; 9.7)	14.2 (14.2; 14.3)	40.8 (40.8; 40.9)

Table 5.6: Systematic uncertainties of the π^0 spectra, measured with the PbSc. The uncertainty of the peak extraction has a very high slope at low p_T. Each uncertainty is given for minimum bias, and additionally for central and for peripheral events if there is a centrality dependence. All uncertainties are given in %.

p_T [GeV/c]	3	6	10	14
centrality	0-92 % (0-10 %; 60-92 %)			
peak extraction	18.0 (17.7;16.4)	10.0 (12.3;9.4)	7.7 (10.6;7.3)	6.8 (10.0;6.6)
acceptance	5	5	5	5
efficiency	7.8 (9.9;6.3)	7.6 (9.7;6.3)	7.5 (9.4;6.2)	7.3 (9.2;6.2)
energy scale	6.9 (6.5;7.1)	7.7 (7.5;8.1)	7.2 (7.2;7.6)	6.7 (6.6;7.1)
e-scale nonlin.	3.9	1.5	1.0	4.6
conversion corr	2.0	2.0	2.0	2.0
total sys uncert.	21.8 (22.3;20.1)	15.7 (18.2;14.9)	14.0 (16.8;13.4)	14.0 (16.7;13.5)

Table 5.7: Systematic uncertainties of the η spectra. The uncertainty of the peak extraction has a very high slope at low p_T. Each uncertainty is given for minimum bias, and additionally for central and for peripheral events if there is a centrality dependence. All uncertainties are given in %.

fit. Since the background is influenced by the event multiplicity, the systematic uncertainty is in general larger than average in central events, and it is also larger than average at low transverse momenta. The uncertainty is estimated by using different fits – a constant fit compared to a linear fit and a second order polynomial – to the background and comparing the raw yields obtained with these different fits (see Figure 5.17). This uncertainty is centrality dependent, for in very central events the background is much larger, and in very peripheral events the number of invariant mass pairs becomes small. In general, it is larger for the PbSc due to the coarser granularity of the detector which leads to a larger background.

5.3.2 Acceptance Correction

The acceptance correction is well understood and relies only on the decay kinematics of the mesons and on the well-known detector geometry. The main challenge in the acceptance calculation was the use of a run-dependent bad module map for the PbGl calorimeter. However, it turned out, that the overall acceptance in the PbGl does not change much for the different run periods. Overall, it differs by less than $\sim 5\%$. Therefore the uncertainty on the correction is larger than in earlier analyses. For the PbSc, the acceptance uncertainty is smaller since only one map for bad modules is used over the whole run period.

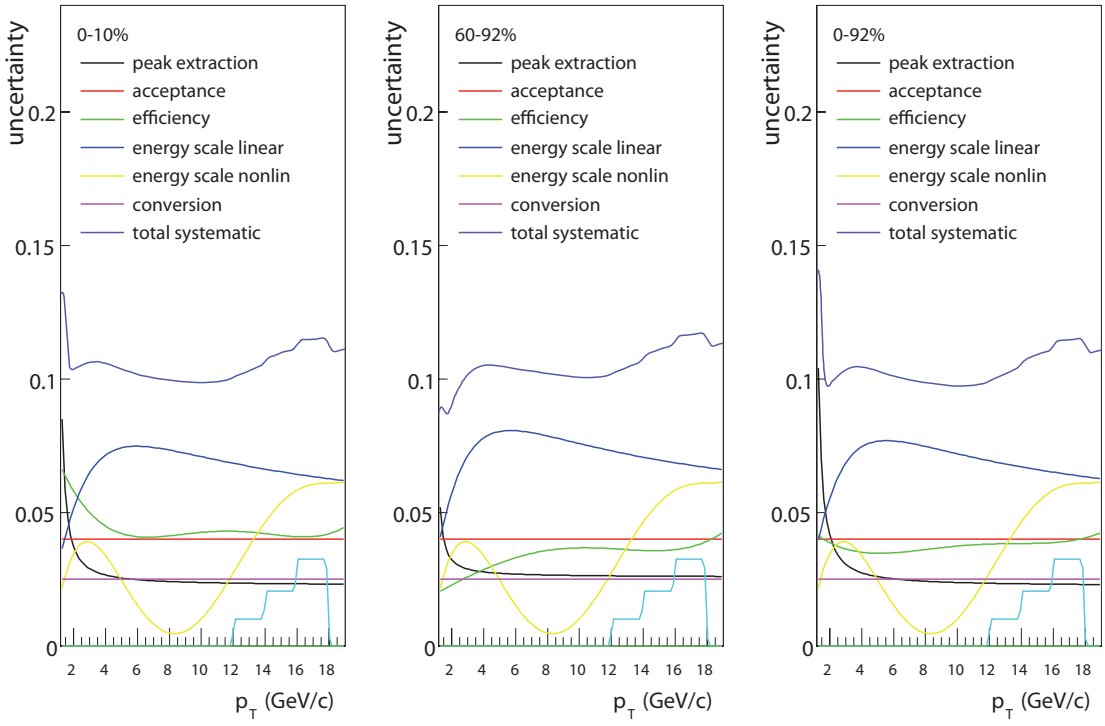

Figure 5.14: Different sources of so-called "type B" systematic uncertainties for the π^0 spectrum with the PbGl. The uncertainties from different sources are added quadratically to obtain the total systematic uncertainty.

5.3.3 Efficiency Correction

The uncertainty of the efficiency correction is affected by the simulation of PID cuts, the energy smearing, and the shower overlap. The PID efficiency is estimated by comparing the corrected yield before and after the cuts, but as the energy cut has almost no effect on the finally analyzed spectrum[4], basically two samples are compared, one with and one without using the shower shape cut. An example for the estimation of this uncertainty is shown in Figure 5.18. The energy smearing uncertainty is estimated by varying the energy smearing parameters in the fastMC within a range in which the measured peak widths in the data are still fairly well reproduced by the simulation, i.e. the deviation in width is ~ 10 MeV/c^2. Similarly, the shower overlap uncertainty is estimated by varying the shower overlap probabilities in the simulation and comparing the efficiency after that. The shower overlap parameters are simply multiplied by 0.5 for the estimation, leading to a safe estimate of the uncertainty. It turned out that the efficiency uncertainty is largest

[4]Only photons with $E < 0.2$ GeV are removed, together with the asymmetry cut, the energy cut only plays a small role in the first bin of the spectra

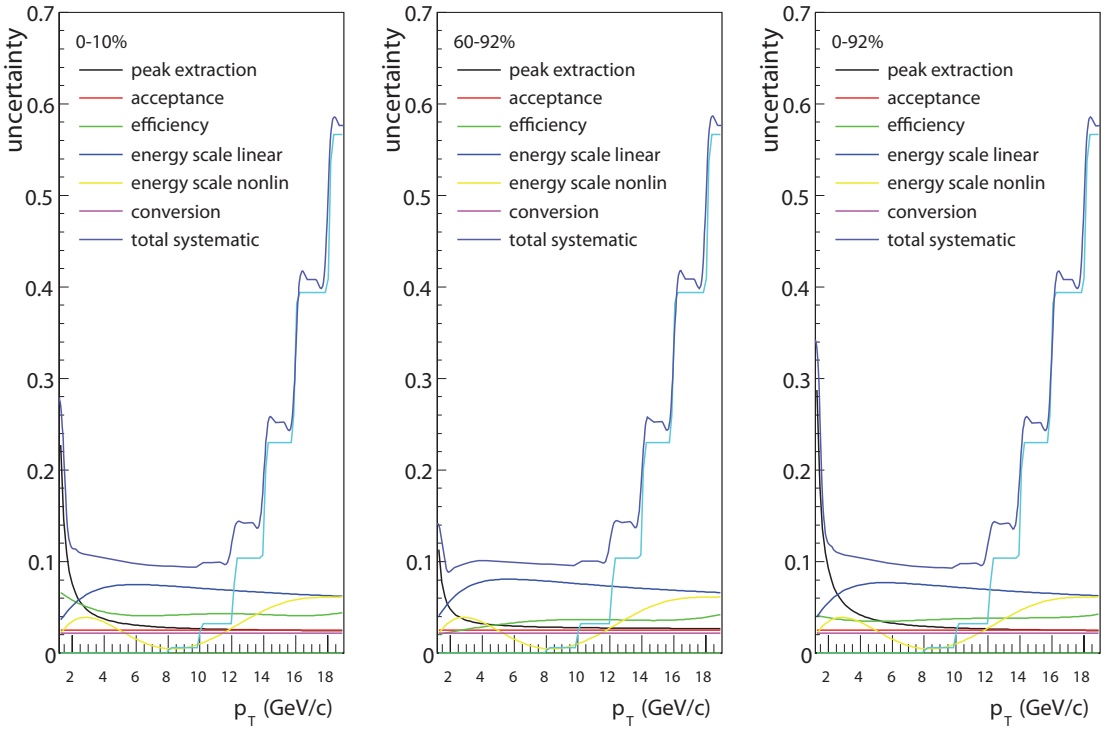

Figure 5.15: Different sources of so-called "type B" systematic uncertainties for the π^0 spectrum with the PbSc. The uncertainties from different sources are added quadratically to obtain the total systematic uncertainty.

for the most central collisions. This was expected, since an additional influence – the shower overlap – on the detector's reconstruction efficiency has to be considered at higher multiplicities. All three uncertainties are finally added quadratically to get the overall uncertainty for the efficiency correction. This can be seen in Figure 5.19.

5.3.4 Energy Scale

As described in [Iso05], and as visible in the comparison of the π^0 peak positions shown in Figures 4.4 and 4.5, the uncertainty in the energy scale is safely estimated to be 1%. Due to the steeply falling spectrum, this constant uncertainty leads to an uncertainty in the yield which is dependent on p_T as referred to in the table. It is calculated by multiplying the p_T scale of a function describing the spectra by a factor of 1.01 ($f'(p_T) = f(p_T \cdot 1.01)$) and subsequently calculating the difference between the original and the modified function. Since the spectra for the different centrality selections are described by different functions with slightly different shapes - which is due to the rising suppression of both mesons towards more central collisions - there is a slight centrality dependence on the

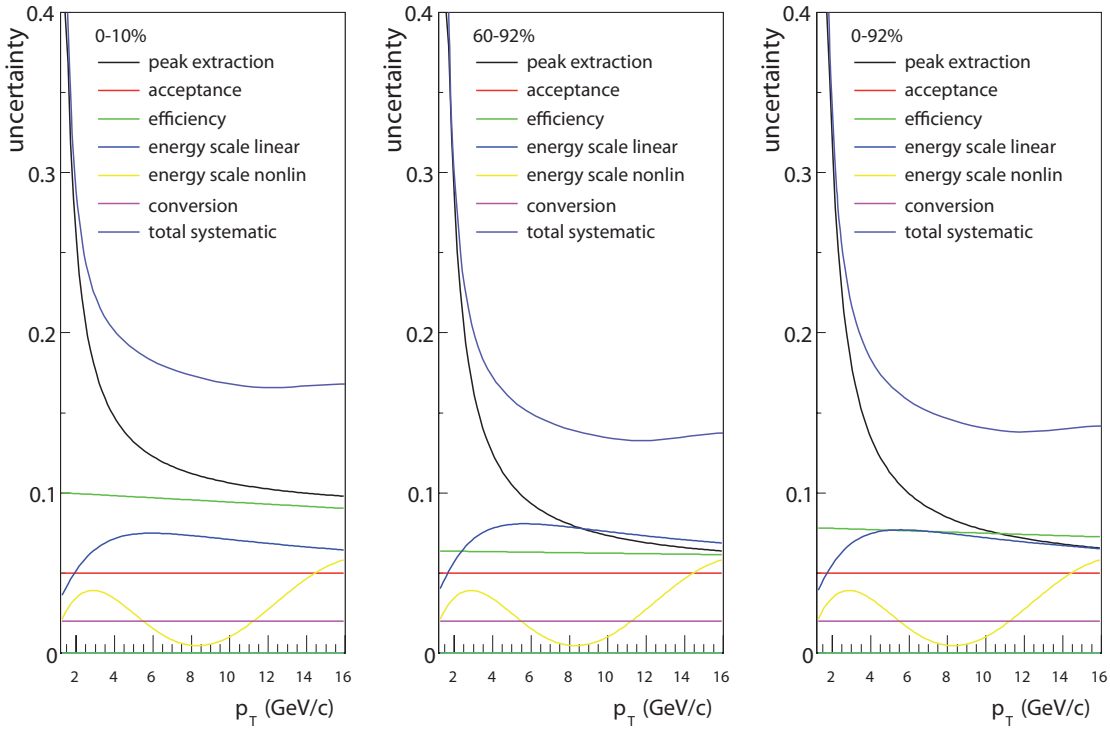

Figure 5.16: Different sources of so-called "type B" systematic uncertainties for the η spectrum. The uncertainties from different sources are added quadratically to obtain the total systematic uncertainty.

uncertainty from the imperfectly known energy scale.
There is also a non-linear component in the energy scale uncertainty. This component needs to be considered since the energy scale is fixed by comparing the data with a simulation and the comparison is dominated by a certain photon p_T range. Therefore, the energy scale is best known for photon transverse momenta of $p_T \approx 3-4$ GeV/c. At lower transverse momenta, the energy scale correction includes an incompletely understood nonlinear part while at higher transverse momenta, the statistical errors in the data itself become too large for a strong constraint on the energy scale. This uncertainty is estimated with the Monte-Carlo simulation for the efficiency calculation, reversing the last step applied during the nonlinear energy calibration.

5.3.5 Correction for Shower Merging

The merging correction requires very good knowledge of effects in the detector and the parameterization of the energy distribution of each cluster within the calorimeter even at high photon energies. Furthermore, the clustering algorithm itself and its feasibility to separate slightly merged clusters plays a role in the correction. All this can result in

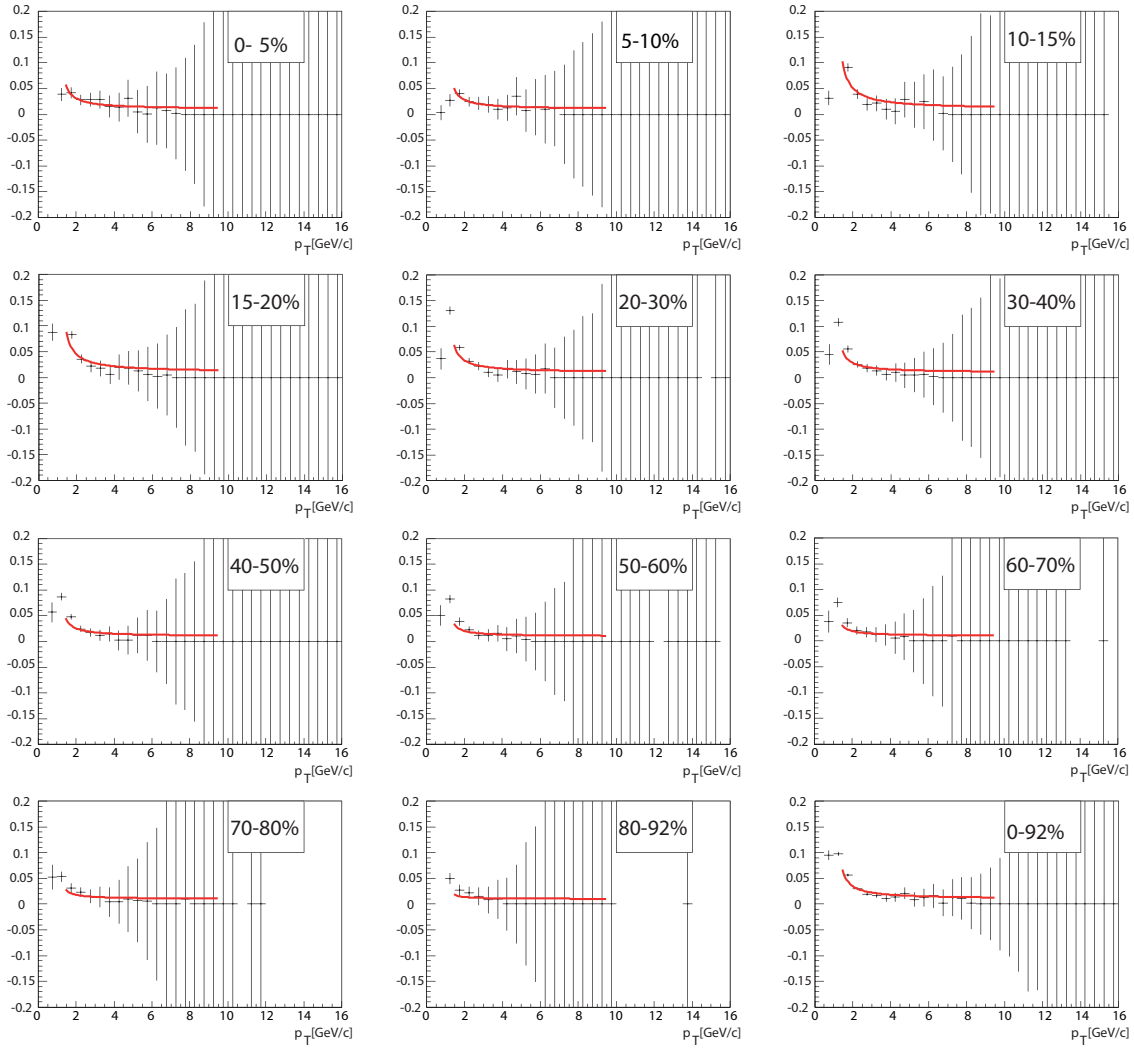

Figure 5.17: Systematic uncertainty estimation for the peak extraction. The ratio of the yield with two different background parameterizations is fitted with the red curve.

systematic uncertainties that are hard to estimate. Therefore it is assumed to be most safe to assume a large uncertainty for the merging correction. The uncertainty is conservatively estimated to be 50 % of the correction itself. The corresponding uncertainty in the π^0 yield is given in Table 5.5 and depicted in Figures 5.14, and 5.15.

5.3.6 Differences for the η Meson

The general sources of systematic uncertainties are the same for the η and the π^0, however, there are some differences. First, two uncertainties occuring for the π^0 do not play a role in the η analysis: Since no merging correction has to be applied in the η analysis, there is of course no uncertainty associated with such a correction. Also,

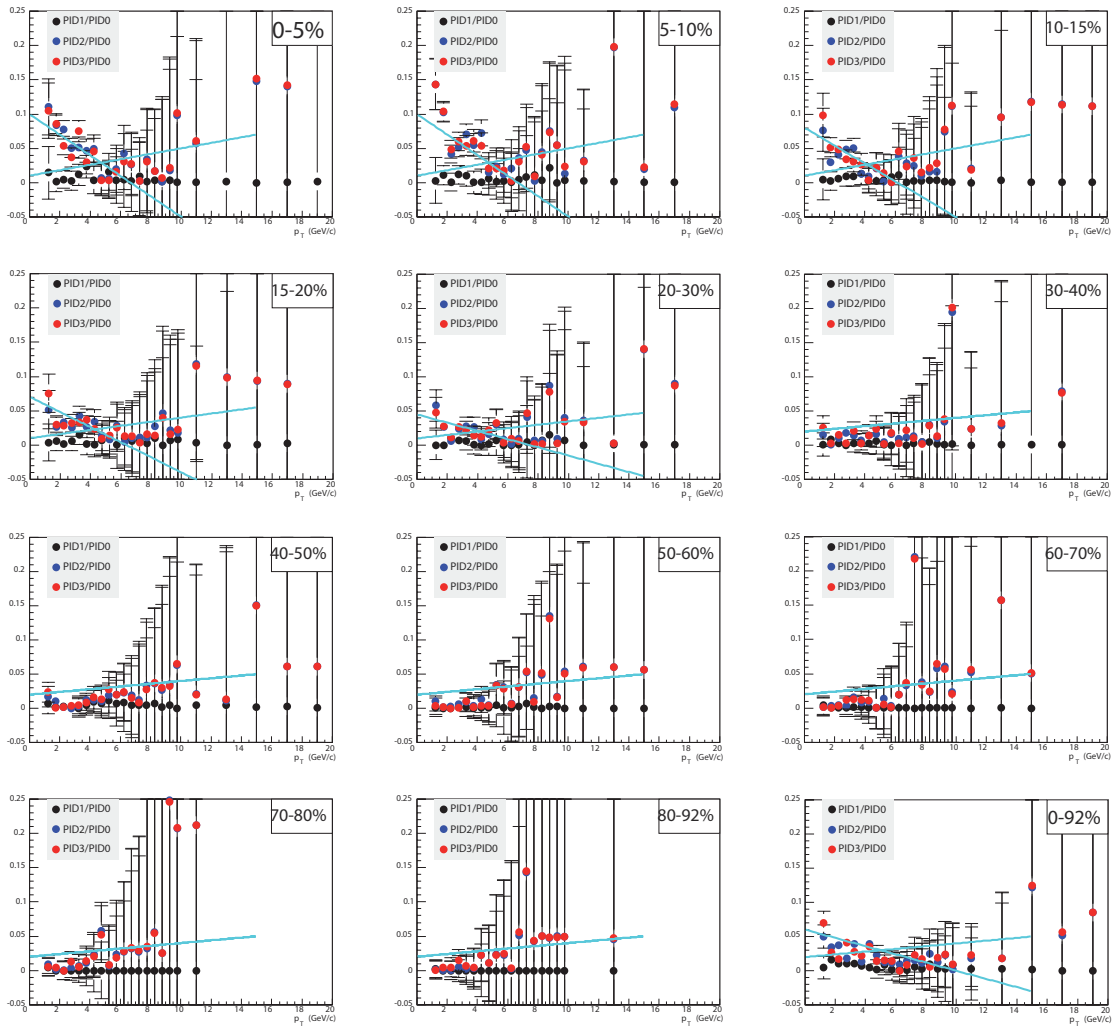

Figure 5.18: Comparison of the different PID cuts in the π^0 analysis. The final yields obtained with the different PID cuts are divided by the final yields without any PID cut. The function is the estimation of the systematic uncertainty.

no correction is applied for η mesons not originating from the event vertex, removing another source of uncertainty. The remaining uncertainties are the same, but some differ in size, they are usually larger for the η.

The most notable difference in the systematics between the η and the π^0 is the peak extraction uncertainty which is much larger for the η. This can be explained by the parameterization of the residual background. As already mentioned above, its shape is unknown. Using different possible background parameterizations for the background around the η peak, the obtained raw yield may differ by about 20% at low transverse momenta, and even at higher p_T, an uncertainty of 6.5 to 10% remains. The energy scale uncertainty is

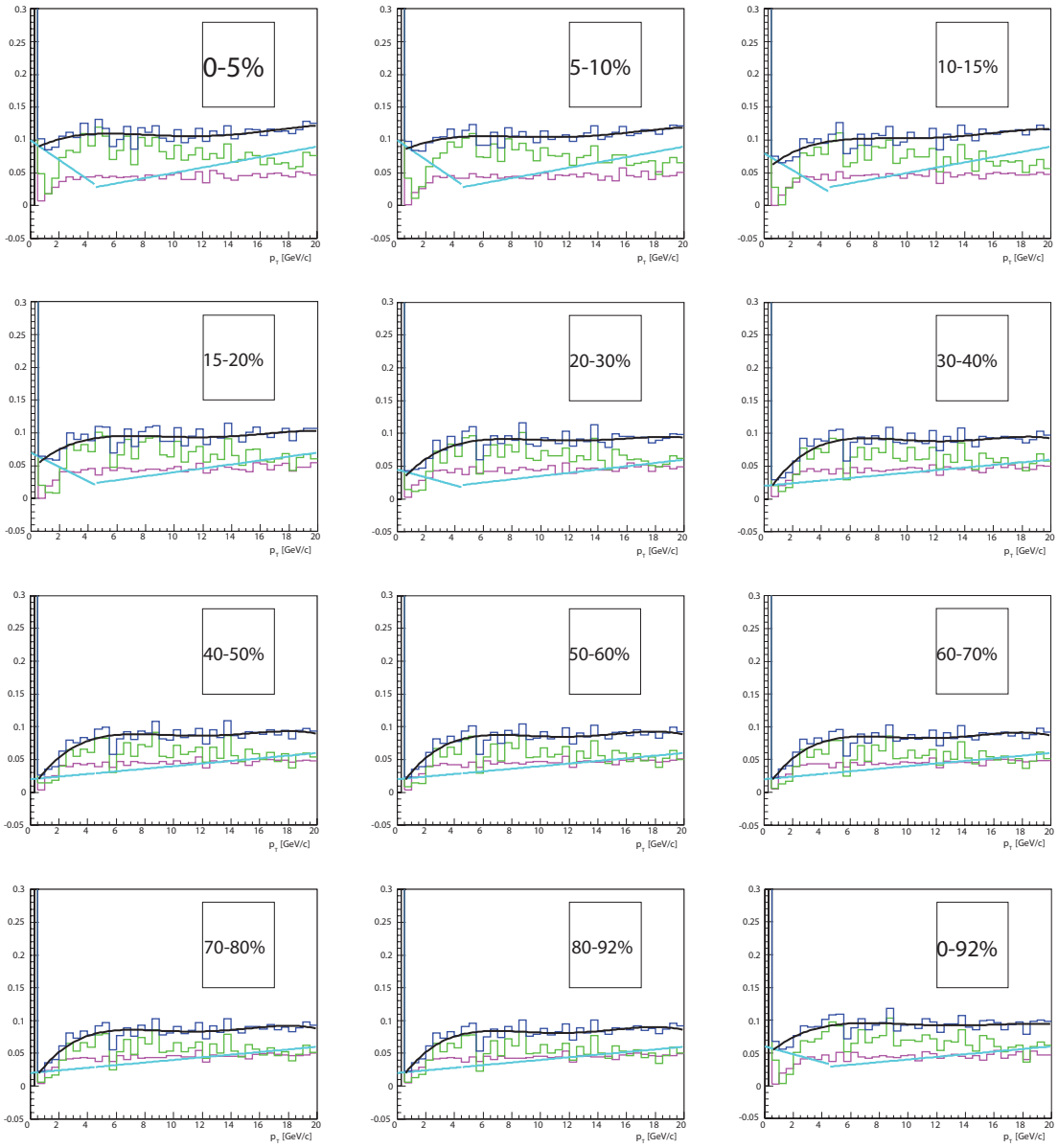

Figure 5.19: π^0 systematic uncertainty due to the efficiency calculation. The different sources (pink: energy smearing parameterization, green: shower overlap parameterization, red: PID efficiency) are added quadratically (blue), the sum of the uncertainties is fit with a function (black).

in principle the same, the (small) differences come from the different shapes of the π^0 and η spectra versus p_T. The uncertainty in efficiency is also estimated to be larger, since especially the shower overlap parameterization was explicitly tuned with π^0 embedding. Though this should be feasible in principle, the larger opening angle of the η may result in slightly different multiplicity effects as compared to the π^0. Therefore, this uncertainty has a much larger centrality dependence for the η.

6. Direct-Photon Analysis

```
The seventh ... flashes like lightning, and no one can
deflect it.
```

The Gilgamesh Epos

As outlined in Section 2.5, direct photons are in principle all photons that do not originate from hadron decays, therefore including photons from initial hard scattering processes such as $q+g \rightarrow q+\gamma$, or $q+\bar{q} \rightarrow g+\gamma$, from next-to-leading order processes such as bremsstrahlung emission by a scattered quark or photon emission during the fragmentation of a parton jet, from the interaction of a jet with the hot and dense medium, or from thermal emission during the QGP or hadron gas phase. Thus, the experimental task is to find the signal of direct photons in the background of decay photons from hadrons, mostly coming from the decays $\pi^0 \rightarrow \gamma+\gamma$ or $\eta \rightarrow \gamma+\gamma$. Since in the high-multiplicity environment of a heavy-ion collision it is not possible to reconstruct particle decays and taking out the decay photons from the overall photon sample on an event-by-event basis, the method applied to obtain the direct-photon spectrum used in the following is the so-called statistical method. Generally, it follows three steps that will be outlined in more detail later in this work. The first step comprises obtaining a spectrum of inclusive photons from all different particles that contribute to a signal in the detector. In a next step, the ratio of the neutral pion and the inclusive photon spectrum $(\gamma^{incl}/\pi^0)_{meas}$ is calculated, as is the ratio of the neutral pion and the simulated hadronic decay photon spectrum $(\gamma^{decay}/\pi^0)_{sim}$. In a third step, one can - by calculating the ratio of the two mentioned pion/photon ratios (the so-called double-ratio) - finally calculate the direct-photon spectrum itself. This double ratio

$$R_\gamma = \frac{(\gamma^{incl}/\pi^0)_{meas}}{(\gamma^{decay}/\pi^0)_{sim}} \tag{6.1}$$

is a measure of the excess of photons above the decay photon background, it would be unity in case there are no direct photons and above unity in case of a direct-photon signal. The direct-photon signal can be derived from the double ratio and the inclusive photon spectrum via

$$\gamma^{direct} = \gamma^{incl} - \gamma^{decay} = \left(1 - \frac{1}{R_\gamma}\right) \cdot \gamma^{incl} \,. \tag{6.2}$$

This indirect method of getting the direct-photon signal via the ratios offers an advantage over a direct subtraction of the decay photons from the inclusive photons as systematic

errors e.g. on the energy scale cancel when calculating the ratio, since the same data sets with identical energy calibration, acceptance and efficiency calculation parameters are used. Also, the decay photon spectrum is easily simulated in a fast Monte-Carlo simulation, using the neutral pion spectrum (see Chapter 5) as input spectrum for the simulation.

6.1 Inclusive Photons

As outlined above, the first step in the direct-photon measurement is the measurement of an inclusive photon spectrum. This inclusive photon spectrum is defined as the spectrum of photons from the collision system and from particle decays. To obtain it from the originally measured hit distribution on the EMCal, several corrections have to be applied, since not only photons are measured by the calorimeter but also hadrons and electrons. In addition, the calorimeter has limited acceptance, and different detector and physics effects affect the detector's response function. These will be outlined in more detail later. When denoting the cluster spectrum as measured by the EMCal as ΔN_{clus}, the final inclusive photon yield can be derived from ΔN_{clus} as (see e.g. [Zau07])

$$\frac{\mathrm{d}^2 N_{\gamma}^{incl}}{\mathrm{d}p_{\mathrm{T}}\mathrm{d}y} = \frac{(1-X_{\mathrm{ch}})\cdot(1-X_{\mathrm{n\bar{n}}})}{\alpha_{\gamma}\cdot\varepsilon_{\gamma}\cdot(1-p_{\mathrm{conv}})}\cdot\frac{\Delta N_{clus}}{\Delta p_{\mathrm{T}}\Delta y}\,, \tag{6.3}$$

with X_{ch} denoting the fraction of charged particles in the cluster spectrum, and $X_{\mathrm{n\bar{n}}}$ being the fraction of neutrons and anti-neutrons in the neutral cluster spectrum. This is necessary, as some of these particles are not removed by the PID cuts. Furthermore, the acceptance correction α_{γ}, accounting for the detector geometry, and the efficiency correction ε_{γ}, accounting for both different effects on the detector such as its limited energy and position resolution as well as overlapping showers due to high occupancy in more central collisions and the merging of decay photons at high π^0 transverse momenta, and the PID cuts, are applied in the analysis. Another correction accounts for the probability p_{conv} that photons convert into electrons and positrons in the detector material between the collision point and the calorimeter and do not reconstruct as a single cluster. Equation 6.3 describes the differential inclusive photon yield per unit transverse momentum Δp_{T} and rapidity Δy. The fully corrected Lorentz invariant yield per event for minimum bias collisions or for different centrality selections can be calculated by multiplying Equation 6.3 using the factor $\frac{1}{2\pi p_{\mathrm{T}} N_{\mathrm{evt}}}$ with N_{evt} as the number of analyzed events.

The Uncorrected Cluster Spectrum In the first analysis step, different cluster energy distributions from the calorimeter are obtained. These distributions can be measured for

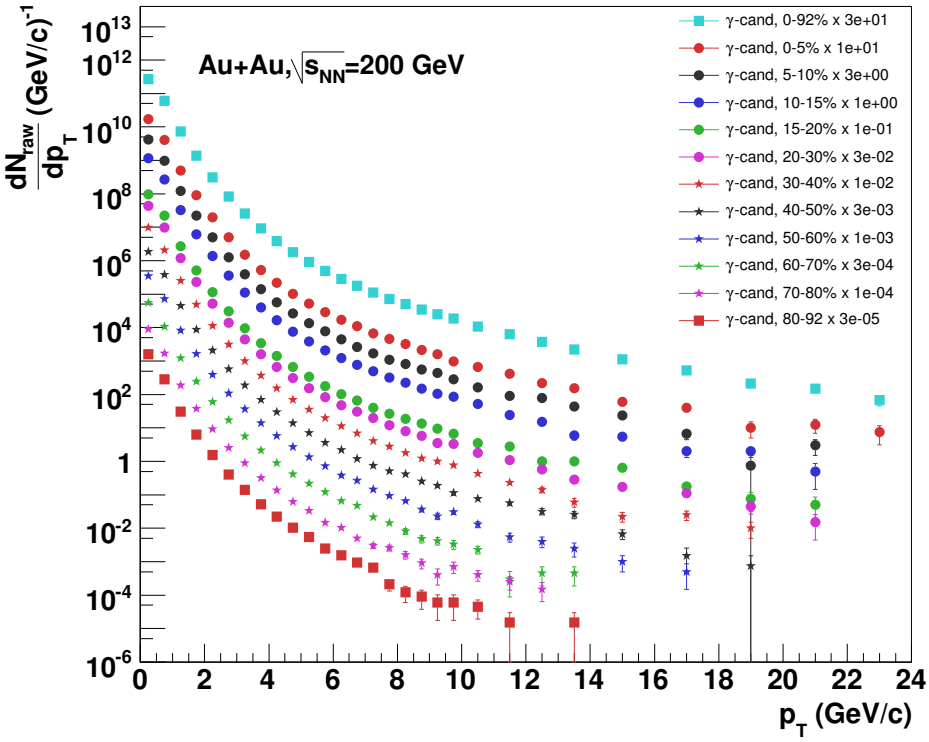

Figure 6.1: Uncorrected (raw) cluster spectrum as measured with the PbGl in all analyzed events.

different sectors of the EMCal, for different PID cuts, for different centrality selections, and also for different angles with respect to the reaction plane. These spectra contain all hits on the calorimeter that are not removed by the PID cuts, therefore they do not represent a clean photon sample but also contain a certain fraction of charged hadrons such as π^+ or π^-, neutrons, as well as electrons and positrons. Other neutral hadrons will not reach the EMCal since their livetimes are too short, therefore the so-called neutral contribution to the cluster spectrum consists only of neutrons and anti-neutrons. The spectra of uncorrected clusters are shown in Figures 6.1, and 6.2, for the PbGl and the PbSc, respectively.

6.1.1 Charged Particle Veto

The most straightforward idea of removing charged particles from the original EMCal hit distribution would be to use the pad chamber PC3 as a veto detector and simply remove all EMCal hits connected to a PC3 hit within a certain radius. Though this method should remove all charged particles, it would also remove photon hits from the sample since charged particles can always hit the PC3 within this veto radius of a photon on the calorimeter. Therefore, a method was devised to remove such uncorrelated charged particle vetoes from the correction being applied in the end. Here, the first method is event

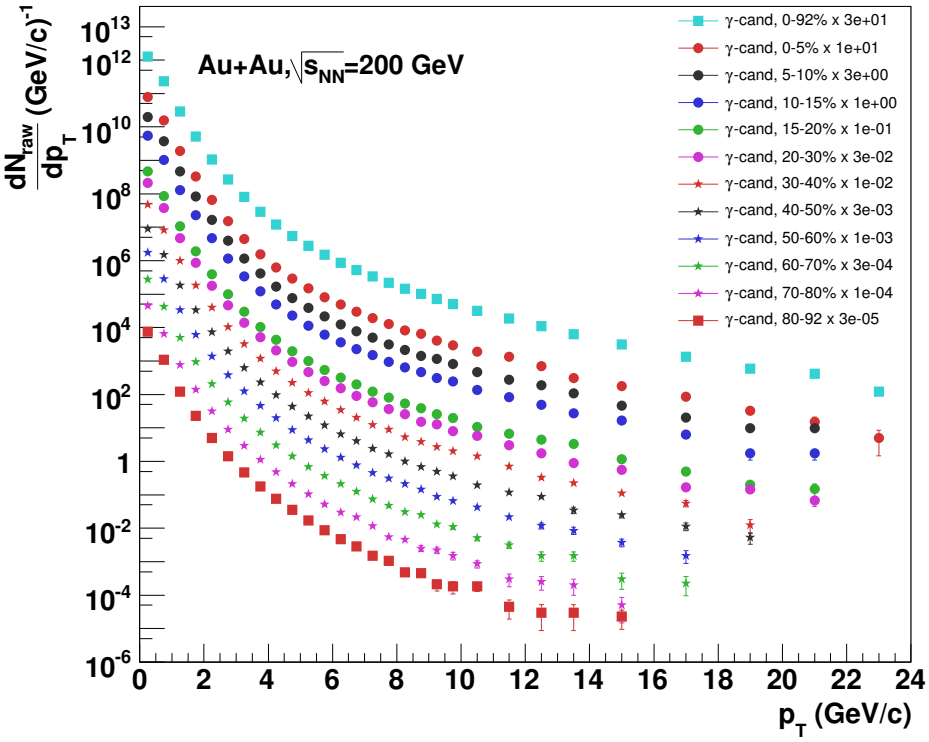

Figure 6.2: Uncorrected (raw) cluster spectrum as measured with the PbSc in all analyzed events.

mixing, that means, calculating the distance between EMCal and PC3 hits for one event, and doing the same with the EMCal hits from one event and the PC3 hits from another event from the same centrality selection to estimate the background from uncorrelated associations of a PC3 hit with an EMCal hit, for two hits from different events are not correlated by definition. This method has been applied in earlier analyses [KB04]. As this method does not remove charged hadrons and leptons on the basis of single clusters in each event, it is a statistical method, removing a certain fraction of clusters per transverse momentum from the overall data sample. Though it yields to a meaningful and precise estimation of the fraction of charged particles within the cluster spectrum, this method is not used in this analysis, because not all necessary information has been stored in the DSTs. To do a correct background estimation via event mixing, it is necessary to have the information about all hits in the PC3 available, but for data reduction, in the 2004 run DSTs, only the closest PC3 hit to each EMCal hit was stored. Therefore, especially in more central events, a large amount of PC3 hits, namely those not being the closest one to a cluster in the EMCal, are lost, and so the event mixing method does not lead to a good estimate of the uncorrelated background, especially in central events. This is seen in Figure 6.3 where the event mixing method using the insufficient PC3 information is applied to estimate the uncorrelated background. The left panel illustrates the failure of the event mixing in central events, the background estimation clearly does not match the

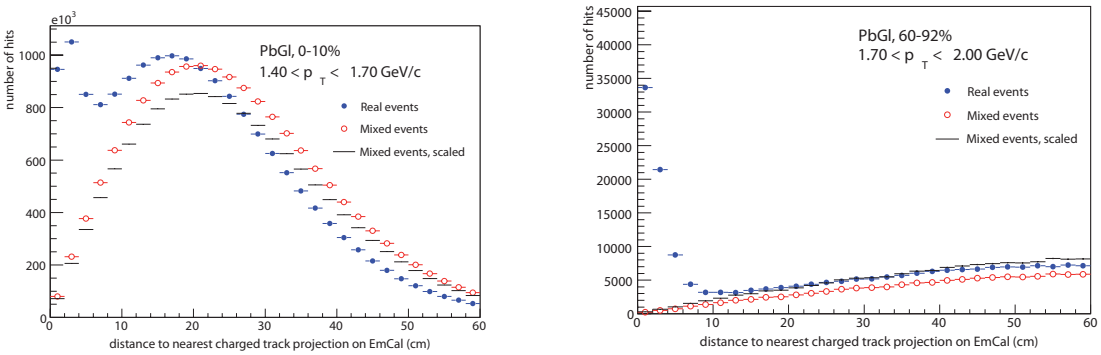

Figure 6.3: The distance of the closest charged track to each EMCal hit with (left) 1.4 GeV/$c \leq p_{\mathrm{T}} \leq$ 1.7 GeV/c, for 0-10% most central events and (right) 1.7 GeV/$c \leq p_{\mathrm{T}} \leq$ 2.0 GeV/c, for 60-92% most central events in the PbGl sectors for the PID 3 cut. The blue points show the distance within the same event (real events), the red circles depict the distance from event mixing for background estimation, and the black lines are the scaled mixed-event distribution. The event mixing is done with the available PC3 information, a clear mis-estimation of the background in real events is seen, especially in central events.

"true" background; the right panel shows peripheral events where the deviation of the background estimation from the "true" background is smaller but still visible.

There are two different ways out of the dilemma. The first one is using tracks measured by the Drift Chamber and projected onto the EMCal as charged particle veto. The analysis method here is basically the same as the one using the Pad Chamber, the main difference is that the conversion of photons into electron-positron pairs behind the Drift Chamber needs to be estimated in addition. Furthermore, due to the inner magnetic field, charged particles can leave the collision vertex without penetrating the drift chamber, but entering the central spectrometer afterwards. On the other hand, the mixed event estimation of the uncorrelated background is well doable with the DC information, because all charged tracks per event are stored.

It is also possible to estimate the distribution of the uncorrelated background via a fit function applied to the distance distribution outside a certain radius around the EMCal clusters and taking into account that at zero distance there should also be no uncorrelated background. Outside that radius, it can be assumed that the distribution is composed only of uncorrelated background, therefore it can be used to obtain a reasonable background fit. This fitting method can therefore also be used with the PC3 hit information available from the DST. The condition to apply a fit for the estimation the background is of course a certain knowledge of the expected background distribution. Since in the PHENIX analysis of the 2002 data [KB04], the full mixed event method

was used, this knowledge is available, since the general picture of the charged particle veto should be the same for the different experimental runs. In this analysis and another analysis of direct photons from Cu+Cu collisions at PHENIX [Lue07], it was found that the best fit for the description of the background is a fourth-order polynomial.

The charged particle contribution to the inclusive EMCal cluster spectrum is calculated as follows. First, for each hit – i.e. for each cluster – on the EMCal, the distance of the closest charged hit in PC3 as projected onto the EMCal is calculated. This is done for each EMCal hit in all events, and for each p_T a distribution is obtained with the distance of the closest charged hit, for different centrality selections, sector combinations, and PID cuts.

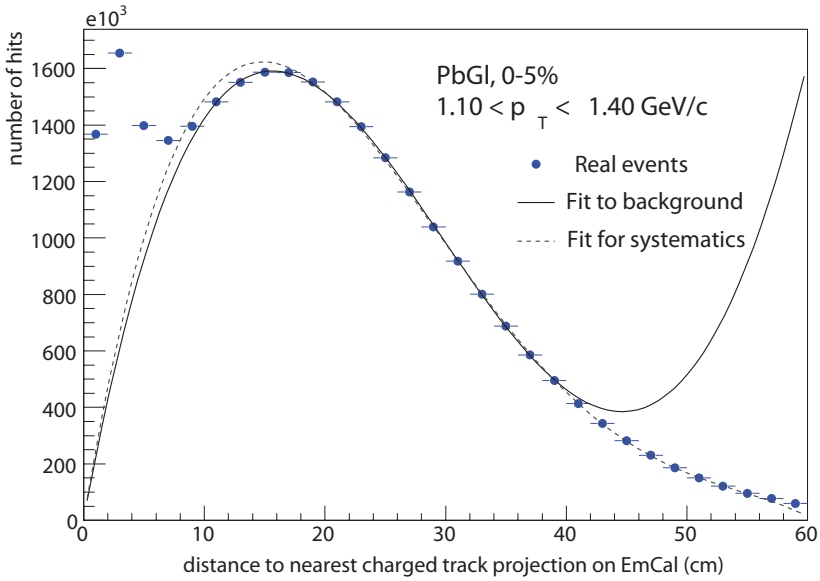

Figure 6.4: Distance of the nearest charged track to each EMCal hit with 1.1 GeV/$c \leq p_T \leq$ 1.4 GeV/c, for 0-5% most central events in the PbGl sectors for the PID 3 cut. The continuous line shows the background fit, the dashed line is the background fit used for estimating systematic uncertainties.

Such distributions are shown examplarily in Figures 6.4, and 6.5. On both pictures, two regions can be distinguished in the distribution: a peak close to zero distance, which is attributed to correlated charged hits, that means with charged hits that contribute to the cluster in the EMCal they are close to, and a distribution outside the peak, varying in shape depending on the centrality. This distribution is the background, coming from non correlated associations of a charged and a neutral particle or also from EMCal hits where the next charged cluster is further away. Both sources of background would be eliminated by event mixing, but as it is not applicable with the data structure, as mentioned above, a fit function is used to estimate the overall shape of the background both outside

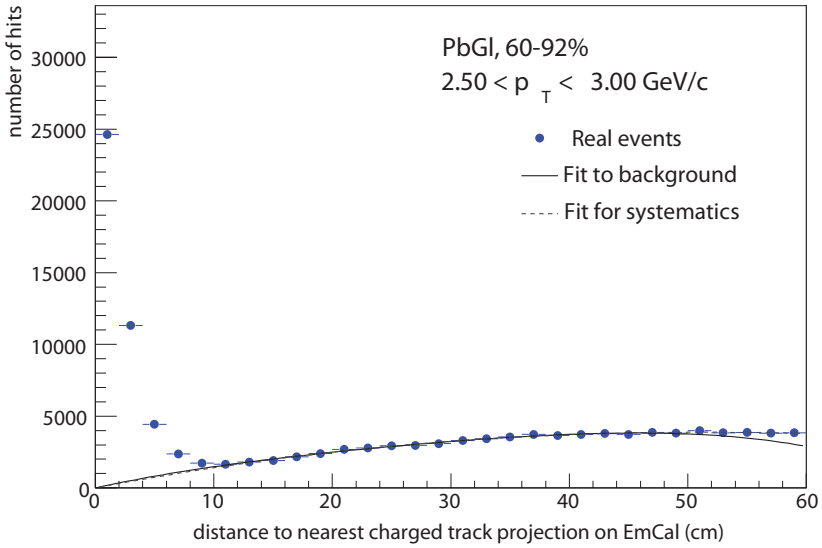

Figure 6.5: The distance of the nearest charged track to each EMCal hit with 2.5 GeV/$c \leq p_{\mathrm{T}} \leq$ 3.0 GeV/c, for 60-92% most central events in the PbSc sectors for the PID 3 cut. The continuous line shows the background fit, the dashed line is the background fit used for estimating systematic uncertainties.

and inside the correlated peak. This fit function is a fourth order polynomial with the constraint of being zero at zero distance, it is drawn in Figures 6.4, and 6.5. The fourth order polynomial was found to be the lowest order polynomial to provide an accurate description of the background distribution outside the peak region until a distance of at least $\sim$ 40 cm. The fit is applied outside the peak region, the actual fit window depends on the width of the peak and is thus different for different centrality selections or transverse momenta. The background is then subtracted and the remaining peak is integrated within a certain veto radius. To calculate the fraction of charged hits to the complete cluster spectrum, finally the ratio of the number of charged hits and the number of all hits for each p_{T} bin, centrality and PID selection is calculated. To account for systematic uncertainties of the background fit, the fit has been performed using another fit range, the resulting background parameterization is plotted in Figures 6.4, and 6.5 as dashed line.

For the correction, it has to be taken into account that the PC3 is not a perfect detector, i.e. parts of it were not operational during data taking or data was discarded during the DST production. Basically, the efficiency of the PC3 is the PC3 acceptance matched with the acceptance of the EMCal, since the intrinsic efficiency of the PC3 is assumed to be 100%. That means, that each charged particle on the active surface of the PC3 induces a signal in the detector. The method to calculate the PC3 efficiency was established in an earlier analysis [Zau07]. In short, the acceptance of the PC3 is projected onto the EMCal by looking at EMCal hits with a PC3 hit within a radius of 4 cm, the

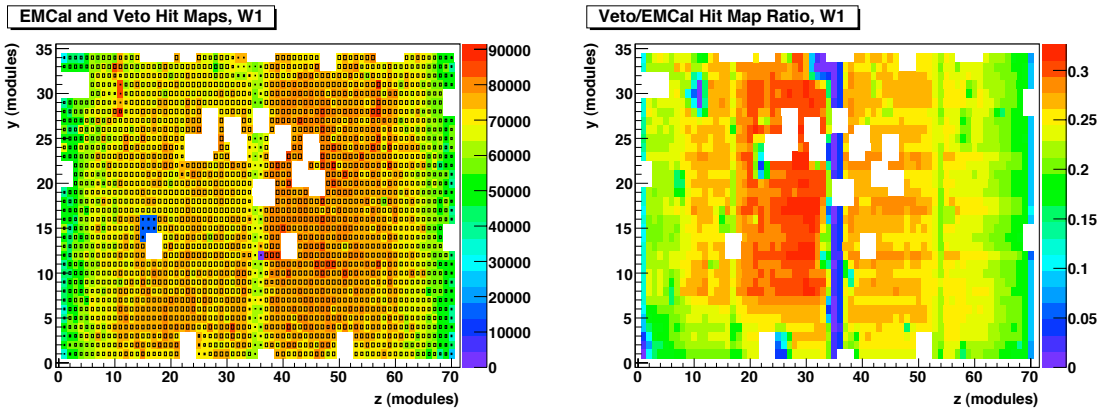

Figure 6.6: Left: EMCal hit map for sector W1 (colored boxes) and associated PC3 veto map (open boxes). White areas show towers that are not used in the analysis (dead towers). The size of the boxes represents the number of EMCal hits with an associated PC3 hit. Right: Ratio of EMCal hit map and PC3 veto map. PC3 areas with only few associated hits are blue, they are regarded as inactive in the analysis. The region in the middle is caused by the mechanical layout of the PC3 which has a gap in the middle.

approximate radius covered by a single pad. All these hits are filled into a so-called PC3 veto map. An example of such a PC3 veto map is shown as boxes in the right panel of Figure 6.6 on top of the EMCal hit map. The size of the boxes represents the number of EMCal hits with an associated PC3 hit within the aforementioned radius. In a next step, the PC3 acceptance is compared with the EMCal acceptance by comparing the PC3 veto map with the EMCal hit map for the same sector. In this ratio which is shown in the right panel of Figure 6.6, areas with significantly less PC3 hits corresponding to EMCal hits become visible. Such areas are attributed either to the structure of the PC3 or to some problems in PC3 pads. To define active and inactive PC3 regions, a cut on the ratio is defined that renders the structural gap in the middle as inactive. Furthermore, from earlier analyses [KB04, Zau07] it is expected that at least about 10% of the hits in the calorimeter are charged hits. Therefore, the cut is set to 9% to account for possible statistical fluctuations. The inactive region of the PC3 are visible in Figure 6.7 for the W1 sector.

Another method of calculating the PC3 efficiency was also used in [Zau07], in this method bad PC3 regions are not found by dividing the hit maps but by looking at the multiplicity of PC3 hits in front of each EMCal tower and by removing those regions that show significantly lower than average multiplicities in the corresponding sector. This methods leads to similar results as the aforementioned method. The uncertainties in the estimated PC3 efficiency are assumed to be 5%, the maximum difference of the two methods. Though the methods agree well, it is important to keep in mind that both provide only an estimate of the PC3 efficiency. The intrinsic PC3 efficiency, i.e. the efficiency of PC3

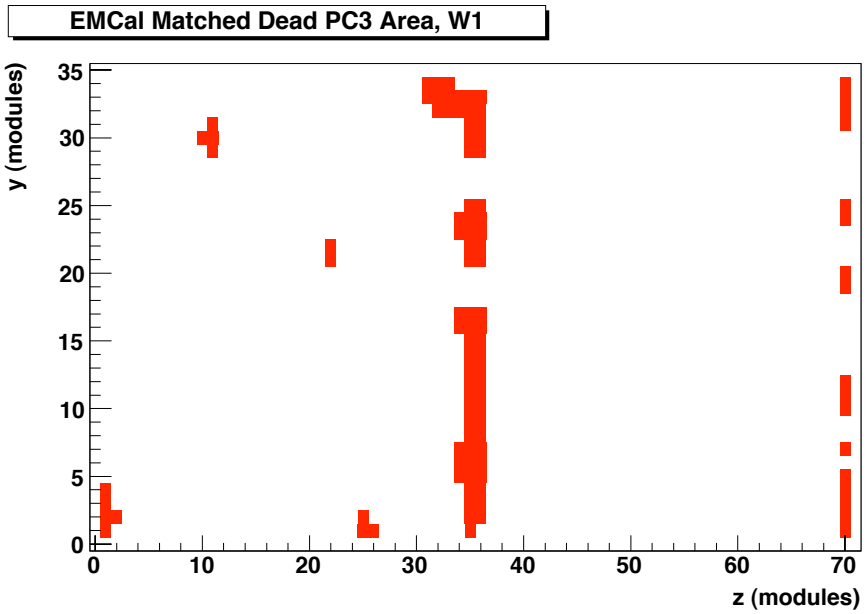

Figure 6.7: PC3 deadmap matched with the acceptance of the W1 sector. The region in the middle is caused by the mechanical structure of PC3 which has a gap in the middle. The region appears discontinuous in this plot due to bad modules in the calorimeter.

to detect a charge particle hitting its active volume, is assumed to be 100%. The PC3 efficiency $\varepsilon_{\mathrm{PC3}}$ is then used to calculate the final correction for charged particles:

$$X_{\mathrm{Ch}} = \frac{1}{\varepsilon_{\mathrm{PC3}}} \cdot \frac{N^{\mathrm{cluster}}_{\mathrm{charged}}}{N^{\mathrm{cluster}}_{\mathrm{total}}} \,, \tag{6.4}$$

with $N^{\mathrm{cluster}}_{\mathrm{charged}}$ being the number of charged clusters and $N^{\mathrm{cluster}}_{\mathrm{total}}$ being the number of all clusters projected onto the calorimeter. The charged particle correction for all centralities are shown in Figure 6.8, the results for the sample before and after applying the PID cuts are plotted for both the PbGl and the PbSc.

6.1.2 Neutrons and Anti-Neutrons

After correcting for charged particles, the remaining spectrum is still not a clean photon spectrum, it contains other neutral particles that are not removed by the aforementioned corrections, i.e. neutrons and anti-neutrons. For those, another correction has to be applied. Again this is done on a statistical basis.
The fraction of (anti-)neutrons contributing to the overall neutral cluster spectrum, i.e. after subtraction of charged particles, was already determined for Au+Au collisions in an earlier analysis [KB04]. To estimate the calorimeter's efficiency for (anti-)neutrons, these particles were simulated and embedded into real events. Afterwards, the data were

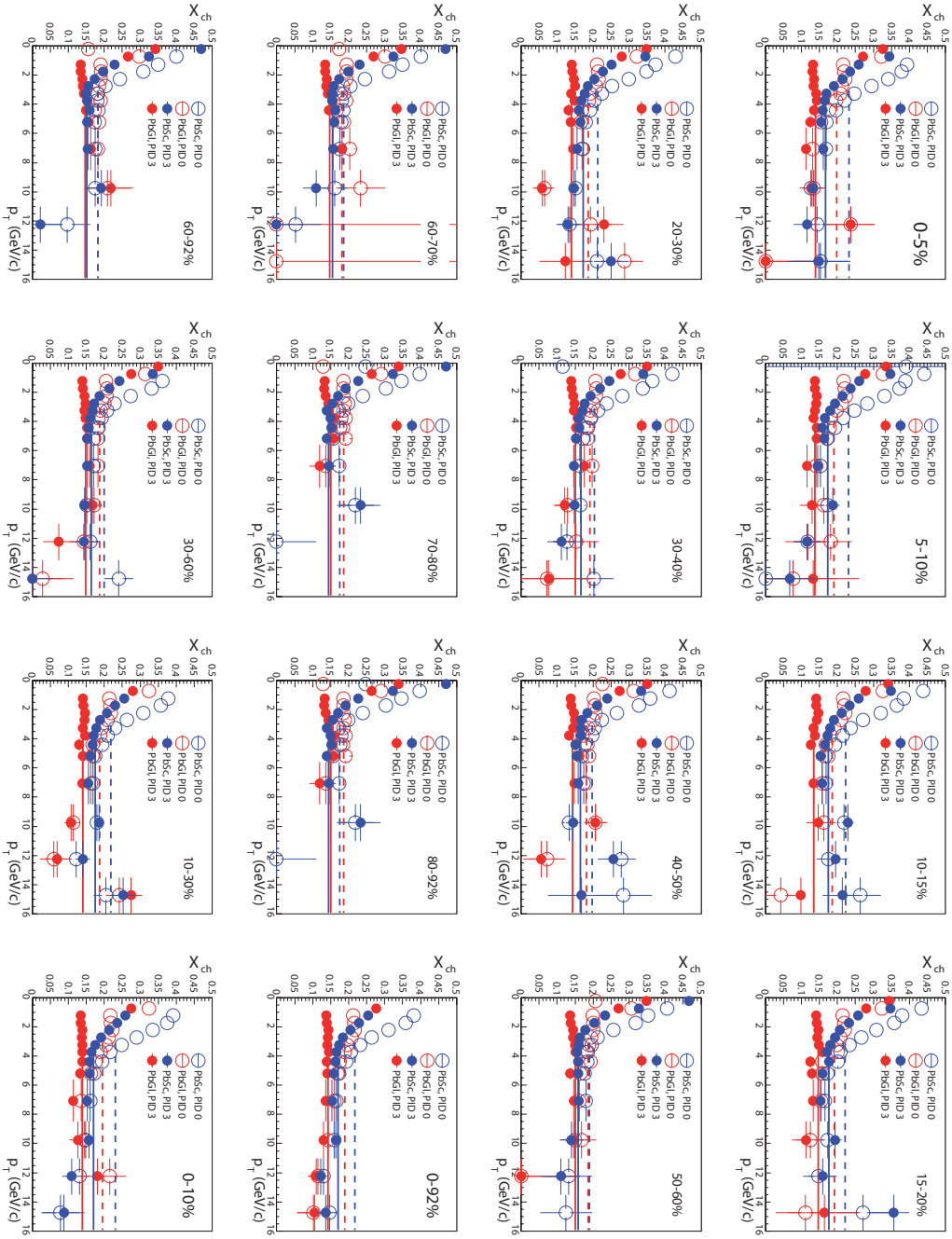

Figure 6.8: Charged particle correction X_{Ch} for all centrality classes. The open circles show the correction for PID0, the closed circles for PID3. The red data are for the PbGl, the blue data for the PbSc. The lines represent a fit for $p_{\mathrm{T}} \geq 3$ GeV/c that is used to correct at higher p_{T} .

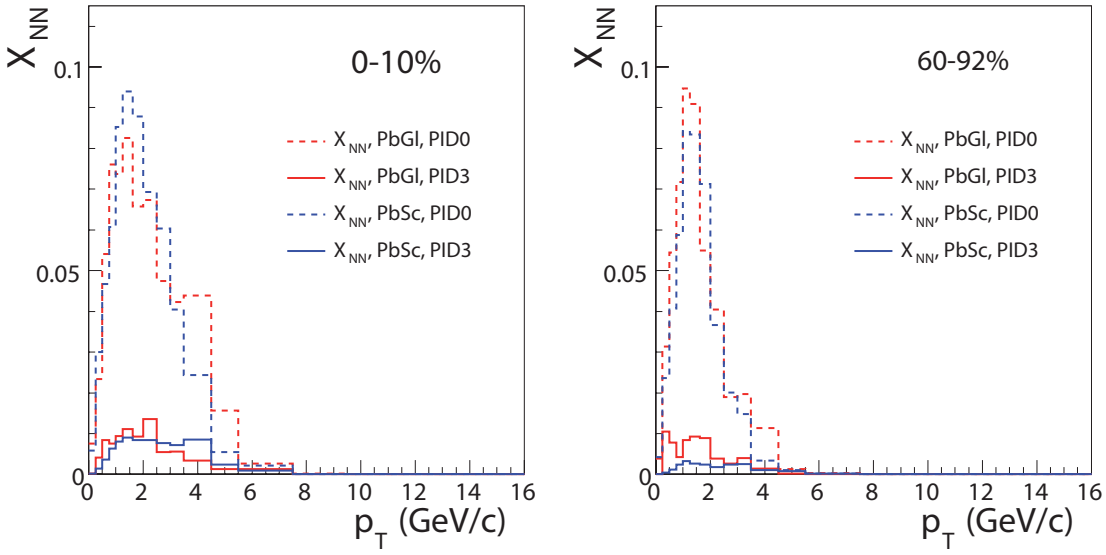

Figure 6.9: Neutral correction X_{NN} for 0-10% (left) and 60-92% (right) most central events. The dashed lines show the correction for PID0, the continuous lines for PID3. The red data are for the PbGl, the blue data for the PbSc.

analyzed within the same framework as the real data using identical analysis cuts as well. The response of the calorimeter to neutrons and anti-neutrons is calculated with the help of a GEANT [Bru93] simulation of the PHENIX experiment, the EMCal response to neutrons and anti-neutrons can then be determined with the help of the detector efficiency and the input spectrum, i.e. the spectrum of those particles produced in Au+Au collisions at PHENIX. Under the assumption of isospin independence of nucleon production in ultrarelativistic collisions, the measured proton and anti-proton spectra have been used to calculate the neutron and anti-neutron input spectra.

In order to determine the fraction of neutrons and anti-neutrons in the neutral cluster spectrum, the neutron spectrum calculated with the detector efficiency and the neutron and anti-neutron input spectrum is divided by the inclusive neutral cluster spectrum. The correction for neutral particles is shown in Figure 6.9 for both detector systems in central and in peripheral events. The correction is shown for the two cases of absence of PID cuts as well as for applying both those cuts. The PID cuts, especially the shower shape cuts in the two detectors, remove a significant fraction of the neutrons measured with the EMCal, therefore only $\approx 1-2\%$ of the particles passing the PID cuts are neutrons for all centralities.

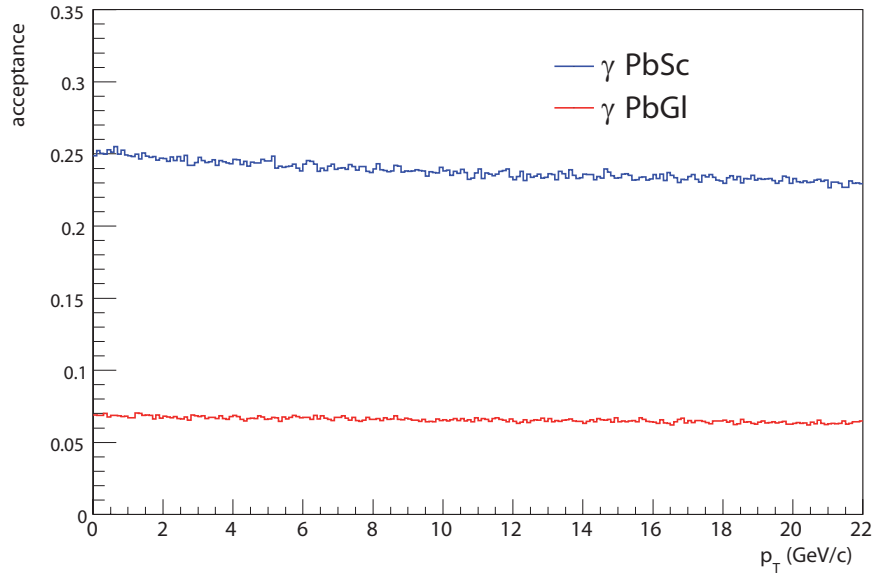

Figure 6.10: Acceptance for single photons in the PbSc (blue) and the PbGl (red).

6.1.3 Acceptance and Efficiency Corrections

Like with the neutral meson spectra, the inclusive photon spectra have to be corrected for limited detector acceptance and photon reconstruction efficiency. Therefore, the same methods as in the π^0 case were used. The acceptance for single photons is almost flat, since no decay kinematics need to be considered. Also, photons are not affected by the magnetic field near the collision vertex.

Acceptance Correction The acceptance of photons in PHENIX is calculated using the same fast Monte Carlo simulation program as the acceptance of π^0's, as described in Section 5.2.1. In short, photons are simulated over the full azimuthal range of $\Delta\phi = 2\pi$ for a transverse momentum range between 0 and 32 GeV/c and a pseudorapidity range of $|\eta < 0.45|$ using a flat vertex distribution and a Gaussian rapidity distribution with $\sigma(\eta) = 30$ cm. Thus the rapidity distribution is almost flat in the simulation range. Non-flat transverse momentum distributions are used to account for the non-flat distributions of photons in the real experiment. In order to produce a large enough sample over the whole p_T range, a flat p_T distribution is simulated. Photons are later weighted with the experimental distribution to get to the "true", non-flat distribution. The photon acceptance is the determined by the ratio of photons reaching the active detector surface and the input photon distribution. The acceptance for photons in PHENIX is mostly flat versus transverse momentum which is be expected for single non-decaying particles Only the emission angle of the particle itself plays a role for the acceptance. However, towards high transverse momenta, the acceptance decreases slightly. This is attributed to the increasing

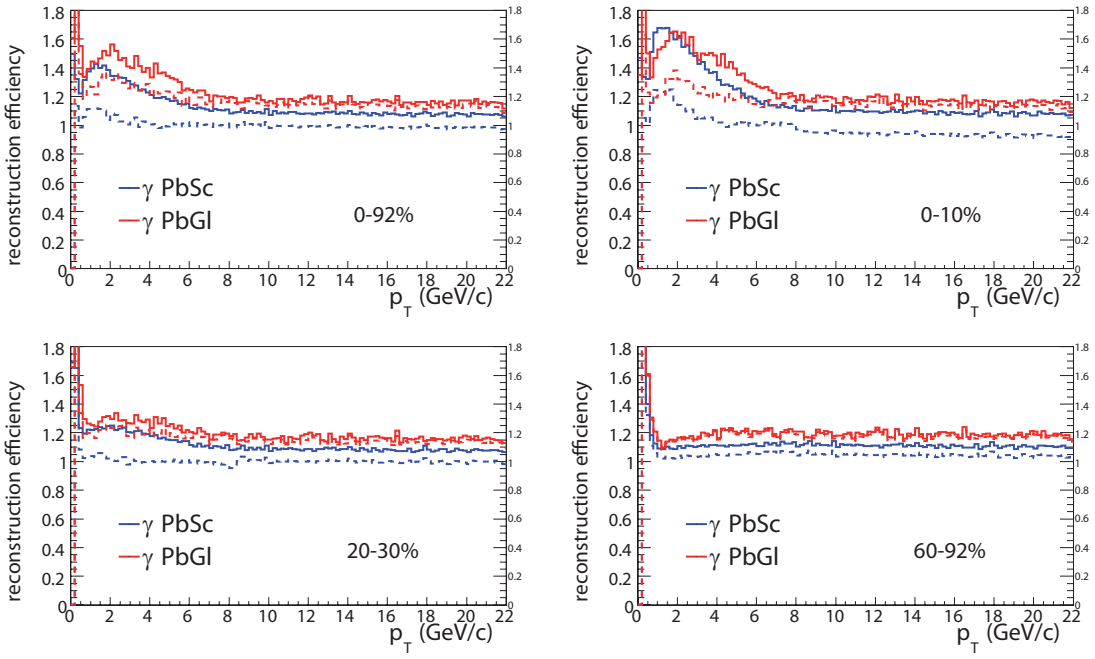

Figure 6.11: Single photon reconstruction efficiency in the PbSc (blue) and the PbGl (red), for four different centrality selections for PID0. The effect of overlapping showers in more central events is seen as an increase of the efficiency for $p_{\mathrm{T}} \leq\approx 0.2$ GeV/c, it is larger in the PbSc.

depth of electromagnetic showers at higher particle energies. It leads to leakage effects at the edges of the calorimeter, where particles have incident angles large enough that the tower with the maximum energy and the tower actually hit by the photon differ from each other, this effect is parameterized in the fast MC. The acceptance for single photons in the PbGl and in the PbSc are depicted in Figure 6.10 for minimum bias collisions. The acceptance for the PbSc is more than three times larger than the acceptance for the PbGl, for there are more towers excluded in the latter during the analysis.

Efficiency Correction The efficiency correction is again calculated with the same fast Monte Carlo simulation as above. The simulation is tuned to match the efficiency obtained by embedding simulated photons into real events and analyzing the output with the same analysis program as the real data. The procedure is described in more detail in Section 5.2.2 and is thus only summarized briefly in the following.

The photon reconstruction efficiency is calculated with the fast Monte Carlo simulation program that has been tuned already in the π^0 analysis, as described in Section 5.2.2. The same parameters for the parameterization of energy and position smearing and overlapping showers are used for photons as well. The input spectrum is the measured inclusive photon spectrum, including the correction for the merging of π^0 decay photons described

	Conversion correction factors			
	PbGl	PbSc East	PbSc West	PbSc total
inclusive γ	1.039 ± 0.01	1.029 ± 0.01	1.041 ± 0.016	1.037 ± 0.014

Table 6.1: Correction factors for the inclusive photon yield that are applied due to conversion, for different sector combinations.

later in Section 6.1.4. An iterative procedure is used to extract the true input spectrum, the iterations are stopped when the efficiency does not change anymore within small fluctuations. The functional form of the spectra can be described with the same functions as the π^0 and η spectra, the functions are discussed in Section 5.2.1.
For all photons within the detector acceptance, the energy and position information is smeared according to the parameterization, and with a certain probability, the energy of another photon is added to the reconstructed photon energy. Furthermore, it is checked whether the photon passes the PID cuts. The two different shower shape cuts are parameterized with an energy dependent probability for photons to pass the cut. The reconstruction efficiency is given by the ratio of the reconstructed photon spectrum and the input spectrum of photons into the detector acceptance:

$$\varepsilon^{\gamma}(p_T) = \frac{dN^{\gamma}/dp_{\mathrm{T}}|_{\mathrm{output}}}{dN^{\gamma}/dp_{\mathrm{T}}|_{\mathrm{input}}}\,, \tag{6.5}$$

where $dN^{\gamma}/dp_{\mathrm{T}}|_{\mathrm{output}}$ is denoting the measured photon spectrum and $dN^{\gamma}/dp_{\mathrm{T}}|_{\mathrm{input}}$ is denoting the true input spectrum of photon within the acceptance of the calorimeter.

6.1.4 Further corrections

Besides the detector acceptance and the reconstruction efficiency, other effects on the measured photon spectrum have to be accounted for. These effects include the conversion of photons in the detector material in front of the EMCal, the so-called bin shift, resulting from the steeply falling spectrum, and the contribution of neutrons and anti-neutrons to the measured spectrum.

Photon conversion The material between the collision vertex and the EMCal leads to the conversion of photons into e^+e^- pairs. The probability p_{conv} that a photon converts, depends on the material it traverses between its origin and the calorimeter. Not all conversions have to be taken into account, especially conversions occurring between PC3 and the EMCal create e^+e^- pairs that form a single cluster in the calorimeter which will be identified as a single photon with the original energy. They do not separate enough to be

removed by the shower shape cut. The conversion correction has been estimated with a PISA simulation for the PHENIX 2003 setup [Oka05]. As mentioned in Section 5.2.5, for the PbSc the aerogel detector has to be taken into account which was installed in front of the W1 sector after Run 03. It adds $\sim 20\%$ of radiation length in that one sector. This translates into a total of about 3.6% additional conversions in the west arm. Due to the small distance between the aerogel and the EMCal, the majority of the e^+e^- pairs will however be reconstructed as single clusters, therefore, the conversion probability for the west arm is increased by only 1% compared to the value in [Oka05]. The correction factors due to conversion are given in Table 6.1.

Bin-Shift Correction The bin-shift correction for the inclusive photon spectrum is carried out the same way as for π^0 and η described in Section 5.2.3.

Merging Correction As will be outlined in Section 6.2.1, the inclusive photon yields do not have to be corrected for the merging of π^0 decay photons in order to calculate the direct photons via the double ratio. However, it is useful to correct the inclusive photon spectra for merging before fitting them with the function used to calculate the single photon acceptance and efficiency. Otherwise the input spectrum in the simulation would have a wrong shape at high transverse momenta and both corrections would be calculated incorrectly. The number of π^0 decay photons $\Delta\gamma^{\text{merging}}$ is therefore calculated using the simulated γ/π^0 ratio $(\gamma/\pi^0)_{\text{sim}}$ and the merging probability for the decay photons and the measured π^0 spectrum π^0_{meas}:

$$\Delta\gamma^{\text{merging}} = \left[(\gamma/\pi^0)_{\text{sim}} - (\gamma/\pi^0)^{\text{uncorr}}_{\text{sim}}\right] \cdot \pi^0_{\text{meas}} \,. \tag{6.6}$$

$(\gamma/\pi^0)^{\text{uncorr}}_{\text{sim}}$ denotes the simulated γ/π^0 ratio without applying the merging correction. The simulation of decay photons and the correction for merging is discussed in more detail in Section 6.2. $\Delta\gamma^{\text{merging}}$ is added to the measured inclusive photon spectrum to correct for the loss of photons due to merging. The resulting inclusive photon spectrum is then used as input spectrum for the simulation.

6.1.5 Systematic Uncertainties on the Inclusive Photons

As discussed in Section 5.3, each correction implies systematic uncertainties that have to be estimated. For the analysis of inclusive photons, these uncertainties are summarized in Tables 6.2, and 6.3 for the PbGl and the PbSc, respectively.

The uncertainties from the acceptance and the efficiency correction as well as those on the energy scale have the same origin as in the π^0 and η analysis. In the acceptance case, the uncertainty is the same as the same data is used. The systematic error on the reconstruction efficiency was estimated the same way as described for the π^0 in Section 5.3.3.

p_T (GeV/c)	3	8	13	18
Centrality	0-92 % (0-10 %; 60-92 %)			
Acceptance	4.0	4.0	4.0	4.0
Efficiency	7.5 (8.4; 3.6)	6.4 (3.8; 1.5)	6.4 (3.4; 1.5)	6.4 (3.3; 1.5)
Energy scale	6.9 (7.0; 6.8)	6.4 (6.3; 6.6)	5.7 (5.7; 5.9)	5.3 (5.3; 5.5)
Nonlin. escale	1.5	5.8	6.1	6.1
Conversion corr.	1.0	1.0	1.0	1.0
Charged corr.	3.7 (4.7; 1.2)	3.7 (4.7; 1.2)	3.7 (4.7; 1.2)	3.7 (4.7; 1.2)
Neutral corr.	1.0	1.0	1.0	1.0
Total sys. error	11.8 (12.7; 9.0)	12.2 (11.3; 10.0)	12.0 (11.0; 9.7)	11.8 (10.8; 9.5)

Table 6.2: Systematic uncertainties of the inclusive photon spectra, measured with the PbGl. Each uncertainty is given for minimum bias, and additionally for central and for peripheral events if there is a centrality dependence. All uncertainties are given in %.

p_T (GeV/c)	3	8	13	18
Centrality	0-92 % (0-10 %; 60-92 %)			
Acceptance	2.5	2.5	2.5	2.5
Efficiency	9.3 (11.7; 5.5)	5.3 (5.2; 4.3)	5.3 (4.7; 4.3)	5.3 (4.6; 4.3)
Energy scale	6.9 (7.0; 6.8)	6.4 (6.3; 6.6)	5.7 (5.7; 5.9)	5.3 (5.3; 5.5)
Nonlin. escale	1.5	5.8	6.1	6.1
Conversion corr.	1.4	1.4	1.4	1.4
Charged corr.	3.7 (4.7; 1.2)	3.7 (4.7; 1.2)	3.7 (4.7; 1.2)	3.7 (4.7; 1.2)
Neutral corr.	1.0	1.0	1.0	1.0
Total sys. error	12.6 (14.8; 9.4)	11.2 (11.5; 10.3)	11.0 (11.1; 10.1)	10.8 (10.9; 9.9)

Table 6.3: Systematic uncertainties of the inclusive photon spectra, measured with the PbSc. Each uncertainty is given for minimum bias, and additionally for central and for peripheral events if there is a centrality dependence. All uncertainties are given in %.

The different contributions to this uncertainty in the inclusive photon case are depicted in Figure 6.12. The total systematic uncertainty of the photon reconstruction efficiency is dominated by the PID efficiency uncertainty.

The energy calibration in the π^0, η, and inclusive photon analyses is the same, thus the uncertainty of the energy calibration or the energy scale itself is also the same. However, the uncertainty in the yield depends also on the shape of the yield itself. Hence the global energy scale uncertainty is slightly different for all three particles. In addition it shows a small centrality dependence. The uncertainty of the conversion correction has already been mentioned in Section 6.1.4.

Charged and Neutral Particle Background There are two sources for the uncertainty of the charged particle correction. First, the efficiency of the Pad Chamber has to be estimated. This has been done using different methods, the difference of the results from these methods gives an estimate of the uncertainty of the PC3 efficiency which is $\sim 5\%$. Second, the background from uncorrelated matches between EMCal and PC3 hits is hard to estimate, for the PC3 information is incomplete in the DSTs. The uncertainty of the background estimate is derived by using different fit ranges. The fit remains much more stable in peripheral events, therefore the uncertainty of the charged background shows a strong centrality dependence.
Most neutral hadrons (neutrons and anti-neutrons) do not pass the cuts on the shower shape, thus the correction for neutral particles is only about 1-2% itself. An overall uncertainty of 1% is therefore considered to provide a safe estimate for this correction, as shown in [Zau07].

All systematic uncertainties are finally added in quadrature to obtain the total systematic uncertainty of the inclusive photon spectra. The different corrections are assumed to be uncorrelated. This assumption is the safest estimate for the true correlation. The uncertainties are shown for three different centrality selections in Figures 6.13, and 6.14, for the PbGl and the PbSc, respectively.

6.1.6 Inclusive Photon Yields

Inclusive photon yields are extracted from the data for the PbGl and the PbSc independently. They are shown for both detectors in Figure 6.15 for 11 different centrality selections and minimum bias collisions. The measurements of the two detectors can be compared and should agree within systematic uncertainties. This comparison is shown in Figure 6.16, the two data sets agree within the systematic uncertainties.

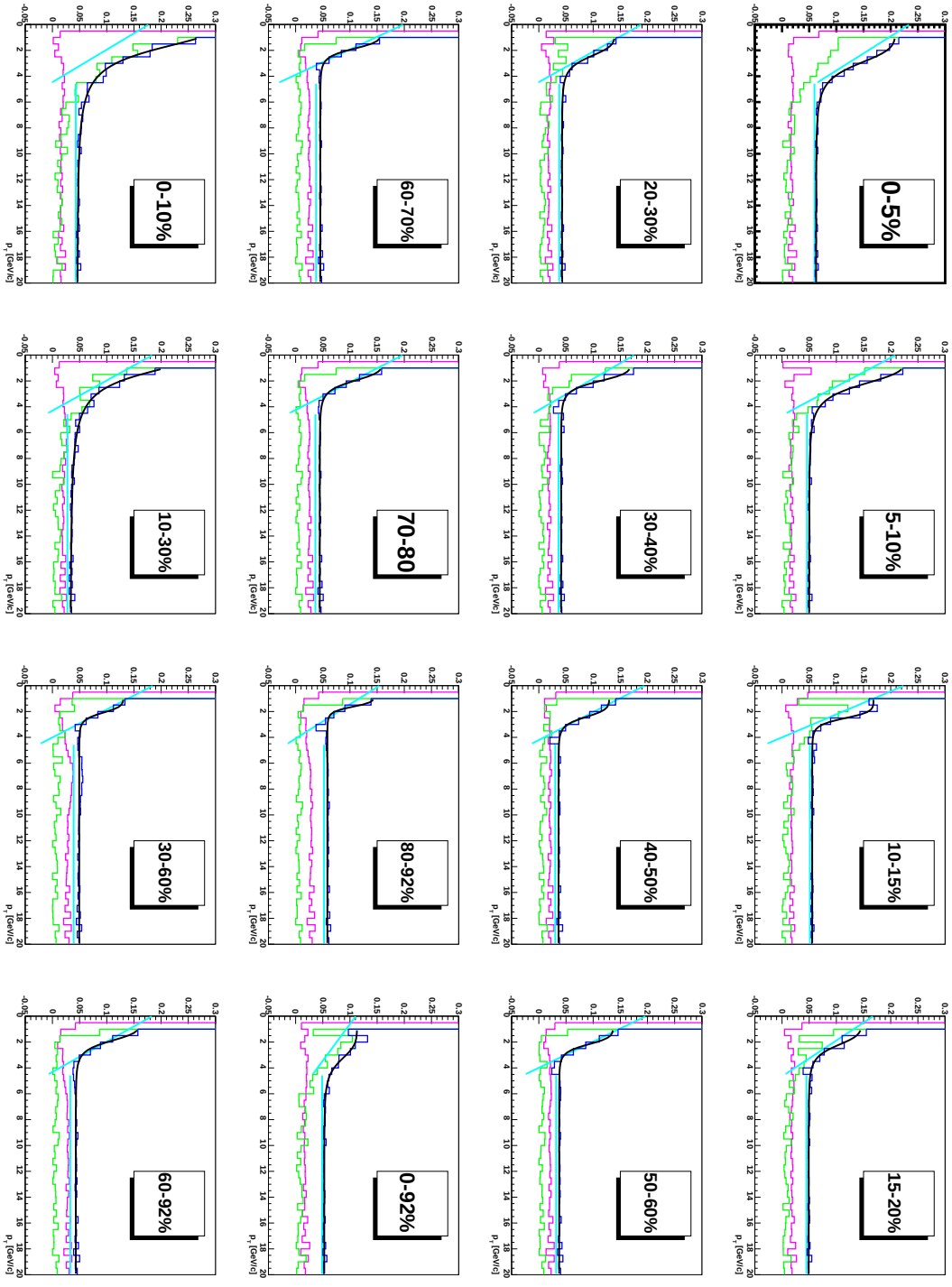

Figure 6.12: Inclusive photon systematic uncertainty due to the efficiency calculation. The different sources (pink: energy smearing parameterization, green: shower overlap parameterization, light blue: PID efficiency) are added quadratically (dark blue), the sum of the uncertainties is fit with a function (black).

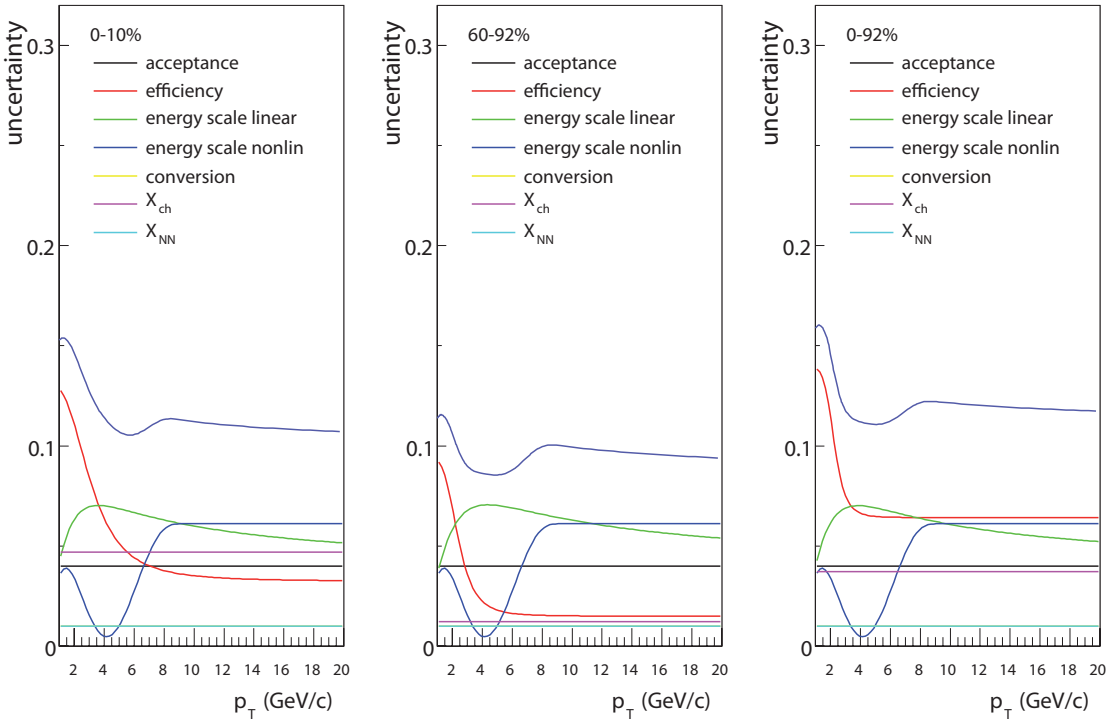

Figure 6.13: Different sources of so-called "type B" systematic uncertainties for the inclusive spectrum with the PbGl. The uncertainties from different sources are added quadratically to obtain the total systematic uncertainty.

6.2 Determination of the Direct-Photon Spectra

With the measured inclusive photon spectrum and the help of the measured neutral pion spectrum, it is now possible to calculate the direct-photon yield. Therefore the decay photons of different mesons such as π^0 and η have to be estimated. Again, this is done in a simulation. The direct-photon yield is then calculated with the help of the aforementioned so-called double ratio.

6.2.1 Simulation of the Decay Photons

The decay photons are simulated using the same fast Monte-Carlo program that is used for the acceptance and efficiency calculation, i.e. the same detector geometry can be used also for the decay photon simulation. The decay photons from all relevant mesons (π^0, η, ω, η', and K^0_S) are calculated on the basis of the π^0 decay photons and the assumption of m_T-scaling [Bou76]. The experimental results from PHENIX strongly support the assumption of m_T-scaling in $p+p$ collisions [Ada09], this is shown in Figure 6.17.

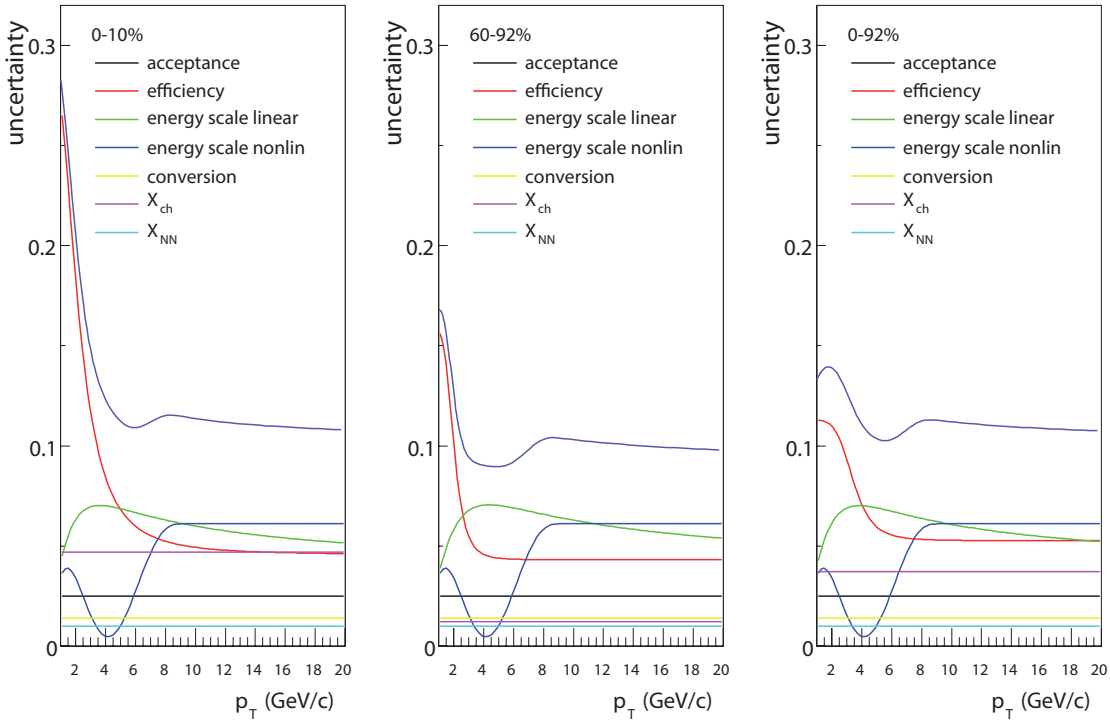

Figure 6.14: Different sources of so-called "type B" systematic uncertainties for the inclusive spectrum with the PbSc. The uncertainties from different sources are added quadratically to obtain the total systematic uncertainty.

The shape of all measured meson spectra (K, η, ω, J/ψ)agrees extremely well with the m_T-scaled π spectrum. The input to the simulation is a parameterization of the measured π^0 spectrum. The simulation is performed for each centrality selection. The Monte-Carlo program simulates neutral pions with a p_T and vertex distribution equal to the distributions of single photons used for the acceptance and efficiency calculations, but to account for all π^0 decay photons, the rapidity distribution is extended beyond the usual $|\eta| < 0.45$ to $|\eta| < 1.0$ as also π^0's with larger (pseudo)rapidities than $|\eta| < 0.45$ can decay such that one decay photon hits the EMCal. All simulated π^0's are decayed according to the branching ratios for the different decays and it is checked for decay photons whether they hit the calorimeter or not. All photons on the calorimeter are stored, weighed with the p_T of the input pion, according to the measured transverse momentum distribution of the π^0.

The decay photon spectra for the other mesons are then calculated from the π^0 spectrum with the help of m_T-scaling, using one constant scaling factor with respect to the π^0 spectrum for each meson, and by applying the according particle decays in the

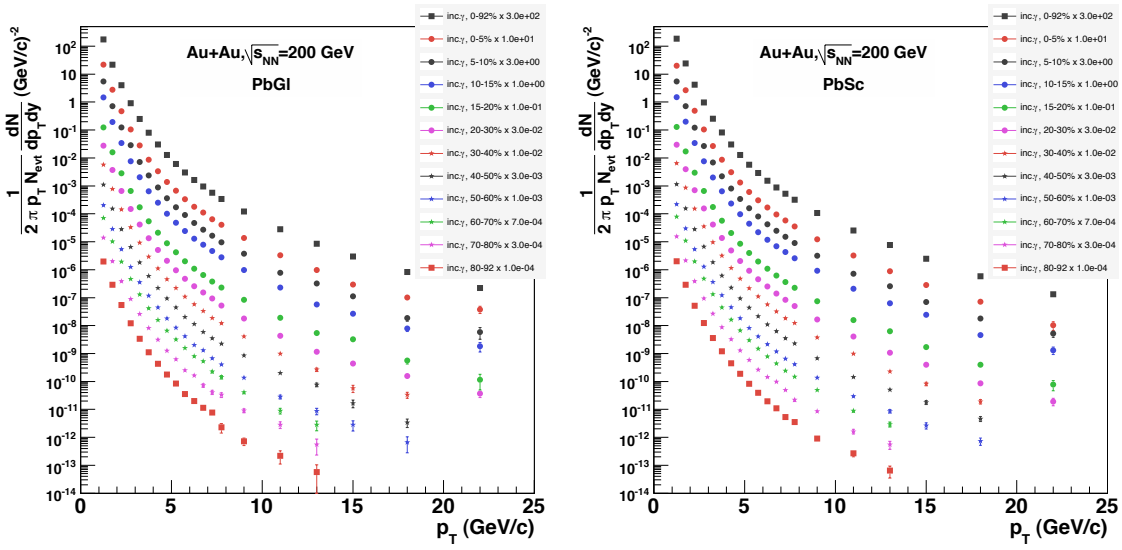

Figure 6.15: Inclusive photon spectra for 11 different centrality selections and minimum bias, measured in Au+Au collisions at $\sqrt{s_{NN}}$ = 200 GeV. The error bars denote statistical errors. Left: measurement with the PbGl calorimeter. Right: measurement with the PbSc calorimeter.

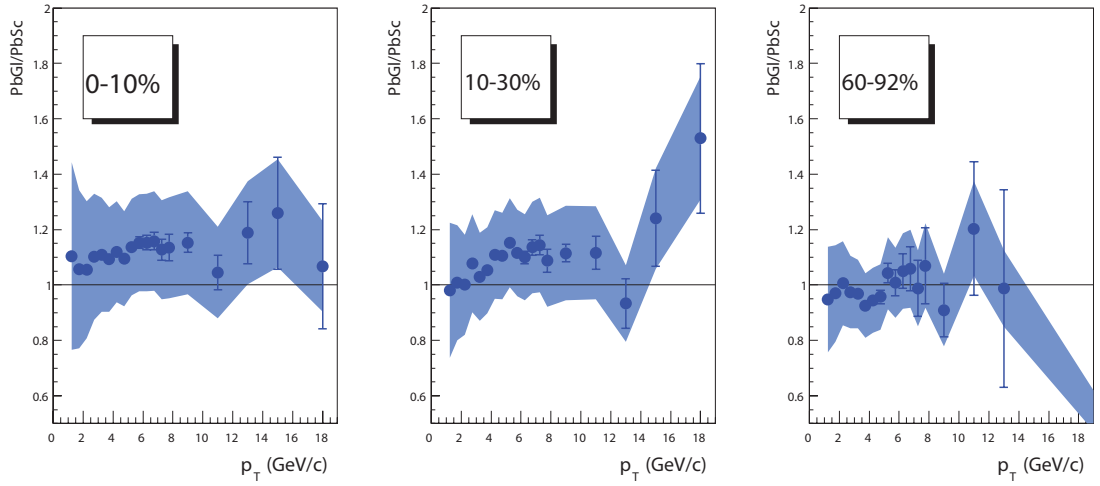

Figure 6.16: Ratio of the inclusive photon yield measured with the PbGl and measured with the PbSc for three different centrality selections. The error bars show the statistical uncertainty, the shaded area depicts the quadratic sum of the systematic uncertainties of the two measurements.

simulation. The scaling factors have been measured by PHENIX in the case of η and ω. Besides the m_T-scaling of the meson spectra, the branching ratio for decays with photons in the end channel have to be considered as well. As mentioned in Section 5, the branching ratios for the two-photon decays of π^0 and η are (98.798 ± 0.032) % and (39.31 ± 0.20) %, respectively. These two decays account for most of the decay

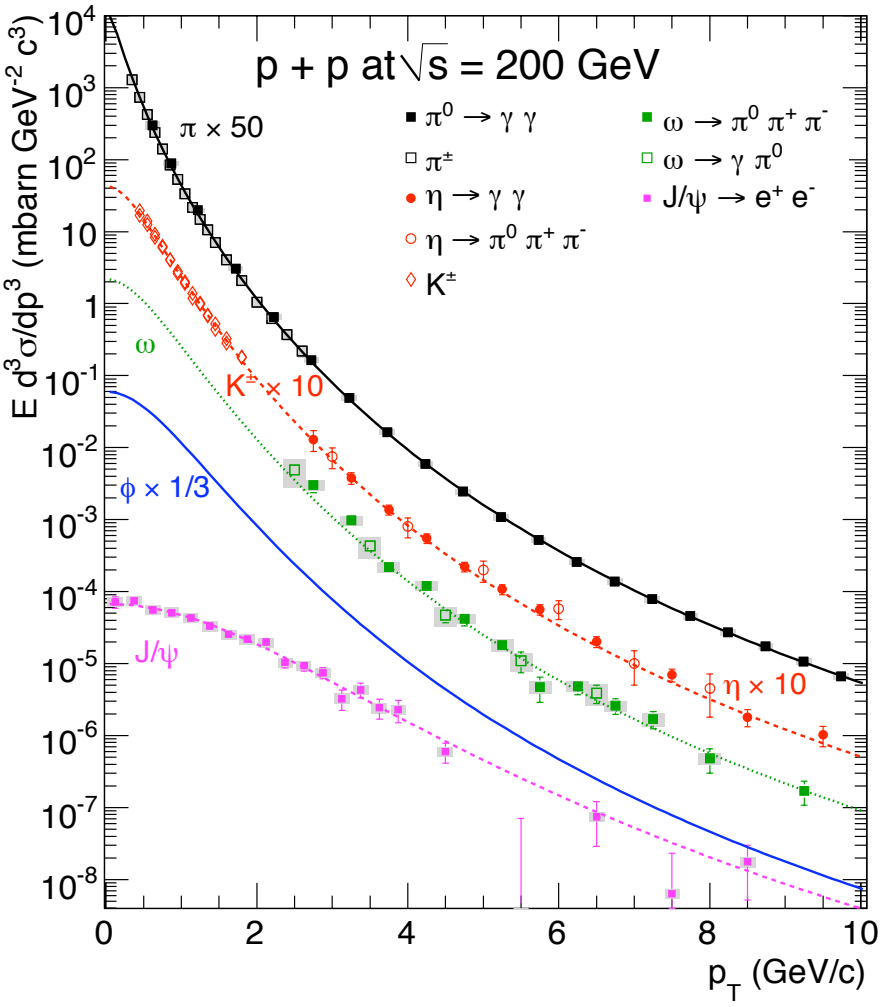

Figure 6.17: Invariant cross sections for different mesons measured with PHENIX in $p+p$ collisions at $\sqrt{s}$ = 200 GeV. The different lines are parameterizations for each meson species, based on m_T scaling of the parameterized πspectrum. [Ada09]

photon background, other non negligible photonic decays of these two mesons are the π^0 Dalitz decay into $e^+e^-\gamma$, and the η decay into $\pi^+\pi^-\gamma$. The other included mesons contribute to the inclusive photons by the following decay channels: The ω has a decay into $\pi^0\gamma$ with a branching ratio of (8.92 ± 0.24) %, the η' decays into $\rho^0\gamma$ with a probability of (29.4 ± 0.9) %, into $\omega\gamma$ with (3.02 ± 0.31) %, and into two photons with (2.10 ± 0.12) %. In the case of the K^0_S, there are no significant decay channels with photons emerging, however due to its relatively long lifetime some of the π^0's from the $K^0_S \rightarrow \pi^0\pi^0$ decay cannot be reconstructed as π^0's, leading to additional non direct and non π^0 photons in the measured inclusive spectrum. In the calculation, it is considered that some of the π^0's from K^0_S decays can be reconstructed, especially at lower K^0_S

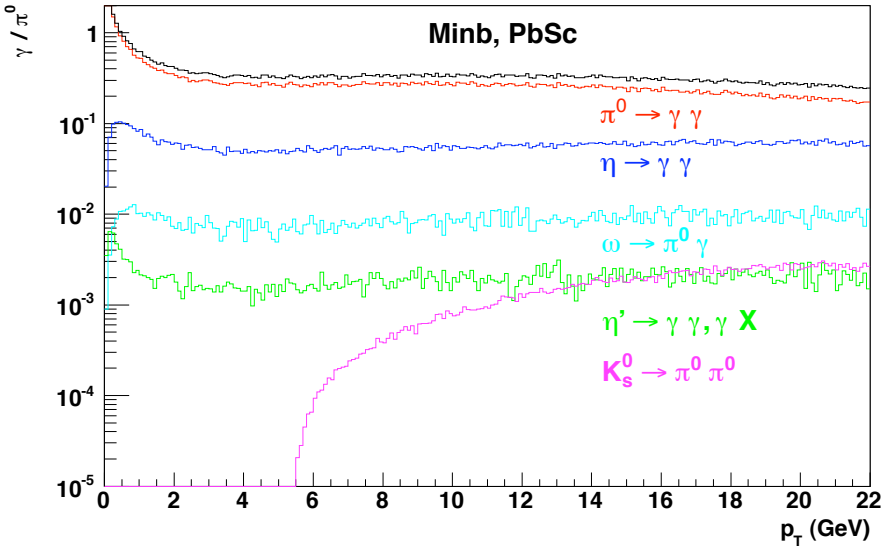

Figure 6.18: Ratio $\gamma_{\text{decay}}/\pi^0$ for decay photons of different mesons (colored lines) and for the sum of all decay photons (black line), for minimum bias Au+Au collisions, for the PbSc.

transverse momenta. This reduces the decay photon contribution from K^0_S decays [KB04].

The $\gamma_{\text{decay}}/\pi^0$ ratios for the different mesons are shown in Figure 6.18, for minimum bias collisions, with the PbSc. The dominant contribution to the overall decay photons are those from π^0's, η's also contribute significantly to the overall decay photons while all other meson's contribute less than 5 %. The merging for π^0 decay photons is accounted for, as described in the following. This leads to a decrease of the $\gamma_{\text{decay}}/\pi^0$ ratio at high p_{T}.

Merging of π^0 Decay Photons As discussed in Section 5.2.4, the showers of π^0 decay photons in the EMCal can merge into a single cluster at high π^0 transverse momenta. This merging needs to be accounted for in the direct-photon analysis. It can either be corrected for while obtaining the inclusive photon spectrum, or it can be taken into account when simulating the decay photons. The more straightforward one is to correct the decay photon simulation for the merging effect. In this case, no prior knowledge of the original fraction of π^0 decay photons within the overall photon sample is required. In this analysis, this second method has been used. In the following, it is shown that it leads to the same result as the method correcting the inclusive photon spectrum.

Direct photons are defined as all non-decay photons, therefore $\gamma_{\text{direct}} = \gamma_{\text{incl}} - \gamma_{\text{decay}}$. When the merging of π^0 decay photons is not corrected for in both the inclusive and

the decay photons, the same number of photons is lost in both samples, and therefore $\gamma_{\text{direct}} = \gamma_{\text{incl}}^{\text{merged}} - \gamma_{\text{decay}}^{\text{merged}}$. Here, as in the following, $\gamma_{\text{xy}}^{\text{merged}}$ denotes photon samples that are uncorrected for merging. This can now be used to calculate the direct photons via the double ratio again:

$$\begin{aligned}\gamma_{\text{direct}} = \gamma_{\text{inclusive}}^{\text{merged}} - \gamma_{\text{decay}}^{\text{merged}} &= \gamma_{\text{inclusive}}^{\text{merged}} - \frac{\gamma_{\text{decay}}^{\text{merged}} \cdot \gamma_{\text{inclusive}}^{\text{merged}}}{\gamma_{\text{inclusive}}^{\text{merged}}} \\ = (1 - \frac{\gamma_{\text{decay}}^{\text{merged}}}{\gamma_{\text{inclusive}}^{\text{merged}}})\gamma_{\text{inclusive}}^{\text{merged}} &= (1 - \frac{\frac{\gamma_{\text{decay}}^{\text{merged}}}{\pi^0}}{\frac{\gamma_{\text{inclusive}}^{\text{merged}}}{\pi^0}})\gamma_{\text{inclusive}}^{\text{merged}} \\ &= (1 - \frac{1}{\frac{\gamma_{\text{inclusive}}^{\text{merged}}/\pi^0}{\gamma_{\text{decay}}^{\text{merged}}/\pi^0}})\gamma_{\text{inclusive}}^{\text{merged}} \end{aligned} \tag{6.7}$$

$$\gamma_{\text{direct}} = (1 - \frac{1}{R'})\gamma_{\text{inclusive}}^{\text{merged}} \tag{6.8}$$

Therefore, in the decay photon simulation, two cases have to be considered. The first case is that either one or no decay photon hits the detector. In this case, merging cannot occur and no correction needs to be applied. In the other case, when both decay photons hit the calorimeter, they can merge into a single cluster. Since the fast MC simulation does not include clusters, a probability of merging was calculated, merged clusters are then removed from the decay photon distribution where both photons hit the calorimeter, on the base of this merging probability. The merging probability is calculated the same way as for the π^0 analysis, as outlined in Section 5.2.4.

6.2.2 The Double Ratio

In order to calculate the double ratio, two γ/π^0 ratios need to be calculated (see Equation 6.1), the ratio of measured inclusive photons and the measured π^0 spectrum, and the ratio of the simulated decay photons from the different mesons and the input π^0 spectrum which is equivalent to the measured π^0 spectrum, but with a different normalization. This difference in the normalization, however, already cancels in the decay photon to π^0 ratio.

Strictly spoken, the method used in this thesis does not calculate the ratio $\gamma_{\text{inclusive}}/\pi^0$, since inclusive photons are not corrected for merging. One could apply this correction, however, it requires prior knowledge of the fraction of π^0 decay photons in the whole photon sample. As mentioned earlier, the merging correction is applied to the π^0 decay photons from the simulation. This can be seen in the ratio of decay photons and π^0's

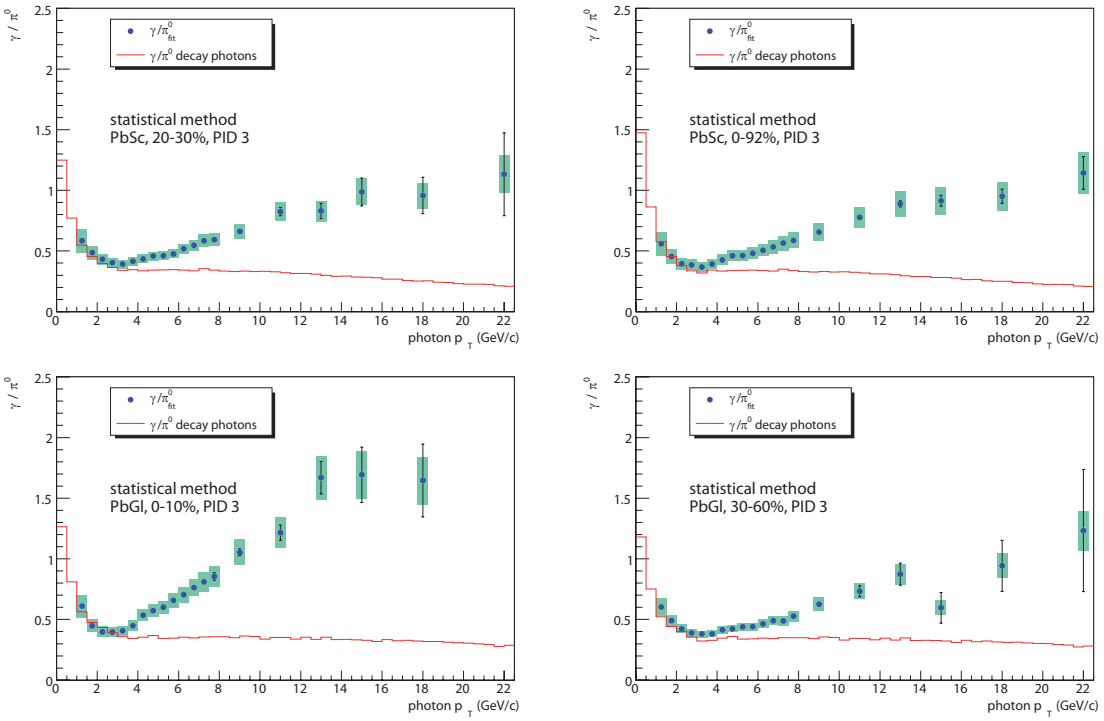

Figure 6.19: γ/π^0 ratios for the measured, fully-corrected data (blue points) and from the decay photon simulation (red line). The error bars denote the statistical, point-to-point uncorrelated uncertainties of the measurement, the green boxes show the systematic, p_T correlated uncertainties. The top row shows two different centralities (left: 20-30 %, right: 0-92 %), measured with the PbSc, the bottom row shows two centrality selections (left: 0-10 %, right: 30-60 %), measured with the PbGl.

already, due to merging it diminishes towards higher p_T. Actually, an approximation of this ratio can be calculated analytically; as almost only π^0 and η decay photons contribute, it is about

$$1.18 \cdot 2/(n-1) \tag{6.9}$$

at high p_T. For π^0 decay photons, assuming a pure power law A/p_T^n, for the π^0 spectrum at high p_T, the ratio of $\gamma^{\pi^0}_{\text{decay}}/\pi^0$ can be derived analytically as $2/(n-1)$ [Tan04], the factor 1.18 includes the η decay photons and derives from the measured η/π^0 ratio of about 0.45 and the respective two photon branching ratio of the η of about 0.40.

Some examples of the γ/π^0 ratios are shown in Figure 6.19. In this figure, the effect of merging π^0 decay photons is represented by the drop of the simulated γ/π^0 ratio at high p_T, this drop is more pronounced in the coarser granulated PbSc. Furthermore, the plot also makes visible the imperfection of the π^0 parameterization, which expresses

itself in a certain non-flatness of the simulated γ/π^0 ratio.

The double ratio is then the ratio of γ/π^0 in data and γ/π^0 in the decay photon simulation. A double ratio above unity indicates the presence of direct photons, while a double ratio of unity means that only decay photons contribute to the measured photon spectrum. Values below unity are unphysical. They are the result of the statistical and systematic uncertainties. A direct-photon signal can be considered significant if the uncertainties are smaller than the excess above unity.

The double ratio is shown in Figure 6.20 for the PbGl, and in Figure 6.21 for the PbSc. The plot also includes the expectation from a binary-scaled NLO pQCD calculation [Gor93, Vog04, KB04], using a scale of $\mu = p_{\mathrm{T}}$. These curves are different for the two detectors, since they are calculated using the measured π^0 spectra from the respective detector, using the theoretical prediction as numerator and the measured π^0 as denominator.

Systematic Uncertainties on γ/π^0

In this analysis, direct photons are measured with the so-called subtraction method, using the γ/π^0 ratio to cancel some of the common systematic uncertainties of the measurements of the two particles. Therefore, the systematic uncertainties of the measured γ/π^0 ratio cannot be regarded as the quadratic sum of the uncertainties of the two particle measurements. Some uncertainties, however, do not cancel at all. They are unique for both the π^0 or the inclusive γ measurement. These uncertainties are associated with the π^0 peak extraction and from the π^0 decay photon merging at high p_{T}, as well as those from the estimation of the charged and neutral backgrounds in the inclusive photon analysis. These uncertainties are already explained in Sections 5.3, and 6.1.5, for the π^0 and the inclusive photons, respectively.

The **energy scale uncertainty** for π^0's and inclusive photons is strongly correlated, however, due to the different shapes of the spectra, it does not completely cancel. The uncertainty can be written as $\varepsilon = f_\gamma(1.01 \cdot p_{\mathrm{T}})/f_{\pi^0}(1.01 \cdot p_{\mathrm{T}}) - f_\gamma(p_{\mathrm{T}})/f_{\pi^0}(p_{\mathrm{T}})$, with $f_\gamma(\cdot p_{\mathrm{T}}), f_{\pi^0}(\cdot p_{\mathrm{T}})$ as functions describing the spectral shape of the particle spectra, respectively. The uncertainty due to the nonlinearity in the energy scale is calculated assuming that this uncertainty is uncorrelated between the π^0's and the inclusive photons. This is the safest estimate for an unknown true correlation, but it is known that the uncertainty is different for the two particles at the same transverse momentum since a given π^0 is reconstructed from photons at different transverse momenta. Hence, this uncertainty is

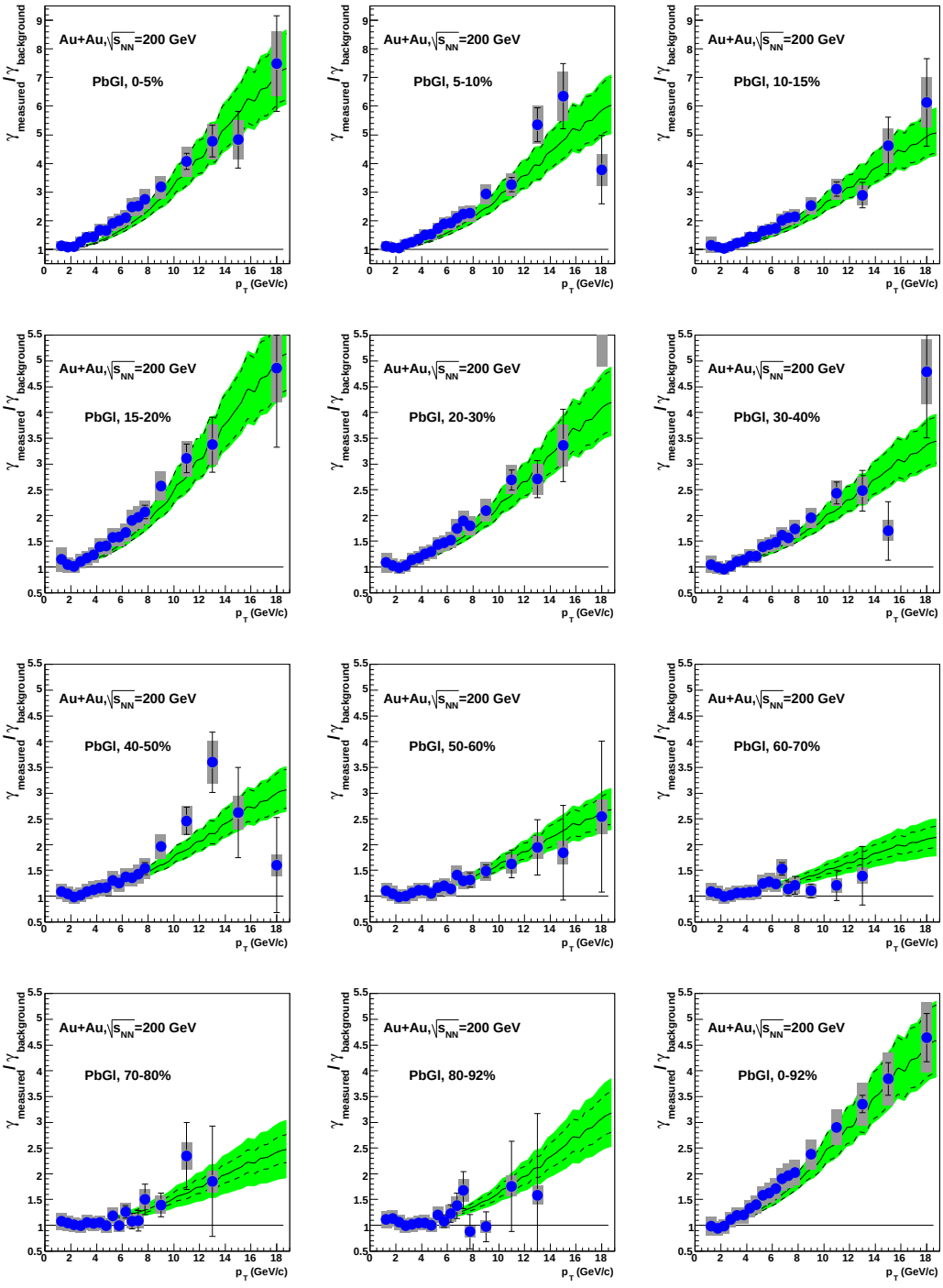

Figure 6.20: Double ratio for photons in Au+Au collisions, measured with the PbGl, for 11 different centrality selections and minimum bias. The uncertainties are plotted as in Figure 6.19. The line is an NLO pQCD calculation [Gor93, Vog04, KB04], multiplied by the number of binary nucleon-nucleon collisions N_{coll}, with the scale $\mu = p_{\mathrm{T}}$, the dashed lines have different scale parameters ($\mu = \frac{p_{\mathrm{T}}}{2}$, $\mu = 2p_{\mathrm{T}}$) to account for systematic uncertainties of the theory. The green band also includes the uncertainty of N_{coll}.

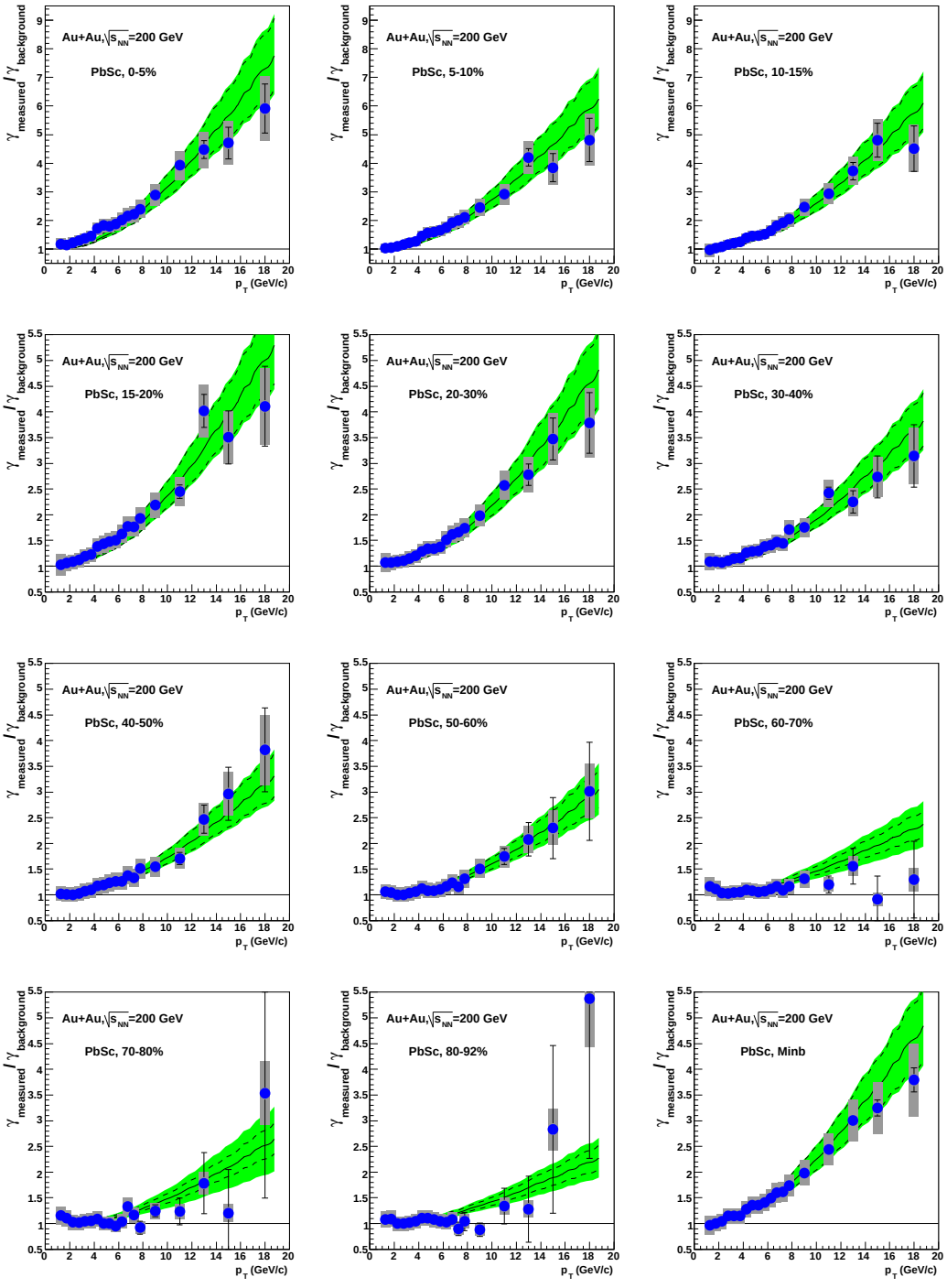

Figure 6.21: Double ratio for photons in Au+Au collisions, measured with the PbSc, for 11 different centrality selections and minimum bias. The uncertainties are plotted as in Figure 6.19. The line is a pQCD calculation [Gor93, Vog04, KB04], multiplied by the number of binary nucleon-nucleon collisions N_{coll}, with the scale $\mu = p_{\mathrm{T}}$, the dashed lines have different scale parameters ($\mu = \frac{p_{\mathrm{T}}}{2}$, $\mu = 2p_{\mathrm{T}}$) to account for systematic uncertainties of the theory. The green band also includes the uncertainty of N_{coll}.

calculated by adding the respective uncertainties of the two particles quadratrically.

Estimating the uncertainty of the **efficiency** is a little more complicated. It depends on both the PID cuts and the simulation of the detector response. As mentioned earlier, three contributions add up to this uncertainty: the uncertainties in the detector's energy smearing, the uncertainty in the parameterization of the shower overlap at higher multiplicities, and the uncertainty due to the PID cuts. For the first two contributions, the efficiencies for π^0's and γ's are recalculated using a different smearing or a different shower overlap probability, respectively. The smearing is changed such that the π^0 peak widths from the measurement and the simulation are still in fair agreement. The γ/π^0 ratio is then calculated for the new efficiency correction and compared to the original ratio to get the uncertainty. Furthermore, the γ/π^0 ratio is compared for the different PID cuts in order to derive the uncertainty due to those cuts. The contributions are finally added in quadrature to derive the overall systematic uncertainty of the efficiency correction.

The decay photon simulation also leads to systematic uncertainties. First, an uncertainty of the used hadron/π^0 ratios from m_{T}-scaling has to be taken into account. This uncertainty was already discussed in [Zau07], its main source is the uncertainty of the η/π^0 ratio, since the contribution of other mesons such as ω or η' to the decay photon cocktail is very small. The uncertainty is about 3 %. The decay photon simulation also depends on the parameterization of the π^0 spectrum used as input to the simulation. Though the parameterization is in principle well known – being exponential at low p_{T}, and a power law at high p_{T} –, especially the transition region between the two functional forms is causing some residual uncertainty of the $\gamma_{\mathrm{decay}}/\pi^0$ ratio. This is accounted for by introducing a Gaussian shaped uncertainty around the transition region. In peripheral events, larger statistical uncertainties furthermore constrain the power of the spectrum worse than in central events, also leading to a larger uncertainty of the $\gamma_{\mathrm{decay}}/\pi^0$ ratio, an effect that can be directly derived from Equation 6.9. Another uncertainty concerning the decay photon background has to be considered due to the inclusion of merged π^0 decay photons. This uncertainty was already discussed in Section 5.3.

6.2.3 Direct-Photon Yield

The direct-photon yields for the different centrality selections can finally be calculated with the double ratio and the inclusive photon spectrum, according to Equations 6.2, and 6.8. As mentioned earlier, in this work, the direct photons have been calculated using Equation 6.8, i.e. using the inclusive photons without the merging correction.

Error type	4.5-5.0 GeV		8-10 GeV		14-16 GeV		type
Peak extraction	7.6%	7.2%	2.5%	2.4%	1.1%	1.0%	B
π^0 merging	0%	0%	0%	0%	0.9%	0.9%	B
π^0 fit	8.7%	8.2%	3.2%	3.0%	1.4%	1.3%	B
Efficiency	24.7%	24.6%	11.8%	11.7%	8.1%	8.1%	B
Global energy scale	8.8%	9.0%	7.3%	7.4%	6.0%	6.0%	B
Non-linearity	8.8%	8.5%	12.4%	12.4%	9.8%	9.67%	B
Acceptance	3.9%	3.9%	3.0%	3.0%	2.7%	2.7%	B
γ conversion	7.0%	7.0%	3.5%	3.4%	2.3%	2.3%	B
Charged background	14.2%	14.2%	7.5%	7.5%	5.4%	5.4%	B
γ shower merging	0.6%	0.6%	2.1%	2.0%	4.0%	3.4%	B
Hadron/π^0	21.3%	18.5%	5.2%	4.7%	2.1%	1.9%	B
Total	40.4%	38.7%	21.8%	21.6%	16.3%	16%	B

Table 6.4: Systematic uncertainties of the direct-photon yield, measured with the PbSc, for minimum bias events.

6.2.4 Systematic Uncertainties on the Direct Photons

The systematic uncertainties from the measured $\gamma_{\text{inclusive}}/\pi^0$ ratio and from the simulated $\gamma_{\text{decay}}/\pi^0$ ratio are propagated into the double ratio R by Gaussian uncertainty propagation, that means by adding them quadratically. The same Gaussian uncertainty propagation is also used when calculating the direct photon spectra from the double ratio. In addition, the uncertainty propagation has also been done as described in [Zau07]. Here it is taken into account that the term $(1-1/R)$ increases rapidly for small R and thus for double ratios close to unity, Gaussian uncertainty propagation does not work properly. Instead, the uncertainties are propagated as

$$\Delta\gamma_{\text{direct},\pm} = \pm\left[\left(1-\frac{1}{R_\gamma \pm \Delta R_\gamma}\right)\cdot(\gamma_{\text{incl}} \pm \Delta\gamma_{\text{incl}}) - \gamma_{\text{direct}}\right] . \tag{6.10}$$

Since the direct-photon signal in more central collisions is larger than in e.g. $p+p$ collisions, the uncertainties at higher p_{T} are almost symmetric though calculated asymmetrically with Equation 6.10. The double ratio in central Au+Au collisions, e.g., reaches values of $R \leq 5\pm \sim 1.5$. Treating the errors symmetrically allows a more straightforward combination of the results from the two different detectors in one final spectrum for each centrality selection.

Error type	4.5-5.0 GeV		8-10 GeV		14-16 GeV		type
Peak extraction	6.8%	6.5%	1.8%	1.7%	0.8%	0.8%	B
π^0 merging	0%	0%	0%	0%	0.7%	0.7%	B
π^0 fit	7.8%	7.3%	2.2%	2.11%	1.1%	1.02%	B
Efficiency	23.2%	23.1%	11.0%	11.0%	8.7%	8.7%	B
Global energy scale	8.6%	8.8%	7.0%	7.1%	5.9%	5.9%	B
Non-linearity	8.0%	7.7%	10.5%	10.5%	9.1%	8.9%	B
Acceptance	5.2%	5.3%	4.4%	4.4%	4.2%	4.2%	B
γ conversion	6.1%	6.0%	2.5%	2.4%	1.7%	1.7%	B
Charged background	13.1%	13.1%	6.4%	6.4%	5.0%	5.0%	B
γ shower merging	0.3%	0.3%	0.3%	0.3%	1.0%	1.0%	B
Hadron/π^0	19.2%	16.6%	3.7%	3.4%	1.7%	1.5%	B
Total	37.4%	35.9%	19.3%	19.2%	15.7%	15.6%	B

Table 6.5: Systematic uncertainties of the direct-photon yield, measured with the PbGl, for minimum bias events.

7. Results

> Imagination is more important than knowledge. Knowledge is limited. Imagination encircles the world.
>
> *A. Einstein*

The first and foremost results of the analyses presented in the previous chapters are the Lorentz invariant yields of the three particles, π^0, η, and direct γ, versus p_T. These spectra will then be used to calculate the nuclear modification factor R_{AA} to test possible effects of nuclear matter on particle production. Furthermore, the production ratio η/π^0 may exhibit for possible nuclear effects on the production of mesons of different masses. A model independent R_{AA} can also be obtained with the help of the data. The data can furthermore be compared to predictions from theoretical models and can be used to constrain parameters of such models.

7.1 Combining PbGl and PbSc Spectra

Particle spectra have been measured using the two different calorimeter types independently. In a last analysis step, the spectra measured with the PbGl and the PbSc detector need to be combined into one spectrum for each centrality selection. This procedure is done the same way for each particle species and will be explained in the following. To combine the spectra of the two detectors, the uncertainties are used as weights for the two spectra to be combined. The combined value $\bar{x}$ is calculated as

$$\bar{x}(p_T) = \frac{\Sigma_{i=1}^{N} w_i(p_T) x_i(p_T)}{\Sigma_{i=1}^{N} w_i(p_T)} \,, \tag{7.1}$$

where N = 2 and i = 1, 2 for the two detectors.

$$w_i(p_T) = \frac{1}{\delta x_i(p_T)^2} \tag{7.2}$$

is the weight, $x_i(p_T)$ is the invariant yield, and $\delta x_i(p_T)$ is the total uncertainty of the data point of one of the two detectors. It is the quadratic sum of the statistical and the systematic uncertainties. The statistical uncertainty for the combined yield $\bar{x}$ can then be calculated as the square root of

$$\delta\bar{x}(p_T)^2 = \sum_{i=1}^{N} \frac{1}{N} \frac{w_i(p_T)}{\Sigma_{j=1}^{N} w_j(p_T)} \cdot \delta x_i^{stat}(p_T)^2 \,. \tag{7.3}$$

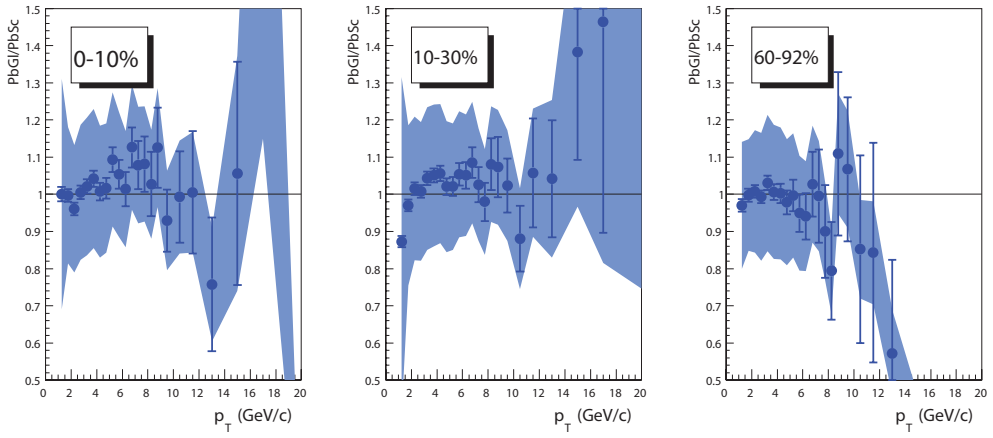

Figure 7.1: Ratio of the π^0 yield measured with the PbGl and measured with the PbSc for three different centrality selections. The error bars show the statistical uncertainty, the shaded area depicts the quadratic sum of the systematic uncertainties of the two measurements.

The combined systematic uncertainty is calculated in the same way. Although occurring at the same analysis steps they are uncorrelated between the two measurements.

7.2 π^0 and η Production

In the following, the results of the measurement of π^0 and η are presented and discussed. Furthermore, the production ratio η/π^0, and the nuclear modification factor R_{AA} are calculated.

7.2.1 Spectra of π^0 and η

Figure 7.2 shows the combined, fully corrected, Lorentz invariant yields of π^0's in Au+Au collisions at $\sqrt{s_{NN}}$ = 200 GeV. Eleven different centrality selections are shown together with the result for minimum bias collisions. The spectra cover the p_T range 1 GeV/$c \leq p_T \leq$ 20 GeV/c for minimum bias collisions[1]. In the different centrality classes, the upper reach in p_T is smaller. The PbGl results of this work have also been combined with the result from the analysis described in [Iso07], this combined result is published in [Ada08d].

The combined, fully corrected Lorentz invariant yields of η's in 200 GeV Au+Au collisions are presented in Figure 7.3. For the η, four different centrality selections are shown together with the minimum bias result. Due to worse acceptance at low p_T as well

[1] This range is based on the p_T width represented by the bins.

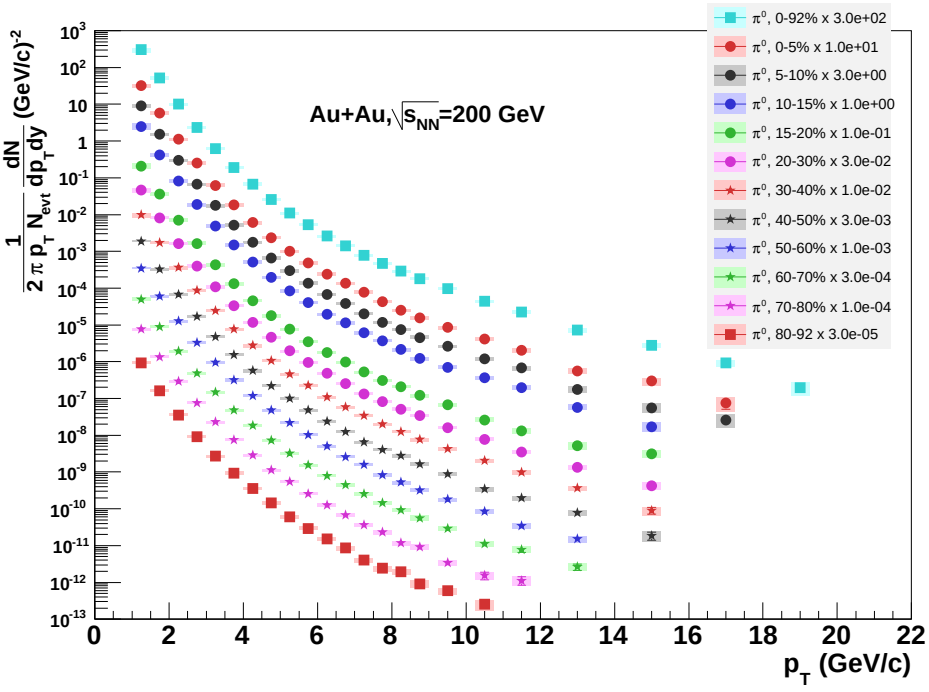

Figure 7.2: Fully corrected invariant yields of π^0's produced in Au+Au collisions at $\sqrt{s_{\mathrm{NN}}}$ = 200 GeV, for 11 different centrality selections and minimum bias, measured with PHENIX. The error bars denote the point-to-point uncertainty, the boxes the p_{T}-correlated uncertainties.

as the smaller 2γ branching ratio, the p_{T} reach of the spectra is smaller, in minimum bias collisions it is 1.5 GeV/$c \leq p_{\mathrm{T}} \leq$ 16 GeV/c, the upper p_{T} reach is lower towards more peripheral collisions.

7.2.2 The Ratio η/π^0

The study of the η/π^0 ratio allows a systematic study of the general system dependence and of the centrality dependence of particle production. It can shed light on the question whether the fragmentation functions for η and π^0 are affected differently by the hot and dense matter created in central Au+Au collisions and if the size of the medium changes the fragmentation functions. A difference between the two mesons may occur due to a hidden strangeness contribution to the wavefunction of the η.

The η/π^0 ratio is also a good measure to compare different measurements of the two mesons as systematic uncertainties cancel mostly in the ratio. Such measurements have been collected by PHENIX [Adl07c], for nucleus-nucleus collisions, the collection is shown in the left panel of Figure 7.4, for hadron-hadron collisions (e.g. $p+p$, $p+\bar{p}$, or $p+\pi^{\pm}$), it is depicted in the right panel of Figure 7.4. In collisions of heavy nuclei, PHENIX has so far been the only experiment to measure this ratio at large transverse

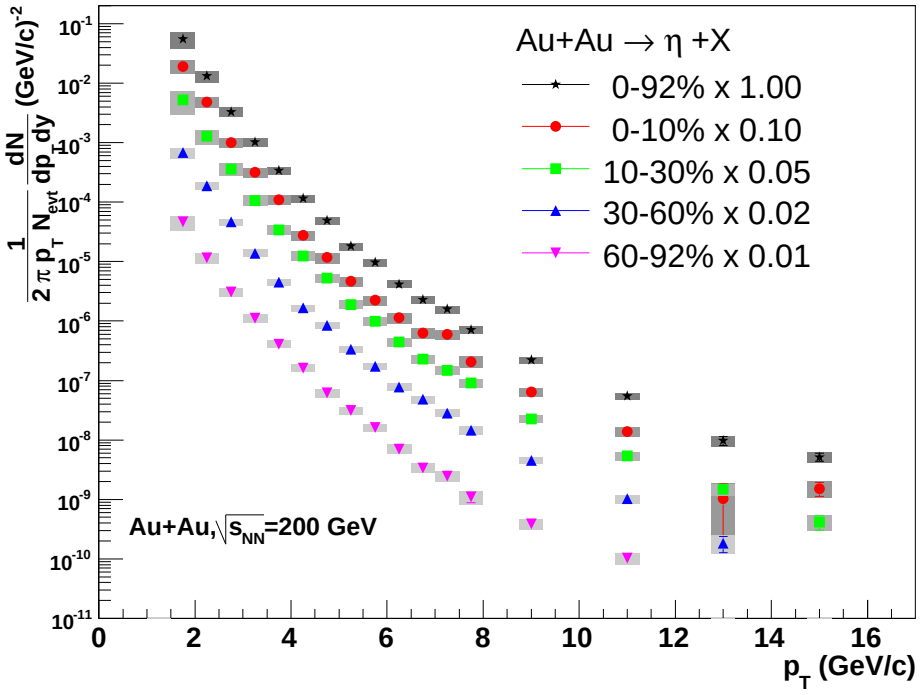

Figure 7.3: Fully corrected invariant yields of η's produced in Au+Au collisions at $\sqrt{s_{\mathrm{NN}}}$ = 200 GeV, for 4 different centrality selections and minimum bias, measured with PHENIX. The error bars denote the point-to-point uncertainty, the boxes the p_{T}-correlated uncertainties.

momenta.

In Figure 7.5, the production ratio η/π^0 is shown for 200 GeV Au+Au collisions, for four different centrality classes and minimum bias events. The error bars in the plot are the total uncertainties. The data are overlaid with the same PYTHIA [Sjo01] calculation[2] as shown in Figure 7.4. Within the uncertainties, no centrality dependence of the ratio is visible. Furthermore, there is also no difference to the ratio observed in $p+p$ collisions. This observation can be clarified by defining the ratio

$$\left.\frac{\eta}{\pi^0}\right|_{\mathrm{AA}} = \frac{\eta/\pi^0|_{p+p}}{\eta/\pi^0|_{\mathrm{Au+Au}}}\,, \tag{7.4}$$

a deviation from unity would indicate that the production of η and π^0 are affected differently in heavy-ion collisions.

[2]PYTHIA is a generator for $p+p$ collisions.

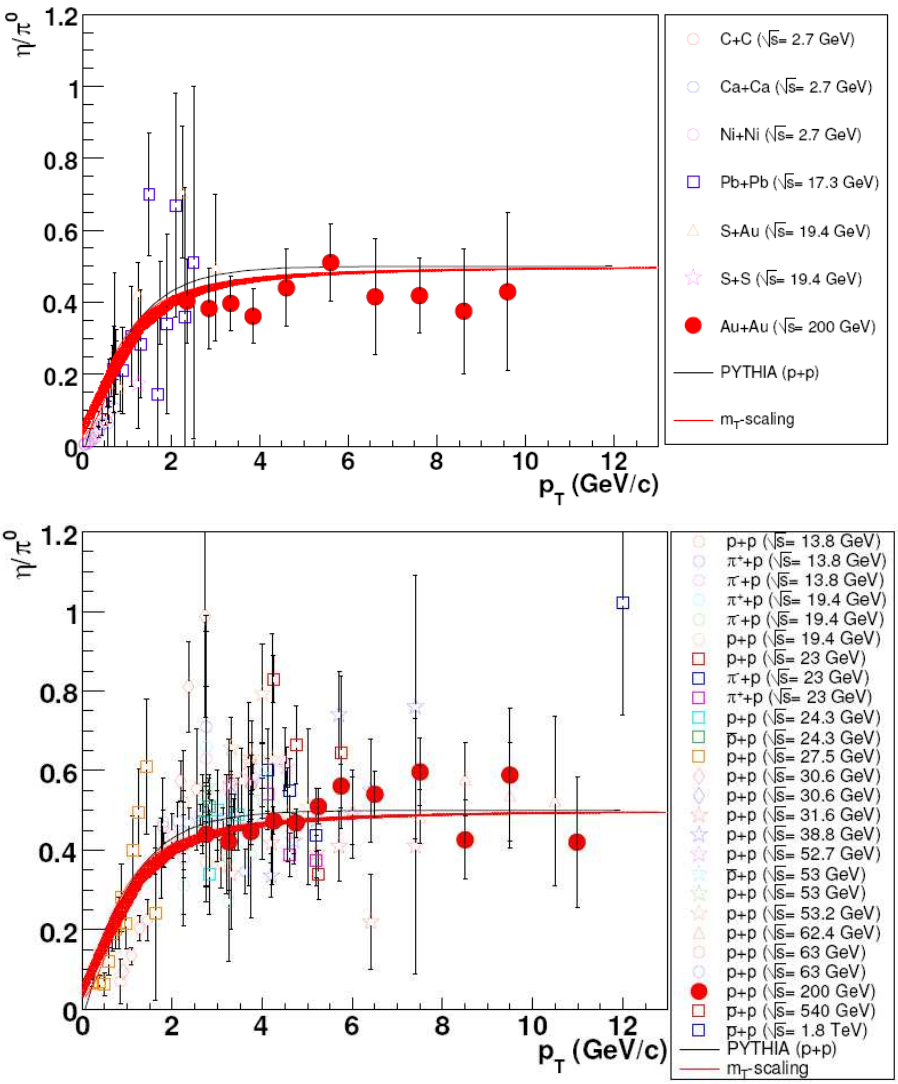

Figure 7.4: "World data" of the production ratio of η and π^0 in nucleus-nucleus (top) and hadron-hadron (bottom) collisions at different experiments and collision energies. [Adl07c]

In Figure 7.6, the ratio defined in Equation 7.4 is shown for the four different centrality classes and minimum bias events, in 200 GeV Au+Au collisions. No significant centrality dependence is observed. Also the ratio does not significantly deviate from unity, therefore the data suggest that the fragmentation functions for π^0 and η are affected by the medium the same way.

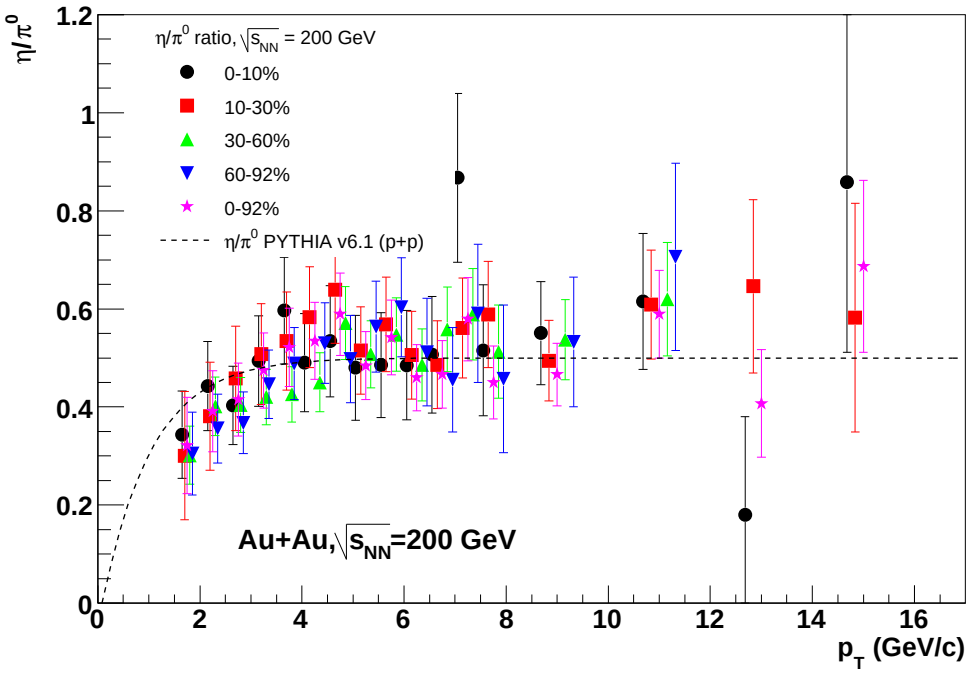

Figure 7.5: Production ratio of η and π^0 in Au+Au collisions at $\sqrt{s_{\rm NN}}$ = 200 GeV, for 4 different centrality selections and minimum bias, measured with PHENIX. The error bars indicate the total uncertainties. The curve is the same ratio from PYTHIA [Sjo01], in $p+p$ collisions.

7.2.3 The Nuclear Modification Factor

In order to quantify possible nuclear effects, the measured spectra that have been discussed in Section 7.2.1 have been used to calculate the nuclear modification factor $R_{\rm AA}$ which is defined as

$$R_{AA}|_{\pi^0,\eta} = \frac{{\rm d}^2N_{\pi^0,\eta}/{\rm d}p_{\rm T}{\rm d}y|_{\rm AA}}{\langle T_{AA}\rangle \cdot {\rm d}^2\sigma^{p+p}_{\pi^0,\eta}/{\rm d}p_{\rm T}{\rm d}y} \,. \tag{7.5}$$

The $p+p$ reference cross sections $\sigma^{p+p}_{\pi^0,\eta}$ are taken from PHENIX analyses of the 2005 $p+p$ run at $\sqrt{s}$ =200 GeV [Ada07, Ell08]. A fit to the data is used due to the different bin positions in the reference data compared to this analysis. As mentioned in Section 2.4.1, the nuclear overlap functions $T_{\rm AA}$ are calculated using the Glauber model and taken from [Rey03][3].

The nuclear modification factor $R_{\rm AA}$ for π^0's produced in Au+Au collisions at $\sqrt{s_{\rm NN}}$ = 200 GeV is shown in Figure 7.7. The figure includes 11 centrality classes and minimum bias events. It is clearly visible that $R_{\rm AA}$ is lowest in central events, reaching ~ 0.2 for

[3] see Appendix for values

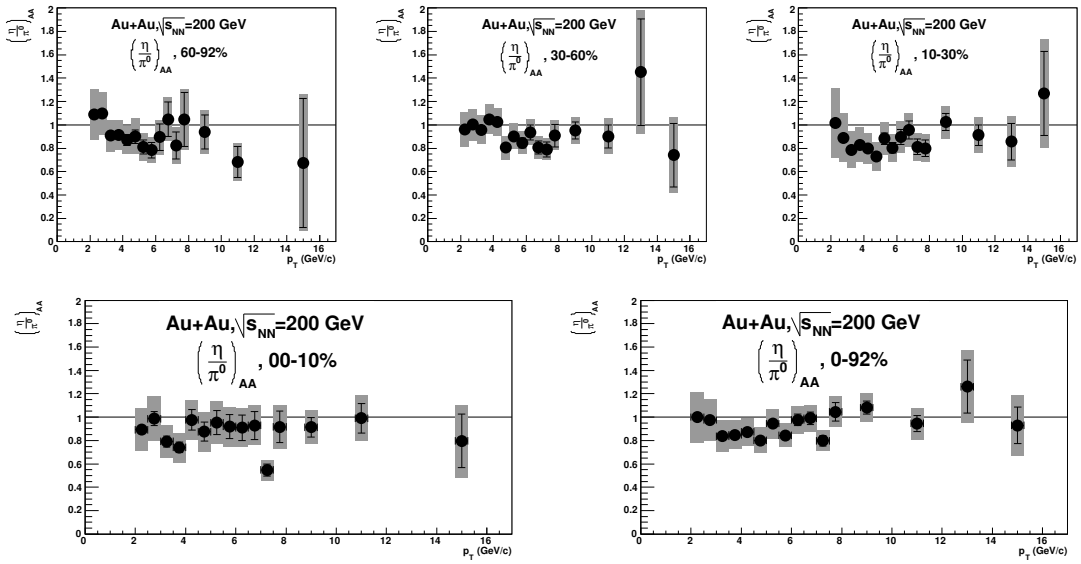

Figure 7.6: Ratio $\frac{\eta}{\pi^0}\Big|_{\mathrm{AA}}$ for four centrality classes and minimum bias events.

the 5% most central events, and increases towards peripheral events where it eventually is consistent with unity. Furthermore, R_{AA} appears to be almost constant for high p_{T}, only a small increase is indicated by the data.

An alternative R'_{AA} can be calculated using d+Au collisions as a reference. A possible advantage of this is that some initial state effects may cancel. Initial state effects such as the Cronin enhancement are expected for both d+Au and Au+Au collisions but are not present in $p+p$ collisions. This R'_{AA} is calculated as following, using the d+Au invariant yield, measured by PHENIX in the 2003 run [Adl07b], as reference:

$$R'_{AA}|_{\pi^0} = \frac{N_{\mathrm{coll}}^{d+\mathrm{Au}} \cdot \mathrm{d}^2N_{\pi^0}/\mathrm{d}p_{\mathrm{T}}\mathrm{d}y|_{\mathrm{AA}}}{\langle T_{AA}\rangle \cdot \mathrm{d}^2N_{\pi^0}/\mathrm{d}p_{\mathrm{T}}\mathrm{d}y|_{d\mathrm{A}}} \,. \tag{7.6}$$

Here, the number of binary nucleon-nucleon scatterings $N_{\mathrm{coll}}^{d+\mathrm{Au}}$ needs to be taken into account as well. The resulting R'_{AA} is shown in Figure 7.8 for the same centrality classes as R_{AA}. The suppression pattern looks the same in general, the π^0 is again suppressed by a factor of ~ 5 in the most central collisions. However, the shape of R'_{AA} differs from R_{AA}, it is a bit steeper at high p_{T} and lower in the region of the Cronin enhancement measured in d+Au. In the transverse momentum region below the Cronin enhancement, R'_{AA} is larger than R_{AA}, indicating the mainly soft particle production at such momenta.

For the η meson, the nuclear modification factor R_{AA} for the same Au+Au collisions is shown in Figure 7.9. Here, four different centrality classes are shown. Again, $R_{\mathrm{AA}} \sim 0.2$ in central events and rises towards peripheral events, it is also rather flat with p_{T}.

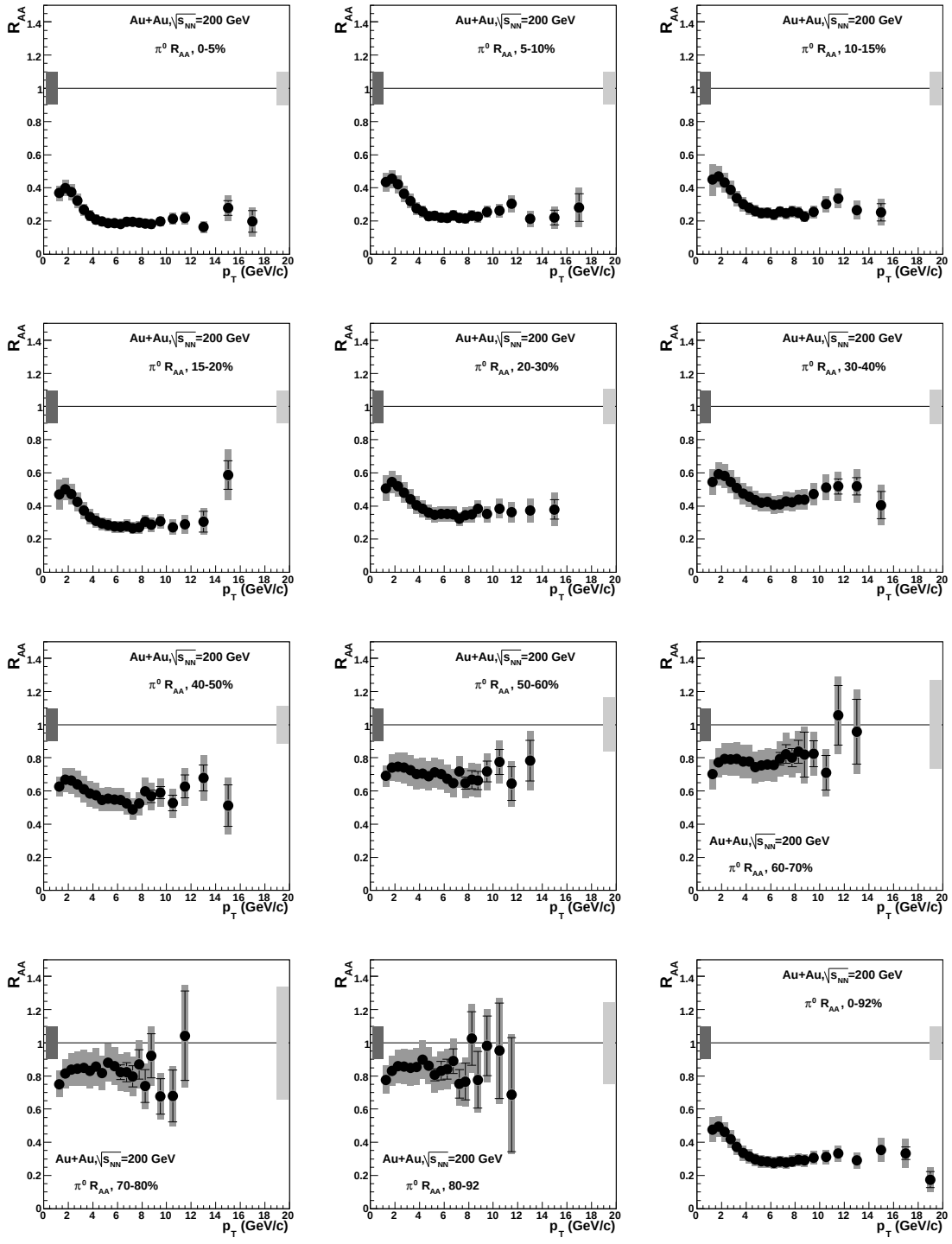

Figure 7.7: Nuclear modification factor R_{AA} for π^0's produced in Au+Au collisions at $\sqrt{s_{\mathrm{NN}}}$ = 200 GeV, for 11 different centrality selections and minimum bias, measured with PHENIX. The error bars denote the point-to-point uncertainty, the boxes the p_{T}-correlated uncertainties.

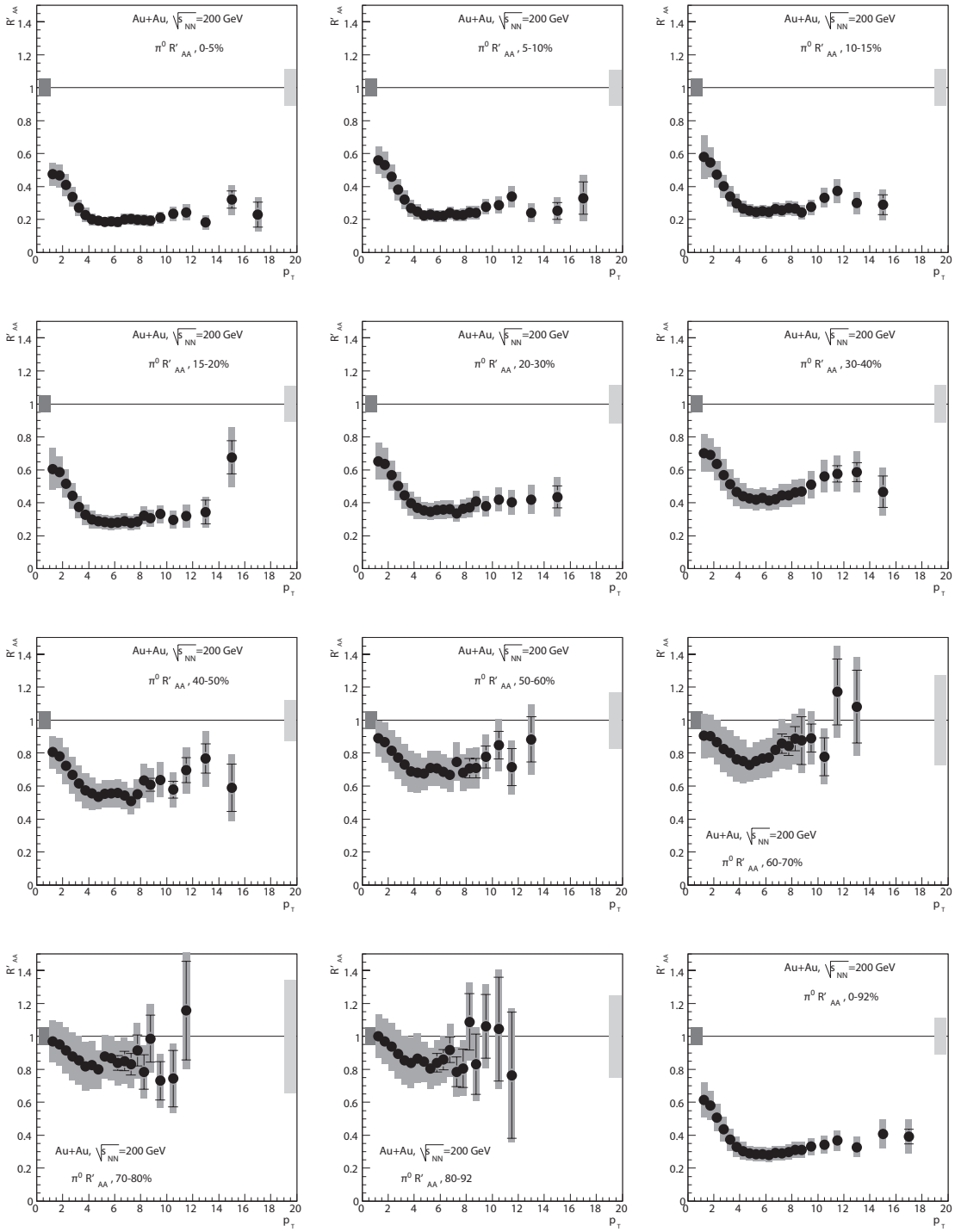

Figure 7.8: Alternative nuclear modification factor R'_{AA} for π^0's produced in Au+Au collisions at $\sqrt{s_{\mathrm{NN}}}$ = 200 GeV, for 11 different centrality selections and minimum bias, measured with PHENIX. The error bars denote the point-to-point uncertainty, the boxes the p_{T}-correlated uncertainties.

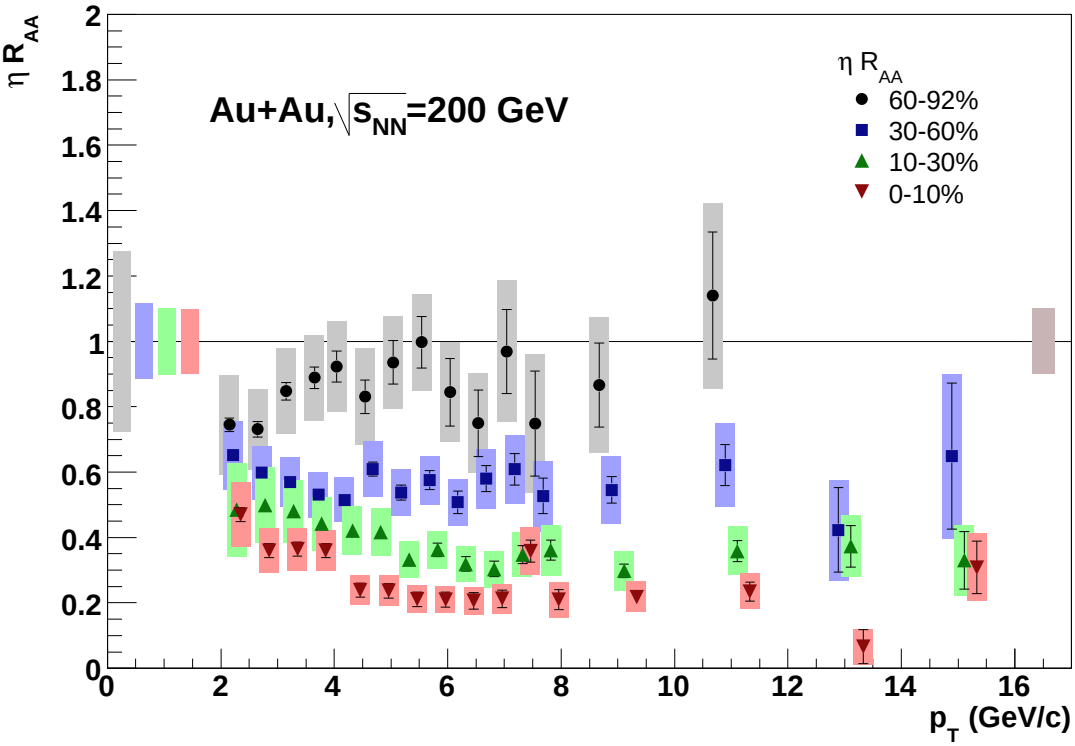

Figure 7.9: Nuclear modification factor R_{AA} for η's produced in Au+Au collisions at $\sqrt{s_{NN}}$ = 200 GeV, for 4 different centrality selections, measured with PHENIX. The error bars denote the point-to-point uncertainty, the boxes the p_T-correlated uncertainties.

7.2.4 Comparison with Theoretical Models

The results on the nuclear modification factor R_{AA} show the presence of jet quenching in central Au+Au collisions at $\sqrt{s_{NN}}$ = 200 GeV, the suppression is of the same size for both π^0 and η, with $R_{AA} \approx 0.2$ in such collisions. Towards more central events, R_{AA} becomes larger, in peripheral events, the suppression vanishes. All this confirms the results from the 2002 data [Adl03f, Adl06]. Since the p_T range could be increased in this measurement compared to the old measurement, and since the size of the uncertainties has been reduced, the new data from the 2004 run, as presented here, can be used for more sophisticated comparisons with theoretical models via a statistical analysis.

PHENIX has performed such a statistical analysis, using the combined data from this work and from [Iso07], this analysis has been published [Ada08c]. Different theoretical models have been compared with the π^0 R_{AA} in the most central 200 GeV Au+Au events. The general idea of the quantitative comparison is to take into account both the statistical, point-to-point uncorrelated uncertainties (σ_i) and the systematic, correlated uncertainties

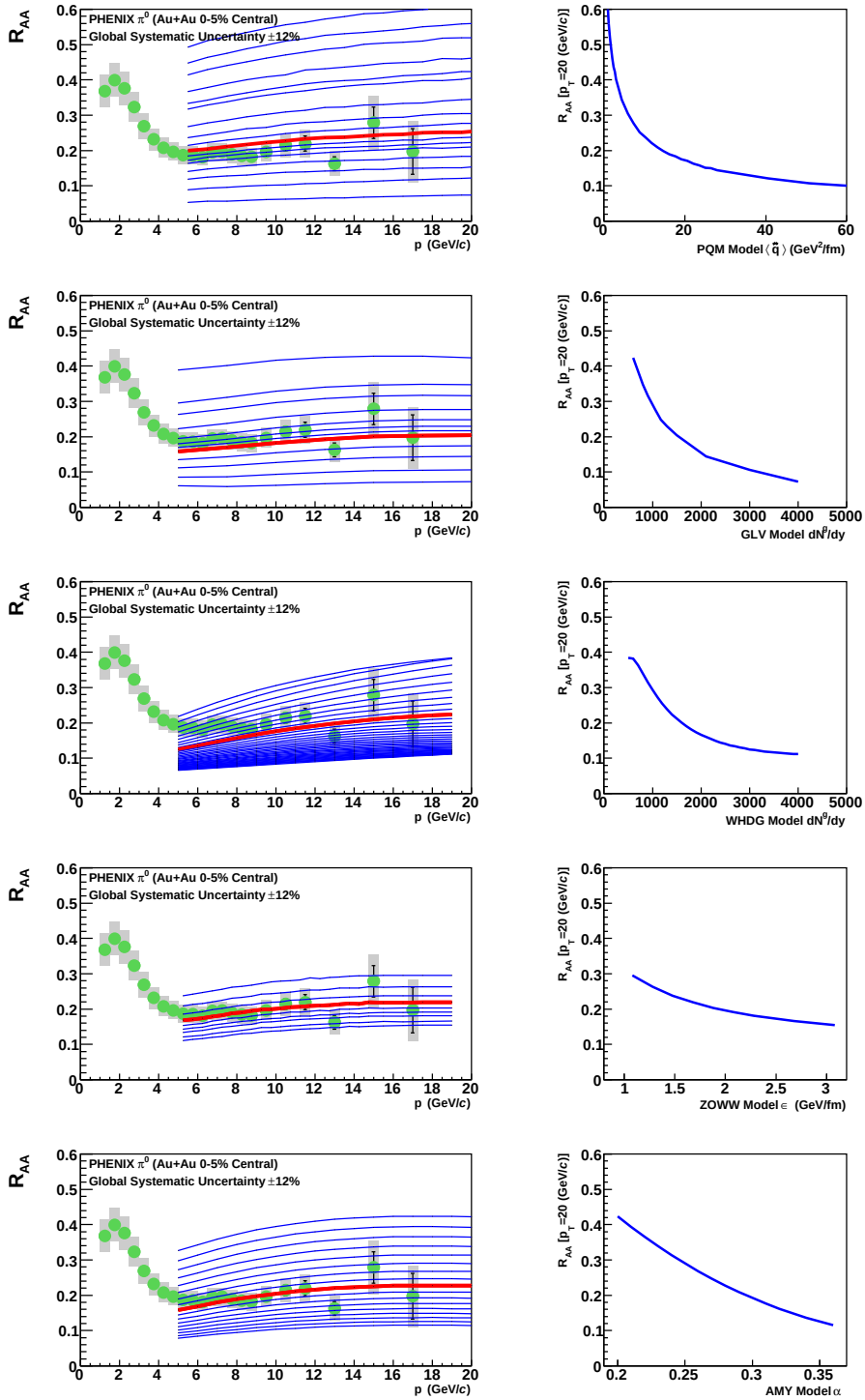

Figure 7.10: Left panels: π^0 $R_{\rm AA}$ for 0-5% most central 200 GeV Au+Au events, overlaid with predictions from five different theoretical models, for different model parameters. The red line denotes the best fits. Right panels: $R_{\rm AA}$ from the models at $p_{\rm T}$ = 20 GeV/c. The models are (from top to bottom): PQM, GLV, WHDG, ZOWW, AMY (see Section 2.4.3).

of type B (σ_{b_i}) and type C (σ_c) to constrain model parameters such as the medium transport coefficient $\hat{q}$, the initial gluon density $dN_g/d\eta$, or the initial energy loss parameter ε_0.

The idea of the statistical analysis is to find the best fit for each theory, data and theory are compared by shifting the measured data points within the uncertainties. The different uncertainties are used to calculate the minimum of

$$\tilde{\chi}^2(\varepsilon_b,\varepsilon_c,p) = \left[\left(\sum_{i=1}^{n}\frac{(y_i+\varepsilon_b\sigma_{b_i}+\varepsilon_c y_i\sigma_c-\mu_i(p))^2}{\tilde{\sigma}_i^2}\right)+\varepsilon_b^2+\varepsilon_c^2\right] \tag{7.7}$$

for each choice of theoretical parameters. Here, $\mu_i(p)$ is the nuclear modification factor at a given p_{T} as predicted by different theoretical models, for a certain parameter p. ε_b and ε_c denote the fractions of the type B and type C systematic uncertainties by which all points are displaced together, and $\tilde{\sigma}_i = \sigma_i(y_i+\varepsilon_b\sigma_{b_i}+\varepsilon_c y_i\sigma_c)/y_i$ is the point-to-point random uncertainty scaled by a multiplicative shift in y_i. To account for the type B systematic uncertainties, two extreme correlation cases are taken into account when looking for the minimum $\tilde{\chi}^2$. One extreme is the total correlation of this uncertainty, where all points move by the same fraction of their respective type B uncertainty; the other extreme case is the total anti-correlation, where the point at the lowest p_{T} moves into the opposite direction than the point at the highest p_{T}. The minimum $\tilde{\chi}^2$ is found by varying ε_b and ε_c. With $\tilde{\chi}^2$, one can then define and calculate the p-value as

$$\mathrm{p-value} = \int_{\tilde{\chi}^2}^{\infty}\chi^2_{(n_d)}(z)dz\,, \tag{7.8}$$

here, $\chi^2_{(n_d)}$ is the chi-square distribution with the appropriate number of degrees of freedom. This calculation can be done because $\tilde{\chi}^2$, the goodness-of-fit statistics, follows a standard χ^2 distribution. Under the assumption that the theoretical model under study – the hypothesis – yields a correct description of "reality", the p-value is the probability to randomly obtain data with a worse fit to the hypothesis than the actual experimental data [Ada08c, Yao06].

After finding the best fit to each theoretical model, we also calculated which values of the respective theoretical parameter are n standard deviations away from the best fit.
In Figure 7.10, the nuclear modification factor from the 5% most central events is overlaid with the results from calculations of R_{AA} for five different theoretical models. The model calculations are done for different parameters of the models. The models and the corresponding parameters are – from top to bottom – the parton quenching model depending on the medium transport coefficient $\hat{q}$ [Dai05, Loi, Nag09], the GLV model depending on the initial gluon density dn_g/dy [Gyu00a, Vit, Nag09], the WHDG model

depending on the initial gluon density dn_g/dy [Wic07, Hor, Nag09], the ZOWW model depending the energy density ε_0 [Zha07, Wan, Nag09], and the AMY model depending on the average effective coupling α_s [Arn00, Nag09]. The best fit, i.e. the calculation for the best parameter choice, is highlighted for each model.

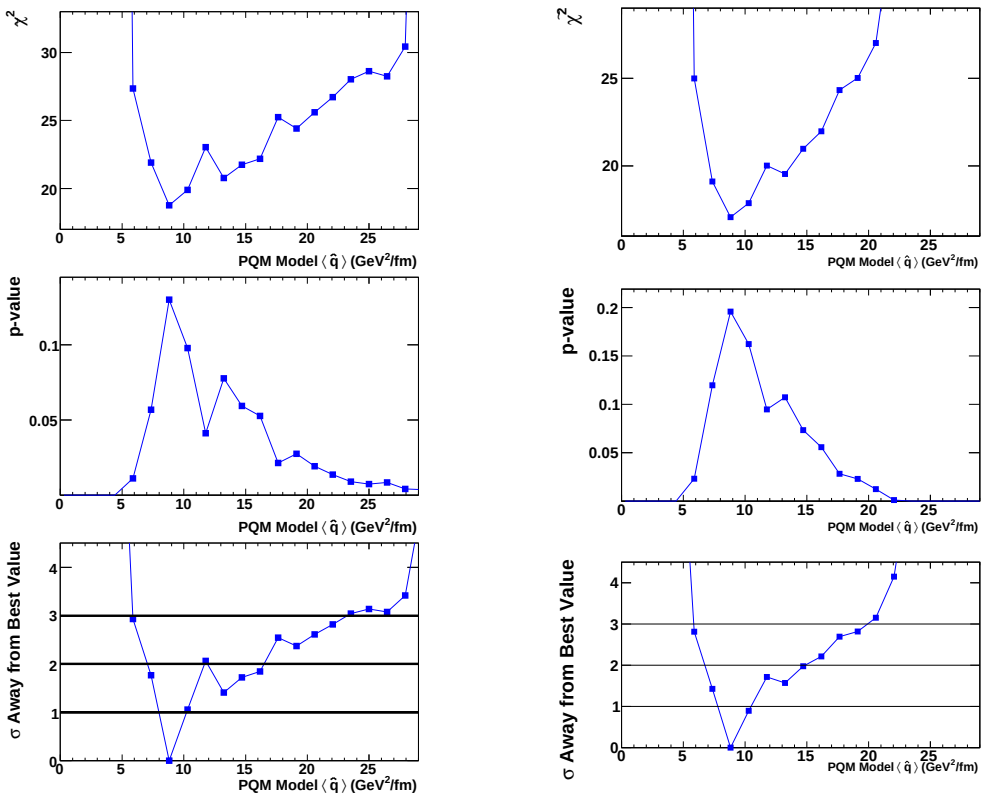

Figure 7.11: Results of the statistical analysis from the comparison of the 0-5% most central π^0 R_{AA} to the PQM model. Top: Distribution of $\tilde{\chi}^2$ for different values of $\hat{q}$. Middle: p-value calculated from $\tilde{\chi}^2$ for the different values of $\hat{q}$. Bottom: Number of standard deviations σ the value of $\hat{q}$ is away from the best value of $\hat{q}$. Left: Calculation using R_{AA}. Right: Calculation using R'_{AA}.

The calculated minimum $\tilde{\chi}^2$ values for the different values of $\hat{q}$ in the PQM model are shown in the top panels of Figure 7.11. The middle panels of the same figure depict the p-value for each choice of $\hat{q}$ as derived from the minimum $\tilde{\chi}^2$. The best theory fit to the data is the one with the maximal p-value. The bottom panels of the figure finally show the deviation for a value for $\hat{q}$ from the best value in terms of standard deviations σ. The same three diagrams are shown in Figure 7.12 for the other four theoretical models and the respective parameters. On can clearly see that each model has a well-defined minimum $\tilde{\chi}^2$. However, the calculated p-values are very different. For example, the maximum p-value in the WHDG model is very small, this is due to the steeper functional

form of this model's prediction which is not favored by the data. The effect of the steepness is shown in the right panel of Figure 7.11 where the modified R'_{AA} is used for the calculation. The larger steepness at high p_{T} leads to a larger maximum p-value which is ~ 0.2 instead of ~ 0.13 when using R_{AA}.

Model	PQM	GLV	WHDG	ZOWW	AMY
Parameter	$\hat{q}$ (GeV^2/fm)	dn_g/dy	dn_g/dy	$\varepsilon_0(GeV/fm)$	α_s
Best value	$8.8^{+1.3}_{-0.9}(^{+7.7}_{-1.8})$	$1500^{+220}_{-270}(^{+380}_{-460})$	$1400^{+400}_{-295}(^{+505}_{-505})$	$1.7^{+0.27}_{-0.33}(^{+0.57}_{-0.48})$	$0.28^{+0.01}_{-0.02}(^{+0.02}_{-0.03})$

Table 7.1: Best fit value of the model parameter for each of the five models the data are compared to. The quoted uncertainties are 1σ (2σ) uncertainties.

The results from the statistical analysis are summarized in Table 7.1. It has to be noted that all model parameters are constrained within a certain range of less than 20% of their respective best values – except the parameter from WHDG, the model that predicts the largest slope of R_{AA} – at the 1σ level, but that the corresponding best p-value's for the models vary over a broad range. For the WHDG model it is only $\sim 0.41 \cdot 10^{-3}$ while for the PQM model it reaches ~ 0.13. In general, all models predict a larger slope than the measurement provides. The PQM, GLV, WHDG, and ZOWW models have been compared to data (the PbGl data of this analysis combined with the PbSc data from [Iso07]) in [Ada08c], the results agree within the quoted uncertainties.

7.3 Direct Photons

The Lorentz-invariant yield of direct photons in 200 GeV Au+Au collisions is shown in Figure 7.13 for the same 11 different centrality classes as for the π^0's, and for minimum bias events. The spectra are shown for p_{T} up to 20 GeV/c in central and in minimum bias events[4], towards more peripheral centrality selections, the p_{T} reach decreases. Upper limits with 90% confidence level are calculated and plotted in case the total uncertainties at 1σ are larger than the direct-photon yield itself. The upper limits are quoted at 1.64σ according to the suggestion in [Fel98]. There a unified ansatz was used to include the transformation from two-sided to one-sided limits is included.

The nuclear modification factor R_{AA} for direct photons is calculated using a $p+p$ reference from PHENIX [Ben07, Adl07d]. The results from two runs with overlapping p_{T} range are fit, the fit is used as the denominator for the R_{AA} calculation. The statistical error from the data are replaced by the systematic uncertainty of the fit function. The

[4]The last bin represents the range 16 GeV/$c \leq p_{\mathrm{T}} \leq$ 20 GeV/c.

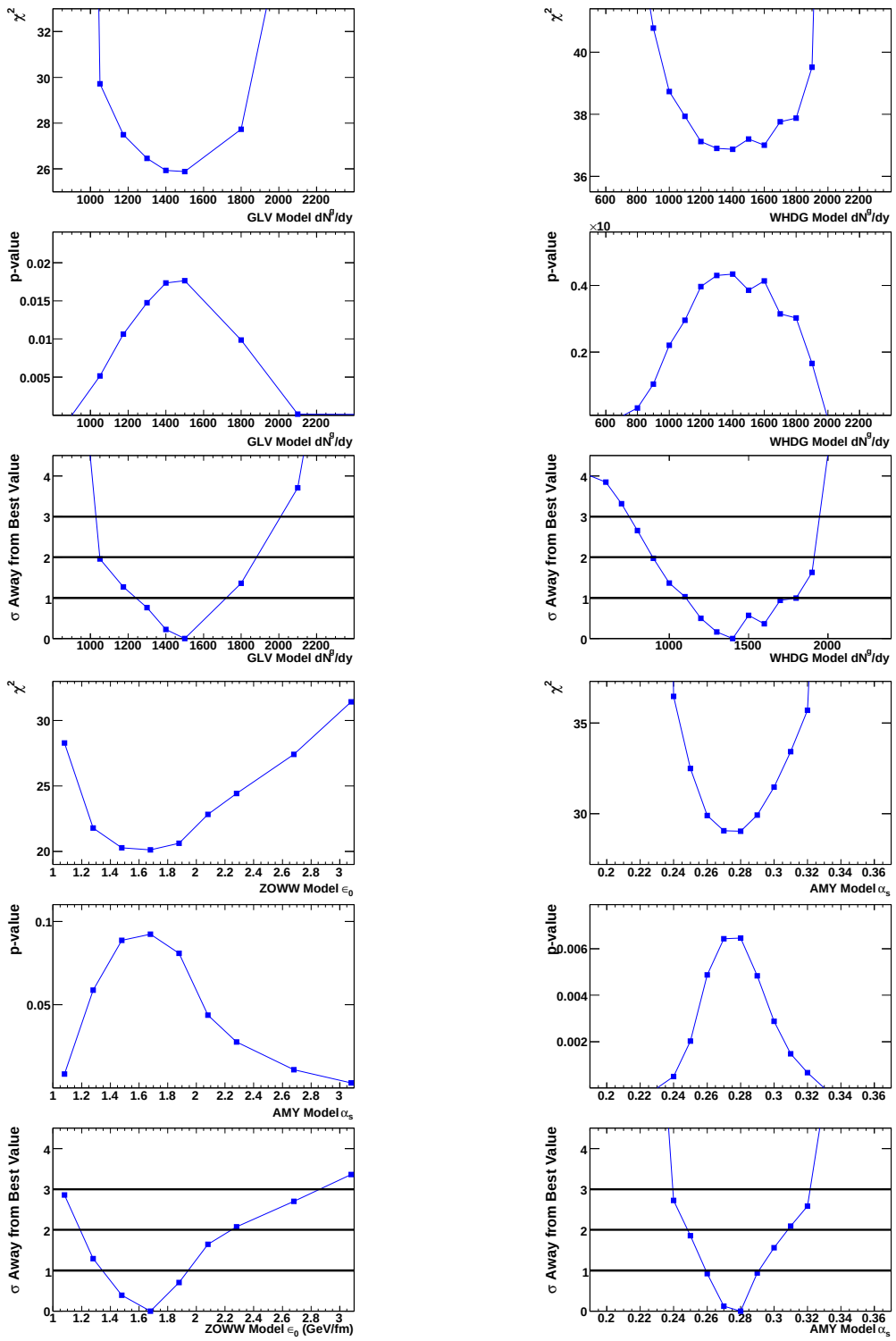

Figure 7.12: Results of the statistical analysis from the comparison of the 0-5% most central π^0 R_{AA} to the GLV (top left), the WHDG (top right), the ZOWW (bottom left), and the AMY (bottom right) models.

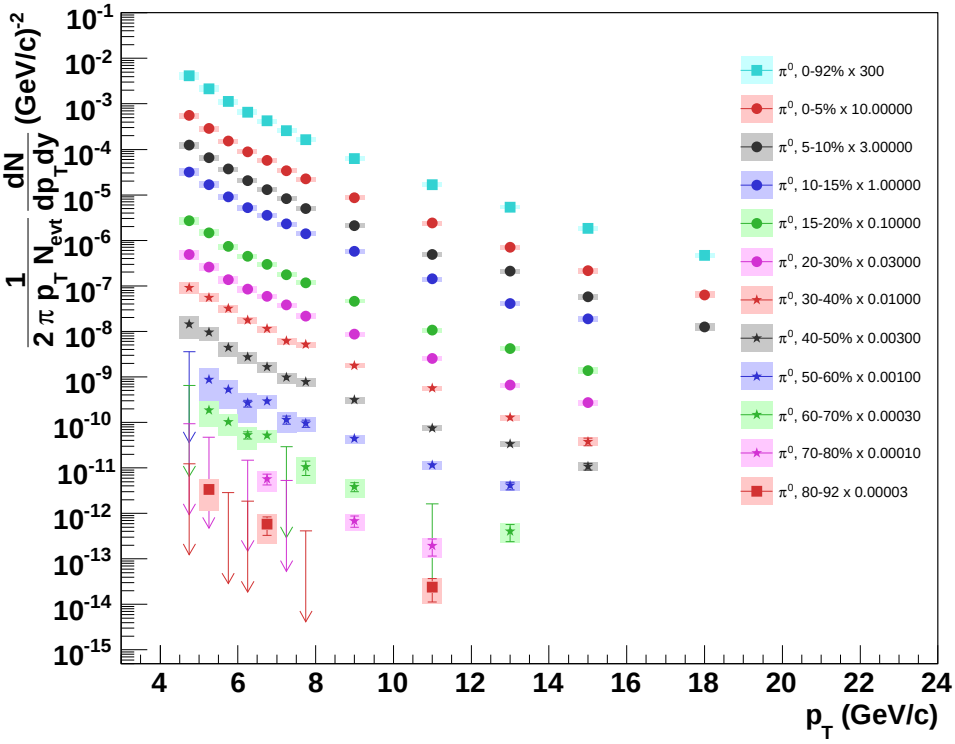

Figure 7.13: Fully corrected invariant yields of direct photons produced in Au+Au collisions at $\sqrt{s_{NN}}$ = 200 GeV, for 11 different centrality classes and minimum bias events, measured with PHENIX. The error bars denote the point-to-point uncertainty, the boxes the p_T-correlated uncertainties. The arrows indicate the 90% c.l. upper limits for the direct photon yield.

resulting R_{AA} is shown in Figure 7.14, for nine different centrality selections and for minimum bias. Again, upper limits are plotted in case the total 1σ uncertainty exceeds the value of the respective R_{AA}. In the most central events, the direct-photon R_{AA} appears to show a suppression at highest p_T, however it should be noted that this effect is dominated by the PbSc measurement which suffers much more from the π^0 decay photon merging. Looking at the PbGl result alone, the trend at highest p_T looks different. The suppression is not visible anymore (see Figure 7.15).

In Figure 7.16, the direct-photon data from the 5% most central collisions are compared to theoretical calculations from [Gal09]. These calculations account for various effects of cold and hot nuclear matter, the predicted R_{AA} depends on which of the effects are included. The curves on the left panel of Figure 7.16 do not take into account effects of the QGP. However, the figure shows that nuclear shadowing and the so-called isospin effect (see Section 2.5), both effects of the cold nuclear matter in the initial state, already are expected to change the direct-photon R_{AA}. The right

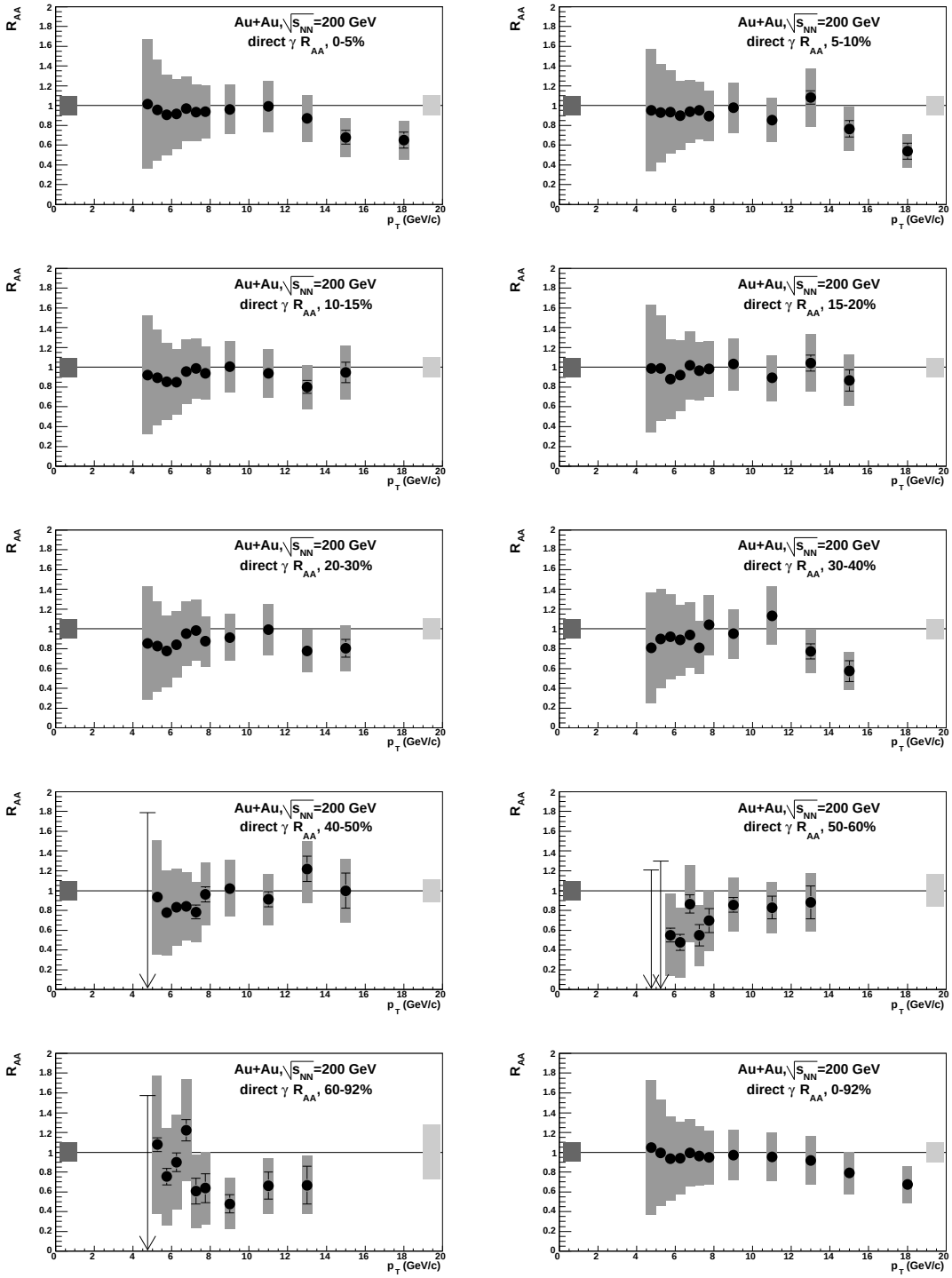

Figure 7.14: Nuclear modification factor R_{AA} for direct photons produced in Au+Au collisions at $\sqrt{s_{\mathrm{NN}}}$ = 200 GeV, for 9 different centrality selections and minimum bias, measured with PHENIX. The error bars denote the point-to-point uncertainty, the boxes the p_{T}-correlated uncertainties.

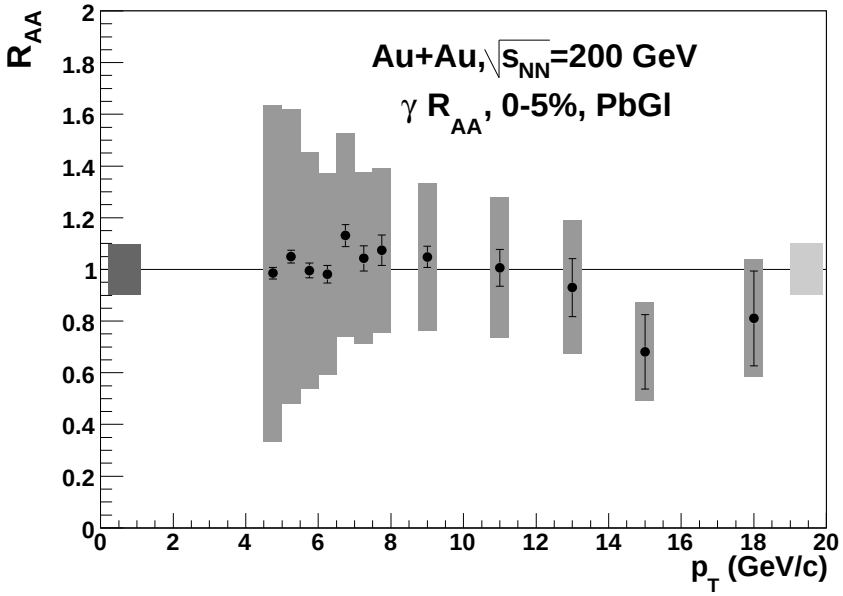

Figure 7.15: Nuclear modification factor R_{AA} for direct photons produced in Au+Au collisions at $\sqrt{s_{\mathrm{NN}}}$ = 200 GeV, for the 5% most central events, measured with the PbGl only. The error bars denote the point–to-point uncertainty, the boxes the p_{T}-correlated uncertainties.

panel of the same figure depicts effects of hot nuclear matter. Especially the inclusion of photons from jet-plasma interactions changes the predicted R_{AA} significantly, and the data are closer to the calculation including such photons at higher p_{T}. However, the large systematic uncertainties do not allow to disentangle the different effects and their possible contributions to the overall direct photon spectrum (or R_{AA}) in central Au+Au collisions.

The direct-photon R_{AA} from the 5% most central Au+Au collisions is compared to other theoretical calculations [Vit08] in Figure 7.17. Again, the theoretical calculations account for different cold and hot nuclear effects. They are plotted separately. In the left panel of the figure, mainly initial state effects are shown, the calculation includes a Cronin enhancement and nuclear shadowing. The isospin effect is also always included, as is the quenching of fragmentation photons due to jet quenching. Furthermore, initial state energy loss due to the broadening of the parton distribution function of the colliding nuclei is taken into account. This energy loss already changes the predicted R_{AA} visibly. The right panel of Figure 7.17 includes other effects of the QGP on direct photons, photons from parton conversion as well as medium-induced bremsstrahlung, in the latter case with (coherent) and without (incoherent) full treatment of the LPM effect. The calculations show only a small effect of medium-induced bremsstrahlung if destructive LPM effects are taken into account. Again, the uncertainties of the data do not allow

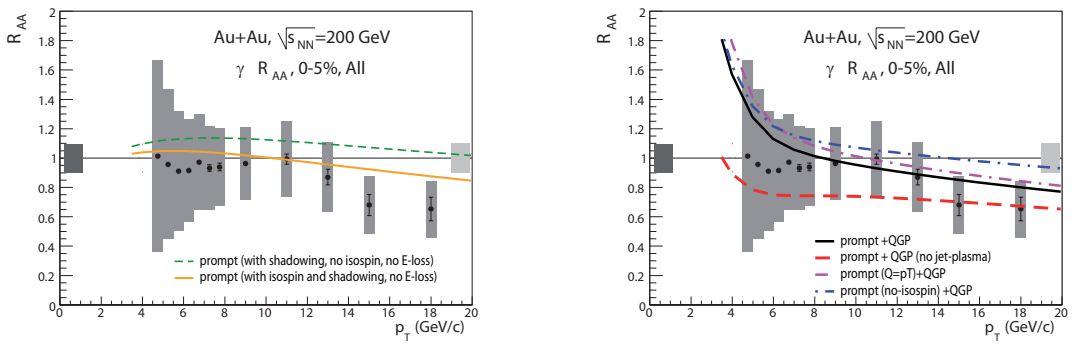

Figure 7.16: Direct-photon R_{AA} in 200 GeV Au+Au collisions for the 5% most central events, compared to different theoretical calculations [Gal09], using the pQCD scale $Q = p_{\mathrm{T}}/2$. Left: Calculations for prompt photons, without including finite temperature effects. The dashed green curve includes shadowing, the orange curve also accounts for effects of the isospin composition of the nuclei. Right: Calculation including effects of a QGP. The black line and the pink dashed-dotted line represent prompt photons for two different pQCD scales ($Q = p_{\mathrm{T}}/2$ and $Q = p_{\mathrm{T}}$) and photons emitted from a QGP. The red dashed line neglects photons from jet-plasma interactions. The blue dashed-dotted line does not account for the isospin.

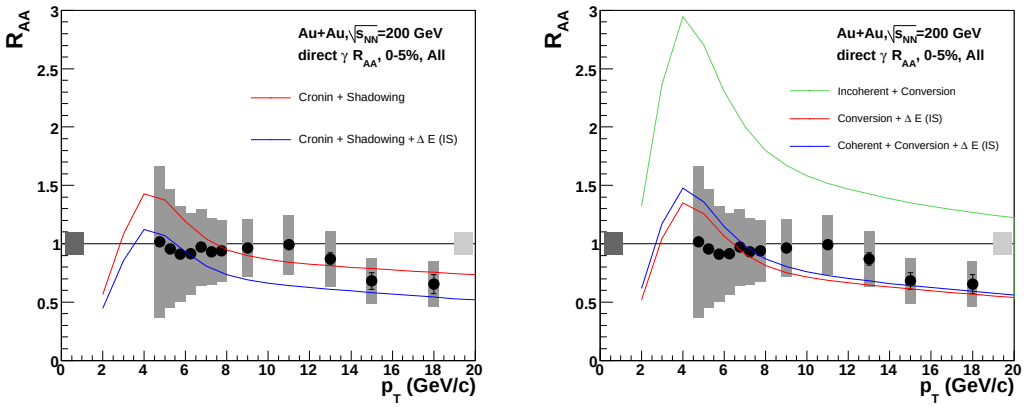

Figure 7.17: Direct-photon R_{AA} in 200 GeV Au+Au collisions for the 5% most central events, compared to different theoretical calculations [Vit08]. Left: Calculations including initial state effects. The red curve accounts for the Cronin effect and shadowing, the blue curve also includes initial state energy loss. The quenching of fragmentation photons is also included. Right: Calculations including final state effects such as jet conversion and medium-induced photon production (at both coherent and incoherent limits).

to disentangle some of the effects, however, the case including conversion photons and medium-induced bremsstrahlung without LPM cancellation effects can be ruled out by the data.

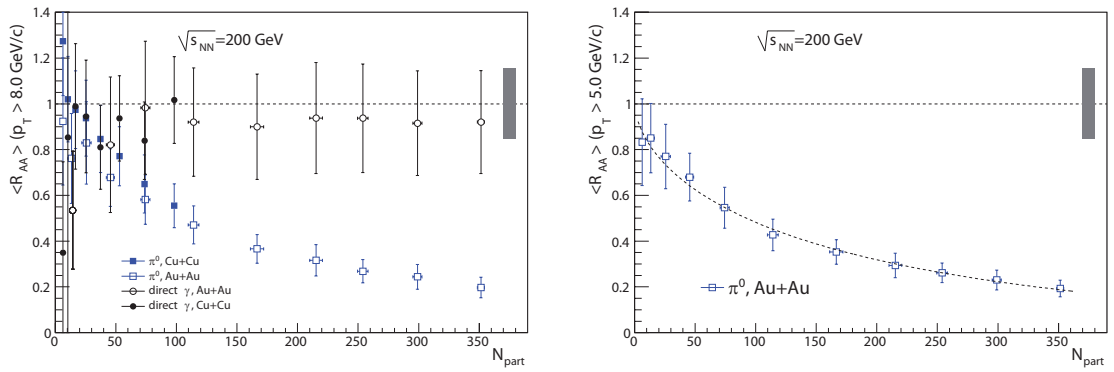

Figure 7.18: Averaged nuclear modification factor $\langle R_{\mathrm{AA}} \rangle$, (left) for direct photons and π^0's in 200 GeV Au+Au and Cu+Cu [Lue07, Ada08b] collisions, for $p_{\mathrm{T}} > 8$ GeV/c, (right) for π^0's in 200 GeV Au+Au collisions, for $p_{\mathrm{T}} > 5$ GeV/c, together with a fit. The box on the right depicts the common normalization uncertainty of $\sigma_{pp}^{\mathrm{inel}}$ in the denominator of R_{AA}.

7.4 The Overall Picture

The averaged nuclear modification factor $\langle R_{\mathrm{AA}} \rangle$ can be used to study the centrality (N_{part}) dependence of a possible suppression pattern. It is plotted in the left panel of Figure 7.18 for neutral pions and direct photons in 200 GeV Au+Au and Cu+Cu collisions [Lue07, Ada08b]. The p_{T} dependent R_{AA} is averaged for $p_{\mathrm{T}} > 8$ GeV/c. While direct photons do not show an apparent suppression in this picture, the suppression of π^0's increases monotonically with N_{part} and is similar for Au+Au and Cu+Cu at similar values of N_{part}. The right panel of Figure 7.18 shows the same $\langle R_{\mathrm{AA}} \rangle$ for π^0's in Au+Au collisions for $p_{\mathrm{T}} > 5$ GeV/c, together with a fit function. The idea behind this fit function is that in the case of spectra following a power law $\propto p_{\mathrm{T}}^n$ – which is the case in $p+p$ and Au+Au collisions at high transverse momenta –, the suppression can be interpreted as a fractional energy loss of the particles. This fractional energy loss is

$$S_{\mathrm{loss}} = \frac{\Delta p_{\mathrm{T}}}{p_{\mathrm{T}}} = 1 - R_{\mathrm{AA}}^{1/(n-2)} , \tag{7.9}$$

this was found to be proportional to N_{part}^a [Adl07a]. Therefore, one can fit the averaged $\langle R_{\mathrm{AA}} \rangle$ with a function $\langle R_{\mathrm{AA}} \rangle = (1 - S_0 N_{\mathrm{part}}^a)^{n-2}$ to obtain the exponent a which is predicted by theoretical models (GLV and PQM) to be $a \approx 2/3$ [Gyu00b, Loi07]. For $p_{\mathrm{T}} > 5$ GeV/c, the fit is shown together with the data in the right panel of Figure 7.18, it yields $a = 0.60 \pm 0.09$ with $S_0 = 0.0070 \pm 0.0035$. The fit has also been performed for $p_{\mathrm{T}} > 8$ GeV/c, resulting in $a = 0.63 \pm 0.12$ and $S_0 = 0.0057 \pm 0.0037$, which is consistent with the mentioned model predictions.

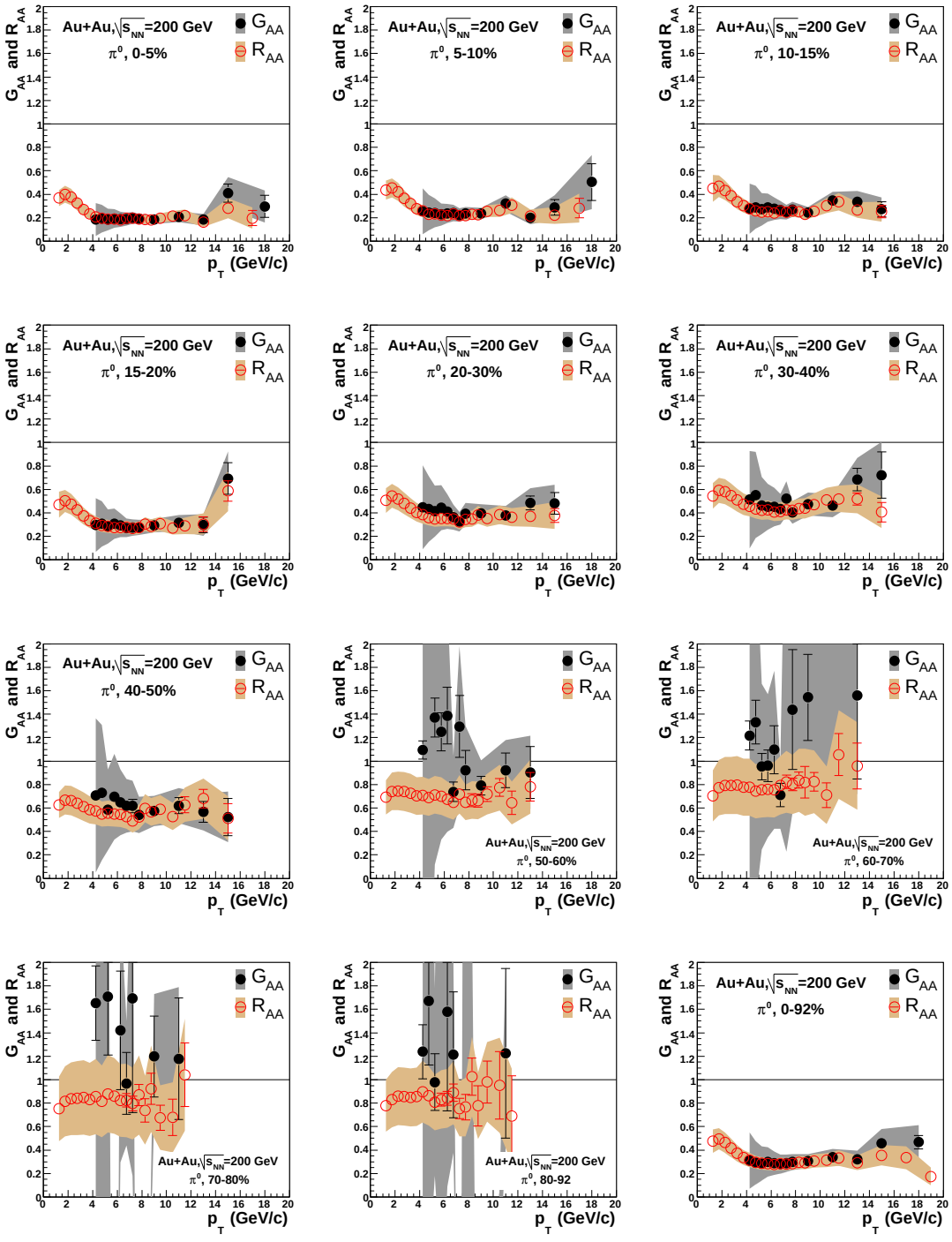

Figure 7.19: Model independent nuclear modification factor G_{AA} (black points) for neutral pions produced in Au+Au collisions at $\sqrt{s_{\mathrm{NN}}}$ = 200 GeV, for 11 different centrality selections and minimum bias, measured with PHENIX, compared with R_{AA} (red points). The error bars denote the point-to-point uncertainty, the boxes the p_{T}-correlated uncertainties. In case of R_{AA}, the scaling uncertainties from T_{AA} and $\sigma_{pp}^{\mathrm{inel}}$ are included in the boxes.

A model independent nuclear modification factor was proposed in 2004 [Rey04]. It expresses the suppression of π^0's at high $p_T$in terms of direct photons and is thus defined as

$$G_{AA}(p_T) = \frac{(\gamma_{direct}/\pi^0)|_{p+p}}{(\gamma_{direct}/\pi^0)|_{A+A}} , \tag{7.10}$$

with γ_{direct} and π^0 denoting the invariant yields of the respective particles. G_{AA} is a strictly data driven measure and uses no model assumptions about the collision geometry, therefore the uncertainty of $\langle T_{AA} \rangle$ can be neglected. On the other hand, the statistical and systematic uncertainties of the direct-photon measurement have to be considered now, though some uncertainties such as the energy scale partially cancel when calculating the ratios. If the direct photons followed strict $\langle T_{AA} \rangle$ scaling, G_{AA} would equal R_{AA}.

Both G_{AA} and R_{AA} are plotted in Figure 7.19 for different centrality selections and minimum bias. The uncertainties in R_{AA} are plotted differently as in Figure 7.7 as the normalization uncertainties now are included in the error boxes around the points by adding them in quadrature. The two quantities R_{AA} and G_{AA} agree well within the quoted uncertainties, and though R_{AA} includes model assumptions with additional uncertainties, it is the quantity with the smaller overall uncertainties. This is due to G_{AA} suffering from the large uncertainties in the direct-photon measurements, especially at lower p_T and in peripheral events.

The main experimental results of this thesis can be summarized in one picture as shown in Figure 7.20. Here, the nuclear modification factor R_{AA} is shown together for the three analyzed particles – π^0, η, and direct γ – for the most central Au+Au events. The suppression pattern of η and π^0 appears to be the same, while direct photons do not appear to be suppressed for $p_T < 15$ GeV/c.

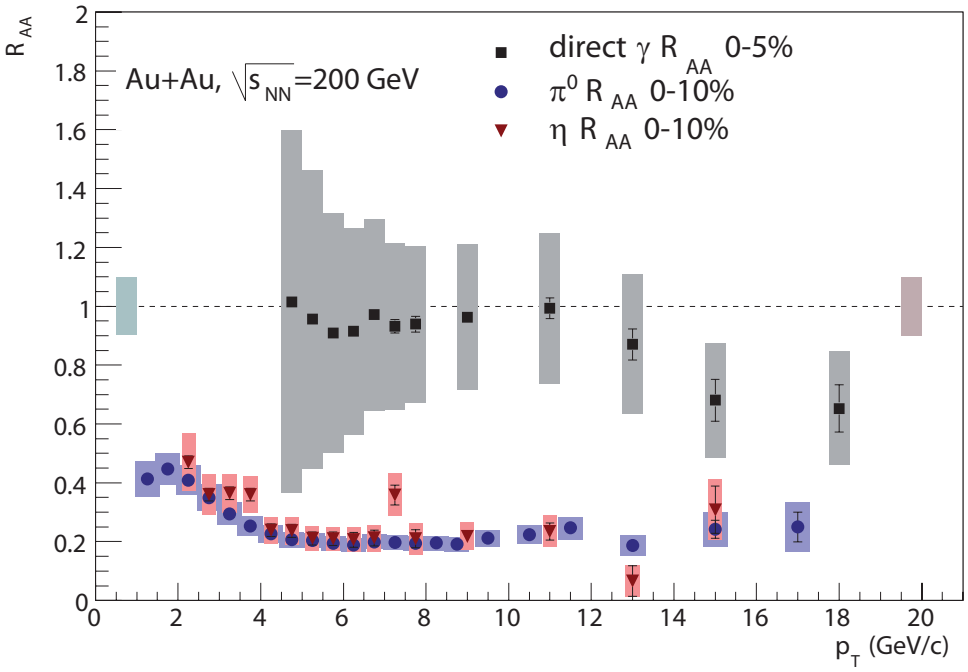

Figure 7.20: Nuclear modification factor R_{AA} for π^0's, η's, and direct photons produced in 0-10% Au+Au collisions at $\sqrt{s_{\mathrm{NN}}}$ = 200 GeV, measured with PHENIX. The error bars denote the point-to-point uncertainty, the boxes the p_{T}-correlated uncertainties.

8. Summary

```
So tell him, with the occurrents, more and less,
Which have solicited. The rest is silence.
```

W. Shakespeare - Hamlet

In this thesis, the measurement of three different particle spectra with the PHENIX detector in Au+Au collisions at center-of-mass energies of 200 GeV per nucleon is discussed. The invariant yields of neutral pions (π^0), η mesons, and direct photons are determined for different centrality selections and then used to calculate the so-called nuclear modification factor R_{AA}. The measured particles are used as probes to investigate the quark-gluon plasma (QGP), an extreme state of matter created in central Au+Au collisions at that energy.

One main goal of the RHIC accelerator complex and the four experiments built around the interaction points of the collider is the discovery and the study of the QGP, a state of matter where quarks and gluons – the partons – are the relevant degrees of freedom. Data taken during the first three years of operation have lead to strong evidence that such a state of matter has been created in central Au+Au collisions at top RHIC energies. Key signatures include, amongst others, a depletion of the yields of neutral pions and other hadrons when compared to the expectation from binary-scaled $p+p$ collisions, and the depletion of the away side jet in events where back-to-back jet correlations are expected. Both observations are manifestations of jet quenching. This jet quenching is explained by the interaction of a hard scattered parton with the strongly interacting medium where the parton loses energy. The effect can also be expressed in a change of parton fragmentation functions in the presence of a QGP. However, jet quenching alone is not a proof for the existence of the QGP.

Direct photons are another powerful probe for investigating heavy-ion collisions at RHIC. They are produced at every stage of such collisions, in initial hard scattering processes and as radiation from the hot hadron gas that evolves after the freeze-out of the QGP phase. The QGP itself also radiates thermal photons. These may be used as a thermometer for the medium. Furthermore, direct photons are produced by the interaction of a hard scattered parton with the medium and in the fragmentation process of such partons. Photons produced in initial hard scattering processes can traverse the strongly interacting medium unaffected since they do not interact strongly themselves. Therefore, they can in principle be used to study binary scaling of such hard scattering processes in Au+Au collisions. However, further initial and final state effects affect the

measured direct-photon yield. Therefore, the interpretation of the measurements relies on theoretical models incorporating different photon sources in an ultrarelativistic heavy-ion collision.

In this thesis, neutral pions and η mesons were measured via their decay into two photons. The photons are measured with the PHENIX EMCal, an invariant mass analysis with event mixing is used to extract the particles from the data. Corrections to account for detector effects are applied to obtain the Lorentz-invariant yields of the particles. Both mesons are measured over a broad p_{T} range, exceeding former measurements at the same energy. Using the same particles measured by PHENIX in $p+p$ collisions at the same energy, the nuclear modification factor is calculated. In central events, both mesons are suppressed by a factor of about 5 when compared to this binary-scaled $p+p$ reference. Towards more peripheral events, the suppression vanishes. The η/π^0 production ratio does not change as a function of centrality. Both mesons show the same suppression behaviour. At large transverse momenta, the suppression appears to be almost flat in terms of R_{AA}, with only a slight increase in slope. To account for possible initial state effects, an alternative nuclear modification factor R'_{AA} is calculated, using d+Au collisions as reference instead of $p+p$. This R'_{AA} is slightly steeper towards higher p_{T}, however, it is unclear how many possible initial state effects in Au+Au collisions are included by doing so.

The measured R_{AA} in the most central events is used to perform a statistical comparison to predictions from theoretical models. Such theoretical models are based on different medium parameters. They can be constrained with the measurement. The higher p_{T} reach and reduced uncertainties compared to older measurements allow a constraint of most of the parameters to $\leq 15-20\%$ at a 1σ confidence level. However, it has to be noted that this constraint is only valid under the assumption that the hypothesis is correct, in other words the data only constrain single parameters of the considered models. As an example, the initial gluon density in the GLV model can be constrained to $dn_g/dy = 1500^{+220}_{-270}(^{+380}_{-460})$ at 1σ (2σ), using the data.

The measurement of direct photons is performed with a statistical method, the main challenge in this measurement is the subtraction of photons from hadronic decays, especially from π^0's and η's. Further corrections are applied to account for detector effects and to subtract hadrons and leptons measured with the EMCal. The measurement results in Lorentz-invariant yields of direct photons in different centrality classes that are used to calculate the nuclear modification factor. In summary, direct photons appear to be unsuppressed, apart from central Au+Au collisions at high transverse momenta $p_{\mathrm{T}} \geq 15$ GeV/c, where a suppression of about 40% is seen. The data are consistent with theoretical models including initial and final state effects, taking into account the interactions of jets within a quark-gluon plasma. However, the large systematic uncertainties do not allow a detailed

distinction between different theoretical predictions. In the future, a reduction of these uncertainties might be achieved by measuring Au+Au and $p+p$ collisions during the same experimental run, using an identical detector setup. In such a case, many systematic uncertainties cancel in the calculation of R_{AA}.

Using the measured π^0 and direct-photon spectra, a model independent nuclear modification factor is calculated. It does not show any significant deviation from the R_{AA} calculated under the assumption of binary scaling. The suppression of π^0's can be regarded as a constant fractional energy loss. The N_{part} dependence of R_{AA} is consistent with such energy loss model predictions.

In summary, the results from this thesis allow a more detailed understanding, and a step from the qualitative observation of the quark-gluon plasma created in central Au+Au collisions at RHIC to a quantitative description of the properties of the medium.

Zusammenfassung

```
Ich war, ich bin, ich werde sein!
```

R. Luxemburg

In dieser Arbeit wird die Messung von drei verschiedenen Teilchenspektren mit dem PHENIX-Detektor in Au+Au-Kollisionen bei Schwerpunktenergien von 200 GeV pro Nukleon diskutiert. Die invarianten Transversalimpulsverteilungen neutraler Pionen (π^0), Eta-Mesonen und direkter Photonen werden für verschiedene Zentralitätsauswahlen bestimmt und dazu benutzt, den so genannten nuklearen Modifikationsfaktor R_{AA} zu berechnen. Die gemessenen Teilchen werden als Sonden benutzt, um das Quark-Gluon-Plasma zu untersuchen, einen extremen Materiezustand, der in zentralen Au+Au-Kollisionen bei dieser Energie erzeugt wird.

Ein Hauptziel des RHIC-Beschleuniger-Komplexes und der vier Experimente, die um die Interaktions-Punkte des Beschleunigers gebaut worden sind, ist die Entdeckung und die Untersuchung des QGP, eines Materiezustands, in dem Quarks und Gluonen - die Partonen - die relevanten Freiheitsgrade darstellen. Daten, die während der ersten drei Betriebsjahre aufgenommen wurden, führten zu starken Hinweisen, dass ein solcher Materiezustand in zentralen Au+Au-Kollisionen bei höchsten RHIC-Energien erzeugt worden ist. Entscheidende Hinweise beinhalten, neben weiteren, eine Verminderung der Anzahl neutraler Pionen im Vergleich zur Erwartung aus binär skalierten $p+p$-Kollisionen, sowie das Verschwinden des Jets auf der abgewandten Seite in Ereignissen, in denen entgegengesetzte Korrelationen von Jets erwartet werden. Beide Beobachtungen sind Erscheinungsformen des Jet-Quenchings. Dieses Jet-Quenching wird erklärt durch die Wechselwirkung eines hart gestreuten Partons mit dem stark wechselwirkenden Medium, wobei das Parton Energie verliert. Dieser Effekt kann auch als eine Änderung der Parton-Fragmentationsfunktion in Gegenwart eines QGP erklärt werden. Allerdings ist Jet-Quenching alleine kein Beweis für das Vorhandensein eines QGPs.

Direkte Photonen sind eine weitere, mächtige Sonde, um Schwerionenkollisionen bei RHIC zu untersuchen. Sie werden in jeder Phase solcher Kollisionen erzeugt, in anfänglichen harten Streuprozessen und aufgrund von Abstrahlung des heißen Hadronengases, das nach dem Ausfrieren der QGP-Phase entsteht. Das QGP selbst strahlt

ebenfalls thermische Photonen ab, die als Thermometer für das Medium benutzt werden können. Darüber hinaus werden direkte Photonen durch die Wechselwirkung eines hart gestreuten Partons mit dem Medium sowie während des Fragmentationsprozesses solcher Partonen erzeugt. Photonen, die in initialen harten Streuprozessen erzeugt werden, können das stark wechselwirkende Medium unbeeinflusst durchqueren, da sie selbst nicht der starken Wechselwirkung unterliegen. Daher können sie prinzipiell benutzt werden, um binäre Skalierung solcher harter Streuprozesse in Au+Au-Kollisionen zu untersuchen. Allerdings beeinflussen weitere Effekte des Anfangs- wie des Endzustands die gemessenen Transversalimpulsverteilungen direkter Photonen. Deshalb beruht die Interpretation der Messungen auf theoretischen Modellen, die verschiedene Photonenquellen in ultrarelativistischen Schwerionenkollisionen einbeziehen.

In der vorliegenden Arbeit wurden neutrale Pionen und η-Mesonen über ihren Zerfall in zwei Photonen gemessen. Die Photonen werden mit dem PHENIX EMCal gemessen, eine invariante Massen-Analyse mit event mixing wurde benutzt, um die Teilchen aus den Daten zu extrahieren. Korrekturen, die Detektoreffekte berücksichtigen, werden angewendet, um die Lorentz-invarianten Transversalimpulsverteilungen der Teilchen zu erhalten. Beide Mesonen werden über einen großen p_{T}-Bereich gemessen, der frühere Messungen bei der gleichen Energie übertrifft. Mittels der PHENIX-Messungen derselben Teilchen in $p+p$-Kollisionen bei der gleichen Energie wird der nukleare Modifikationsfaktor berechnet. In zentralen Kollisionen sind beide Mesonen mit einem Faktor von etwa 5 unterdrückt im Vergleich zu der binär skalierten $p+p$-Referenz. Hin zu periphereren Kollisionen verschwindet die Unterdrückung. Das η/π^0-Produktionsverhältnis zeigt keine Änderung als Funktion der Zentralität, dies macht deutlich, dass beide Mesonen das gleiche Unterdrückungsverhalten aufweisen. Bei hohen Transversalimpulsen erscheint die Unterdrückung fast flach gegen R_{AA}, mit einem nur leichten Anstieg. Um mögliche Effekte des Eingangszustands zu berücksichtigen, wird ein alternativer nuklearer Modifikationsfaktor R'_{AA} berechnet, bei dem d+Au-Kollisionen als Referenz anstelle von $p+p$ benutzt werden. Dieses R'_{AA} ist etwas steiler hin zu höherem p_{T}, allerdings ist unklar, wie viele der möglichen Effekte des Eingangszustands in Au+Au-Kollisionen hierdurch berücksichtigt werden.

Das gemessene R_{AA} in den zentralsten Kollisionen wird benutzt, um einen statistischen Vergleich zu Vorhersagen theoretischer Modelle anzustellen. Solche theoretischen Modelle basieren auf verschiedenen Medium-Parametern, die mit Hilfe der Messung eingeschränkt werden können. Die größere p_{T}-Reichweite und kleinere Messunsicherheiten im Vergleich mit älteren Messungen erlauben die Einschränkung der meisten dieser Parameter mit $\leq 15-20\%$ bei einem 1σ-Vertrauenslevel. Allerdings muss beachtet werden, dass diese Einschränkung nur stichhaltig ist unter der Annahme, dass die Hypothese korrekt ist, anders gesagt schränken die Daten nur die konkreten Para-

meter der betrachteten Modelle ein. Beispielsweise wird die initiale Gluonendichte im GLV-Modell mit Hilfe der Daten zu $dn_g/dy = 1500^{+220}_{-270}(^{+380}_{-460})$ bei 1σ (2σ) eingeschränkt.

Die Messung direkter Photonen wird mit einer statistischen Methode durchgeführt, die größte Herausforderung dieser Messung ist die Subtraktion von Photonen aus Zerfällen von Hadronen, insbesondere von π^0's und η's. Weitere Korrekturen werden angewendet, um Detektoreffekte zu berücksichtigen und um Hadronen und Leptonen, die vom EMCal gemessen werden, zu subtrahieren. Die Messung hat Lorentz-invariante Wirkungsquerschnitte direkter Photonen in verschiedenen Zentralitätsauswahlen zum Ergebnis, die dazu benutzt werden, den nuklearen Modifikationsfaktor zu berechnen. Generell erscheinen direkte Photonen nicht unterdrückt, außer in zentralen Au+Au-Kollisionen bei hohen Transversalimpulsen $p_{\mathrm{T}} \geq 15$ GeV/c, wo eine Unterdrückung von etwa 40% sichtbar ist. Die Daten sind konsistent mit theoretischen Modellen, die Effekte des Eingangs- sowie des Endzustands beinhalten und die Interaktionen von Jets mit dem Quark-Gluon-Plasma berücksichtigen. Allerdings erlauben die großen systematischen Unsicherheiten keine detaillierte Unterscheidung zwischen verschiedenen theoretischen Vorhersagen. In der Zukunft könnte eine Verringerung dieser Unsicherheiten erreicht werden, indem Au+Au- und $p+p$-Kollisionen während derselben Strahlzeit des Experiments gemessen werden, wobei ein identischer Detektoraufbau benutzt wird. In diesem Fall kürzen sich viele systematische Unsicherheiten bei der Berechnung von R_{AA}.

Unter Benutzung der gemessenen Spektren von π^0's und direkten Photonen wird ein modellunabhängiger nuklearer Modifikationsfaktor berechnet. Dieser weicht nicht signifikant vom R_{AA} ab, das unter der Annahme von binärer Skalierung bestimmt wurde. Die Unterdrückung der π^0's kann als ein konstanter partieller Energieverlust betrachtet werden. Die N_{part}-Abhängigkeit von R_{AA} ist konsistent mit Vorhersagen solcher Energieverlust-Modelle.

Zusammenfassend erlauben die Ergebnisse dieser Arbeit ein detaillierteres Verständnis sowie einen Schritt von qualitativen Beobachtungen des Quark-Gluon-Plasmas, das in zentralen Au+Au-Kollisionen am RHIC erzeugt wird, hin zu einer quantitativen Beschreibung der Eigenschaften des Mediums.

A. Kinematic Variables

Ultrarelativistic reactions are described by different kinematic variables to simplify changing the frame of reference (see [Ams08, Won94]).
In high energy physics particles are described with the help of the four momentum

$$p^\mu = (E, \vec{p}) = (E, p_x, p_y, p_z) \; . \tag{A.1}$$

Here, E is the energy of a particle while $\vec{p}$ denotes its momentum in cartesic coordinates. In this notation, the variables c and $\hbar$ are set to $c \equiv \hbar \equiv 1$. Free particles with a rest mass m_0 follow the relativistic energy momentum relation

$$E^2 = m_0^2 + \vec{p}^{\,2} \; . \tag{A.2}$$

The norm of the four momentum p^μ, the invariant mass

$$m_{inv}^2 = p^\mu p_\mu = -\vec{p} \cdot \vec{p} + E^2 \tag{A.3}$$

is Lorentz invariant. The Mandelstam variable s, the squared sum of the momenta of the two scattering particles

$$s = (p_1^\mu + p_2^\mu)^2 \; , \tag{A.4}$$

is used to denote the energy of a collision in its center of mass system. The overall collision energy is given by $\sqrt{s}$.
The z axis of the coordinate system in accelerator experiments is determined by the beam axis. So the three momentum of a particle can be split into two components, the longitudinal momentum p_L and the transverse momentum p_T:

$$p_L = p \cdot \cos\vartheta = p_z \tag{A.5}$$

$$p_T = p \cdot \sin\vartheta = \sqrt{p_x^2 + p_y^2}. \tag{A.6}$$

ϑ denotes the angle of the propagation direction of the particle towards the beam axis, $p = |\vec{p}|$ is the norm of the three momentum. Unlike the transverse momentum p_T, the longitudinal momentum p_L is not Lorentz invariant. Thus the longitudinal velocity $\beta_L = p_L/E$ of particles is described by the rapidity y:

$$y = \operatorname{atanh}(\beta_L) \tag{A.7}$$

$$= \frac{1}{2} \ln \frac{E + p_L}{E - p_L}. \tag{A.8}$$

The rapidity shows an additive behavior when the frame of reference is changed to a system moving with the relative velocity β with respect to the first system

$$y' = y + \text{atanh}(\beta), \tag{A.9}$$

so the shape of the rapidity distribution of a particle is not affected by a change of the frame of reference. The following equations hold:

$$E = m_T \cdot \cosh(y) \tag{A.10}$$

$$p_L = m_T \cdot \sinh(y)\ . \tag{A.11}$$

Here $m_T = \sqrt{p_T^2 + m_0^2}$ denotes the so-called transverse mass of a particle.
If $E \gg m_0$, the rapidity can be approximated by the pseudorapidity η:

$$\eta = \frac{1}{2} \ln \frac{p + p_L}{p - p_L} \tag{A.12}$$

$$= -\ln \left[\tan \left(\frac{\vartheta}{2} \right) \right]\ . \tag{A.13}$$

The pseudorapidity of a particle can be determined with the emission angular to the beam axis ϑ, thus the pseudorapidity is easier to determine in experiments. According to (A.10) and (A.11) it is:

$$p = p_T \cdot \cosh(\eta) \tag{A.14}$$

$$p_L = p_T \cdot \sinh(\eta)\ . \tag{A.15}$$

B. Lorentz Invariant Cross Section

The Lorentz invariant cross section $Ed^3\sigma/dp^3$ is often used to describe the particle production in ultrarelativistic reactions (see [Ams08, Won94]). The following relations are valid:

$$\begin{aligned}
\sigma_{inv} \equiv E\frac{d^3\sigma}{d\vec{p}^3} &= E\frac{1}{p_T}\frac{d^3\sigma}{dp_T\,d\varphi\,dp_L} \\
&\overset{\frac{dp_L}{dy}=E}{=} \frac{1}{p_T}\frac{d^3\sigma}{dp_T\,d\varphi\,dy} \\
&\overset{\varphi\text{ -symmetry}}{=} \frac{1}{2\pi p_T}\frac{d^2\sigma}{dp_T\,dy} \qquad \text{(B.1)} \\
&= \frac{1}{2\pi m_T}\frac{d^2\sigma}{dm_T\,dy}\,. \qquad \text{(B.2)}
\end{aligned}$$

Looking at one special particle species Y produced in inelastic reactions, the integration of the Lorentz invariant cross section leads to the product of the average number of particles produced in each inelastic reaction and the total inelastic cross section:

$$\int E\frac{d^3\sigma}{d\vec{p}^3}\,d\vec{p}^3 = \langle n_Y\rangle\cdot\sigma_{in}\,. \qquad \text{(B.3)}$$

The Lorentz invariant cross section is determined experimentally as

$$E\frac{d^3\sigma}{d\vec{p}^3} = \frac{1}{2\pi p_T N_{in}}\cdot\frac{\Delta N_Y}{\Delta p_T\,\Delta y}\cdot\sigma_{in}\,. \qquad \text{(B.4)}$$

Here, ΔN_Y is the overall number of particles measured in the transverse momentum interval $[p_T, p_T+\Delta p_T]$ and the rapidity interval $[y, y+\Delta y]$ in N_{in} inelastic reactions. Sometimes it is easier to measure the yield per event instead of the cross section as it does not depend on the total inelastic cross section. Therefore the Lorentz invariant cross section is divided by the total inelastic cross section σ_{in}:

$$E\frac{d^3N}{d\vec{p}^3} = \frac{1}{2\pi p_T N_{in}}\cdot\frac{\Delta N_Y}{\Delta p_T\,\Delta y}\,. \qquad \text{(B.5)}$$

C. Values of N_{part}, N_{coll}, and T_{AA}

Centrality	N_{part}	N_{coll}	T_{AA}
0-5%	351.4 ± 2.9	1065.4 ± 105.3	25.37 ± 1.77
5-10%	299.0 ± 3.8	845.4 ± 82.1	20.13 ± 1.36
10-15%	253.9 ± 4.3	672.4 ± 66.8	16.01 ± 1.15
15-20%	215.3 ± 5.3	532.7 ± 52.1	12.68 ± 0.86
20-30%	166.6 ± 5.4	373.8 ± 39.6	8.90 ± 0.72
30-40%	114.2 ± 4.4	219.8 ± 22.6	5.23 ± 0.44
40-50%	74.4 ± 3.8	120.3 ± 13.7	2.86 ± 0.28
50-60%	45.5 ± 3.3	61.0 ± 9.9	1.45 ± 0.23
60-70%	25.7 ± 3.8	28.5 ± 7.6	0.68 ± 0.18
70- 80%	13.4 ± 3.0	12.4 ± 4.2	0.30 ± 0.10
80-92%	6.3 ± 1.2	4.9 ± 1.2	0.12 ± 0.03
0- 92%	108.4 ± 5.1	233.1 ± 34.7	6.30 ± 0.87

Table C.1: Values of N_{part}, N_{coll}, and T_{AA} from Glauber calculations [Rey03].

D. List of Analyzed Runs

108714	108769	108795	108803	108804	108805	108807	108814	108816	108926
108939	108940	108942	108945	109005	109012	109014	109016	109187	109189
109192	109196	109214	109217	109220	109222	109238	109240	109246	109252
109291	109293	109295	109297	109361	109363	109420	109422	109424	109426
109470	109479	109482	109549	109550	109569	109576	109587	109593	109594
109654	109655	109656	109657	109659	109664	109672	109675	109677	109679
109684	109690	109691	109693	109699	109763	109764	109767	109769	109820
109821	109822	110264	110265	110267	110269	110279	110284	110291	110292
110294	110297	110300	110301	110303	110350	110354	110364	110367	110370
110383	110385	110387	110455	110457	110462	110540	110541	110542	110544
110545	110568	110601	110604	110628	110651	110652	110655	110663	110665
110667	110669	110671	110683	110687	110689	110698	110704	110706	110708
110713	110754	110756	110785	110790	110793	110796	110807	110811	110886
110888	110890	110892	110912	110915	110920	110977	110981	110983	111006
111008	111021	111023	111027	111029	111031	111033	111355	111364	111396
111402	111413	111423	111467	111485	111497	111498	111502	111528	111530
111531	111532	111538	111539	111544	111555	111556	111560	111583	111592
111593	111603	111687	111688	111695	111697	111699	111701	111705	111711
111714	111716	111743	111824	111830	111831	111838	111893	111894	111895
111953	111955	111957	111959	111966	111982	111984	111985	112059	112061
112064	112066	112122	112124	112128	112184	112186	112232	112233	112234
112283	112284	112286	112287	112288	112318	112320	112323	112403	112411
112475	112476	112480	112482	112504	112506	112507	112509	112511	112519
112526	112527	112657	112660	112661	112666	113105	113107	113108	113194
113198	113201	113202	113204	113232	113284	113286	113288	113290	113464
113466	113468	113528	113529	113530	113562	113564	113570	113573	113574
113575	113688	113689	113690	113691	113695	113696	113703	113706	113716
113838	113839	113840	113842	113851	113854	113871	113873	113875	113877
113879	113902	113904	113975	113982	113983	113999	114001	114003	114066
114069	114074	114075	114076	114089	114102	114143	114144	114147	114276
114278	114280	114287	114295	114296	114329	114330	114332	114334	114399
114405	114406	114414	114432	114467	114468	114471	114548	114594	114600
114602	114614	114616	114618	114621	114659	114660	114675	114681	114802
114805	114808	114836	114837	114884	114887	114901	114927	114929	114936
114937	114965	114967	114970	114971	114972	114993	114994	114995	114997

Table D.1: List of analyzed Au+Au runs at $\sqrt{s_{\mathrm{NN}}}$ = 200 GeV.

115026	115031	115050	115069	115070	115077	115087	115179	115180	115182
115185	115191	115204	115205	115226	115227	115237	115343	115345	115347
115350	115358	115361	115365	115366	115500	115501	115502	115503	115778
115780	116061	116085	116135	116137	116138	116142	116146	116160	116161
116163	116167	116169	116178	116184	116186	116192	116228	116229	116236
116237	116313	116315	116317	116321	116338	116341	116353	116359	116419
116421	116423	116425	116427	116468	116472	116533	116534	116537	116539
116544	116546	116547	116551	116566	116571	116572	116574	116609	116617
116620	116636	116637	116639	116642	116657	116659	116662	116690	116701
116707	116708	116742	116743	116746	116747	116749	116776	116777	116831
116833	116842	116843	116917	116921	116922	116927	116928	116929	116933
117118	117119	117120	117122	117128	117173	117223	117225	117226	117253
117255	117256	117258	117280	117295	117297	117303	117311	117327	117328
117427	117428	117429	117430	117431	117433	117435	117441	117443	117447
117455	117457	117543	117546	117547	117574	117575	117576	117579	117581
117583	117586	117590	117592	117604	117606	117607	117609	117613	117684
117685	117686	117694	117716	117725	117759	117760	117764	117766	117768
117770	117772	117776	117779	117781	117821	117823	117825	117826	117827
117847	117848	117849	117852	117921	117922	117925	117927	118019	118024
118028	118038	118042	118211	118252	118254	118301	118304	118312	118314
118321	118435	118438	118440	118446	118457	118458	118462	118464	118468
118469	118674	118676	118751	118754	118767	118770	118777	118870	118901
118903	118911	118912	118923	118929	118932	118934	119100	119108	119133
119134	119138	119139	119141	119267	119268	119269	119314	119326	119327
119329	119380	119381	119386	119387	119417	119420	119421	119428	119433
119440	119448	119451	119452	119550	119618	119621	119684	119687	119688
119690	119691	119763	119768	119917	119919	119921	119925	119926	119928
119969	120039	120045	120048	120057	120058	120059	120060	120061	120062
120063	120078	120079	120081	120082	120194	120199	120200	120214	120231
120232	120234	120237	120238	120240	120246	120261	120269	120274	120278
120279	120286	120397	120404	120407	120408	120410	120411	120416	120419
120420	120422	120427	120428	120478	120479	120480	120483	120489	120496
120497	120499	121224	121266	121271	121275	121287	121288	121289	121291
121292	121293	121294	121295	121296	121343	121344	121347	121401	121406
121408	121449	121458	121463	121465	121510	121511	121513	121523	121526
121531	121534	121543	121544	121545	121548	121554	121809	121848	121863
121867	121954	121956	121959	121961	121967	122041	122212	122213	122214
122215	122223								

Table D.2: List of analyzed Au+Au runs at $\sqrt{s_{\mathrm{NN}}}$ = 200 GeV (continued).

E. Detector Hit Maps

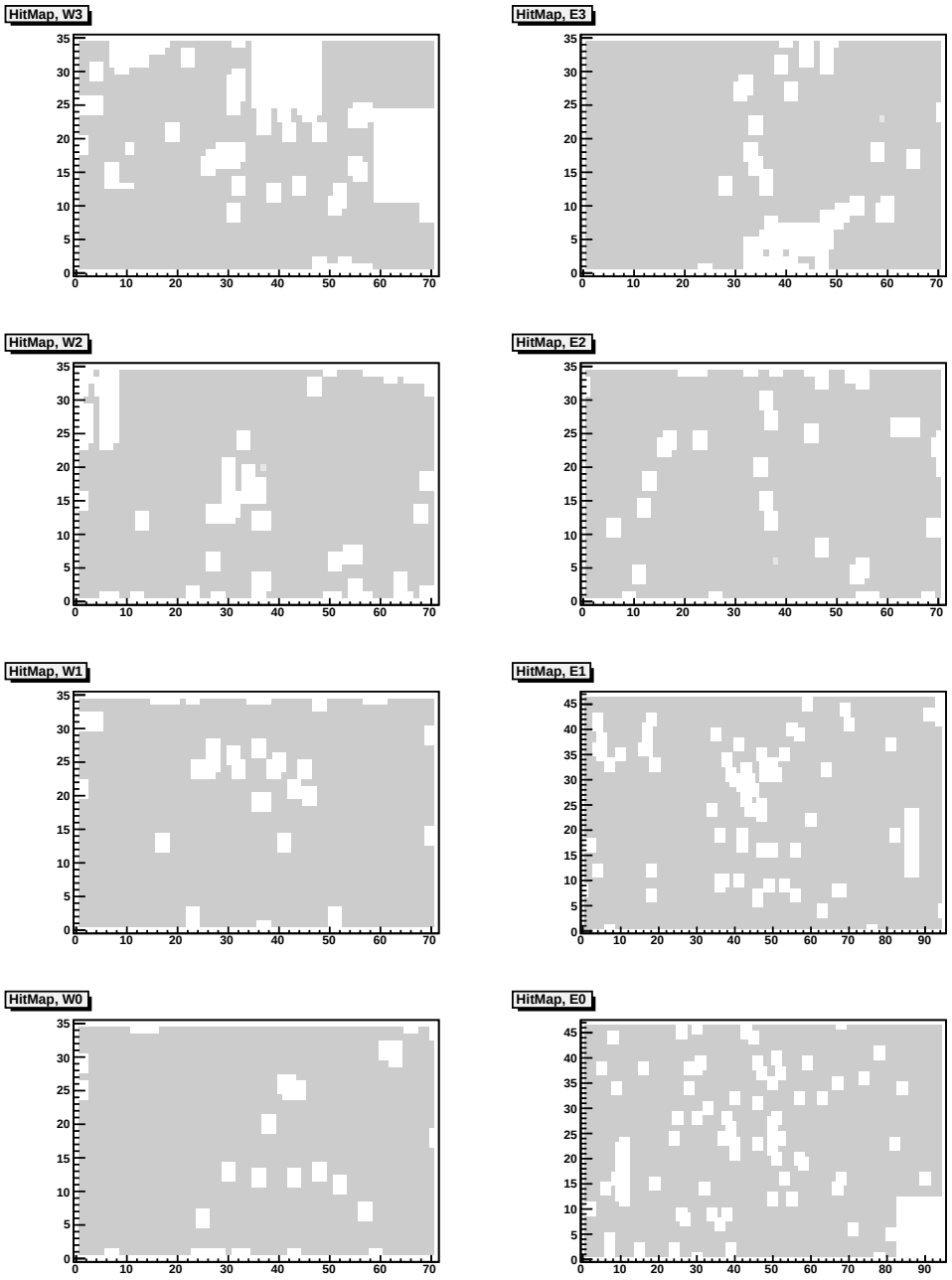

Figure E.1: Hitmaps for the eight EMCal sectors. Masked detector modules appear white on this plot.

F. π^0 Data Tables

p_T	yield	statistical uncertainty	systematic uncertainty	total uncertainty
1.25	3.22728	0.0291046	0.316609	0.317944
1.75	0.568938	0.00518151	0.0491136	0.0493861
2.25	0.113108	0.00101133	0.0102048	0.0102548
2.75	0.0250122	0.000237378	0.00234458	0.00235656
3.25	0.00622282	6.3334e-05	0.000593786	0.000597154
3.75	0.00181086	1.99717e-05	0.000172739	0.000173889
4.25	0.000605483	7.5763e-06	5.70823e-05	5.75829e-05
4.75	0.000236406	3.32814e-06	2.18641e-05	2.21159e-05
5.25	0.000100342	1.60647e-06	9.06622e-06	9.20745e-06
5.75	4.76866e-05	9.07845e-07	4.23244e-06	4.32871e-06
6.25	2.36092e-05	5.44198e-07	2.07814e-06	2.14821e-06
6.75	1.35626e-05	3.47291e-07	1.16785e-06	1.2184e-06
7.25	7.65173e-06	2.36747e-07	6.64846e-07	7.05741e-07
7.75	4.30789e-06	1.61747e-07	3.81128e-07	4.1403e-07
8.25	2.52554e-06	1.17533e-07	2.34575e-07	2.62372e-07
8.75	1.54367e-06	9.00516e-08	1.55058e-07	1.7931e-07
9.5	8.55023e-07	4.5727e-08	8.58509e-08	9.72694e-08
10.5	4.13731e-07	2.99103e-08	4.87383e-08	5.71844e-08
11.5	2.0269e-07	1.98282e-08	2.82704e-08	3.45308e-08
13	5.57166e-08	6.69266e-09	9.91385e-09	1.19614e-08
15	2.98015e-08	4.78021e-09	7.11689e-09	8.57325e-09
17	7.62725e-09	2.49918e-09	3.20166e-09	4.06159e-09

Table F.1: Lorentz invariant yield of π^0's in the 0-5% most central Au+Au events at $\sqrt{s_{NN}}$ = 200 GeV.

p_T	yield	statistical uncertainty	systematic uncertainty	total uncertainty
1.25	3.01759	0.0288558	0.311514	0.312848
1.75	0.513978	0.00448273	0.0443482	0.0445742
2.25	0.100698	0.000886598	0.00898697	0.0090306
2.75	0.0224036	0.000206579	0.00207214	0.00208241
3.25	0.00587748	5.72692e-05	0.000552709	0.000555668
3.75	0.00170443	1.80256e-05	0.000160152	0.000161163
4.25	0.000595124	6.97438e-06	5.52005e-05	5.56394e-05
4.75	0.000218694	2.98274e-06	1.99317e-05	2.01537e-05
5.25	9.85755e-05	1.49746e-06	8.7599e-06	8.88697e-06
5.75	4.48142e-05	8.26899e-07	3.91301e-06	3.99942e-06
6.25	2.24871e-05	4.99415e-07	1.93566e-06	1.99905e-06
6.75	1.29343e-05	3.26909e-07	1.09876e-06	1.14636e-06
7.25	6.75563e-06	2.18723e-07	5.80564e-07	6.20399e-07
7.75	3.89755e-06	1.57355e-07	3.47867e-07	3.81801e-07
8.25	2.49785e-06	1.16263e-07	2.30026e-07	2.57738e-07
8.75	1.51627e-06	8.55482e-08	1.49008e-07	1.71819e-07
9.5	8.82852e-07	4.37686e-08	8.34262e-08	9.42106e-08
10.5	4.01502e-07	2.80304e-08	4.49819e-08	5.30007e-08
11.5	2.23867e-07	1.97712e-08	2.89173e-08	3.50302e-08
13	5.79215e-08	7.68616e-09	1.08598e-08	1.33046e-08
15	1.86495e-08	3.75619e-09	5.05627e-09	6.2988e-09
17	8.64017e-09	2.57273e-09	3.39709e-09	4.26136e-09

Table F.2: Lorentz invariant yield of π^0's in the 5-10% most central Au+Au events at $\sqrt{s_{NN}}$ = 200 GeV.

p_T	yield	statistical uncertainty	systematic uncertainty	total uncertainty
1.25	2.48159	0.0234073	0.499996	0.500544
1.75	0.421044	0.00360135	0.0465857	0.0467247
2.25	0.0822518	0.000710659	0.00828276	0.00831319
2.75	0.0189002	0.000169639	0.00186223	0.00186994
3.25	0.00492435	4.69431e-05	0.000480749	0.000483035
3.75	0.00148987	1.53913e-05	0.000143498	0.000144321
4.25	0.000510339	5.80493e-06	4.82081e-05	4.85563e-05
4.75	0.00019665	2.58404e-06	1.81578e-05	1.83408e-05
5.25	8.35829e-05	1.29236e-06	7.5435e-06	7.6534e-06
5.75	4.02739e-05	7.18214e-07	3.55744e-06	3.62921e-06
6.25	1.96518e-05	4.36107e-07	1.72217e-06	1.77653e-06
6.75	1.12783e-05	2.8604e-07	9.70727e-07	1.01199e-06
7.25	6.06596e-06	1.92442e-07	5.24775e-07	5.58948e-07
7.75	3.68041e-06	1.43363e-07	3.28264e-07	3.58204e-07
8.25	2.1585e-06	1.05117e-07	2.05304e-07	2.3065e-07
8.75	1.21729e-06	7.56549e-08	1.25891e-07	1.46875e-07
9.5	7.0274e-07	3.81257e-08	6.94233e-08	7.92033e-08
10.5	3.69365e-07	2.62273e-08	4.20715e-08	4.9577e-08
11.5	1.96226e-07	1.76701e-08	2.56583e-08	3.11542e-08
13	5.71388e-08	6.76031e-09	9.64809e-09	1.17808e-08
15	1.70033e-08	3.55229e-09	4.73828e-09	5.922e-09

Table F.3: Lorentz invariant yield of π^0's in the 10-15% most central Au+Au events at $\sqrt{s_{NN}}$ = 200 GeV.

p_T	yield	statistical uncertainty	systematic uncertainty	total uncertainty
1.25	2.05157	0.020307	0.366797	0.367358
1.75	0.357349	0.00309366	0.0369982	0.0371273
2.25	0.0711771	0.000615479	0.00684347	0.00687109
2.75	0.016457	0.000148503	0.00156602	0.00157305
3.25	0.00430246	4.10743e-05	0.000408195	0.000410256
3.75	0.001305	1.32935e-05	0.000122519	0.000123238
4.25	0.000452906	5.1365e-06	4.17605e-05	4.20752e-05
4.75	0.000176904	2.28839e-06	1.59388e-05	1.61022e-05
5.25	7.6366e-05	1.15206e-06	6.70387e-06	6.80214e-06
5.75	3.52298e-05	6.44619e-07	3.03146e-06	3.09924e-06
6.25	1.78649e-05	3.91235e-07	1.51403e-06	1.56376e-06
6.75	9.73397e-06	2.61328e-07	8.21652e-07	8.62209e-07
7.25	5.21589e-06	1.74573e-07	4.4373e-07	4.76836e-07
7.75	3.09312e-06	1.30016e-07	2.76017e-07	3.05106e-07
8.25	2.081e-06	9.88098e-08	1.90426e-07	2.14535e-07
8.75	1.2169e-06	7.36693e-08	1.21751e-07	1.42304e-07
9.5	6.67459e-07	3.6137e-08	6.3928e-08	7.34348e-08
10.5	2.62043e-07	2.17036e-08	3.17177e-08	3.84325e-08
11.5	1.33236e-07	1.58018e-08	2.15676e-08	2.67368e-08
13	5.20865e-08	1.07185e-08	1.20087e-08	1.60965e-08
15	3.13855e-08	4.63604e-09	7.08669e-09	8.46842e-09

Table F.4: Lorentz invariant yield of π^0's in the 15-20% most central Au+Au events at $\sqrt{s_{NN}}$ = 200 GeV.

p_T	yield	statistical uncertainty	systematic uncertainty	total uncertainty
1.25	1.55404	0.0142289	0.206704	0.207193
1.75	0.272065	0.00226803	0.0242831	0.0243888
2.25	0.0548095	0.000458427	0.00479473	0.0048166
2.75	0.0130543	0.000111692	0.00116507	0.00117041
3.25	0.00357628	3.14767e-05	0.000323232	0.000324761
3.75	0.00110801	1.02533e-05	9.99277e-05	0.000100452
4.25	0.000392348	3.92694e-06	3.48766e-05	3.5097e-05
4.75	0.00015208	1.68295e-06	1.32094e-05	1.33162e-05
5.25	6.5368e-05	8.33286e-07	5.53432e-06	5.5967e-06
5.75	3.16112e-05	4.65349e-07	2.60723e-06	2.64844e-06
6.25	1.60481e-05	2.82495e-07	1.29885e-06	1.32921e-06
6.75	8.53936e-06	1.78827e-07	6.79127e-07	7.02277e-07
7.25	4.41476e-06	1.21553e-07	3.55337e-07	3.75552e-07
7.75	2.75155e-06	8.83359e-08	2.24175e-07	2.40952e-07
8.25	1.6778e-06	6.65989e-08	1.43245e-07	1.5797e-07
8.75	1.13946e-06	5.00065e-08	9.95e-08	1.11359e-07
9.5	5.36653e-07	2.52966e-08	4.85402e-08	5.47363e-08
10.5	2.59697e-07	1.58589e-08	2.72019e-08	3.14873e-08
11.5	1.17492e-07	1.01647e-08	1.45126e-08	1.77182e-08
13	4.45331e-08	4.16489e-09	6.73361e-09	7.91757e-09
15	1.41954e-08	2.19419e-09	3.28013e-09	3.94635e-09

Table F.5: Lorentz invariant yield of π^0's in the 20-30% most central Au+Au events at $\sqrt{s_{NN}}$ = 200 GeV.

p_T	yield	statistical uncertainty	systematic uncertainty	total uncertainty
1.25	0.983268	0.00900056	0.116877	0.117223
1.75	0.173947	0.00148476	0.0146812	0.0147561
2.25	0.0360856	0.000301616	0.00305305	0.00306791
2.75	0.00871	7.44092e-05	0.000760863	0.000764493
3.25	0.00243192	2.15085e-05	0.000216481	0.000217546
3.75	0.000764287	7.03188e-06	6.81243e-05	6.84863e-05
4.25	0.000274617	2.79303e-06	2.42023e-05	2.4363e-05
4.75	0.0001079	1.24025e-06	9.32163e-06	9.40378e-06
5.25	4.64592e-05	6.25132e-07	3.92107e-06	3.97059e-06
5.75	2.24067e-05	3.61585e-07	1.85358e-06	1.88852e-06
6.25	1.09056e-05	2.13792e-07	8.8594e-07	9.11371e-07
6.75	5.88737e-06	1.3974e-07	4.73506e-07	4.93696e-07
7.25	3.43647e-06	9.99511e-08	2.78835e-07	2.96208e-07
7.75	1.97898e-06	7.53102e-08	1.68919e-07	1.84947e-07
8.25	1.23462e-06	5.50668e-08	1.08422e-07	1.21604e-07
8.75	7.68295e-07	4.29013e-08	7.25313e-08	8.42692e-08
9.5	4.22984e-07	2.06709e-08	3.90084e-08	4.41468e-08
10.5	2.03584e-07	1.31329e-08	2.14604e-08	2.516e-08
11.5	9.87845e-08	8.68481e-09	1.2367e-08	1.51119e-08
13	3.6581e-08	3.65288e-09	5.59112e-09	6.67863e-09
15	8.9427e-09	1.8223e-09	2.43303e-09	3.0398e-09

Table F.6: Lorentz invariant yield of π^0's in the 30-40% most central Au+Au events at $\sqrt{s_{NN}}$ = 200 GeV.

p_T	yield	statistical uncertainty	systematic uncertainty	total uncertainty
1.25	0.618607	0.00548358	0.0354332	0.035855
1.75	0.107533	0.000899429	0.00744565	0.00749978
2.25	0.0225084	0.000188164	0.00176067	0.00177069
2.75	0.00559242	4.78795e-05	0.000469538	0.000471972
3.25	0.00159646	1.40757e-05	0.000138743	0.000139456
3.75	0.00051527	4.87529e-06	4.52212e-05	4.54833e-05
4.25	0.000189364	1.95536e-06	1.65022e-05	1.66177e-05
4.75	7.42999e-05	9.04561e-07	6.37711e-06	6.44095e-06
5.25	3.35087e-05	4.7032e-07	2.81339e-06	2.85243e-06
5.75	1.58792e-05	2.78021e-07	1.31459e-06	1.34367e-06
6.25	8.02748e-06	1.71444e-07	6.54687e-07	6.76763e-07
6.75	4.13572e-06	1.14659e-07	3.40043e-07	3.58854e-07
7.25	2.15286e-06	8.07906e-08	1.86058e-07	2.02841e-07
7.75	1.34422e-06	5.84007e-08	1.18596e-07	1.32196e-07
8.25	9.22881e-07	4.73125e-08	8.49855e-08	9.72678e-08
8.75	5.44247e-07	3.56467e-08	5.5428e-08	6.59011e-08
9.5	2.89569e-07	1.79159e-08	2.87048e-08	3.3837e-08
10.5	1.14985e-07	1.00703e-08	1.43379e-08	1.7521e-08
11.5	6.54361e-08	7.11944e-09	9.27621e-09	1.16934e-08
13	2.62054e-08	3.00973e-09	4.30416e-09	5.25208e-09
15	6.18069e-09	1.51478e-09	1.90058e-09	2.43038e-09

Table F.7: Lorentz invariant yield of π^0's in the 40-50% most central Au+Au events at $\sqrt{s_{NN}}$ = 200 GeV.

p_T	yield	statistical uncertainty	systematic uncertainty	total uncertainty
1.25	0.346496	0.00309251	0.0194869	0.0197307
1.75	0.06049	0.000526004	0.00412869	0.00416206
2.25	0.0128566	0.000108328	0.000991616	0.000997516
2.75	0.00328131	2.82508e-05	0.000271619	0.000273084
3.25	0.000960382	8.68506e-06	8.22546e-05	8.27118e-05
3.75	0.000314019	3.10678e-06	2.71473e-05	2.73245e-05
4.25	0.000117839	1.32164e-06	1.01134e-05	1.01994e-05
4.75	4.75336e-05	6.40747e-07	4.01893e-06	4.06968e-06
5.25	2.18425e-05	3.5644e-07	1.81155e-06	1.84629e-06
5.75	1.02766e-05	2.08069e-07	8.37943e-07	8.63389e-07
6.25	5.01e-06	1.35331e-07	4.09718e-07	4.3149e-07
6.75	2.58108e-06	9.08758e-08	2.16244e-07	2.34563e-07
7.25	1.60128e-06	6.76919e-08	1.37251e-07	1.53036e-07
7.75	8.41205e-07	4.78475e-08	8.17448e-08	9.47185e-08
8.25	5.2272e-07	4.29065e-08	5.6993e-08	7.13384e-08
8.75	3.22156e-07	2.6876e-08	3.64751e-08	4.53073e-08
9.5	1.7891e-07	1.53835e-08	2.02432e-08	2.54251e-08
10.5	8.56694e-08	8.42604e-09	1.10735e-08	1.39147e-08
11.5	3.40638e-08	5.33672e-09	6.18391e-09	8.16831e-09
13	1.52934e-08	2.38797e-09	3.01231e-09	3.84401e-09

Table F.8: Lorentz invariant yield of π^0's in the 50-60% most central Au+Au events at $\sqrt{s_{NN}}$ = 200 GeV.

p_T	yield	statistical uncertainty	systematic uncertainty	total uncertainty
1.25	0.164655	0.00154838	0.0168398	0.0169108
1.75	0.0294593	0.000272052	0.00230804	0.00232401
2.25	0.00638684	5.51748e-05	0.000514675	0.000517624
2.75	0.0016381	1.48314e-05	0.000137737	0.000138534
3.25	0.000491487	4.8366e-06	4.22888e-05	4.25644e-05
3.75	0.000162247	1.83644e-06	1.40191e-05	1.41389e-05
4.25	6.07074e-05	8.61426e-07	5.20768e-06	5.27845e-06
4.75	2.39405e-05	4.46526e-07	2.03236e-06	2.08083e-06
5.25	1.07895e-05	2.58003e-07	9.04586e-07	9.4066e-07
5.75	5.1972e-06	1.46855e-07	4.34977e-07	4.59098e-07
6.25	2.6311e-06	9.50701e-08	2.23896e-07	2.43244e-07
6.75	1.47947e-06	6.95608e-08	1.30898e-07	1.48233e-07
7.25	8.59041e-07	5.86111e-08	1.00785e-07	1.16588e-07
7.75	4.86698e-07	3.302e-08	4.95585e-08	5.95514e-08
8.25	3.06037e-07	2.50614e-08	3.41076e-08	4.23249e-08
8.75	1.85908e-07	3.07664e-08	3.33935e-08	4.54059e-08
9.5	9.58797e-08	9.08901e-09	1.16972e-08	1.48133e-08
10.5	3.66864e-08	5.39828e-09	6.22334e-09	8.2384e-09
11.5	2.60677e-08	4.43522e-09	5.00756e-09	6.68931e-09
13	8.74752e-09	1.78595e-09	2.08177e-09	2.74288e-09

Table F.9: Lorentz invariant yield of π^0's in the 60-70% most central Au+Au events at $\sqrt{s_{NN}}$ = 200 GeV.

p_T	yield	statistical uncertainty	systematic uncertainty	total uncertainty
1.25	0.0765202	0.000735505	0.00583488	0.00588105
1.75	0.0135098	0.000128955	0.00095889	0.000967522
2.25	0.00293515	2.61547e-05	0.000227393	0.000228892
2.75	0.000758792	7.30233e-06	6.26279e-05	6.30522e-05
3.25	0.000228385	2.52782e-06	1.94854e-05	1.96487e-05
3.75	7.55628e-05	1.03093e-06	6.51923e-06	6.60024e-06
4.25	2.90748e-05	5.17574e-07	2.51098e-06	2.56377e-06
4.75	1.14343e-05	2.85909e-07	9.90334e-07	1.03078e-06
5.25	5.48275e-06	1.52473e-07	4.71772e-07	4.958e-07
5.75	2.56144e-06	1.03148e-07	2.28419e-07	2.50629e-07
6.25	1.24447e-06	6.70154e-08	1.17427e-07	1.35204e-07
6.75	6.67948e-07	4.63784e-08	6.95645e-08	8.36072e-08
7.25	3.61909e-07	2.88428e-08	4.0219e-08	4.94921e-08
7.75	2.29692e-07	2.34787e-08	3.00909e-08	3.81669e-08
8.25	1.17554e-07	1.57526e-08	1.82522e-08	2.41099e-08
8.75	9.10131e-08	1.31358e-08	1.49068e-08	1.98687e-08
9.5	3.42437e-08	5.43339e-09	6.06395e-09	8.14206e-09
10.5	1.52693e-08	3.50761e-09	3.74534e-09	5.13136e-09
11.5	1.11971e-08	2.90113e-09	3.07204e-09	4.2254e-09

Table F.10: Lorentz invariant yield of π^0's in the 70-80% most central Au+Au events at $\sqrt{s_{NN}}$ = 200 GeV.

p_T	yield	statistical uncertainty	systematic uncertainty	total uncertainty
1.25	0.0312868	0.000306302	0.00248214	0.00250097
1.75	0.00543673	5.30899e-05	0.000390769	0.000394359
2.25	0.00118855	1.09104e-05	9.24827e-05	9.31241e-05
2.75	0.000304578	3.13675e-06	2.5167e-05	2.53617e-05
3.25	9.02869e-05	1.16649e-06	7.70524e-06	7.79304e-06
3.75	3.06719e-05	5.308e-07	2.65407e-06	2.70663e-06
4.25	1.20329e-05	2.82588e-07	1.04477e-06	1.08231e-06
4.75	4.77435e-06	1.65775e-07	4.23292e-07	4.54596e-07
5.25	1.98627e-06	8.91037e-08	1.8321e-07	2.03728e-07
5.75	9.7873e-07	6.53325e-08	9.99048e-08	1.1937e-07
6.25	5.03365e-07	3.62429e-08	5.34714e-08	6.45968e-08
6.75	2.84978e-07	2.40176e-08	3.32911e-08	4.10505e-08
7.25	1.3506e-07	1.55558e-08	1.87765e-08	2.43832e-08
7.75	8.00447e-08	1.14597e-08	1.30016e-08	1.73311e-08
8.25	6.45039e-08	1.00876e-08	1.12402e-08	1.51031e-08
8.75	3.03033e-08	6.67949e-09	7.07436e-09	9.72945e-09
9.5	1.96306e-08	3.59252e-09	3.90046e-09	5.30282e-09
10.5	8.46043e-09	2.55243e-09	2.6999e-09	3.71543e-09
11.5	2.9221e-09	1.46138e-09	1.49633e-09	2.09156e-09

Table F.11: Lorentz invariant yield of π^0's in the 80-92 most central Au+Au events at $\sqrt{s_{NN}}$ = 200 GeV.

p_T	yield	statistical uncertainty	systematic uncertainty	total uncertainty
1.25	1.00934	0.00837738	0.136273	0.13653
1.75	0.170843	0.00137704	0.0156525	0.015713
2.25	0.0338284	0.000271522	0.00302705	0.0030392
2.75	0.00783483	6.31562e-05	0.000711001	0.0007138
3.25	0.00207791	1.68824e-05	0.000189832	0.000190581
3.75	0.000634183	5.2398e-06	5.74317e-05	5.76702e-05
4.25	0.000222145	1.88445e-06	1.97072e-05	1.97971e-05
4.75	8.62264e-05	7.64216e-07	7.42689e-06	7.46611e-06
5.25	3.71552e-05	3.42581e-07	3.09296e-06	3.11188e-06
5.75	1.75341e-05	1.73282e-07	1.41003e-06	1.42064e-06
6.25	8.65123e-06	9.45033e-08	6.73598e-07	6.80195e-07
6.75	4.76433e-06	5.64614e-08	3.60689e-07	3.65081e-07
7.25	2.63128e-06	3.64932e-08	1.95738e-07	1.99111e-07
7.75	1.56271e-06	2.43724e-08	1.14816e-07	1.17374e-07
8.25	9.73997e-07	1.77135e-08	7.18479e-08	7.39993e-08
8.75	5.99016e-07	1.26352e-08	4.46035e-08	4.63586e-08
9.5	3.2286e-07	6.3332e-09	2.41163e-08	2.4934e-08
10.5	1.46454e-07	3.92302e-09	1.20419e-08	1.26648e-08
11.5	7.42401e-08	2.65713e-09	6.79981e-09	7.30053e-09
13	2.39876e-08	1.40201e-09	2.86856e-09	3.19284e-09
15	9.17752e-09	5.79852e-10	1.41316e-09	1.52749e-09
17	3.12925e-09	3.55593e-10	6.83639e-10	7.70589e-10
19	6.64294e-10	1.82152e-10	2.56972e-10	3.14982e-10

Table F.12: Lorentz invariant yield of π^0's in the 0-92% most central Au+Au events at $\sqrt{s_{NN}}$ = 200 GeV.

G. η Data Tables

p_T	yield	statistical uncertainty	systematic uncertainty	total uncertainty
1.75	0.0553185	0.00139679	0.0168572	0.0169149
2.25	0.0132129	0.000287022	0.00278321	0.00279797
2.75	0.00328442	7.61464e-05	0.00058391	0.000588854
3.25	0.00101626	2.40906e-05	0.000162274	0.000164052
3.75	0.00033955	8.60332e-06	5.10214e-05	5.17416e-05
4.25	0.000116155	3.36287e-06	1.67309e-05	1.70655e-05
4.75	4.91685e-05	1.47233e-06	6.86147e-06	7.01766e-06
5.25	1.80516e-05	6.84399e-07	2.50344e-06	2.5953e-06
5.75	9.65762e-06	3.65559e-07	1.30708e-06	1.35724e-06
6.25	4.17058e-06	2.01231e-07	5.74491e-07	6.08714e-07
6.75	2.26907e-06	1.20743e-07	3.12979e-07	3.35462e-07
7.25	1.57782e-06	8.51034e-08	2.14792e-07	2.31038e-07
7.75	7.14468e-07	5.17807e-08	1.05775e-07	1.17769e-07
9	2.20105e-07	1.06813e-08	2.83772e-08	3.03209e-08
11	5.47159e-08	3.85735e-09	7.38993e-09	8.33608e-09
13	9.76041e-09	1.66758e-09	2.03286e-09	2.62932e-09
15	5.16136e-09	7.9954e-10	1.04925e-09	1.31916e-09

Table G.1: Lorentz invariant yield of η's in the 0-92% most central Au+Au events at $\sqrt{s_{NN}}$ = 200 GeV.

p_T	yield	statistical uncertainty	systematic uncertainty	total uncertainty
1.75	0.190242	0.0103106	0.0481825	0.0492733
2.25	0.0484521	0.00220757	0.00968289	0.00993135
2.75	0.0100758	0.000599877	0.0019022	0.00199455
3.25	0.00317003	0.0001878	0.000562986	0.000593483
3.75	0.00108853	6.52352e-05	0.000187912	0.000198913
4.25	0.000277033	2.48081e-05	5.07196e-05	5.64617e-05
4.75	0.000116885	1.07353e-05	2.24134e-05	2.48517e-05
5.25	4.68901e-05	4.99204e-06	9.18882e-06	1.04573e-05
5.75	2.24925e-05	2.5031e-06	4.27805e-06	4.95653e-06
6.25	1.13407e-05	1.36765e-06	2.21793e-06	2.6057e-06
6.75	6.29908e-06	8.02696e-07	1.24028e-06	1.47737e-06
7.25	5.99853e-06	5.64522e-07	1.04789e-06	1.19028e-06
7.75	2.06113e-06	2.9786e-07	4.43667e-07	5.3438e-07
9	6.45618e-07	5.77946e-08	1.09261e-07	1.23605e-07
11	1.39007e-07	1.69957e-08	2.62801e-08	3.1297e-08
13	1.03361e-08	8.05325e-09	8.16727e-09	1.14699e-08
15	1.52119e-08	3.9488e-09	4.69787e-09	6.13702e-09

Table G.2: Lorentz invariant yield of η's in the 00-10% most central Au+Au events at $\sqrt{s_{NN}}$ = 200 GeV.

p_T	yield	statistical uncertainty	systematic uncertainty	total uncertainty
1.75	0.104577	0.00377985	0.0454225	0.0455795
2.25	0.0255609	0.000803228	0.00732552	0.00736943
2.75	0.00713755	0.000223689	0.00164675	0.00166187
3.25	0.00213511	7.06115e-05	0.000425913	0.000431727
3.75	0.00068399	2.53772e-05	0.000125829	0.000128363
4.25	0.000250093	1.01847e-05	4.29779e-05	4.41682e-05
4.75	0.000104995	4.53332e-06	1.73428e-05	1.79255e-05
5.25	3.76814e-05	2.11594e-06	6.1865e-06	6.53835e-06
5.75	1.98446e-05	1.11801e-06	3.16602e-06	3.35763e-06
6.25	8.95514e-06	6.19653e-07	1.45362e-06	1.58018e-06
6.75	4.6043e-06	3.6168e-07	7.6331e-07	8.44662e-07
7.25	2.97225e-06	2.4077e-07	4.81674e-07	5.38498e-07
7.75	1.81092e-06	1.55222e-07	2.95113e-07	3.33445e-07
9	4.50926e-07	3.11662e-08	6.79867e-08	7.47898e-08
11	1.08516e-07	9.7879e-09	1.71884e-08	1.97799e-08
13	2.96091e-08	5.03215e-09	6.34523e-09	8.09842e-09
15	8.32804e-09	2.22623e-09	2.48358e-09	3.33531e-09

Table G.3: Lorentz invariant yield of η's in the 10-30% most central Au+Au events at $\sqrt{s_{NN}}$ = 200 GeV.

p_T	yield	statistical uncertainty	systematic uncertainty	total uncertainty
1.75	0.034045	0.000994396	0.00660494	0.00667937
2.25	0.00939153	0.000210521	0.00138885	0.00140471
2.75	0.00233853	5.91592e-05	0.000318219	0.000323671
3.25	0.000693911	1.9515e-05	9.13762e-05	9.34369e-05
3.75	0.00022493	7.20546e-06	2.91083e-05	2.99869e-05
4.25	8.36557e-05	3.07337e-06	1.07816e-05	1.12111e-05
4.75	4.20957e-05	1.47066e-06	5.29851e-06	5.49882e-06
5.25	1.67118e-05	7.27301e-07	2.1319e-06	2.25254e-06
5.75	8.63655e-06	4.2832e-07	1.10225e-06	1.18254e-06
6.25	3.90443e-06	2.64194e-07	5.29728e-07	5.91954e-07
6.75	2.40691e-06	1.64314e-07	3.32521e-07	3.70903e-07
7.25	1.42455e-06	1.1116e-07	1.95549e-07	2.24936e-07
7.75	7.22988e-07	7.40688e-08	1.11257e-07	1.33658e-07
9	2.2588e-07	1.6838e-08	2.99977e-08	3.44003e-08
11	5.1463e-08	5.20588e-09	8.07555e-09	9.60811e-09
13	9.18952e-09	2.80816e-09	3.08379e-09	4.1708e-09
15	4.48165e-09	1.54353e-09	1.62673e-09	2.24249e-09

Table G.4: Lorentz invariant yield of η's in the 30-60% most central Au+Au events at $\sqrt{s_{NN}}$ = 200 GeV.

p_T	yield	statistical uncertainty	systematic uncertainty	total uncertainty
1.75	0.00462935	0.000145332	0.00127119	0.00127947
2.25	0.00116427	3.27681e-05	0.000226448	0.000228807
2.75	0.000310189	9.89472e-06	5.17771e-05	5.27141e-05
3.25	0.000111946	3.55677e-06	1.71616e-05	1.75263e-05
3.75	4.08605e-05	1.5216e-06	5.98091e-06	6.17143e-06
4.25	1.62626e-05	8.29794e-07	2.38255e-06	2.52292e-06
4.75	6.22591e-06	3.84441e-07	1.04456e-06	1.11306e-06
5.25	3.15546e-06	2.25891e-07	4.6783e-07	5.19512e-07
5.75	1.62323e-06	1.28189e-07	2.39969e-07	2.72062e-07
6.25	7.04188e-07	8.64683e-08	1.24371e-07	1.51476e-07
6.75	3.37289e-07	4.58702e-08	6.39866e-08	7.87296e-08
7.25	2.46004e-07	3.27198e-08	4.86644e-08	5.86414e-08
7.75	1.11301e-07	2.38895e-08	2.7839e-08	3.6684e-08
9	3.88704e-08	5.75238e-09	7.74793e-09	9.64989e-09
11	1.02485e-08	1.74875e-09	2.15342e-09	2.77405e-09

Table G.5: Lorentz invariant yield of η's in the 60-92% most central Au+Au events at $\sqrt{s_{NN}}$ = 200 GeV.

H. Direct Photon Data Tables

p_T	yield	statistical uncertainty	systematic uncertainty	total uncertainty
4.75	5.56627e-05	6.0084e-07	8.32016e-06	8.34182e-06
5.25	2.85983e-05	3.55122e-07	3.82889e-06	3.84532e-06
5.75	1.51348e-05	2.26731e-07	1.90825e-06	1.92167e-06
6.25	8.84938e-06	1.55952e-07	1.04366e-06	1.05525e-06
6.75	5.68236e-06	1.1258e-07	6.27439e-07	6.37459e-07
7.25	3.42099e-06	8.31716e-08	3.81425e-07	3.90387e-07
7.75	2.22975e-06	6.29092e-08	2.44282e-07	2.52252e-07
9	8.60782e-07	1.72271e-08	8.6532e-08	8.82301e-08
11	2.39698e-07	8.54535e-09	2.39186e-08	2.53992e-08
13	7.0605e-08	4.33177e-09	7.91361e-09	9.02161e-09
15	2.16913e-08	2.28494e-09	3.09579e-09	3.84771e-09
18	6.33106e-09	7.8053e-10	9.87618e-10	1.25882e-09

Table H.1: Lorentz invariant yield of direct photons in the 0-5% most central Au+Au events at $\sqrt{s_{NN}}$ = 200 GeV.

p_T	yield	statistical uncertainty	systematic uncertainty	total uncertainty
4.75	4.15248e-05	5.50223e-07	6.95239e-06	6.97413e-06
5.25	2.20514e-05	3.26178e-07	3.15992e-06	3.17671e-06
5.75	1.23116e-05	2.11165e-07	1.5972e-06	1.6111e-06
6.25	6.88149e-06	1.43693e-07	8.52765e-07	8.64787e-07
6.75	4.35206e-06	1.0403e-07	5.00222e-07	5.10925e-07
7.25	2.77109e-06	7.79225e-08	3.14583e-07	3.24091e-07
7.75	1.68628e-06	5.80327e-08	1.92781e-07	2.01326e-07
9	6.94714e-07	1.55747e-08	6.98565e-08	7.15716e-08
11	1.63822e-07	6.95941e-09	1.69173e-08	1.82929e-08
13	6.96584e-08	4.23308e-09	7.57649e-09	8.67884e-09
15	1.93192e-08	2.10442e-09	2.79861e-09	3.50154e-09
18	4.14935e-09	6.27599e-10	7.41615e-10	9.71531e-10

Table H.2: Lorentz invariant yield of direct photons in the 5-10% most central Au+Au events at $\sqrt{s_{NN}}$ = 200 GeV.

p_T	yield	statistical uncertainty	systematic uncertainty	total uncertainty
4.75	3.18751e-05	4.96861e-07	5.8935e-06	5.9144e-06
5.25	1.68984e-05	2.94575e-07	2.6331e-06	2.64953e-06
5.75	8.96047e-06	1.8877e-07	1.29786e-06	1.31152e-06
6.25	5.18388e-06	1.28721e-07	6.96785e-07	7.08574e-07
6.75	3.53112e-06	9.31585e-08	4.17701e-07	4.27963e-07
7.25	2.29228e-06	7.07175e-08	2.65108e-07	2.74378e-07
7.75	1.41008e-06	5.27576e-08	1.63946e-07	1.72225e-07
9	5.69355e-07	1.41166e-08	5.78389e-08	5.95367e-08
11	1.42784e-07	6.38472e-09	1.48444e-08	1.61593e-08
13	4.10411e-08	3.29179e-09	5.11458e-09	6.08234e-09
15	1.90559e-08	2.0896e-09	2.73363e-09	3.44081e-09

Table H.3: Lorentz invariant yield of direct photons in the 10-15% most central Au+Au events at $\sqrt{s_{NN}}$ = 200 GeV.

p_T	yield	statistical uncertainty	systematic uncertainty	total uncertainty
4.75	2.71165e-05	4.66212e-07	4.97488e-06	4.99668e-06
5.25	1.4782e-05	2.78828e-07	2.22752e-06	2.2449e-06
5.75	7.34335e-06	1.78793e-07	1.07635e-06	1.0911e-06
6.25	4.4442e-06	1.2227e-07	5.8269e-07	5.9538e-07
6.75	2.98156e-06	8.80012e-08	3.45248e-07	3.56287e-07
7.25	1.76802e-06	6.48495e-08	2.10348e-07	2.20117e-07
7.75	1.1658e-06	4.90093e-08	1.34735e-07	1.43372e-07
9	4.61396e-07	1.26252e-08	4.58658e-08	4.75717e-08
11	1.07649e-07	5.47946e-09	1.138e-08	1.26305e-08
13	4.23178e-08	3.32822e-09	5.01325e-09	6.01745e-09
15	1.38073e-08	1.7357e-09	2.15987e-09	2.77087e-09

Table H.4: Lorentz invariant yield of direct photons in the 15-20% most central Au+Au events at $\sqrt{s_{NN}}$ = 200 GeV.

p_T	yield	statistical uncertainty	systematic uncertainty	total uncertainty
4.75	1.64454e-05	3.32082e-07	3.91232e-06	3.92639e-06
5.25	8.65476e-06	1.89876e-07	1.69916e-06	1.70973e-06
5.75	4.53858e-06	1.19131e-07	8.20933e-07	8.29531e-07
6.25	2.85583e-06	7.96123e-08	4.38011e-07	4.45187e-07
6.75	1.95321e-06	5.57911e-08	2.53252e-07	2.59325e-07
7.25	1.26719e-06	4.13583e-08	1.58265e-07	1.6358e-07
7.75	7.28222e-07	3.01382e-08	9.40952e-08	9.88039e-08
9	2.86926e-07	7.53722e-09	3.08047e-08	3.17134e-08
11	8.40111e-08	3.48898e-09	8.3271e-09	9.02849e-09
13	2.21596e-08	1.66568e-09	2.65427e-09	3.13363e-09
15	9.00612e-09	9.93169e-10	1.28632e-09	1.62511e-09

Table H.5: Lorentz invariant yield of direct photons in the 20-30% most central Au+Au events at $\sqrt{s_{NN}}$ = 200 GeV.

p_T	yield	statistical uncertainty	systematic uncertainty	total uncertainty
4.75	9.16504e-06	2.65649e-07	2.62647e-06	2.63987e-06
5.25	5.54656e-06	1.55525e-07	1.14965e-06	1.16013e-06
5.75	3.16568e-06	9.89172e-08	5.63648e-07	5.72262e-07
6.25	1.77192e-06	6.63905e-08	2.97398e-07	3.04718e-07
6.75	1.1315e-06	4.63255e-08	1.68758e-07	1.75001e-07
7.25	6.12506e-07	3.39589e-08	1.01332e-07	1.06871e-07
7.75	5.09574e-07	2.54143e-08	6.71367e-08	7.17859e-08
9	1.755e-07	6.16966e-09	2.04571e-08	2.13672e-08
11	5.64553e-08	2.90744e-09	5.8784e-09	6.55811e-09
13	1.29241e-08	1.29549e-09	1.83273e-09	2.24437e-09
15	3.77238e-09	6.93326e-10	8.09009e-10	1.06546e-09

Table H.6: Lorentz invariant yield of direct photons in the 30-40% most central Au+Au events at $\sqrt{s_{NN}}$ = 200 GeV.

p_T	yield	statistical uncertainty	systematic uncertainty	total uncertainty
4.75	4.76241e-06	2.15073e-07	2.43899e-06	2.44845e-06
5.25	3.15537e-06	1.28034e-07	1.06069e-06	1.06839e-06
5.75	1.45778e-06	8.22681e-08	5.0779e-07	5.14411e-07
6.25	9.07058e-07	5.54926e-08	2.63108e-07	2.68896e-07
6.75	5.53863e-07	3.83363e-08	1.42659e-07	1.47721e-07
7.25	3.24972e-07	2.82297e-08	8.51944e-08	8.97497e-08
7.75	2.58266e-07	2.05613e-08	5.22099e-08	5.61128e-08
9	1.03144e-07	4.9991e-09	1.54364e-08	1.62257e-08
11	2.48486e-08	2.08721e-09	3.66176e-09	4.21485e-09
13	1.11737e-08	1.17494e-09	1.58186e-09	1.97047e-09
15	3.59842e-09	6.33987e-10	7.1928e-10	9.58803e-10

Table H.7: Lorentz invariant yield of direct photons in the 40-50% most central Au+Au events at $\sqrt{s_{NN}}$ = 200 GeV.

p_T	yield	statistical uncertainty	systematic uncertainty	total uncertainty
4.75	1.00839e-06	1.72813e-07	1.56708e-06	1.57658e-06
5.25	8.7523e-07	1.04926e-07	6.7857e-07	6.86634e-07
5.75	5.24669e-07	6.73854e-08	3.2569e-07	3.32588e-07
6.25	2.63882e-07	4.52303e-08	1.68034e-07	1.74015e-07
6.75	2.89818e-07	3.08478e-08	9.23416e-08	9.73579e-08
7.25	1.15216e-07	2.29782e-08	5.50734e-08	5.96747e-08
7.75	9.46527e-08	1.62845e-08	3.34237e-08	3.71797e-08
9	4.38214e-08	3.86344e-09	9.31948e-09	1.00886e-08
11	1.14562e-08	1.57684e-09	2.30758e-09	2.79488e-09
13	4.08657e-09	7.74422e-10	9.156e-10	1.19919e-09

Table H.8: Lorentz invariant yield of direct photons in the 50-60% most central Au+Au events at $\sqrt{s_{NN}}$ = 200 GeV.

p_T	yield	statistical uncertainty	systematic uncertainty	total uncertainty
4.75	8.42104e-07	1.16308e-07	7.91127e-07	7.99631e-07
5.25	6.22595e-07	7.24028e-08	3.48145e-07	3.55594e-07
5.75	3.45057e-07	4.75003e-08	1.72086e-07	1.78521e-07
6.25	1.75346e-07	3.23206e-08	9.1631e-08	9.7164e-08
6.75	1.72481e-07	2.24294e-08	5.24423e-08	5.70375e-08
7.25	3.75872e-08	1.70501e-08	3.23173e-08	3.65393e-08
7.75	3.5103e-08	1.22153e-08	2.02176e-08	2.36212e-08
9	1.2833e-08	2.93289e-09	5.55758e-09	6.28399e-09
11	2.2877e-09	1.19454e-09	1.49041e-09	1.91003e-09
13	1.35325e-09	5.52083e-10	6.09506e-10	8.22371e-10

Table H.9: Lorentz invariant yield of direct photons in the 60-70% most central Au+Au events at $\sqrt{s_{NN}}$ = 200 GeV.

p_T	yield	statistical uncertainty	systematic uncertainty	total uncertainty
4.75	2.44526e-08	9.51251e-08	5.4603e-07	5.54254e-07
5.25	1.76412e-07	5.12723e-08	1.74199e-07	1.81587e-07
6.25	6.39919e-08	2.24949e-08	4.6301e-08	5.14763e-08
6.75	5.71978e-08	1.51027e-08	2.69453e-08	3.08892e-08
7.25	1.98837e-08	1.13215e-08	1.71249e-08	2.0529e-08
9	6.89089e-09	1.90434e-09	2.79522e-09	3.38227e-09
11	1.94517e-09	7.87342e-10	8.85696e-10	1.18506e-09

Table H.10: Lorentz invariant yield of direct photons in the 70-80% most central Au+Au events at $\sqrt{s_{NN}}$ = 200 GeV.

p_T	yield	statistical uncertainty	systematic uncertainty	total uncertainty
4.75	1.33734e-07	4.35126e-08	1.64199e-07	1.69867e-07
5.25	1.11679e-07	2.71497e-08	7.30751e-08	7.79556e-08
5.75	2.73863e-08	1.82096e-08	3.71464e-08	4.13696e-08
6.25	2.32872e-08	1.23402e-08	2.05814e-08	2.39974e-08
6.75	1.94627e-08	8.45455e-09	1.22374e-08	1.48739e-08
7.75	2.6662e-09	5.46667e-09	4.09557e-09	6.83068e-09
11	7.99572e-10	4.25024e-10	4.5633e-10	6.23604e-10

Table H.11: Lorentz invariant yield of direct photons in the 80-92 most central Au+Au events at $\sqrt{s_{NN}}$ = 200 GeV.

p_T	yield	statistical uncertainty	systematic uncertainty	total uncertainty
4.75	1.38825e-05	1.33466e-07	2.6086e-06	2.61202e-06
5.25	7.1772e-06	6.6682e-08	1.15487e-06	1.1568e-06
5.75	3.76122e-06	3.77714e-08	5.65641e-07	5.66901e-07
6.25	2.20113e-06	2.35674e-08	3.0214e-07	3.03057e-07
6.75	1.4093e-06	1.5832e-08	1.73921e-07	1.7464e-07
7.25	8.53979e-07	1.12723e-08	1.05063e-07	1.05666e-07
7.75	5.44017e-07	8.18379e-09	6.42756e-08	6.47945e-08
9	2.10449e-07	2.0589e-09	2.21806e-08	2.22759e-08
11	5.56694e-08	9.31618e-10	5.35351e-09	5.43397e-09
13	1.80158e-08	4.89127e-10	1.7086e-09	1.77723e-09
15	6.09405e-09	2.67367e-10	6.18435e-10	6.73756e-10
18	1.57888e-09	8.54288e-11	1.67694e-10	1.88201e-10

Table H.12: Lorentz invariant yield of direct photons in the 0-92% most central Au+Au events at $\sqrt{s_{\mathrm{NN}}}$ = 200 GeV.

Bibliography

[Ack03] K. H. Ackermann et al. *Nucl. Instrum. Meth.* **A499** (2003) 624.

[Ada03a] M. Adamczyk et al. *Nucl. Instrum. Meth.* **A499** (2003) 437.

[Ada03b] J. Adams et al. *Phys. Rev. Lett.* **91** (2003) 072304. nucl-ex/0306024.

[Ada03c] J. Adams et al. *Phys. Rev. Lett.* **91** (2003) 172302. nucl-ex/0305015.

[Ada04a] J. Adams et al. *Phys. Rev. Lett.* **93** (2004) 012301. nucl-ex/0312009.

[Ada04b] J. Adams et al. *Phys. Rev. Lett.* **92** (2004) 052302. nucl-ex/0306007.

[Ada05] J. Adams et al. *Nucl. Phys.* **A757** (2005) 102. nucl-ex/0501009.

[Ada07] A. Adare et al. *Phys. Rev.* **D76** (2007) 051106. 0704.3599.

[Ada08a] A. Adare et al. 0804.4168.

[Ada08b] A. Adare et al. *Phys. Rev. Lett.* **101** (2008) 162301. 0801.4555.

[Ada08c] A. Adare et al. *Phys. Rev.* **C77** (2008) 064907. 0801.1665.

[Ada08d] A. Adare et al. *Phys. Rev. Lett.* **101** (2008) 232301. 0801.4020.

[Ada09] A. Adare et al. *Phys. Lett.* **B670** (2009) 313. 0802.0050.

[Adc02] K. Adcox et al. *Phys. Rev. Lett.* **88** (2002) 022301. nucl-ex/0109003.

[Adc03a] K. Adcox et al. *Phys. Lett.* **B561** (2003) 82. nucl-ex/0207009.

[Adc03b] K. Adcox et al. *Nucl. Instrum. Meth.* **A499** (2003) 489.

[Adc03c] K. Adcox et al. *Nucl. Instrum. Meth.* **A499** (2003) 469.

[Adc05] K. Adcox et al. *Nucl. Phys.* **A757** (2005) 184. nucl-ex/0410003.

[Adl02] C. Adler et al. *Phys. Rev. Lett.* **89** (2002) 202301. nucl-ex/0206011.

[Adl03a] C. Adler et al. *Phys. Rev. Lett.* **90** (2003) 082302. nucl-ex/0210033.

[Adl03b] C. Adler et al. *Nucl. Instrum. Meth.* **A499** (2003) 433.

[Adl03c] S. S. Adler et al. *Phys. Rev. Lett.* **91** (2003) 072303. nucl-ex/0306021.

[Adl03d] S. S. Adler et al. *Phys. Rev. Lett.* **91** (2003) 182301. nucl-ex/0305013.

[Adl03e] S. S. Adler et al. *Nucl. Instrum. Meth.* **A499** (2003) 560.

[Adl03f] S. S. Adler et al. *Phys. Rev. Lett.* **91** (2003) 072301. nucl-ex/0304022.

[Adl04a] S. S. Adler et al. *Phys. Rev. Lett.* **93** (2004) 152302. nucl-ex/0401003.

[Adl04b] S. S. Adler et al. *Phys. Rev.* **C69** (2004) 034910. nucl-ex/0308006.

[Adl05] S. S. Adler et al. *Phys. Rev. Lett.* **94** (2005) 232301. nucl-ex/0503003.

[Adl06] S. S. Adler et al. *Phys. Rev. Lett.* **96** (2006) 202301. nucl-ex/0601037.

[Adl07a] S. S. Adler et al. *Phys. Rev.* **C76** (2007) 034904. nucl-ex/0611007.

[Adl07b] S. S. Adler et al. *Phys. Rev. Lett.* **98** (2007) 172302. nucl-ex/0610036.

[Adl07c] S. S. Adler et al. *Phys. Rev.* **C75** (2007) 024909. nucl-ex/0611006.

[Adl07d] S. S. Adler et al. *Phys. Rev. Lett.* **98** (2007) 012002. hep-ex/0609031.

[Afa07] S. Afanasiev et al. 0706.3034.

[Agg00] M. M. Aggarwal et al. nucl-ex/0006007.

[Aiz03] M. Aizawa et al. *Nucl. Instrum. Meth.* **A499** (2003) 508.

[Aki03] H. Akikawa et al. *Nucl. Instrum. Meth.* **A499** (2003) 537.

[All03] M. Allen et al. *Nucl. Instrum. Meth.* **A499** (2003) 549.

[Ams08] C. Amsler et al. *Phys. Lett.* **B667** (2008) 1.

[And06] A. Andronic, P. Braun-Munzinger and J. Stachel. *Nucl. Phys.* **A772** (2006) 167. nucl-th/0511071.

[Ant79] D. Antreasyan et al. *Phys. Rev.* **D19** (1979) 764.

[Aph03] L. Aphecetche et al. *Nucl. Instrum. Meth.* **A499** (2003) 521.

[Arl06] F. Arleo. *JHEP* **09** (2006) 015. hep-ph/0601075.

[Arn95] M. Arneodo et al. *Nucl. Phys.* **B441** (1995) 12. hep-ex/9504002.

[Arn00] P. Arnold, G. D. Moore and L. G. Yaffe. *JHEP* **11** (2000) 001. hep-ph/0010177.

[Aro03] S. H. Aronson et al. *Nucl. Instrum. Meth.* **A499** (2003) 480.

[Ars03] I. Arsene et al. *Phys. Rev. Lett.* **91** (2003) 072305. nucl-ex/0307003.

[Ars05] I. Arsene et al. *Nucl. Phys.* **A757** (2005) 1. nucl-ex/0410020.

[Aub83] J. J. Aubert et al. *Phys. Lett.* **B123** (1983) 275.

[Ave03] R. Averbeck. *EXODUS Event Generator*. PHENIX CVS Repository offline/analysis/exodus, 2003.

[Awe01a] T. C. Awes et al. *Neutral Pion Spectra from the Leadglass Calorimeter*. PHENIX Internal Analysis Note 69, 2001.

[Awe01b] T. C. Awes et al. *Neutral Pion Spectra from the Leadglass Calorimeter with Limited Photon Pair Energy Asymmetry* . PHENIX Internal Analysis Note 73, 2001.

[Bac03a] B. B. Back et al. *Nucl. Instrum. Meth.* **A499** (2003) 603.

[Bac03b] B. B. Back et al. *Phys. Rev. Lett.* **91** (2003) 052303. nucl-ex/0210015.

[Bac04] B. B. Back et al. *Phys. Lett.* **B578** (2004) 297. nucl-ex/0302015.

[Bac05] B. B. Back et al. *Nucl. Phys.* **A757** (2005) 28. nucl-ex/0410022.

[Bai97a] R. Baier, Y. L. Dokshitzer, A. H. Mueller et al. *Nucl. Phys.* **B484** (1997) 265. hep-ph/9608322.

[Bai97b] R. Baier, Y. L. Dokshitzer, A. H. Mueller et al. *Nucl. Phys.* **B483** (1997) 291. hep-ph/9607355.

[Bai98] R. Baier, Y. L. Dokshitzer, A. H. Mueller et al. *Phys. Rev.* **C58** (1998) 1706. hep-ph/9803473.

[Bai00] R. Baier, D. Schiff and B. G. Zakharov. *Ann. Rev. Nucl. Part. Sci.* **50** (2000) 37. hep-ph/0002198.

[Bai03] R. Baier. *Nucl. Phys.* **A715** (2003) 209. hep-ph/0209038.

[Bar77] B. C. Barrois. *Nucl. Phys.* **B129** (1977) 390.

[Bat05] S. Bathe, A. Bazilewsky and H. Buesching. *Neutral Pion Spectra measured with the EMCal in $\sqrt{s} = 200$ GeV $p+p$ Collisions, PHENIX Run 3 Preliminary Result*. PHENIX Internal Analysis Note 470, 2005.

[Bau09] C. Baumann. *Neutral Pion and Direct Photon Production in the SPS Energy Regime*. Phd thesis, University of Muenster, 2009.

[Baz09] A. Bazavov et al. *Phys. Rev.* **D80** (2009) 014504. 0903.4379.

[Ben07] R. Bennett, T. Horaguchi and K. Okada. *Measurement of the direct photon cross section and double helicity asymmetry in polarized proton-proton collision at sqrts=200 GeV from Run5*. PHENIX Internal Analysis Note 528, 2007. And personal communication with K. Okada.

[Bet34] H. Bethe and W. Heitler. *Proc. Roy. Soc. Lond.* **A146** (1934) 83.

[Bjo76] J. D. Bjorken. *Lect. Notes Phys.* **56** (1976) 93.

[Bjo82] J. D. Bjorken FERMILAB-PUB-82-059-THY.

[Bjo83] J. D. Bjorken. *Phys. Rev.* **D27** (1983) 140.

[Blo69] E. D. Bloom et al. *Phys. Rev. Lett.* **23** (1969) 930.

[BM07] P. Braun-Munzinger and J. Stachel. *Nature* **448** (2007) 302.

[BM09] P. Braun-Munzinger and J. Stachel 0901.2500.

[Bou76] M. Bourquin and J. M. Gaillard. *Nucl. Phys.* **B114** (1976) 334.

[Bre69] M. Breidenbach et al. *Phys. Rev. Lett.* **23** (1969) 935.

[Bru93] R. Brun and F. Carminati Cern Program Library Long Writers W5013.

[Cap02] A. Capella, A. B. Kaidalov and D. Sousa. *Phys. Rev.* **C65** (2002) 054908. nucl-th/0105021.

[Cho74] A. Chodos, R. L. Jaffe, K. Johnson et al. *Phys. Rev.* **D9** (1974) 3471.

[Col75] J. C. Collins and M. J. Perry. *Phys. Rev. Lett.* **34** (1975) 1353.

[Col85] J. C. Collins, D. E. Soper and G. Sterman. *Nucl. Phys.* **B261** (1985) 104.

[Cro75] J. W. Cronin et al. *Phys. Rev.* **D11** (1975) 3105.

[Dai05] A. Dainese, C. Loizides and G. Paic. *Eur. Phys. J.* **C38** (2005) 461. hep-ph/0406201.

[d'E04] D. d'Enterria. *Photon conversions in the central-arms for Runs 1-3*. PHENIX Internal Analysis Note 322, 2004.

[d'E09] D. d'Enterria 0902.2011.

[Ell08] F. Ellinghaus 0808.4124.

[Fab03] C. W. Fabjan and F. Gianotti. *Rev. Mod. Phys.* **75** (2003) 1243.

[Fel98] G. J. Feldman and R. D. Cousins. *Phys. Rev.* **D57** (1998) 3873. physics/9711021.

[Fer09] Fermilab. *Acronyms of High-Energy Physics* . Website, 2009. http://www.fnal.gov/pub/inquiring/more/acronyms.html.

[Fri03] R. J. Fries, B. Muller and D. K. Srivastava. *Phys. Rev. Lett.* **90** (2003) 132301. nucl-th/0208001.

[Gal09] C. Gale 0904.2184.

[GM64] M. Gell-Mann. *Phys. Lett.* **8** (1964) 214.

[Gor93] L. E. Gordon and W. Vogelsang. *Phys. Rev.* **D48** (1993) 3136.

[Gyu00a] M. Gyulassy, P. Levai and I. Vitev. *Nucl. Phys.* **B571** (2000) 197. hep-ph/9907461.

[Gyu00b] M. Gyulassy, P. Levai and I. Vitev. *Phys. Rev. Lett.* **85** (2000) 5535. nucl-th/0005032.

[Gyu01] M. Gyulassy, P. Levai and I. Vitev. *Nucl. Phys.* **B594** (2001) 371. nucl-th/0006010.

[Gyu05] M. Gyulassy and L. McLerran. *Nucl. Phys.* **A750** (2005) 30. nucl-th/0405013.

[Hag84] R. Hagedorn. *Riv. Nuovo Cim.* **6N10** (1984) 1.

[Hah03] H. Hahn et al. *Nucl. Instrum. Meth.* **A499** (2003) 245.

[Har96] J. W. Harris and B. Muller. *Ann. Rev. Nucl. Part. Sci.* **46** (1996) 71. hep-ph/9602235.

[Har03] M. Harrison, T. Ludlam and S. Ozaki. *Nucl. Instrum. Meth.* **A499** (2003) 235.

[Hei00] U. W. Heinz and M. Jacob nucl-th/0002042.

[Hie05] H. Hiejima. *Photon Conversion Study for pi^0 and eta in Run-3*. PHENIX Internal Analysis Note 388, 2005.

[Hor] Horowitz, W. *(personal communication)*.

[Iso05] T. Isobe, G. David, T. Sakaguchi et al. *Neutral Pion Spectra measured with the EMCal in sqrts$_{NN}$ = 200GeV Au+Au Collisions at Run4*. PHENIX Internal Analysis Note 444, 2005.

[Iso07] T. Isobe. *Production of Direct Photons and Neutral Pions in Relativistic Au+Au Collisions*. Phd thesis, University of Tokyo, 2007.

[Jan08] K. Jansen 0810.5634.

[Kap91] J. I. Kapusta, P. Lichard and D. Seibert. *Phys. Rev.* **D44** (1991) 2774.

[KB00] C. Klein-Boesing. *Simulation der Detektoreingenschaften des Bleiglaskalorimeters in den Experimenten WA98 und PHENIX*. Diploma thesis, University of Muenster, 2000.

[KB04] C. Klein-Boesing. *Production of Neutral Pions and Direct Photons in Ultra-Relativistic Au+Au Collisions*. Phd thesis, University of Muenster, 2004.

[KB08] C. Klein-Boesing. *J. Phys.* **G35** (2008) 044026. 0710.2960.

[Kel00] S. Kelly, D. Morrison, J. Nagle et al. *Calculation of the Number of Participating Nucleons for Centrality Classes Defined with the ZDC and the BBC Title*. PHENIX Internal Analysis Note 33, 2000.

[Lan53a] L. D. Landau. *Izv. Akad. Nauk SSSR Ser. Fiz.* **17** (1953) 51. Reprinted in *Collective Papers of L. D. Landau*, ed. D. T. ter Haar New York: Gordon & Breach (1965) 569.

[Lan53b] L. D. Landau and I. Pomeranchuk. *Dokl. Akad. Nauk Ser. Fiz.* **92** (1953) 735. Reprinted in *Collective Papers of L. D. Landau*, ed. D. T. ter Haar New York: Gordon & Breach (1965) 586.

[Len99] B. Lenkeit et al. *Nucl. Phys.* **A661** (1999) 23. nucl-ex/9910015.

[Loi] Loizides, C. *(personal communication)*.

[Loi05] C. A. Loizides nucl-ex/0501017.

[Loi07] C. Loizides. *Eur. Phys. J.* **C49** (2007) 339. hep-ph/0608133.

[Lue07] R. Luechtenborg. *Produktion direkter Photonen in ultrarelativistischen Cu+Cu Stößen am PHENIX-Experiment*. Diploma thesis, University of Muenster, 2007.

[Mat86] T. Matsui and H. Satz. *Phys. Lett.* **B178** (1986) 416.

[Mig56] A. B. Migdal. *Phys. Rev.* **103** (1956) 1811.

[Mil07] M. L. Miller, K. Reygers, S. J. Sanders et al. *Ann. Rev. Nucl. Part. Sci.* **57** (2007) 205. nucl-ex/0701025.

[Nag09] J. Nagle. *personal communication*, 2009.

[Oka05] K. Okada and H. Hiejima. *Photon Conversion Study in Run-3 p-p direct photon analysis*. PHENIX Internal Analysis Note 449, 2005.

[PC03] PHENIX-Collaboration. *Conceptual Design Report for High p_T Upgrade*. Technischer Bericht, 2003. http://www.phenix.bnl.gov/WWW/upgrades/highpt/2003/CDR/CDR_final-highpt.pdf.

[Per00] Perkins, D.H. *Introduction to High Energy Physics*. Cambridge University Press, Cambridge, 4th edition, 2000.

[Pet09] P. Petreczky 0908.1917.

[Pos98] A. M. Poskanzer and S. A. Voloshin. *Phys. Rev.* **C58** (1998) 1671. nucl-ex/9805001.

[Pov06] Povh, Bogdan and Rith, Klaus and Scholz, Christoph and Zetsche, Frank. *Teilchen und Kerne. Eine Einführung in die physikalischen Konzepte*. Springer, Heidelberg, 6th edition, 2006.

[Pra09] S. Pratt 0907.1094.

[Rey03] K. Reygers. *Results of Au+Au Glauber Calculations*. Website, 2003. https://www.phenix.bnl.gov/WWW/p/draft/reygers/glauber/tables_auau_200gev.html.

[Rey04] K. Reygers. *Die Suche nach dem Quark-Gluon-Plasma mit dem PHENIX-Experiment am RHIC*. Habilitation thesis, University of Muenster, 2004.

[Rut11] E. Rutherford. *Phil. Mag.* **21** (1911) 669.

[Shu80] E. V. Shuryak. *Phys. Rept.* **61** (1980) 71.

[Sjo94] T. Sjostrand. *Comput. Phys. Commun.* **82** (1994) 74.

[Sjo01] T. Sjostrand et al. *Comput. Phys. Commun.* **135** (2001) 238. hep-ph/0010017.

[Tan04] Tannenbaum, M.J. *(personal communication)*, 2004.

[Tho77] W. Thome et al. *Nucl. Phys.* **B129** (1977) 365.

[Tho95] M. H. Thoma hep-ph/9503400.

[Tse05] I. Tserruya. *Eur. Phys. J.* **C43** (2005) 399. nucl-ex/0505002.

[Tur05] S. Turbide, C. Gale, S. Jeon et al. *Phys. Rev.* **C72** (2005) 014906. hep-ph/0502248.

[Tur08] S. Turbide, C. Gale, E. Frodermann et al. *Phys. Rev.* **C77** (2008) 024909. 0712.0732.

[Ull] T. Ullrich Prepared for 16th International Workshop on Deep Inelastic Scattering and Related Subjects (DIS 2008), London, England, 7-11 Apr 2008.

[Vit] Vitev, I. *(personal communication)*.

[Vit06] I. Vitev. *Phys. Lett.* **B639** (2006) 38. hep-ph/0603010.

[Vit08] I. Vitev and B.-W. Zhang. *Phys. Lett.* **B669** (2008) 337. 0804.3805.

[Vog04] Vogelsang, W. *(personal communication)*, 2004.

[Vog07] Vogt, Ramona. *Ultrarelativistic Heavy-Ion Collisions*. Elsevier, Amsterdam, 1st edition, 2007.

[Wan] Wang, X.-N. *(personal communication)*.

[Wic07] S. Wicks, W. Horowitz, M. Djordjevic et al. *Nucl. Phys.* **A784** (2007) 426. nucl-th/0512076.

[Wie09] U. A. Wiedemann 0908.2306.

[Won94] C. Wong. *Introduction to High-Energy Heavy-Ion Collisions*. World Scientific, Singapore, 1st edition, 1994.

[Woo54] R. D. Woods and D. S. Saxon. *Phys. Rev.* **95** (1954) 577.

[Yag08] Yagi, Koshuke and Hatsuda, Tetsuo and Miake, Yasuo. *Quark-Gluon Plasma*. Cambridge University Press, Cambridge, 1st edition, 2008.

[Yao06] W. M. Yao et al. *J. Phys.* **G33** (2006) 1.

[Zaj04] Zajc, W.A. *(personal communication)*, 2004.

[Zak97] B. G. Zakharov. *JETP Lett.* **65** (1997) 615. hep-ph/9704255.

[Zak07] B. G. Zakharov. *JETP Lett.* **86** (2007) 444. 0708.0816.

[Zap08] K. C. Zapp. *A Monte Carlo Model for Jet Evolution With Energy Loss*. Phd thesis, Ruperto-Carola University of Heidelberg, 2008.

[Zau07] O. Zaudtke. *Measurement of Direct-Photon Production and Neutral Pion Double Helicity Asymmetry in Ultra- Relativistic p+p Collisions*. Phd thesis, University of Muenster, 2007.

[Zha07] H. Zhang, J. F. Owens, E. Wang et al. *Phys. Rev. Lett.* **98** (2007) 212301. nucl-th/0701045.

[Zwe64] G. Zweig CERN-TH-412.

Danksagung

Zu guter Letzt möchte ich mich bei alle jenen Menschen bedanken, die Anteil am Gelingen dieser Dissertation hatten.

Herrn Prof. Dr. Johannes P. Wessels danke ich dafür, mir diese Arbeit in seiner Arbeitsgruppe ermöglicht zu haben und meine Aufenthalte am Brookhaven National Laboratory und die Teilnahme an nationalen und internationalen Konferenzen unterstützt zu haben.

Mein Dank gilt Herrn Priv.-Doz. Dr. Klaus Reygers für die Betreuung meiner Arbeit. Seine Ratschläge und seine Diksussionsbereitschaft haben entscheidend zu dieser Arbeit beigetragen, die Gespräche mit ihm haben mein Verständnis physikalischer Vorgänge deutlich erweitert.

本研究のパイ中間子や直接光子の解析において、実りあるご協力をいただいた磯部忠昭氏に感謝致します。Köszönöm Dr Dávid Gábornak a jó együttműködést, a javaslatait, és a kritikai megjegyzéseit. また、坂口貴男氏には、多大なご支援とPHENIX光子解析グループにおけるご助言をいただきました。心よりお礼申し上げます。

Herrn Dr. Stefan Bathe und Herrn Dr. Henner Büsching danke ich für die hilfreichen Erläuterungen gerade zu Beginn der Promotion.

For the good collaboration in publishing the π^0 data, I would like to thank the papger preparation group (PPG 080), namely Dr Gabor David, Jozsef Imrek, Dr TadaAki Isobe, Dr Christian Klein-Bösing, Dr Martin Purschke, Dr Takao Sakaguchi, and Dr David Winter.

I thank Prof James Nagle for providing me with his code for the statistical analysis. Furthermore, I thank the PHENIX hard/photon physics working group for the fruitfuil discussions.

Für die kritsche Durchsicht des Manuskripts bedanke ich mich vor allem bei Dr. Christian Klein-Bösing, Dr. Gabor David, Dr. Stefan Bathe, Eva Sicking, und auch bei Dr. Christoph Baumann und Dr. Matus Kalisky.

Alexander Wilk danke ich besonders für die gute Atmosphäre im gemeinsamen Büro, ebenso bedanke ich mich bei den anderen Kollegen, die dieses Büro zweitweilig mit uns geteilt haben: Dr. Oliver Zaudtke, Markus Rammler, Manuel Moreno Garcia und Anton Sperling.

Allen aktuellen und ehemaligen Mitgliedern der Arbeitsgruppe danke ich für das angenehme Arbeitsgruppenklima und die gute Zusammenarbeit: Björn Albrecht, Jonas Anielski, Jan Auffenberg, Dr. Christoph Baumann, Cyrano Bergmann, Katharina Büscher, Dr. Thomas Dietel, David Emschermann, Henriette Gatz, Dr. Richard Glasow, Holger Gottschlag, Helge Grimm, Jan Fiete Grosse-Oetringhaus, Markus Heide, Norbert Heine, Matus Kalisky, Sebastian Klamor, Dr. Christian Klein-Bösing, Dr. Melanie Klein-Bösing, Stefan Korsten, Michael Kowalik, Ansgar Kumpmann, Robert Lüchtenborg, Manuel Moreno Garcia, Jan Pietschmann, Friederike Poppenborg, Markus Rammler, Priv.-Doz. Dr. Klaus Reygers, Prof. em. Dr. Rainer Santo, Eva Sicking, Anton Sperling, Wolfgang Verhoeven, Matthias Walter, Uwe Westerhoff, Alexander Wilk, Svenja Wulff, Dr. Oliver Zaudtke.

Für die notwendigen kleineren und größeren Ablenkungen während der Arbeit am Institut in Münster sowie während der Aufenthalte in Brookhaven bedanke ich mich bei Stefan Bathe, Bastian Bathen, Christoph Baumann, Dr. Thomas Dietel, Henriette Gatz, Holger Gottschlag, Markus Heide, Jiamin Jin, Matus Kalisky, Christian Klein-Bösing, Melanie Klein-Bösing, Àstrid Morreale, Misaki Ouchida, Markus Rammler, Eva Sicking, Uwe Westerhoff und Alexander Wilk, sowie ASAP at BNL.

Last but not least bedanke ich mich bei meinen Eltern, dass sie mir mein Studium ermöglicht haben, und bei meinen Freunden für eine schöne Zeit, die ich in Münster (und anderswo) mit ihnen hatte und hoffentlich weiterhin haben werde.